

**Modeling Homo- and Heterogeneous Catalysis
with Applications Ranging from Hydrocarbon Activation to the Synthesis
of Sustainable Polymers**

A THESIS
SUBMITTED TO THE FACULTY OF THE GRADUATE SCHOOL
OF THE UNIVERSITY OF MINNESOTA
BY

Mukunda Mandal

IN PARTIAL FULFILLMENT OF THE REQUIREMENTS
FOR THE DEGREE OF
DOCTOR OF PHILOSOPHY

Professor Christopher J. Cramer, Advisor

August, 2020

© Mukunda Mandal, 2020

ALL RIGHTS RESERVED

Acknowledgment

First and foremost, I would like to thank my advisor Prof. Christopher J. Cramer for his guidance and support over the last five years. He has always shown profound belief in my work and my abilities in general. The scientific freedom that he has given me with regards to taking ownership of my research projects, while offering guidance as necessary, has been decisive in my growth as an independent researcher. I truly appreciate his valuable feedback during my various research presentations in the group, which have contributed greatly towards my development as a professional.

I am extremely grateful to Prof. William B. Tolman for his insightful discussions during our multiple collaborative projects. All this time I have not only benefited scientifically, but also gained invaluable professional training in terms of communicating my research, particularly while writing research papers. I would also like to extend my deepest gratitude to Prof. Laura Gagliardi for her help throughout my time at UMN, specifically for her guidance during the final months in finishing our collaborative project.

I must also thank Prof. Matthew Neurock and, Laura and Bill once again, for agreeing to be my thesis committee members and providing me with helpful suggestions. In addition, I wish to thank a number of faculty who I have collaborated with and have helped and encouraged me along the way: Profs. Donald G. Truhlar, Joachim Sauer, Omar K. Farha, Shannon S. Stahl, and Theresa M. Reineke.

I immensely value my time spent at the NCL, Pune in the group of Prof. Debashree Ghosh, who guided me in getting started with computation and helped me gain some invaluable practical experience in doing research. I am very grateful to all my previous teachers and mentors, especially to Prof. Arogya V. Saha at the RKMR College, Narendrapur for his indispensable role in my development as a chemist.

I am fortunate to collaborate with many experimental colleagues and friends from within and outside the Department. The completion of my dissertation would not have been possible without their help. They have most certainly played a crucial role in helping expand my understanding of chemistries beyond computational chemistry. Utmost thanks to Amani L. Lee, Dr. Anna M. Luke, Caitlin J. Bouchey, Dr. Courtney E. Elwell, Dr. Daniel E. Stasiw, Derek J. Saxon, Dr. Joahanna A. Macaranas, Dr. Joshua A. Buss, Dr. Ken-ichi Otake, Dr. Megan E. Fieser, Si-Jie Chen, and Dr. Sung-Eun Suh for all their efforts and hard work, which have been instrumental in bringing most of our collaborative projects to completion.

I would like to thank all past and current members of the Cramer group for their enjoyable company and insightful discussions. Special thanks to people in the Cramer group I have collaborated with: Dr. Aaron B. League, Dr. Buşra Dereli, Dr. Christine R. Dunbar, Dr. Daniel J. Marell, Dr. Jingyun Ye, Dr. Manuel A. Ortuño, Dr. Ravithree Senanayake, Dr. Saied Md Pratik, and Sina Chiniforoush. Many thanks to Dr. Carlo A. Gaggioli, Dr. J.E.M.N. Klein, and Xuelan Wen for insightful scientific discussions on multiple occasions. Thanks should also go to several members of the staff including Benjamin Lynch of MSI for assistance with computing and to Laura Seifert and Melanie Burns for their remarkable work as managing directors of two research centers I have worked at, the CSP and ICDC, respectively.

I consider myself extremely lucky to have a caring family, standing by me with their love and unconditional support. I am and will always be grateful to my parents, who, by example of their own hard work ethic, always push me to dedicate myself towards my goals. I am very thankful to them for providing me with the best education, even in the face of adversity. My two brothers, especially Surajit have been a resolute support of my studies and interests; and while I am away, Prasenjit takes great care of parents so that I do not have to worry about their health and happiness. A big hug to both! I must also thank all my friends from RKMRC Narendrapur, IIT Bombay, NCL Pune and here at UMN; some really wonderful people who have assisted me with my research, enriched my stay at the respective institute and have had an impact upon me as a person.

Finally, I would like to thank a very special person, my wife Sangita, for her continued and unfailing love, support, and constant encouragement, as I have worked to finish my graduate studies. She has been a wonderful partner, a great friend, and has been critical to my success in Grad School. I cannot underestimate her patience and all the sacrifices she has made for me every step of the way. Thank you for your company. Here is to the future!

Dedication

Dedicated to my family:

My beloved parents, wonderful brothers, and my lovely wife.

Abstract

The diverse chemical properties of compounds containing metal atoms are inherently highly tunable. In terms of size, they may be small molecular complexes consisting of only 1 or 2 metal atoms or, at the other extreme of scale, they may be crystalline solids with clusters of metal ions periodically dispersed in the structure of a metal–organic framework (MOF). In both cases, relevant chemistries can be tailored to fit specific needs, especially with respect to catalytic reactivity. For a molecular catalyst, the combination of metal atom and its ancillary ligand can be chosen carefully to optimize selectivity and activity, while in three-dimensional MOFs, the metal clusters (called nodes) and connecting organic molecules (called linkers) can be ‘mixed and matched’ to best suit a particular application.

Because of the inherent complexity of these systems, experimental characterization of structure/activity relations can often be challenging. Starting from a set of reactants, obtaining a mechanistic picture of the steps leading to the product formation is also demanding since isolation of an intermediate does not necessarily guarantee involvement of the species in the ‘productive’ pathway of the mechanism. Theory and computation can be immensely helpful in these instances to gain molecular-level understanding of the reaction mechanism(s). One can explore multiple pathways that yield the product and then evaluate the feasibility of each pathway by comparing computed energetics. Mechanistic knowledge can then be exploited to establish a structure/property relation, thereby fostering the design of subsequent generations of the catalytic species, ideally having improved performance, and helping to further refine the overall model.

This dissertation demonstrates the use of computational methodologies, primarily quantum mechanical density functional theory, to explore the electronic structures of various metal-organic systems and the roles they play in carrying out targeted catalytic processes. In particular, computational modeling efforts are presented that illuminate (i) mechanisms of sustainable polymer production and principles for designing new catalysts (Chapter 2), (ii) site-selective C–H bond functionalization having relevance in drug discovery and chemical biology (Chapter 3) (iii) C–H activation reactions in light hydrocarbons using bio-mimetic copper-complexes having the potential to address challenges in fuel liquefaction (Chapter 4), and (iv) MOF-based single-site heterogeneous catalysts capable of oxidation reactions having industrial relevance (Chapter 5).

Table of Contents

Acknowledgment.....	i
Dedication.....	iii
Abstract.....	iv
List of Tables.....	x
List of Figures.....	xi
List of Schemes.....	xv
Preface.....	xvi
Chapter 1.....	1
1.1 Computational Chemistry: General Remarks.....	2
1.2 Overview of Computational Methods.....	4
1.2.1 Time-Independent Schrodinger Equation.....	4
1.2.2 <i>Ab initio</i> Hartree-Fock Theory.....	5
1.2.2.1 Hartree Product.....	5
1.2.2.2 Electron Spin and the Slater Determinant.....	6
1.2.2.3 Hartree-Fock Energy Expression.....	7
1.2.2.4 Minimization of HF Energy: the SCF Method.....	7
1.2.3 Density Functional Theory (DFT).....	9
1.2.3.1 Density as the Central Variable.....	9
1.2.3.2 Early Approaches.....	9
1.2.3.3 Kohn-Sham Density Functional Theory.....	10
1.2.3.4 Exchange-Correlation Functionals.....	13
1.2.3.5 Dispersion Corrections to DFT.....	15
1.3 Organization of the Thesis.....	19
Chapter 2.....	21
2.1 Sustainable Polymers: General Remarks.....	22
2.1.1 Introduction.....	22
2.1.2 Aliphatic Polymers to the Rescue.....	23
2.1.3 Monomer Enchainment Processes.....	23

2.1.4 Ring-Strain Dictates the Choice of Monomer	24
2.1.5 Ring-Opening Polymerization of Lactone/Lactide.....	25
2.1.6 Catalysts for ROTEP of Lactone/Lactide	26
2.1.7 Variations in ROP Mechanism.....	28
2.1.7.1 Activated Monomer Mechanism.....	29
2.1.7.2 Coordination-Insertion Mechanism.....	29
2.1.8 Kinetic Model for ROP of ϵ -Caprolactone	31
2.1.9 Framework Distortion Energy (FDE) Hypothesis.....	32
2.2 Modeling Slow Polymerization of ϵ -Caprolactone Using Al(TMTAA) Catalyst.....	35
2.2.1 Introduction	35
2.2.2 Results and Discussions.....	36
2.2.2.1 Experimental Results.....	36
2.2.2.2 Computational Modeling.....	37
2.2.3 Conclusion.....	40
2.3 Effects of Sterically Induced Ligand Framework Distortion on ROTEP of Cyclic Esters.....	41
2.3.1 Introduction	41
2.3.2 Results and Discussions.....	42
2.3.2.1 Experimental Results: Catalyst Synthesis and Characterization	42
2.3.2.2 Experimental Results: Polymerization Kinetics	43
2.3.2.3 Computational Studies	44
2.3.3 Conclusion.....	46
2.3.4 Appendix.....	46
2.3.4.1 Computational Details.....	46
2.3.4.2 Buried Volume and Steric Map.....	47
2.4 Fast Ligand Screening Using FDE Model and Identification of an Aluminum Indolide/Schiff-Base Complex for ϵ -Caprolactone Polymerization.....	49
2.4.1 Introduction	49
2.4.2 Results and Discussions.....	50
2.4.2.1 Summary of Computational Screening.....	50
2.4.2.2 Experimental Results.....	53
2.4.3 Conclusions.....	54
2.4.4 Appendix.....	55
2.4.4.1 Computational Details.....	55
2.4.4.2 Sensitivity of Density Functionals in Reactivity of 246 vs. 255	56
2.4.4.3 Variation of $\Delta G^\ddagger(\text{TS1})$ as a Function of CL Orientation	56

2.4.4.4 Bridging Tether Design: P_n , Q_n , R_n Series and Pyridine-Based Catalysts	57
2.5 Mechanistic Investigation of Isosorbide-Based Polyether Synthesis.....	59
2.5.1 Introduction	59
2.5.2 Results and Discussions.....	60
2.5.2.1 Isosorbide Ring-Strain	60
2.5.2.2 Ring-Opening Energetics using MeOTf and BF_3OEt_2 Initiators	60
2.5.2.3 Ring-Opening Selectivity Induced by Propylene Oxide	62
2.5.2.4 Lowering of Activation Barrier with PO Initiator	65
2.5.2.5 Polymer Architecture Control Exploiting Solvent Dielectric Constant	65
2.5.2.6 Effect of Counterion Mobility on Kinetic Barriers	66
2.5.3 Conclusion.....	66
2.5.4 Appendix.....	67
2.5.4.1 Computation Protocol.....	67
Chapter 3	69
3.1 Site-Selective Copper-Catalyzed Azidation of Benzylic C–H Bonds.....	70
3.1.1 Introduction	70
3.1.2 Results and Discussion.....	71
3.1.2.1 Experimental Results.....	71
3.1.2.2 Computational Studies	73
3.1.2.3 Experimental Site-Selectivity Studies	75
3.1.3 Conclusion.....	77
3.1.4 Appendix.....	77
3.1.4.1 Computational Methods.....	77
3.1.4.2 Electronic Structure of the $[\text{LCu}^{\text{II}}(\text{N}_3)_2]_2$ Dimer and Analysis of the Dimer/Monomer Equilibria	79
3.1.4.3 Computed Reduction Potentials.....	80
3.1.4.4 Thermodynamics of Radical Polar Crossover Pathway	83
3.2 Copper-Catalyzed Benzylic Etherification via Radical Relay Enabled by Redox Buffering	84
3.2.1 Introduction	84
3.2.2 Results	86
3.2.2.1 Identifying the Redox Buffer Effect.....	86
3.2.2.2 Reaction Development.....	88
3.2.2.3 Computational Analysis of the Proposed Mechanism.....	90
3.2.3 Conclusions.....	93

Chapter 4	94
4.1 Mechanisms for X–H Bond Activation by Mononuclear Copper(III) Cores: HAT or cPCET? ...	95
4.1.1 Introduction	95
4.1.2 Experimental Results	97
4.1.2.1 Synthesis and Characterization of LCu(III)O ₂ CAr ¹	97
4.1.2.2 Experimental Reactivity Studies	99
4.1.3 Computational Results	101
4.1.3.1 Computed Spectra	101
4.1.3.2 Unraveling Reactive Sites for HAA	102
4.1.3.3 Comparative Reactivity with Ar ² OH and DHA	103
4.1.3.4 Mechanistic Diagnostics: Component of Dipole Moment Along the IRC	104
4.1.3.5 Mechanistic Diagnostics: Intrinsic Bond Orbital Analysis	105
4.1.4 Conclusions	109
4.1.5 Appendix	111
4.1.5.1 Reactivity of 402 and 403 Towards DHA: Site O ^a vs. O ^b and O ^c vs. O ^d	111
4.1.5.2 Reactivity of 402 and 403 Towards Ar ² OH: Site O ^a vs. O ^b and O ^c vs. O ^d	112
4.1.5.3 Computation Protocol	112
4.1.5.4 Asynchronicity Factor	114
4.2 Carboxylate Electronic Effects on the PCET Reactivity of [CuO ₂ CR] ²⁺ Cores	116
4.2.1 Introduction	116
4.2.2 Experimental Studies: Reactivity of [Cu ^{III} O ₂ CR] ²⁺ Complexes	117
4.2.3 Computational Reactivity Trend	118
4.2.4 Conclusions	121
Chapter 5	123
5.1 Structure and Reactivity of MOF-Supported Single-Site Heterogeneous VO _x Catalyst	124
5.1.1 Introduction	124
5.1.2 Structural Features of the Support and V-MOFs	125
5.1.3 Computation protocol	126
5.1.3.1 Methods for Exploring V-MOF Structures	126
5.1.3.2 Methods for Reactivity Studies	127
5.1.4 Modeling VO _x Attachment to the MOF Node	127
5.1.5 Results and Discussions	129
5.1.5.1 Free Energies	129

5.1.5.2 Computed IR Spectral Data	130
5.1.5.3 Reaction Mechanism on Zr-NU-1000	133
5.1.5.4 IBO Analysis for C–H Activation on Zr-NU-1000: HAT vs. cPCET	135
5.1.6 Conclusions.....	136
5.1.7 Appendix.....	137
5.1.7.1 Detailed Exploration of Conformers for Hf-MOF-808-V Having Acetate Linker	137
5.1.7.2 IR Spectral Data	138
5.2 Enhanced Activity of Heterogeneous Pd(II) Catalysts on Acid Functionalized MOFs.....	139
5.2.1 Introduction	139
5.2.2 Results and Discussions.....	141
5.2.2.1 Phosphation and Sulfation of Hf-MOF-808.....	141
5.2.2.2 Stability of the Coordinated Pd(II) Species in an H ₂ Atmosphere.....	143
5.2.2.3 Catalytic Reactions.....	144
5.2.2.4 Computational Characterization.....	145
5.2.3 Conclusion.....	147
Bibliography.....	149

List of Tables

Table 2.1 Thermodynamic parameters for ROTEP of different lactones at 298 K	25
Table 2.2 Geometric index τ_s , activation parameters, framework distortion energies (FDE), and activation free energies (ΔG^\ddagger) through TS1 for catalysts 235, 241, 239, and 245	44
Table 2.3 Buried volumes ($\%V_{Bur}$) computed for the catalysts using different radius of the coordination sphere.....	48
Table 2.4 Computed geometry indices (τ_s), activation free energies (ΔG^\ddagger ; kcal/mol), framework distortion energies (FDE, kcal/mol), and key bond lengths (Å) for N_4 -donor systems	52
Table 2.5 Comparison of activation free energies (kcal/mol) required for the turnover-limiting TS1 during ROTEP of CL using catalysts 246 and 255 using different density functionals.....	56
Table 2.6 Gibbs free energies in kcal/mol computed at SMD(CH ₂ Cl ₂)/M06-2X-D3/6-311+G(d,p) SDD(Br)//M06-L/6-31+G(d,p) SDD(Br) level of theory	57
Table 2.7 Catalysts in P_n , Q_n and R_n series (entries 1–10) and pyridine-based catalysts (entries 11–15) with their computed geometry indices, activation free energies and framework distortion energies	58
Table 2.8 Ring-opening energetics of 202 with BF ₃ OEt ₂ , MeOTf and MeOTf/PO initiator	62
Table 2.9 Ring-opening energetics of 202 using Sc(OTf) ₃ in the absence and presence of PO initiator.....	63
Table 3.1 Reaction optimization ^a	72
Table 3.2 Calculated (vs Fc ^{0/+}), and experimental (vs Fc ^{0/+}) reduction potentials (V) of various species at 298.15 K using reaction schemes (eqs S3 and S4).....	82
Table 4.1 Experimental second order rate constants (M ⁻¹ s ⁻¹) for HAA from Ar ³ OH and DHA.....	100
Table 4.2 Most intense molecular excitation energies computed for different Cu(III) complexes. Experimental excitation energies are provided in parentheses for comparison.....	102
Table 4.3 Free energies of activation (ΔG^\ddagger , kcal/mol) calculated for different reactive sites O ^a , O ^b , O ^c , or O ^d with Ar ² OH and DHA substrates	103
Table 4.4 Computed free energies of activation (ΔG^\ddagger , kcal/mol) for HAA from Ar ² OH and DHA	104
Table 4.5 Calculated asynchronicity factors (η) in mV.....	114
Table 4.6 Second-order rate constants (k_2) for reactions of [LCu ^{III} (O ₂ CR)] with the indicated substrates and computed ΔG^\ddagger and other parameters for the reactions of [LCu ^{III} O ₂ CR] with DTBP	119
Table 5.1 Computed Free Energies of Activation (ΔG^\ddagger , kcal/mol) for HAA from Benzylic Position of the Substrate at Two Adsorption Sites Using Various V-MOF Catalysts	134

List of Figures

Figure 1.1 Number of publications having “DFT” as a keyword	2
Figure 1.2 Depiction of the short-, medium- or long-range behavior of the dispersion/correlation energy	15
Figure 2.1 Plastic industry and modern life	22
Figure 2.2 Demonstration for framework distortion energy	33
Figure 2.3 Schematic for calculating framework distortion energy	34
Figure 2.4 Puckered geometry of the (TMTAA)Al(OMe) complex	36
Figure 2.5 Selected aluminum complexes representing the range of rates reported for ROTEP of CL	37
Figure 2.6 Comparison of the reaction coordinates for 333 K CL ROTEP catalyzed by 228 and 229	39
Figure 2.7 (salen)Al catalysts studied in polymerizations of cyclic esters	41
Figure 2.8 Eyring plots of $\ln(k_2/T)$ versus $1/T$ for 235 (blue circles), 241 (black circles), 239 (blue squares), and 245 (black squares). Data for 235 and 241 are from refs 51 and 49, respectively, and those for 239 and 245 are from this work	43
Figure 2.9 Standard-state free energies (kcal/mol) for CL ring-opening relative to the infinitely separated precatalyst and monomer with line drawings of relevant stationary points, and 3D-diagram of the TS structures. Solid lines refer to <i>t</i> -Bu substituted catalysts (235 and 241), while dotted lines refer to Ad-substituted catalysts (239 and 245)	45
Figure 2.10 Steric maps for the four catalysts explored, using a coordination sphere of radius 7.5 Å. The map shows that both the <i>ortho</i> -substituents are quite far from the catalytic pocket	48
Figure 2.11 (a) Parent salen catalyst and modifications with additional alkyl tethers. (b) Pyridine-based systems as a sidearm modification to salen. (c) Pyrrole/indole-based { <i>N,N,N,N</i> }-complexes	51
Figure 2.12 Optimized structures for 246 and 255 and their corresponding turnover-limiting TS structures for CL polymerization	53
Figure 2.13 Effect of CL orientation on TS1 for catalyst 246 and 255	57
Figure 2.14 (a) Catalyst design for bridging linkers. P_n , Q_n and R_n chains. (b) Proposed pyridine-based Al-catalysts.	58
Figure 2.15 Relative ring-opening energetics of Sc(OTf) ₃ - and Sc(OTf) ₃ /PO-initiated polymerization of 202	64
Figure 2.16 Computed CMS partial charges on α -carbon involved during the ring-opening of 202 . INT9 is the intermediate formed after the monomer coordinates to Sc(OTf) ₃ via the bridgehead oxygen atom. INT14 is the corresponding intermediate when the PO initiator is used. See Scheme 2.11 for details on how they are formed	65
Figure 2.17 Relative ring-opening energetics of MeOTf/PO- and Sc(OTf) ₃ /PO-initiated polymerization of 202	66
Figure 3.1 Azides are important intermediates in organic syntheses (A) and medicinal chemistry (B) and are ideally prepared by direct azidation of sp^3 C–H bonds (C)	70
Figure 3.2 (A) Synthesis and crystal structure of [(BPhen)Cu ^{II} (N ₃)(μ -N ₃)] ₂ (hydrogen atoms and chlorobenzene molecule omitted for clarity). (B) Reaction of [(BPhen)Cu ^{II} (N ₃)(μ -N ₃)] ₂ with Gomberg’s dimer	73

Figure 3.3 Three proposed pathways for azidation of the benzyl radical (A), and simplified energy diagrams comparing the three pathways (B).....	74
Figure 3.4 Azidation site selectivity with different catalytic methods	76
Figure 3.5 Gibbs free energy change (kcal/mol) due to dimerization.....	79
Figure 3.6 Optimized transition-state (TS) structures leading to product formation via reductive elimination (RE) and direct radical addition to the azide ligand (RAL) for both pro-R and pro-S faces of the benzylic radical derived from 1-ethylnaphthalene.....	80
Figure 3.7 Derivation of Gibbs free energy change (ΔG°) for the oxidation of the 1-Naph-CH(\bullet)Me radical by the Cu ^{II} -dimer yielding the corresponding benzylic cation. Reduction potentials were obtained from Table 3.2	83
Figure 3.8 Cross-coupling reactions of benzylic C–H bonds and alcohols via a radical relay pathway. (a) Conceptual similarity between traditional cross-coupling reactions of aryl halides and the targeted benzylic C–H functionalization reactions. (b) Important examples of existing drug molecules containing benzylic ether moieties. (c) Proposed radical relay mechanism for benzylic C–H etherification enabling the coupling of two diverse pools of substrates.	86
Figure 3.9 Cu-catalyzed benzylic C–H functionalization with NFSI as the oxidant. (a) Cu-catalyzed benzylic C–H functionalization reactions. (b) Changes in the Cu redox state between +1 (brown) and +2 (blue-green) upon addition of NFSI to a solution of the Cu ^I catalyst precursor, followed by addition of cross-coupling partners. (c) Modified radical relay mechanism to account for quenching of the \bullet NSI by Cu ^I and regeneration of Cu ^I by a reducing substrate or additive. (d) Reaction time course for benzylic etherification conducted in the absence (red) and presence of 0.5 equiv. of dimethylphosphite (blue). Reaction conditions: 4-ethylbiphenyl (0.2 mmol), NFSI (0.4 mmol), MeOH (1.0 mmol), CuCl (0.02 mmol), 2,2'-bioxazoline (0.02 mmol), DCM (1 mL), room temperature 88	
Figure 3.10 Electronic effects and site selectivity observed in the oxidative coupling of ethylarenes and methanol. (a) Results observed from the reaction under standard (red) and individually optimized (blue) (b) Analysis of benzylic versus tertiary site selectivity observed in etherification of isobutylbenzene and ibuprofen methyl ester	90
Figure 3.11 Calculated reaction pathways and energy landscape for (biox)Cu ^I /NFSI-mediated methoxylation of ethylbenzene	91
Figure 4.1. Two organic substrates, DHA and Ar ⁿ OH ($n = 2$ in theoretical studies, $n = 3$ in experimental studies), used in this study together with three [LCu(III)–Y] complexes. The α,α -dimethylbenzyl group in 402 is abbreviated as “Cm” and the <i>meta</i> -chlorophenyl group in 403 is referred to as “Ar ¹ ”	95
Figure 4.2 X-ray crystal structure of anionic 403' with the NEt ₄ cation and H atoms omitted for clarity.....	98
Figure 4.3 Overlay of UV-Vis spectra of LCu(III)OH (401 , black), LCu(III)OOCm (402 , blue) and LCu(III)O ₂ CAr ¹ (403 , red), in THF at –80 °C.....	99
Figure 4.4 Spectroscopically relevant highest occupied molecular orbital (HOMO) and HOMO–5, together with the lowest unoccupied molecular orbital (LUMO) for complex 403	102
Figure 4.5 Evolution of the total dipole moment vector (Hirshfeld) projected along the axis of H-atom abstraction. (a), (b), and (c) corresponds to HAA reactivity of complexes 401 (blue), 402 (black), and 403 (green) respectively. Solid lines are used for the Ar ² OH substrate, while dashed lines represent the DHA substrate.....	105
Figure 4.6 Plots of the change in electronic energies (computed at UB3LYP-D3(BJ)/basis-I level) along the intrinsic reaction coordinate (IRC/amu ^{1/2} ·bohr) for (a) 401 /DHA, (d) 401 /Ar ² OH and (g) 403 /DHA pairs. Intrinsic bond orbital (IBO) transformations of the C–H bond along the IRC are shown in (b) purple (α -IBO) and (c) green (β -IBO). Changes in the O–H β -IBO for 401 /Ar ² OH are shown in (e), while (f) shows changes in the β -IBO of the π -electron density of the aryl ring that eventually ends up on the Cu-atom. Transformation of the C–H β -IBO for 403 /DHA is presented in (h), which again stays on the DHA moiety. Changes in two β -IBOs corresponding to the	

π -density of DHA (blue-green) and that of diisopropylphenyl moiety of the ligand (pink-orange) are represented simultaneously in (i). IBO transformations indicate that the density on DHA is transferred to the Cu-center through a ligand-assisted pathway. In all cases, isopropyl groups of the ligand and tert-butyl groups of the Ar²OH substrate are omitted for clarity 106

Figure 4.7. Electron flow during HAA from (a) **401**/DHA, (b) **401**/Ar²OH, and (c) **403**/DHA..... 107

Figure 4.8 Changes in the Hirshfeld spin-population for **401**/Ar²OH (green) and **403**/DHA (blue), along their respective cPCET reaction coordinates. Solid lines represent total spin on Cu-complexes (Fragment^{Cu}), while dotted lines reflect the total spin on organic substrates (Fragment^{Sub}). At the start of the reaction, both Fragment^{Cu} and Fragment^{Sub} are closed-shell systems, thus the total spin on both fragments starts from zero. At/near the TS, single electron transfer leads to local spin on both fragments..... 108

Figure 4.9 Computed change in electronic energy (ΔE^{rxn}) and Gibbs free energy (ΔG^{rxn}) leading to product formation, upon HAA from the DHA substrate. 111

Figure 4.10 Computed change in electronic energy (ΔE^{rxn}) and Gibbs free energy (ΔG^{rxn}) leading to product formation, upon HAA from the Ar²OH substrate 112

Figure 4.11 Copper complexes supported by L²⁻ (focus of this work in box)..... 117

Figure 4.12 Plot of log k_2 for the reaction of LCu^{III}O₂CR with TTBP at -80 °C in THF vs. $E_{1/2}$ for the [LCu(O₂CR)]^{0/-} couple. Red line is linear fit to log $k_2 = 10.7 \times E_{1/2} - 2.98$, $R^2 = 0.90$ 118

Figure 4.13 Representative transition-state structure for the reaction of LCu^{III}O₂CC₆H₅ with DTBP. H-atoms and the 2,6-diisopropylphenyl groups on the L²⁻ ligand are omitted for clarity..... 120

Figure 5.1 Node of Hf-MOF-808, with a focus on the site responsible for chemisorption of VO_x (inset). Possible modes for the deposition of a formally V^(V) species over the MOF-808 node..... 128

Figure 5.2. Gibbs free energies of reaction (in the condensed phase, ΔG° (vib), where translational and rotational degrees of freedom of the released H₂O molecule(s) were not allowed, and in the gas phase, ΔG° , considering all degrees of freedom of all species; kcal/mol) at 298.15 K with a standard state of 1 atm for various structures of V-MOFs: (a) Hf-MOF-808-V and (b) Zr-NU1000-V, calculated by M06-L/basis-II//M06-L/basis-I . Electronic energies (ΔE) and Gibbs free energies of reaction are calculated in accordance with eq. 1–3, and thus, the number of water molecules (n) released as a result of OV(OH)₃ deposition over bare MOF node are: $n = 1$ (V3), $n = 2$ (V4, V5a, V5b), $n = 3$ (V6) 130

Figure 5.3. (a) Computed IR spectra for the bare Hf-MOF-808 support and various V-MOF structures shown in Figure 5.2a: a, O–H bending modes of H₂O molecules coordinated to Hf centers; b and c, anti-symmetric and symmetric stretching of the carboxylate group of benzoate linkers coordinating Hf₆ cluster, respectively; d, C–H rocking modes of benzoate linkers; e, Hf–O–V stretching modes; f, V=O stretching modes; g, O–H bending modes of hydrogen bonded V–OH. (b) Experimental IR spectra (F–I) in the 800–1300 cm⁻¹ region as reported in ref. 243: (F) bare Hf-MOF-808 at room temperature; (G) Hf-MOF-808-V at room temperature; (H) Hf-MOF-808-V at room temperature, cooled after treating the sample with heat at 125 °C; (I) Hf-MOF-808-V at room temperature after heating in the presence of humid air. (c) Computed IR spectra (A–E) of bare Hf-MOF-808 (A) and vanadia-deposited Hf-MOF-808-V conformers having various other species (e.g. MeOH, –OMe, acetylacetonate ligand from V^(IV) precursor, VO_x species) available to coordinate to the metal ions at the node under reaction conditions; these species are represented by their line-drawn structures at the top of the figure (A–E, each having the benzoate linker): h, C–O stretching modes of coordinated methanol; j, CH₃ bending modes of coordinated methoxy groups; k, features due to coordinated acetylacetonate ligand..... 131

Figure 5.4. Standard-state free energies and free energies of activation (kcal/mol) calculated by M06/basis-II//M06/basis-I for oxidation of benzyl alcohol to benzaldehyde. The green line describes alcohol chemisorption at a V–OH bond and subsequent benzyl C–H bond activation, and the blue line represents reactivity via chemisorption

at a Zr–OH bond. The singlet intermediates (INT1a/1b) are spin-symmetry stable, but the transition-state structures TS2a/2a'/2b are calculated as broken-symmetry singlets, and INT2a/2b are triplets 133

Figure 5.5. (a) Change in electronic energy (computed by spin-unrestricted M06/basis-I) along the minimum energy path through TS2a for hydrogen-atom abstraction from the methylene group of the chemisorbed benzyl alcohol. (b) Intrinsic bond orbitals of the C–H bond corresponding to the calculations in panel a. (c) A simplified representation of the proton and electron transfer process 136

Figure 5.6 Key modes for VO_x deposition on Hf-MOF-808 (acetate linker), along with their computed reaction free energies. Gibbs free energies are reported in kcal/mol computed at M06-L/basis-II//M06-L/basis-I level of theory at 298.15K 137

Figure 5.7 Computed IR data for model vanadium dioxo (F7) and mono-oxo (F8) species, Hf-MOF-808-V conformers V2 and V3, compared against experimental IR spectra of bare Hf-MOF-808 (H) and Hf-MOF-808-V (G) at room temperature. Note that M06-L/basis-I vibrational frequencies were scaled by a factor of 0.958..... 138

Figure 5.8 (a) Crystal structures (100 K) of Hf-MOF-808 and (b,c) the crystal structures after phosphation and (d) sulfation. Occupancies of SO₄ and PO₄ are 40% (2.4 S and 2.4 P per Hf₆ node). (e,f) Crystal structures of Pd(II) sites incorporated in MOFs at 100 K. Representation of the Pd(II) site on the node of Pd@Hf-MOF-808 (e) and representation of two different Pd(II) sites on the node of Pd@Hf-MOF-808-PO₄ (f) 142

Figure 5.9 Reaction scheme of the C–H activation reaction of 2-phenylphenol (**501**) with ethyl acrylate to form (**502**) along with reaction time profiles for the catalytic formation of **502**. Black open circles, blue filled circles, and red filled circles represent the reaction time profiles for Pd@Hf-MOF-808, Pd@Hf-MOF-808-SO₄, and Pd@Hf-MOF-808-PO₄, respectively..... 145

Figure 5.10 The reaction network for the formation of Pd(II)@Hf-MOF-808 and Pd(0)@Hf-MOF-808 with or without phosphate or sulfate modification. The Gibbs free energies of reaction ΔG° (kcal/mol) are calculated at 298.15 K, with standard state of 1 atm for gases and 1 M for solutes and including the solvation effect of dichloromethane. In compound names, we use the shorthand SO₄, PO₄, and H₂O for Hf-MOF-808-SO₄, Hf-MOF-808-PO₄, Hf-MOF-808, respectively..... 147

List of Schemes

Scheme 2.1 (a) Step-growth condensation yielding polyester. (b) Ring-opening transesterification polymerization (ROTEP) of lactones/lactides.....	24
Scheme 2.2 (a) Generic metal salen/salan complexes. (b) Metal salen/salan/salalen/salophen complexes for ring-opening polymerization of lactones/lactides.....	27
Scheme 2.3 Activated monomer mechanism of simple lactones	29
Scheme 2.4 Coordination-insertion mechanism of simple lactones	30
Scheme 2.5 Mechanism for ROTEP. K_{eq} is the equilibrium constant for monomer binding, k_2 is the catalytic rate constant for monomer enchainment and k_2' is the ratio of k_2 and K_{eq}	31
Scheme 2.6 (a) (TMTAA)Al-alkoxide complex and Al(Salen) Complex (b) Key stationary points along the CL ROTEP reaction coordinate	38
Scheme 2.7 Biomass derived monomer isosorbide and its annulation	59
Scheme 2.8 Isodesmic reaction used for ring-strain computation	60
Scheme 2.9 Possible pathways for the ring-opening of 202 using (a) $BF_3 \bullet OEt_2$, (b) MeOTf alone, and (c) MeOTf in combination with PO initiator	61
Scheme 2.10 Cationic ring-opening polymerization of 202 . (1) MeOTf initiator alone causes both bridgehead and terminal ring-opening; (2) MeOTf/PO induces selectivity towards bridgehead ring-opening; $Sc(OTf)_3/PO$ in (3) low- ϵ solvent (CH_2Cl_2) prefers cyclic polymer formation, while (4) high- ϵ solvent (CH_3CN) favors linear polymer	62
Scheme 2.11 Detailed mechanistic consideration for ring-opening of 202 , with key stationary points identified on the relevant potential energy surface using (a) $Sc(OTf)_3$ catalyst alone and (b) $Sc(OTf)_3/PO$ catalytic system	63
Scheme 4.1. Stepwise (ET/PT or PT/ET) vs. CPET pathways for X–H bond activation by a representative Cu(III) species (401). Two key variations of CPET reaction, namely HAT and cPCET are also shown	96
Scheme 4.2. Synthesis of $[NBu_4][LCu(II)O_2CAr^1]$, 403' , starting from $[NBu_4][LCu(II)OH]$, 401'	98
Scheme 4.3 Species relevant for computing asynchronicity factor. $G(\text{species})$ refers to the Gibbs free energy of the relevant species. $[Sub^\cdot]$ refers to the usual radical product after HAA, $[SubH^+]$ is the substrate structure, either DHA or Ar^2OH oxidized by 1-electron, and $[Sub^-]$ is the substrate structure after deprotonating the acidic proton from the X–H bond.....	115
Scheme 5.1 MOF nodes in (a) Zr-NU-1000 and (b) Hf-MOF-808. (left) One node and associated linkers except that the actual H_4TBAPy (1,3,6,8-(p-benzoic acid)pyrene) and H_3BTC (benzene-1,3,5-tricarboxylic acid) linkers are truncated to benzoate in this schematic. (middle) One node without linkers. (right) A linker.....	126
Scheme 5.2 The catalytic cycle and deactivation of oxidative Heck catalyst. NPs = nanoparticles, Ar = aryl group	140

Preface

Parts of this thesis have been reproduced from previously published work. Permissions to reproduce these sections have been obtained, and are as follows:

Chapter 2

2.2. Modeling Slow Polymerization of ϵ -Caprolactone Using Al(TMTAA) Catalyst

Adapted with permission from:

Stasiw, D. E.; Mandal, M.; Neisen, B. D.; Mitchell, L. M.; Cramer, C. J.; Tolman, W. B. *Inorg. Chem.* **2017**, *56*, 725–728. DOI: 10.1021/acs.inorgchem.6b02849 — Copyright © 2016, American Chemical Society.

2.3. Effects of Sterically Induced Ligand Framework Distortion on ROTEP of Cyclic Ester

Adapted with permission from:

Macaranas, J. A.; Luke, A. M.; Mandal, M.; Neisen, B. D.; Marell, D. J.; Cramer, C. J.; Tolman, W. B. *Inorg. Chem.* **2018**, *57*, 3451–3457. DOI: 10.1021/acs.inorgchem.8b00250 — Copyright © 2018, American Chemical Society.

2.4. Fast Ligand Screening Using FDE Model and Identification of an Aluminum Indolide/Schiff-Base Complex for ϵ -Caprolactone Polymerization

Adapted with permission from:

Mandal, M.; Luke, A. M.; Dereli, B.; Elwell, C. E.; Reineke, T. M.; Tolman, W. B.; Cramer, C. J. *ACS Catal.* **2019**, *9*, 885–889. DOI: 10.1021/acscatal.8b04540 — Copyright © 2018, American Chemical Society.

2.5. Mechanistic Investigation of Isosorbide-Based Polyether Synthesis

Adapted with permission from:

Saxon, D. J.; Nasiri, M.; Mandal, M.; Maduskar, S.; Dauenhauer, P. J.; Cramer, C. J.; LaPointe, A. M.; Reineke, T. M. *J. Am. Chem. Soc.* **2019**, *141*, 5107–5111. DOI: 10.1021/jacs.9b00083 — Copyright © 2019, American Chemical Society.

Chapter 3

3.1. Site-Selective Copper-Catalyzed Azidation of Benzylic C–H Bonds

Adapted with permission from:

Suh, S.-E.; Chen, S.-J.; Mandal, M.; Guzei, I.; Cramer, C. J.; Stahl, S. S. *J. Am. Chem. Soc.* **2020**, *142*, 11388–11393. DOI: 10.1021/jacs.0c05362 — Copyright © 2020, American Chemical Society.

3.2. Copper-Catalyzed Benzylic Etherification via Radical Relay Enabled by Redox Bufferin

Adapted with permission from:

Hu, H.; Chen, S.-J.; Mandal, M.; Pratik, S. M.; Buss, J. A.; Krska, S. W.; Cramer, C. J.; Stahl, S. S. *Nat. Catal.* **2020**, 3, 358–367. DOI: 10.1038/s41929-020-0425-1 — Copyright © 2020, Springer Nature.

Chapter 4

4.1. Mechanisms for X–H (X = C, O) Bond Activation by Mononuclear Copper(III) Cores: HAT or cPCET?

Adapted with permission from:

Mandal, M.; Elwell, C. E.; Bouchey, C. J.; Zerk, T. J.; Tolman, W. B.; Cramer, C. J. *J. Am. Chem. Soc.* **2019**, 141, 17236–17244. DOI: 10.1021/jacs.9b08109 — Copyright © 2019, American Chemical Society.

4.2. Carboxylate Electronic Effects on the PCET Reactivity of [CuO₂CR]²⁺ Cores

Adapted with permission from:

Elwell, C. E.; Mandal, M.; Bouchey, C. J.; Que, L., Jr.; Cramer, C. J.; Tolman, W. B. *Inorg. Chem.* **2019**, 58, 15872–15879. DOI: 10.1021/acs.inorgchem.9b02293 — Copyright © 2019, American Chemical Society.

Chapter 5

5.1. Structure and Reactivity of MOF-Supported Single-Site Heterogeneous VO_x Catalyst

Adapted with permission from:

Mandal, M.; Cramer, C. J.; Truhlar, D. G.; Sauer, J.; Gagliardi, L. *ACS Catal.* **2020**, 10, 10051–10059. DOI: 10.1021/acscatal.0c02300 — Copyright © 2020, American Chemical Society.

5.2. Enhanced Activity of Heterogeneous Pd(II) Catalysts on Acid Functionalized MOFs

Adapted with permission from:

Otake, K. I.; Ye, J.; Mandal, M.; Islamoglu, T.; Buru, C. T.; Hupp, J. T.; Delferro, M.; Truhlar, D. G.; Cramer, C. J.; Farha, O. K. *ACS Catal.* **2019**, 9, 5383–5390. DOI: 10.1021/acscatal.9b01043 — Copyright © 2019, American Chemical Society.

Chapter 1

General Overview of Computational Methods and Thesis Organization

Synopsis. In this first chapter, importance of experiment/computation synergistic studies is discussed. A brief overview of computational methods is then provided, summarizing basics of the Hartree-Fock method and density functional theory. Organization of the thesis is then discussed, providing a synopsis of each subsequent chapters.

1.1 Computational Chemistry: General Remarks

Computational chemistry exploits the principles of theoretical chemistry incorporated into efficient computer codes to evaluate and predict structure and property of various molecules and is certainly one of the most fascinating branches of chemistry. Over the past few decades, it has gradually become an integral component of nearly all subdisciplines of chemistry and chemical engineering (Figure 1.1), making experiment/computation synergy essential, now more than ever.

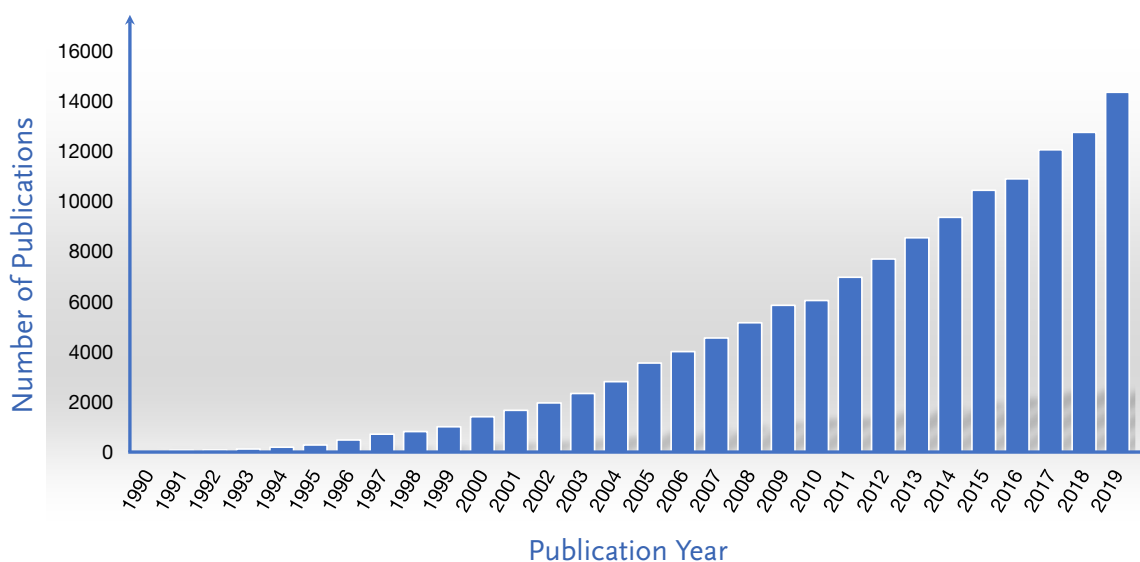


Figure 1.1 Number of publications having “DFT” as a keyword: Trend compiled from data provided by the Web of Science database, based on a search with “DFT” as a topic keyword.

Thus, complimentary to X-ray crystallography, which provides access to solid-state structural parameters of, e.g., a reactive intermediate, computation allows recognition of structural features of reacting intermediates in *operando* conditions, even for species having fleeting lifetimes. Moreover, mechanistic understanding of a complex chemical transformation can be obtained by careful modeling of the relevant potential energy landscape, which, for kinetic reasons, are often difficult to characterize via experiment. Mechanistic knowledge thus obtained is not only helpful in, for instance, explaining the experimentally observed rate difference of two or more catalysts, or rationalizing the origin of enantioselectivity in an asymmetric synthesis—careful modeling can engender design principles that can be exploited for rational modification of catalytic moieties having improved performance. Based on those design principles, efficient computational

paradigms could then be developed for fast screening of hypothetical catalysts facilitating discovery.

Among various methods developed over the last century, for instance semiempirical, wave function, and density functional theory (DFT), the later has emerged as the most popular electronic structure method in computational chemistry, (Figure 1.1) as it offers a great balance between chemical accuracy and computational cost.¹ While typically more accurate, the traditional *ab initio* wave function-based approaches are still prohibitively expensive for larger systems and are employed only for benchmark purposes. This thesis contains multiple examples where wave function-based calculations have been performed first to benchmark different “flavors” of DFT; full computational exploration is then carried out employing the “best” performing DFT functional. Thus, it is now a good time to review some of the basics of both wave function and DFT-based methods.

1.2 Overview of Computational Methods

1.2.1 Time-Independent Schrodinger Equation

In the realm of quantum mechanics, various properties of a molecule can be evaluated by solving the non-relativistic time-independent Schrödinger equation,

$$\hat{H}\psi = E\psi \quad (1)$$

The Hamiltonian operator \hat{H} returns the associated energy eigenvalue of the system, E , when operated on the corresponding state of the system described by wave function ψ . Now, of the three quantities in Eqn. (1), only the Hamiltonian operator \hat{H} is known explicitly by virtue of postulates of quantum mechanics. For a system with n -electrons and N -nuclei, the corresponding Hamiltonian can be expressed as:

$$\hat{H} = \underbrace{-\sum_{i=1}^n \frac{\hbar^2}{2m_e} \nabla_i^2}_{T \text{ (electronic)}} - \underbrace{\sum_{I=1}^N \frac{\hbar^2}{2m_I} \nabla_I^2}_{T \text{ (nuclear)}} - \underbrace{\sum_{J=1}^N \sum_{i=1}^n \frac{Z_I e^2}{4\pi\epsilon_0 r_{iI}}}_{V \text{ (nuclear-electronic attraction)}} + \underbrace{\sum_{i=1}^{n-1} \sum_{j=i+1}^n \frac{e^2}{4\pi\epsilon_0 r_{ij}}}_{V \text{ (electron-electron repulsion)}} + \underbrace{\sum_{I=1}^{N-1} \sum_{J=I+1}^N \frac{Z_I Z_J e^2}{4\pi\epsilon_0 r_{IJ}}}_{V \text{ (nuclear-nuclear repulsion)}} \quad (2)$$

where m_e is the mass of an electron, and m_I is the mass of nucleus; Z is the atomic number, T is the kinetic energy, V is the potential energy, lower case indices i and j go over the electrons, and the corresponding uppercase letters have been used for the nuclei (e.g. r_{iI} is the distance between the I^{th} nucleus, and i^{th} electron and so on). The first and second terms of the righthand side of eq. (2) represents the kinetic energies of the electrons ($T_{\text{electronic}}$) and the nuclei (T_{nuclear}), respectively. The third term describes the Coulombic attraction between the electrons and the nuclei (V_{ne}). The fourth and fifth term describes potential arising due to repulsion between similar charges: the electron-electron repulsion (V_{ee}) and the nuclear-nuclear repulsion (V_{nn}).

The Born-Oppenheimer Approximation. A nucleus is much heavier than an electron, the latter moves much faster. Consequently, one often invokes the so-called *Born-Oppenheimer (BO) approximation* and treats the nucleus to be stationary.² Thus under this approximation, the nuclear kinetic energy, T_{nuclear} becomes zero, and for a fixed nuclear position, the last term in eq.

(2), the nuclear-nuclear repulsion term (h_{nucl}) is also a constant quantity. Thus, under the BO approximation, the Hamiltonian of the system can be rewritten in atomic units (where $\hbar = m_e = 4\pi\epsilon_0 = e = 1$) as:

$$\begin{aligned}\hat{H} &= \sum_i -\frac{1}{2}\nabla_i^2 - \sum_{i,I} \frac{Z_I}{r_{iI}} + \sum_{i<j} \frac{1}{r_{ij}} + h_{nucl} \\ &= \sum_i h_i + \sum_{i<j} \frac{1}{r_{ij}}\end{aligned}\quad (3)$$

where h_i (defined by $h_i = -\frac{1}{2}\nabla_i^2 - \sum_I \frac{Z_I}{r_{iI}}$) is the one-electron Hamiltonian for the i^{th} electron, and we have dropped the constant term h_{nucl} in the last step, and is now a pure electronic Hamiltonian.

1.2.2 *Ab initio* Hartree-Fock Theory

1.2.2.1 Hartree Product

The exact solution of a one-electron hydrogen-atom problem is well-known in quantum mechanics. The presence of the electron-electron repulsion term (V_{ee}) in a multi-electron system, however, makes the problem complicated. Since the H-atom problem is solvable *exactly*, it can be regarded as a starting point for the description of a multi-electron system. Thus, one can imagine a situation where one extra electron is fed into a H-atom system to form an H^- anion and pretend that the added electron does not interact with the other one (that is to say, $V_{ee} = 0$). Under this hypothetical situation, the Hamiltonian describing the H^- anion would be separable, and the wave function describing the system, $\psi(r_1, r_2)$ would just be the product of two H-atom wave functions: $\psi_{H^-}(r_1, r_2) = \psi_H(r_1) * \psi_H(r_2)$. Based on this idea of non-interacting electrons, Hartree proposed the “independent particle model” in 1928 where he suggested that the N -electron wave function, $\psi(1,2,3 \dots, N)$ can be expressed as a product of N one-electron *spatial* functions, $\varphi(i)$, called the Hartree product:³

$$\psi(1,2,3 \dots, N) = \varphi(1) * \varphi(2) * \varphi(3) \dots \dots \dots \varphi(N) \quad (4)$$

1.2.2.2 Electron Spin and the Slater Determinant

In Hartree's theory, electron spin was not accounted for, and hence was modified later by Fock, who invoked antisymmetry in the wave function.⁴ In the realm of Hartree-Fock (HF) theory, the one-electron functions (called "orbitals") in eq. (4) are no longer simple *spatial* orbitals $\varphi(r)$, but rather are *spin-orbitals* defined as $\phi(x) = \varphi(r)\sigma(\omega)$, where the spin part $\sigma(\omega)$, can either be $\alpha(\omega)$ or $\beta(\omega)$, which are orthonormal.

Nevertheless, a simple product of spin-orbitals is still not antisymmetric with respect to interchange of any two electrons, which must be true because electrons are fermions. This can be achieved by taking an anti-symmetrized linear combination of Hartree product in eq. 4. Slater suggested,⁵ that for an N -electron system, antisymmetry in the wave function can be obtained simply by using a determinant, the so-called Slater determinant, because antisymmetry "feature" is already incorporated in a determinant. Thus, in terms of a Slater Determinant (SD), the N -electron wave function can be expressed as:

$$\psi_{SD}(1,2,3 \dots, N) = \frac{1}{\sqrt{N!}} \begin{vmatrix} \phi_1(1) & \phi_1(2) & \dots & \phi_1(N) \\ \phi_2(1) & \phi_2(2) & \dots & \phi_2(N) \\ \vdots & \vdots & \ddots & \vdots \\ \phi_N(1) & \phi_N(2) & \dots & \phi_N(N) \end{vmatrix} \quad (5)$$

where the pre-factor $\frac{1}{\sqrt{N!}}$ is used for normalization.

One should, however, note that eq. (5) is not the exact representation of the 'true' N -electron wave function ($\Psi_{N-electron}^{true}$). One could, at least in principle, select any N -orbitals ϕ_i 's (other than the ones used in eq. (5)) from an infinite number of them, to construct the SD, and the 'true' N -electron wave function should be a linear combination of all those SDs. Thus,

$$\Psi_{N-electron}^{true} = \sum_{i=0}^{\infty} C_i \psi_{SD_i} \quad (6)$$

However, HF-theory assumes that the sum represented by eq. (6) can be approximated by a single SD, the variationally optimized ψ_{HF} . In shorthand, this is written as:

$$|\psi_{HF}\rangle = |\phi_1\phi_2 \dots \phi_N\rangle \quad (7)$$

1.2.2.3 Hartree-Fock Energy Expression

At this point, we have an expression for the Hamiltonian (eq. (3)) and the functional form of the wave function describing the system, ψ_{HF} (eq. (7)). Using these two tools, the HF-energy expression (E_{HF}) could be obtained by simply by taking the expectation value of the Hamiltonian:

$$\begin{aligned}
 E_{HF} &= \langle \psi_{HF} | \hat{H} | \psi_{HF} \rangle \\
 &= \left\langle \phi_1 \phi_2 \dots \phi_N \left| \sum_i h_i + \sum_{i < j} \frac{1}{r_{ij}} \right| \phi_1 \phi_2 \dots \phi_N \right\rangle \\
 &= \sum_i \langle \phi_1 \phi_2 \dots \phi_N | h_i | \phi_1 \phi_2 \dots \phi_N \rangle + \sum_{i < j} \left\langle \phi_1 \phi_2 \dots \phi_N \left| \frac{1}{r_{ij}} \right| \phi_1 \phi_2 \dots \phi_N \right\rangle \quad (8) \\
 &= \sum_a h_{aa} + \frac{1}{2} \sum_a \sum_b (J_{ab} - K_{ab}) \quad (9)
 \end{aligned}$$

Orthonormality of the spin-orbitals has been exploited to obtain eq. (9) from eq. (8). The new indices a and b now go over the orbitals rather than the electrons. The first term in eq. (8) is the one-electron term which reduces to $\sum_a h_{aa}$, where h_{aa} is given by:

$$h_{aa}(i) = \left\langle \phi_a(i) \left| -\frac{1}{2} \nabla_i^2 - \sum_l \frac{Z_l}{r_{il}} \right| \phi_a(i) \right\rangle \quad (10)$$

The second term in eq. (8) is the two-electron term that reduces to $\frac{1}{2} \sum_a \sum_b (J_{ab} - K_{ab})$, where the Coulomb integral J_{ab} , and exchange integral K_{ab} are defined as:

$$J_{ab}(i, j) = \left\langle \phi_a(i) \phi_a(i) \left| \frac{1}{r_{ij}} \right| \phi_b(j) \phi_b(j) \right\rangle \quad (11)$$

$$K_{ab}(i, j) = \left\langle \phi_a(i) \phi_b(i) \left| \frac{1}{r_{ij}} \right| \phi_a(j) \phi_b(j) \right\rangle \quad (12)$$

1.2.2.4 Minimization of HF Energy: the SCF Method

The HF-energy expression in eq. (9) is, however, not the minimum energy (under the current scheme). One must minimize eq. (9) with respect to variations in the spin orbitals, so as to find the 'best' SD. Thus, we set:

$$\delta E_{HF} = \sum_a \delta h_{aa} + \frac{1}{2} \sum_a \sum_b (\delta J_{ab} - \delta K_{ab}) = 0 \quad (13)$$

From this, one could easily arrive at eq. (14) using the orthonormality of the spin orbitals,

$$\left[\hat{h}(i) + \sum_b (\hat{J}_b(i) - \hat{K}_b(i)) \right] \phi_a(i) = \epsilon_a \phi_a(i) \quad (14)$$

where, $\hat{J}_b(i)$ is the Coulomb operator, giving the average local potential at point 'i', arising due to the charge distribution of electron 'j' in ϕ_b orbital, defined by:

$$\hat{J}_b(i)\phi_m(i) = \phi_m(i) \int \phi_b^*(j)\phi_b(j) \frac{1}{r_{ij}} dj \quad (15)$$

And, $\hat{K}_b(i)$ is the exchange operator, arising because of the antisymmetry requirement of ψ_{HF} , defined by:

$$\hat{K}_b(i)\phi_m(i) = \phi_b(i) \int \phi_b^*(j)\phi_m(j) \frac{1}{r_{ij}} dj \quad (16)$$

The term within the bracket in eq. (14) constructs the one-electron Fock operator:

$$\hat{F}(i) = \hat{h}(i) + \sum_b (\hat{J}_b(i) - \hat{K}_b(i)) \quad (17)$$

One can now rewrite eqn. (14) as the Fock equation,

$$\hat{F}(i)\phi_a(i) = \epsilon_a\phi_a(i) \quad (18)$$

Solutions to eqn. (18) will yield molecular orbitals ϕ_a , and eventually ψ_{HF} which will then give us all the properties of the system under consideration. However, solving the Fock equation is not straight-forward, because we are solving for ϕ_a using the Fock operator that itself depends on ϕ_a . This seeming paradox, fortunately, was solved by Roothaan,⁶ who suggested expanding the molecular orbitals (ϕ_a) as a linear combination of previously known, linearly independent 'basis functions'.

$$\phi_a(i) = \sum_{j=1}^m C_{ja}\chi_j(i) \quad (19)$$

Here χ_j are the basis functions, m is the number of basis functions used and C_{ja} is the expansion coefficient. Substitution of eq. (19) in eq. (18), followed by further simplification yields,

$$\sum_{j=1}^m F_{kj}C_{ka} = \sum_{j=1}^m \epsilon_a C_{ka} S_{kj} \quad (20)$$

In matrix notation, eq. (20) yields: $\mathbf{FC} = \mathbf{SC}\epsilon$. The new term in eq. (20), $S_{jk} = \langle \chi_j(i) | \chi_k(i) \rangle$ is called the overlap integral, and \mathbf{S} is the overlap matrix.

Eqn. (20) is the so-called Hartree-Fock-Roothaan equation, which is solved iteratively using the *self-consistent field* (SCF) method starting from an initial guess of the density matrix ($\mathbf{C} =$

$\sum_{k=1}^m C_{ka}^* C_{ka}$).⁶ At a point when the difference between the input and output density becomes very small, below some previously set cut-off value, self-consistency is said to be reached, and SCF energy is obtained.

1.2.3 Density Functional Theory (DFT)

1.2.3.1 Density as the Central Variable

So far, we have discussed the approach where we solve the time-independent Schrödinger equation (eq. (1)) to obtain the wavefunction ψ describing the system, and thereby extract all properties of interest. However, ψ is a rather complicated quantity, because for N -electrons it depends on $4N$ -variables (3-spatial and one spin for each electron), making wave function-based treatment of large systems practically intractable. In order to bypass the intricacies of a wave function and make things simpler, *electron density* was proposed as the central variable. In contrast to a wave function, electron density, defined as $\rho(r) = \sum_i^{occ} |\phi(i)|^2$ is a physical observable and is much easier to deal with since it depends only on 3-spatial coordinates. The reasoning why $\rho(r)$ can potentially be used as a fundamental variable is straightforward: The Hamiltonian operator for any system is defined uniquely by the number of electrons of the system, the position of nuclei in space, and its charge. All these three basic ingredients are indeed provided by $\rho(r)$. Thus, given a density, one can set up the Hamiltonian and extract all relevant properties of the system.

1.2.3.2 Early Approaches

One of the early approaches that attempted to use density as the central quantity dates back to 1927, and was pioneered by Thomas and Fermi.⁷ In their quantum statistical model, Thomas and Fermi treated the kinetic energy (T) of electrons quantum mechanically, while nuclear-electron attraction (V_{Ne}), and electron-electron repulsion (V_{ee}) were treated classically. The next milestone in density functional theory (DFT) came in 1964 due to Hohenberg and Kohn (HK), who proved two theorems that laid the foundations of modern DFT.⁸

According to the first HK theorem, which is an existence theorem, the ground state electron density uniquely determines an external potential, $V_{ext}(r)$, which comprises the interaction of electrons with nucleus/other external field. $V_{ext}(r)$, in turn, determines the Hamiltonian of the system, thereby determining the wave function and all properties of interest. That is to say, there is a one-to-one correspondence between the ground state electron density and the ground state energy of a system.

The second HK theorem, a variational theorem, is very analogous to the variational principle in MO theory, which demonstrates that the ground state energy obtained from a well-behaved candidate ground state density cannot be less than the “true” ground state energy. However, HK theorems do not provide a prescription for calculating the ground state energy E_0 from the ground state density ρ_0 , nor does it provide a systematic approach for finding ρ_0 without finding ψ_0 first.⁴

1.2.3.3 Kohn-Sham Density Functional Theory

The biggest breakthrough in DFT came the very next year in 1965, due to Kohn and Sham.⁹ They recognized two major reasons for the poor accuracy of early DFT-based approaches. Realizing all complexities in solving the time-independent Schrödinger equation (eq. (1)) arise from the electron-electron interaction term in the correct Hamiltonian (eq. (3)), Kohn-Sham suggested deliberately avoiding them by replacing it with a reference Hamiltonian of a non-interacting system. Secondly, one of the main reasons for the “failure” of the Thomas-Fermi scheme is the oversimplified expression for the kinetic energy term, which depends simply on $\int \rho^{5/3}(r) dr$. They noted that orbital-based approaches, such as Hartree-Fock, do a much better job in handling kinetic energy.¹⁰

In an effort to improve DFT-based model, Kohn-Sham introduced a fictitious non-interacting reference system built from a set of one-electron functions (orbitals), so that the effective Hamiltonian could be expressed as a sum of one-electron terms, thereby avoiding the complexity of the electron-electron interaction. Additionally, the use of orbitals as reference would allow for

more accurate representation of the major part of the kinetic energy, while the remainder can be computed from an approximate functional (*vide infra*).

So far, the discussion has been focused on a hypothetical *non-interacting* system. The question then is, how to connect this artificial system to the *interacting* one. This can be done by carefully choosing the ground state density of the fictitious system, $\rho_s(r)$ so that it becomes exactly equal to the ground state density of the real interacting system, $\rho_0(r)$:¹⁰ i.e., by setting, $\rho_s(r) = \rho_0(r)$.

Following Kohn-Sham's prescription, by analogy to the HF-method, the Hamiltonian for the noninteracting reference system is given by,

$$\hat{H}_s = \sum_i^N -\frac{1}{2} \nabla_i^2 + \sum_i^N V_s(r_i) \quad (21)$$

where $V_s(r)$ is the effective local potential, without any electron-electron interaction.¹¹ Again in analogy to the HF method, the ground state wave function ψ_S of this non-interacting system can be given by a Slater Determinant,

$$\psi_S = \frac{1}{\sqrt{N!}} \begin{vmatrix} \phi_1(1) & \phi_1(2) & \cdots & \phi_1(N) \\ \phi_2(1) & \phi_2(2) & \cdots & \phi_2(N) \\ \vdots & \vdots & \ddots & \vdots \\ \phi_N(1) & \phi_N(2) & \cdots & \phi_N(N) \end{vmatrix} \quad (22)$$

where the spin orbitals ϕ_i are determined by the eigenvalue equation,

$$\hat{f}_{KS} \phi_i = \varepsilon_i \phi_i \quad (23)$$

\hat{f}_{KS} being the one electron KS-operator defined as $\hat{f}_{KS} = -\frac{1}{2} \nabla^2 + V_s(r)$. These 'optimum' KS orbitals can now be used to compute the major part of the kinetic energy (T_s):

$$T_s = \sum_i^N \langle \phi_i | -\frac{1}{2} \nabla^2 | \phi_i \rangle \quad (24)$$

Knowing that T_s is not the true kinetic energy (T , where $T \geq T_s$) of the real interacting system, we add the difference ($T - T_s$) in the exchange-correlation term E_{xc} , defined as:

$$E_{XC} = T[\rho] - T_s[\rho] + E_{NC}[\rho] \quad (25)$$

where $E_{NC}[\rho]$ is the non-classical contribution to the electron-electron interaction, given as a difference between the ‘true’ electron-electron interaction energy, $E_{ee}[\rho]$ and the classical Coulomb repulsion, $J[\rho]$. Using eqs. (24) and (25), we can now write down the total energy expression for our real *interacting* system:

$$\begin{aligned}
E_{KS}[\rho(r)] &= T_S[\rho] + J[\rho] + E_{Ne}[\rho] + E_{XC}[\rho] \\
&= \sum_i^N \langle \phi_i | -\frac{1}{2} \nabla^2 | \phi_i \rangle + \frac{1}{2} \sum_{i,j}^N \iint \frac{|\phi_i(r_1)|^2 |\phi_j(r_2)|^2}{r_{12}} dr_1 dr_2 \\
&\quad - \sum_i^N \int \sum_A^M \frac{Z_A}{r_{1A}} |\phi_i(r_1)|^2 dr_1 + E_{XC}[\rho]
\end{aligned} \tag{26}$$

Again, in analogy to HF-theory, variational minimization of the energy expression (26), subject to the constraint that the KS-orbitals are orthonormal, $\langle \phi_i | \phi_j \rangle = \delta_{ij}$ yields,

$$\left(-\frac{1}{2} \nabla^2 + \underbrace{\left[\int \frac{\rho(r_2)}{r_{12}} dr_2 - \sum_A^M \frac{Z_A}{r_{1A}} + V_{XC}(r_1) \right]}_{V_{eff}(r), \text{ effective local potential for the real system}} \right) \phi_i = \epsilon_i \phi_i \tag{27}$$

Now, we immediately realize the striking similarity between eq. (23) and (27), and note,

$$V_s(r) \equiv V_{eff}(r) = \int \frac{\rho(r_2)}{r_{12}} dr_2 - \sum_A^M \frac{Z_A}{r_{1A}} + V_{XC}(r_1) \tag{28}$$

From eq. (27) and (28), it is evident that if we can get an estimate of the Kohn-Sham potential $V_s(r)$, we can plug that into one-particle KS-equations (eq. (27)) to get the KS-orbitals and eventually the ground state density and energy.¹⁰

The first step towards obtaining the ground state density and energy, one first needs access to the V_{XC} term, which is the potential due to the exchange-correlation energy, E_{XC} (eq. (25)). This E_{XC} is a place where we deliberately hid all the unknown quantities: the non-classical part of the electron-electron interaction (exchange and correlation), the self-interaction correction and the part of the true kinetic energy not accounted for by the non-interacting reference system.¹⁰ Given that we don’t know the exact functional form of E_{XC} , quite naturally we do not know the same for the corresponding potential V_{XC} , and thus it is simply defined as $V_{XC} = \frac{\partial E_{XC}}{\partial \rho}$.

Based on the Kohn-Sham formalism discussed so far, we can safely say that if the exact functional forms for E_{XC} and V_{XC} were known, we would have obtained the exact energy. Thus, in principle, Kohn-Sham strategy is exact. The approximation only appears when one must decide upon using an approximate explicit function to describe the E_{XC} . Thus, the quality of the density functional approach depends solely on the accuracy of the approximation used for describing E_{XC} , and the central goal of modern DFT is to find better and better approximations for this quantity.

1.2.3.4 Exchange-Correlation Functionals

The local density approximation (LDA) is based on the uniform electron gas model, which assumes electron density to be spatially uniform.

$$E_{XC}^{LDA} = \int \rho(r) \varepsilon_{XC}(\rho(r)) dr \quad (29)$$

VWN¹² is one such LDA functional. For treating open-shell systems with different α and β electrons, however, one often employs the local spin density approximation (LSDA), where two spin densities, $\rho_\alpha(r)$ and $\rho_\beta(r)$ are used instead of one, $\rho(r)$, with the constraint: $\rho(r) = \rho_\alpha(r) + \rho_\beta(r)$.

$$E_{XC}^{LSDA} = \int \rho(r) \varepsilon_{XC}(\rho_\alpha(r), \rho_\beta(r)) dr \quad (30)$$

In LDA, electrons with opposite spins have the same spatial KS-orbitals, whereas LSDA allows electrons with different spins to be in different spatial KS orbitals, offering more flexibility. Thus, sometimes even with an even number of electrons, LSDA performs better than LDA (e.g. an H₂ molecule at higher separation) because it allows symmetry breaking.

LDA/LSDA was found to be a fairly good approximation for simple metals like sodium. However, the approximation that the density is spatially uniform, is far from accurate, and in fact, densities in real systems vary rapidly. Moreover, V_{XC} in LSDA decays exponentially and does not follow the correct long-range asymptotic Coulombic behavior ($-1/r$), resulting in electrons that are very weakly bound.¹³

To this end, attempts were made to improve upon the local approximation. In the early eighties came the ingenious prescription to include the information about the gradient of the

density, in addition to the density itself, so as to account for the non-homogeneity of the true electron density.¹⁰ This formalism is known as the generalized gradient approximation (GGA; eq. 31). Some of the most popular GGA functionals are PW91,¹⁴ PBE¹⁵ etc.

$$E_{XC}^{GGA} = \int f(\rho_\alpha(r), \rho_\beta(r), \nabla\rho_\alpha(r), \nabla\rho_\beta(r)) dr \quad (31)$$

The next logical step towards functional development is then to include the Laplacian of the density ($\nabla^2\rho(r)$), which constitutes the *meta*-GGA family of functionals. However, the Laplacian $\nabla^2\rho(r)$ in the functional sometimes causes numerical instabilities, and thus most of the *meta*-GGA functionals now replace $\nabla^2\rho(r)$ with non-interacting kinetic energy density, $\tau = \sum_i^{occ} \frac{1}{2} |\nabla\psi_i|^2$.² TPSS¹⁶, M06-L etc. are some of the popular *meta*-GGA functionals.

Exchange-correlation (E_{XC}) energy has two parts: the exchange part and the correlation part, and in general the exchange contributions are much larger than the corresponding correlation term. So, in order to construct a more accurate exchange-correlation functional, one should describe the exchange functional as accurately as possible. Given that the exchange energy of a Slater determinant can be calculated exactly based on the HF scheme, some functionals replace part of their exchange-correlation energy with HF exact exchange. This class of functionals is called hybrid functionals. Even though different functionals include HF exchange in a variety of ways, one of the simplest of them is given by,²

$$E_{XC} = (1 - a)E_{XC}^{DFT} + a E_X^{HF} \quad (32)$$

B3LYP, PBE0, M06, ω B97X etc. are the most popular hybrid functionals in modern DFT, with 20%, 25%, 27%, 22–100% HF exchange, respectively. Unfortunately, there is no systematic way to improve density functionals, since E_{XC} does not have a variational behavior. Typically, the choice of a particular functional depends on the chemical system of interest. Validation of its performance against high-level (often, wave function-based) theory or experiments is usually recommended.

1.2.3.5 Dispersion Corrections to DFT

In many chemical systems like molecular aggregates, host-guest systems, and biological systems like DNA and protein, dispersion interaction plays an important role.^{17a} Dispersion interaction can empirically be defined as the attractive part of the van der Waals'-type interaction potential between atoms/molecules which are not directly bonded via a(n) covalent/ionic bond.^{17b} Theoretically speaking, the dispersion part is actually a pure electron correlation effect (dynamic correlation), that results due to fluctuating charge distribution.^{17c} In fact, the difference between electron correlation and dispersion is not very clear except for the fact that they operate on different interatomic distance regimes (short- vs. long-ranged, respectively).¹⁸ By applying perturbation theory to the electrons of interacting atoms, these two distance regimes can be identified. In Figure 1.2, the dashed line represents the interpolation used in many correction methods, and indicates the medium-range ($\sim 2.5\text{--}3.5 \text{ \AA}$, non-bonded regime) correlation energy, and asymptotically at large distances, the dispersion energy is given by the well-known $-\frac{1}{R^6}$ dependence on the interaction distance.^{17b}

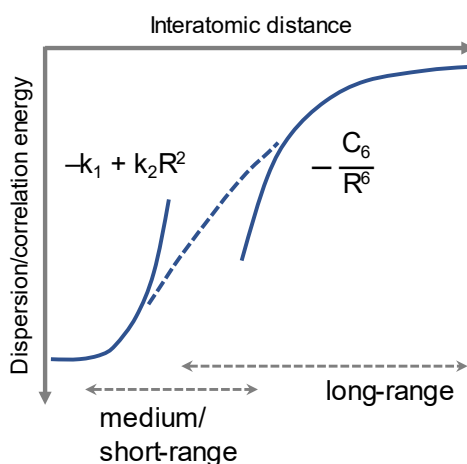


Figure 1.2 Depiction of the short-, medium- or long-range behavior of the dispersion/correlation energy (ref. 18). © Wiley-VCH Verlag GmbH & Co. KGaA.

In the realm of wave function theory, dispersion is described by double excitations between occupied and virtual orbitals, and can be computed almost accurately by employing wave function based methods like CCSD(T).^{17b} This procedure for capturing the van der Waals' (vdW)-interaction, however, is not computationally efficient even for medium-sized systems, and as a

way out, one often has to take the help of mean-field (MF) approaches like Hartree-Fock, Kohn-Sham DFT, or semiempirical MO theory. However, these MF approaches consider only the set of N one-particle functions used for describing the N electrons of the system, and virtual orbital (or, nonlocal density, depending on the situation) is not taken into consideration. As a result of which, they lack long-range London dispersion interactions.²³ Thus, attempts are made to incorporate dispersion interactions inside the DFT framework semiclassically: dispersion energy (E^{disp}) is first evaluated between atom pairs and then added to the electronic energy (E^{MF}) obtained via the MF approach, i.e., $E^{tot} = E^{MF} + E^{disp}$. Keeping in mind the wave function based origin of the dispersion energy (E^{disp}), we now look back at the electron-correlation energy expression derived for the interacting fragments A and B , from second-order perturbation theory (PT2). After application of the Slater-Condon rules, this is given by,^{17b}

$$E_{corr}^{PT2} = - \sum_{ij}^{n_{occ}} \sum_{ab}^{n_{virt}} \frac{[(ia|jb) - (ib|ja)]^2}{\omega_{ai} + \omega_{bj}} \quad (33)$$

where the indices ij and ab go over the occupied and the virtual orbitals respectively, ω_{ai} represents the energy required to excite an electron from orbital i to orbital a (localized on A), and the two-electron integral is given by:

$$(ia|jb) = \int \phi_i(r_1)\phi_a(r_1) \frac{1}{r_{12}} \phi_j(r_2)\phi_b(r_2) dr_1 dr_2 \quad (34)$$

Now when the orbitals i, a and j, b are localized on fragment A and B respectively, the first term in the numerator of eq. (33), the Coulomb term, decays slowly, but the second term (exchange term $(ib|ja)$) falls off exponentially in the asymptotic limit. So, in the asymptotic limit, the PT2 correlation energy reduces to the square of Coulomb interactions between transition densities ia and jb localized on fragments A and B respectively. Thus, we have,

$$\lim_{R \rightarrow \infty} E_{corr}^{PT2} = E_{disp}^{AB} = - \sum_{i,a \in A} \sum_{j,b \in B} \frac{(ia|jb)^2}{\omega_{ai} + \omega_{bj}} \quad (35)$$

Now if the Coulomb potential is expanded in a multipole expansion, it can be shown that the lowest order term (dipole-dipole term) gives rise to the much well-known $E_{disp}^{(6)}$ term (α is the dipole-dipole polarizability):^{17b}

$$E_{disp}^{(6)} = -\frac{3}{\pi R^6} \int_0^{\infty} \alpha_A(i\omega) \alpha_B(i\omega) d\omega = -\frac{C_6^{AB}}{R^6} \quad (36)$$

As evident from eq. (36), if the dispersion coefficient C_n^{AB} for the fragments A and B are known, the pairwise dispersion, $E_{disp}^{(n)}$ can easily be evaluated. However, since C_n^{AB} coefficients are not known for arbitrary fragments A, B, etc., it is fragmented into atoms and expressed as a sum of atom pairwise terms: $C_n^{AB} = \sum_{I \in A} \sum_{J \in B} C_n^{IJ}$.

Based on the idea discussed so far, Grimme and coworkers reported the DFT-D formalism for capturing dispersion energy semiclassically which, while computationally affordable, was found to be quite accurate for studying large van der Waals' complexes.^{17a,19a} While the DFT-D and DFT-D2 formalisms consider interactions due to all possible pairs of atoms (two-body dipole-dipole dispersion energy, $E_{disp}^{(6)}$), the more recent DFT-D3 formalism considers triplet of atoms as well, so as to capture three-body effect ($E^{[3]}$) in addition to accounting for the two-body energies ($E^{[2]}$).^{19b}

$$E^{DFT-D3} = E^{KS-DFT} + E^{disp}, \text{ where } E^{disp} = E^{[2]} + E^{[3]} \quad (37)$$

The most important two-body term ($E^{[2]}$) in Eqn. (36) is given by,

$$E^{[2]} = -\frac{1}{2} \sum_{A \neq B} \sum_{n=6,8} s_n \frac{C_n^{AB}}{r_{AB}^n} \quad (38)$$

where C_n^{AB} is the n^{th} -order dispersion coefficient for atom pair AB, r_{AB} is the interatomic distance, and s_n is a functional dependent scaling factor.^{19c} For short distances (r_{AB}), however, the dispersion contribution must be damped to avoid near singularities, and one of the most common practice of doing so is proposed by Becke and Johnson,²⁰

$$E^{[2],BJ} = -\frac{1}{2} \sum_{A \neq B} \sum_{n=6,8} s_n \frac{C_n^{AB}}{r_{AB}^n + f(R_0^{AB})^n} \quad (39)$$

where $R_0^{AB} = \sqrt{\frac{C_8^{AB}}{C_6^{AB}}}$, and the damping function, $f(R_0^{AB}) = a_1 R_0^{AB} + a_2$ (a_1 , and a_2 are free fit parameters introduced by Becke and Johnson).^{19d} Noncovalent interactions can also be added during the construction of some density functionals. This is the case for the Minnesota suite of

functionals. In addition to describing medium-range correlation energies quite accurately, these functionals, particularly M06 suite of functionals have been reported to be very good in describing thermochemistry, barrier heights, main group chemistry and transition metal chemistry.²¹

For most part of the work reported in this thesis, M06 suite of meta-GGA local functional M06-L has been used. In addition, hybrid functional B3LYP combined with Grimme's D3 dispersion correction and Becke-Johnson damping, and M06 suite of hybrid meta-GGA functional M06, M06-2X were also used in some instances.

1.3 Organization of the Thesis

This thesis highlights the various ways quantum chemical methodologies can be applied to metal-organic complexes of varying size and complexity. With contributions from experimental collaborators, each of the following chapters reports the use of computational chemistry to solve one or more real-world problems.

Synthesis of aliphatic polyesters from biomass-derived feedstocks is a promising route to combat the looming threat of plastic pollution. Ring-opening transesterification polymerization (ROTEP) catalyzed by metal alkoxide $[M]-OR$ complexes is often employed as a routine procedure to yield such polymers. Detailed knowledge of the mechanism for such a process is crucial to designing better and faster catalysts, and in recent years significant progress has been made in this regard. Chapter 2 summarizes our detailed computational studies in understanding instances of ϵ -caprolactone (CL) polymerization catalyzed by various $[M]-OR$ complexes. Using this mechanistic knowledge, we have introduced an efficient computational protocol, called the framework distortion energy (FDE) model to rapidly screen a large number of ligand frameworks, with the goal of designing better/faster ROTEP catalysts having improved performance. On the basis of our screening, new aluminum-based complexes have been designed *in silico* with predicted ROTEP activities higher than those now known. Our prediction was verified experimentally through the synthesis and characterization of one such complex and evaluation of its ROTEP reactivity, underscoring the importance of fast screening of hypothetical catalysts prior to subsequent more complete computational evaluation, and ultimate experimental realization. The last section of the chapter summarizes our work on developing an isosorbide-based polyether and highlights the importance of experiment/computation synergy.

Site-selective functionalization of benzylic C-H bonds is very attractive in drug discovery, chemical biology, and materials synthesis. While C-H functionalization methods allow for efficient synthesis of target molecules, the availability of multiple C-H bonds within a given molecule, however, introduces the challenge of site selectivity. Chapter 3 discusses our collaborative effort in understanding the mechanism of selective functionalization (azidation and etherification) of benzylic C-H bonds using copper catalysts in combination with *N*-

fluorobenzenesulfonimide (NFSI). Detailed mechanistic study employing density functional theory suggests a radical-polar crossover pathway, providing a basis for the observed lack in enantioselectivity.

Exploring C–H activation reactions in light hydrocarbons is of special interest as it has the potential to address challenges in fuel liquefaction. As possibly biomimetic species, small-molecule mononuclear copper(III) hydroxo-, peroxy-, and benzoate species have been shown to activate C–H bonds. Such reactivity can be characterized as a hydrogen atom transfer (HAT) or a concerted proton-coupled electron transfer (cPCET). The distinction between these two mechanisms is important as they can have implications in the reaction rate: cPCET reactions are typically faster compared to HAT cases. Chapter 4 demonstrates the use of state-of-the-art theoretical tools to distinguish these mechanisms for different reagent/substrate combinations and delineates the coupled nature of proton and electron transfer from the substrate to different copper-oxygen species which can be exploited for strategic tuning of reactivity and selectivity toward various substrate X–H (X = C, O) bonds.

Heterogeneous catalysts synthesized by anchoring catalytically active species over metal–organic frameworks (MOFs), which themselves are a class of porous crystalline material consisting of inorganic nodes connected via organic linkers arranged in three-dimensional networks, has garnered significant interest in the last decade. High energy efficiency and atom economy make this class of material highly attractive for industrial applications. However, given the complexity of the material, a detailed structure–activity correlation is hard to obtain experimentally. Thus, in Chapter 5, the final chapter of this thesis, I have summarized our current efforts in identifying the local structure of the catalytically active species in MOF-based single-site catalysts. Moreover, by modeling the catalytic reaction pathway (e.g., selective oxidation of benzyl alcohol to benzaldehyde), we have identified the factors dictating catalytic performance and prescribed strategies for improving their activity. Two specific cases are discussed: in the first case vanadium oxo species is anchored over MOF ($\text{VO}_x\text{@MOF}$) and in the second one Pd^{II} is deposited over acid modified MOF-support (Pd@MOF).

Chapter 2

Modeling Polymerization Reactions

Synopsis. Synthesis of aliphatic polyesters from biomass-derived feedstocks is a promising route to combat the looming threat of plastic pollution. Ring-opening transesterification polymerization (ROTEP) catalyzed by metal alkoxide $[M]-OR$ complexes is often employed as a routine procedure to yield such polymers. Detailed knowledge of the mechanism for such a process is crucial to designing better and faster catalysts, and in recent years significant progress has been made in this regard. This chapter summarizes our detailed computational studies in understanding instances of ϵ -caprolactone polymerization catalyzed by various $[M]-OR$ complexes. Using this mechanistic knowledge, we have introduced an efficient computational protocol, called the framework distortion energy model to rapidly screen a large number of ligand frameworks, with the goal of designing better/faster ROTEP catalysts having improved performance. On the basis of our screening, new aluminum-based complexes have been designed *in silico* with predicted ROTEP activities higher than those now known. Our prediction was verified experimentally through the synthesis and characterization of one such complex and evaluation of its ROTEP reactivity, underscoring the importance of fast screening of hypothetical catalysts prior to subsequent more complete computational evaluation, and ultimate experimental realization. The last section of the chapter summarizes our work on developing an isosorbide-based polyether and highlights the importance of experiment/computation synergy.

2.1 Sustainable Polymers: General Remarks

2.1.1 Introduction

In 1920, Hermann Staudinger defined polymers as a class of compounds composed of identical small molecules linked through strong covalent bonds.²² However, most of his colleagues disagreed and argued polymers to be only a loose aggregation of smaller molecules. Eventually, Staudinger's idea was proved and placed on a sound basis and he went on to win the 1953 Nobel Prize in Chemistry. The macromolecules that Staudinger hypothesized are ubiquitous in today's world. From common household items like bottles, bags and clothes to more advanced applications like 3D-printing, and drug delivery—plastics have invaded almost every aspect of modern life, owing to their diverse and remarkably useful properties like durability, lightweight, conductivity, the ability to self-heal etc.²³ Unfortunately, as Marc A. Hillmyer puts: “The durability of plastics is both their strong suit and their Achilles' heel”, since discarded plastics hang around forever and ultimately ends up in our waterways. For instance, plastic bags made from polyethylene can take nearly 400 years to degrade in the open field.²⁴ Indiscriminate disposal of plastics after their fleeting use produces a myriad of wastes that persist in the landfill and thereby releases a huge amount of pollutants—the environmental impact of which can be detrimental.²⁵

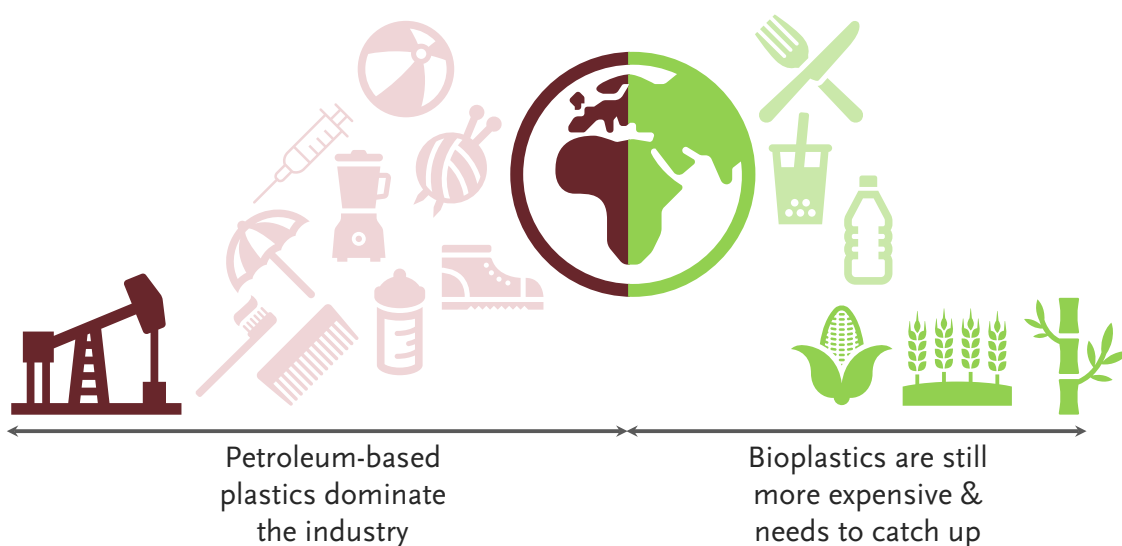


Figure 2.1 Plastic industry and modern life: Everyday commodities are made of plastics. However, the plastic industry is dominated by polymers from petroleum-based sources, which are neither bio-renewable nor the resulting plastics are bio-degradable. Plastics from plant-based sources, which *can* be

biodegradable/compostable, are still under-developed and their usage is limited by their high production cost. More research in this area and new policies are thus needed to make their usage widespread.

2.1.2 Aliphatic Polymers to the Rescue

The looming threat of pollution combined with the inevitable depletion of fossil resources has encouraged researchers around the globe to shift attention away from petroleum-based plastics and develop macromolecular materials from renewable resources with low carbon footprints.²⁶ Aliphatic polymers could serve as a great substitute for their petroleum-based counterparts, as they can be prepared from biomass-derived feedstocks and can be recycled, composted, and disposed of relatively easily.²³ In current polymer research, bio-renewable monomeric units like epoxides, anhydrides, lactones, and lactides are being used routinely in a conscious effort to find suitable substitutes for their petroleum-based analogs like ethylene, styrene, and vinyl chloride, among others. Controlled polymerization of these bio-renewable monomers produces bio-based environmentally less-toxic plastics that can contribute significantly to the sustainable development of humankind.²⁷

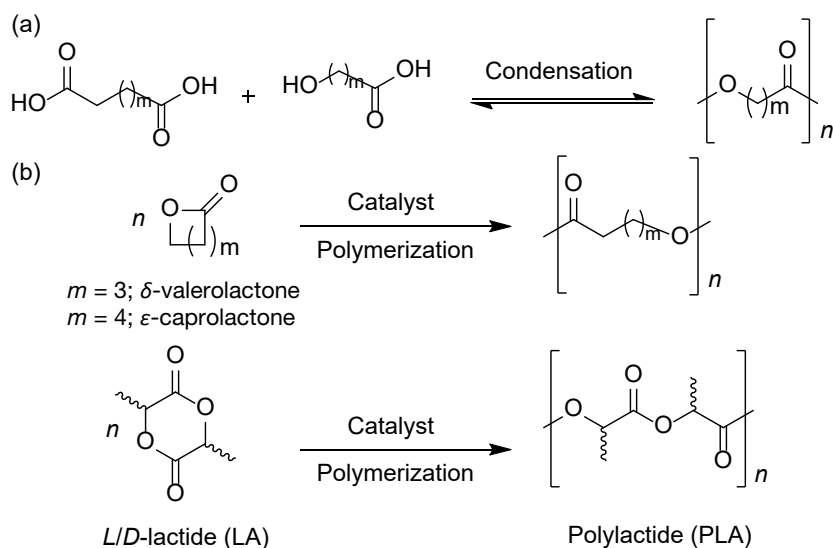
2.1.3 Monomer Enchainment Processes

In general, there are two enchainment processes for any polymerization reaction:²⁸ a step-growth process and a chain-growth process. Step-growth condensation (Scheme 2.1(a)) is one of the earliest methods by which aliphatic polyesters are synthesized.²⁹ However, these processes are associated with some serious shortcomings, requiring high temperatures and long reaction times—artifacts that often lead to numerous side reactions. Removal of water from the reaction medium is also necessary to drive the equilibrium forward. Additionally, these processes lack control, resulting in a broad molecular weight distribution, as described by the polydispersity index[†] of the formed polymer, which has a large effect on the properties of the material.³⁰

[†]Polydispersity index (PDI) is defined by the ratio of weight-average molecular weight, M_w and number-average molecular weight, M_n)

In contrast, for a chain-growth process, molecular weight increases because of repeated addition of monomeric units to the chain-end. Here we focus on one particular case, the ring-opening polymerization (ROP), which circumvents the limitations associated with the condensation polymerization.³¹ ROP and its different variants are more exciting, as they allow efficient control over molecular weight, molecular weight distribution, stereochemistry, functionality, architecture (*viz.* diblock/multiblock etc.) and topology (*viz.* linear/branched etc.) of the synthesized polymer.³² Scheme 2.1(b) outlines some typical aliphatic polyesters synthesized via ring-opening transesterification polymerization (ROTEP), a specific type of ROP.

Scheme 2.1 (a) Step-growth condensation yielding polyester. (b) Ring-opening transesterification polymerization (ROTEP) of lactones/lactides (Ref. 30)



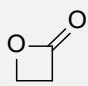
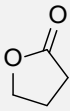
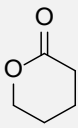
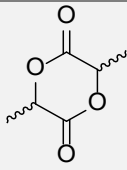
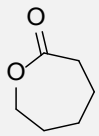
2.1.4 Ring-Strain Dictates the Choice of Monomer

Polymerization reactions are entropically unfavorable since several monomer units are ‘tethered’ into *one* polymer chain. Thus, in many instances, cyclic monomers are used as repeat-units of the polymer wherein the ring-strain enthalpy of cyclic monomers is exploited as the thermodynamic driving force for chain propagation.²⁹ Table 2.1 shows a series of simple lactones/lactides of different ring-size and their associated ring-strain. Clearly, 4/7-membered cyclic monomers

possess larger ring-strain that can be released during polymerization in comparison to their 5/6-membered congeners, and hence the former are more reactive towards ROTEP.

Since ring-strain of a given monomer is a key determining factor for its subsequent polymerization, one interesting aspect of computational research in this regard is to use molecular mechanics-based conformer sampling, followed by density functional calculations to predict ring-strain, thereby guiding the choice of monomers that will be prioritized for synthesis and eventual polymerization. This is demonstrated in our collaborative work on developing an isosorbide-based polyether, where ring-strain enthalpy calculation guided the derivatization of the isosorbide monomer as a complex cyclic ether followed by its ROP, and was a key step in the overall discovery (see section 2.4.4).³³

Table 2.1 Thermodynamic parameters for ROTEP of different lactones at 298 K (Ref. 34).

species					
	β -propiolactone	γ -butyrolactone	δ -valerolactone	<i>rac</i> -lactide	ϵ -caprolactone
ring size	4	5	6	6	7
ΔH (kJ/mol)	-82.3	5.1	-27.4	-22.9	-28.8
ΔS (J/mol-K)	-74	-29.9	-65.0	-25.0	-53.9

2.1.5 Ring-Opening Polymerization of Lactone/Lactide

Lactone/lactide are an exciting class of monomer that easily yield aliphatic polyester via ROP. Amongst the compounds listed in Table 2.1, *rac*-lactide (LA) polymerization is very popular and in fact, is employed on industrial scales. However, the additional stereochemical feature(s) complicates the polymerization of *rac*-LA, and hence to understand the mechanism of aliphatic polyester synthesis via ring-opening trans-esterification polymerization (ROTEP), the 7-membered monomer ϵ -caprolactone (CL) is chosen for our study as it offers convenience both computationally and experimentally.

2.1.6 Catalysts for ROTEP of Lactone/Lactide

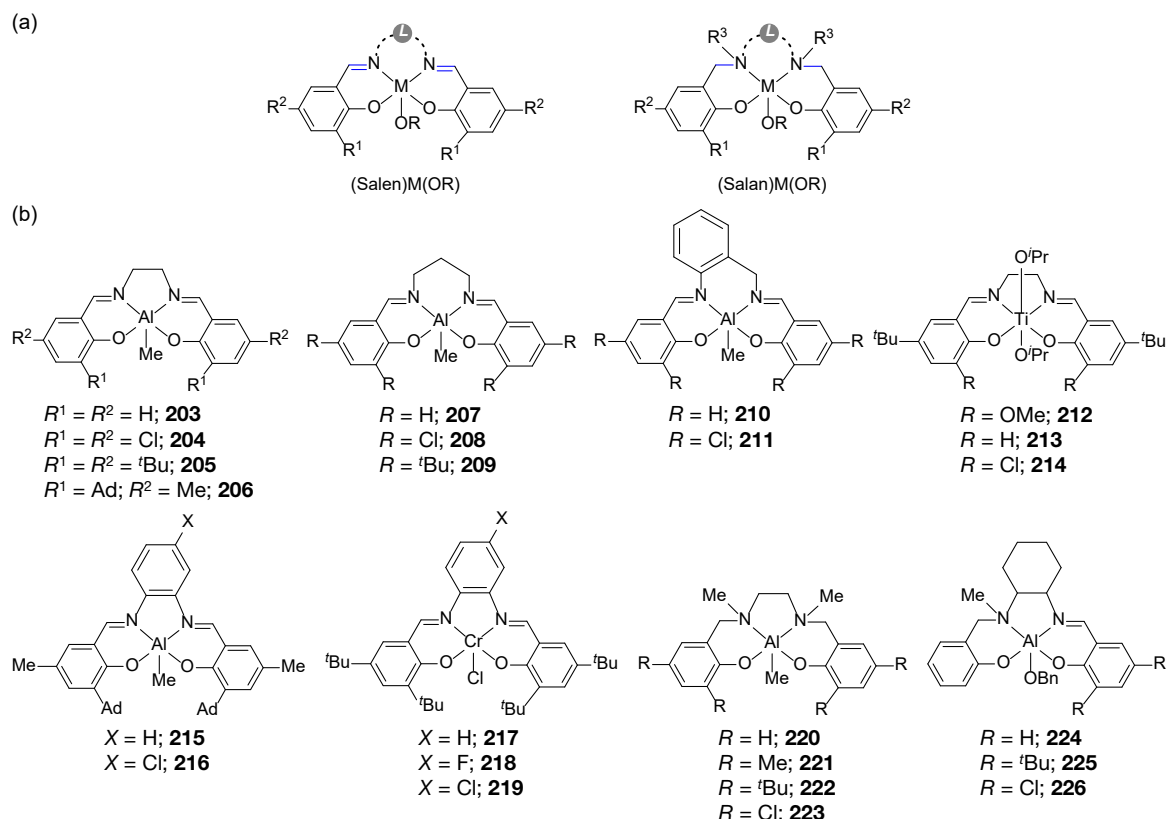
Ring-opening polymerization of cyclic esters is performed traditionally by using metal catalysts such as $\text{Al}(\text{O}^i\text{Pr})_3$, $\text{AlEt}_3/\text{H}_2\text{O}$ or $\text{ZnEt}_2/\text{H}_2\text{O}$, with β -butyrolactone (β -BL) being the typical choice for the monomer owing to its high ring-strain.³⁵ When the monomer scope broadened to include lactides, the tin-based catalyst $\text{Sn}(\text{Oct})_2$ (Oct= 2-ethylhexanoate) became popular.³⁶ Even though these early catalysts produced promising results, they often required high reaction temperatures ($\sim 140^\circ\text{C}$) and were often associated with inter- and intramolecular transesterification.³⁷ Thus, in an effort to achieve more controlled polymerization, metal complexes supported by ancillary ligands were introduced. Many complexes of different metals, like calcium, magnesium, aluminum, zinc, titanium, and lanthanides have been studied over the years.³⁷ Of these, substantial work has been done on metal complexes supported by tetradentate ligands with *O*- and *N*-donors, specifically, salen (*N,N'*-bis(salicylaldimine)-1,2-ethylenediamine) and salan (*N,N'*-bis(*o*-hydroxybenzyl)-1,2-diaminoethane) ligands. A salen ligand has an *imine* linker, which is to be distinguished from the *amine* linker of a salan-moiety (Scheme 2.2a).

Advantages of using salen/salan ligands are manifold. They can be synthesized readily and have high complexation ability with a wide range of metals, allowing systematic screening (simply by changing central metal ion *M*; Scheme 2.2a). One can also systematically tune the steric and electronic effects of the catalyst very easily, by changing the substituents on the aryloxy ring (R^1 and R^2 substituents). Additionally, the imine/amine linker of the catalyst (*L*) can be altered to observe the effect of flexibility of the pre-catalyst structure on the rate of polymerization. Tuning of these linker lengths or substitution patterns also provide novel ways to induce asymmetry in the catalyst, thus making it suitable for stereoselective polymerization.

In 1991, Vincens et al.³⁸ first reported ROP of cyclic esters using an $\text{Al}(\text{salen})$ complex **203** (Scheme 2.2b), which showed moderate control for ROP of *rac*-LA. From then on, a series of modifications have been invoked to improve its catalytic activity. Hormnirun et al.³⁹ introduced electron withdrawing substituents on the aryloxy group and reported an increase in the rate of *rac*-LA polymerization, while a decrease in the rate is observed with an increase in the steric bulk at

ortho-aryloxy position. Thus, when $R^1 = \text{H}$ (**203**) was replaced with Cl (**204**), significant enhancement in reaction rate could be observed, while $R^1 = \text{tert-butyl}$ ($t\text{Bu}$) substitution (**205**) slowed down the rate (**203** polymerizes *rac*-LA ~50 times faster compared to **205**), and the overall reactivity trend follows **204** > **203** > **205**.³⁹ More interestingly, the authors reported an ~11-fold increase in the rate of *rac*-LA polymerization, when the diimine tether of the salen moiety was changed from a two-carbon linker, referred to as L^2 -salen (e.g. **203**) to a three-carbon linker, referred to as L^3 -salen (**207**, for instance).³⁹ Consistent with this study, an increase in rigidity of the amine tether in the form of a phenyl ring: L^2 -salen (**206**) to L^2 -salophen (**215**) resulted in a decrease in the rate of polymerization of both *rac*-LA and *rac*- β -BL (i.e., rate with **206** > **215**).⁴¹ Surprisingly, similar modification in the L^3 -linker resulted in an increase in the rate of *rac*-LA polymerization: **210** > **207** and **211** > **208**.³⁹

Scheme 2.2 (a) Generic metal salen/salan complexes. (b) Metal salen/salan/salalen/salophen complexes for ring-opening polymerization of lactones/lactides.



Contrary to the reactivity trend of Al(salen) complex, Ti(salen) catalysts demonstrated a slower rate of *rac*-LA polymerization when more electron withdrawing substituents were added;

the reactivity order follows $R = \text{Cl} \text{ (214)} < \text{H} \text{ (213)} < \text{OMe} \text{ (212)}$.⁴⁰ Similarly, for Al(salophen) initiator, rate of *rac*-LA and *rac*- β -BL polymerization decreased with electron withdrawing substituents: $X = \text{H} \text{ (215)} > \text{Cl} \text{ (216)}$.⁴¹ In contrast, an exact opposite trend is reported by Zintl et al.⁴² during poly(hydroxybutyrate) formation from *rac*- β -BL using Cr(salophen) catalysts, and the relative rate is $X = \text{F} \text{ (218)} > \text{Cl} \text{ (219)} > \text{H} \text{ (217)}$.

While Al(salen) complexes have been studied extensively, the corresponding salan complexes are relatively less explored. The ROP of cyclic esters using an Al(salan) compound was first reported in 2004 by Hormnirun et al.⁴³ For Al(salan) complexes, an increase in the steric bulk at *ortho*-aryloxy position decreased the rate of polymerization: $R = \text{'Bu} \text{ (222)} < \text{Me} \text{ (221)} < \text{H} \text{ (220)}$. Assuming methyl group to be sterically similar to chloro-substituent, enhanced polymerization rate could be observed due to electron withdrawing chloro-substitution: $R = \text{Cl} \text{ (223)} > \text{Me} \text{ (221)}$.⁴³ In the case of a mixed salen/salan, i.e., a salalen framework, similar trends could be observed. For *rac*-LA polymerization, substitution on the aryloxy fragment of a salalen catalyst yields the trend $R = \text{Cl} \text{ (226)} > \text{H} \text{ (224)} > \text{'Bu} \text{ (225)}$.⁴⁴

Evidently, the rate of polymerization is very sensitive to apparently subtle alterations in the steric/electronic factors of the ancillary ligand. While some catalysts showed increased polymerization rate with electron withdrawing substituents, others preferred electron releasing groups. While some catalysts favored more rigidity in the imine/amine tether, others preferred a flexible linker for faster polymerization. Owing to such apparently conflicting experimental observations, the importance of a detailed mechanistic study aided with DFT modeling is of utmost importance to gain an unambiguous and unified understanding of the intrinsic factors that dictate rates of such polymerization processes.

2.1.7 Variations in ROP Mechanism

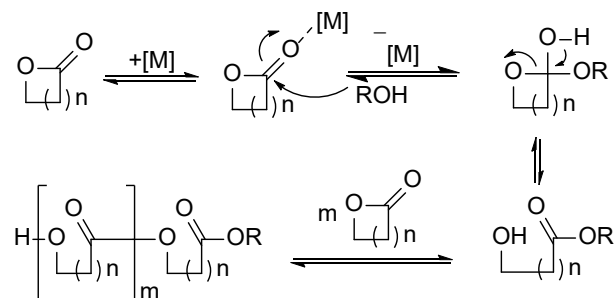
Depending on the specific monomer/catalyst combination, ring-opening polymerization reactions can proceed either via a cationic, anionic, activated monomer or a coordination-insertion pathway.⁴⁵ Polymerization of ethers generally follow a cationic mechanism. The specific

case of cationic ROP of isosorbide-derived monomer **203** is discussed in section 2.5. Polymerization of vinyl monomers having strong electronegative groups is an example of anionic polymerization, which is not the focus of our discussion. ROP of lactones/lactides, generally involves either an activated monomer mechanism or a coordination-insertion pathway, both of which are discussed in the following section, given our interest in aliphatic polyesters.

2.1.7.1 Activated Monomer Mechanism

In the activated monomer mechanism for lactone polymerization (Scheme 2.3), the metal catalyst first coordinates to the monomer through the carbonyl oxygen atom, thus increasing the electrophilicity of the carbonyl carbon atom. Any nucleophile present in the medium, like alcohol or even water then attacks that activated carbonyl carbon and initiates the polymerization process. This pathway is often observed for polymerization reactions catalyzed by organocatalysts such as N-heterocyclic carbenes (NHC).⁴⁶

Scheme 2.3 Activated monomer mechanism of simple lactones (Ref. 30)

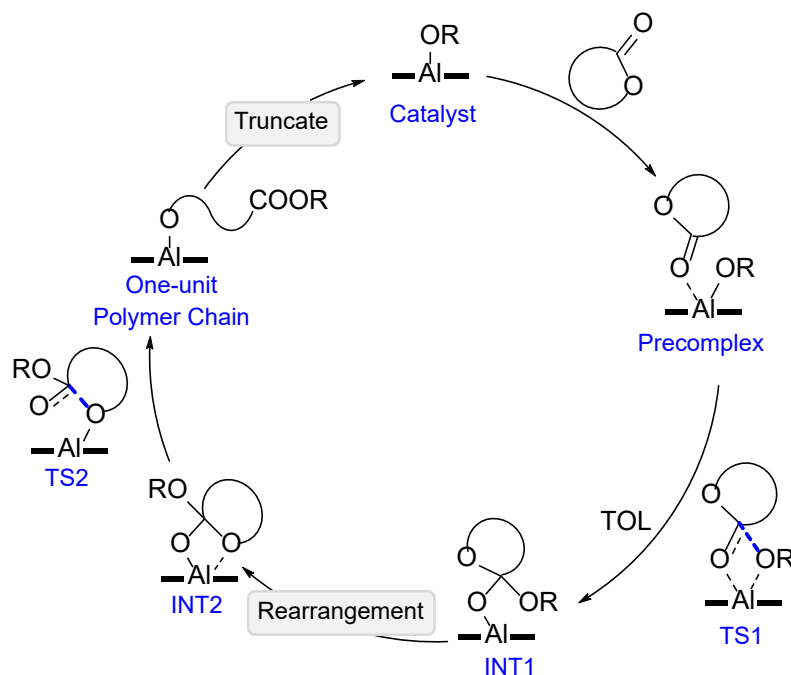


2.1.7.2 Coordination-Insertion Mechanism⁴⁷

Over the past decade, experiment and theory combined have made significant progress with respect to elucidating the details of ROTEP mechanisms.^{48,49,51} For ROTEP reactions catalyzed by metal alkoxide $[M]-OR$ species, like those mentioned in Scheme 2.2, the “coordination-insertion” mechanism (Scheme 2.4) is often invoked as the preferred pathway for the monomer-to-polymer conversion.⁴⁹

According to the coordination-insertion pathway, the reaction proceeds through four elementary steps: (i) lactone initially coordinates the Lewis acidic metal center of the (penta-coordinated) $[M]-OR$ catalyst, which activates its carbonyl carbon. (ii) insertion of the alkoxide into the activated monomer ester via TS1, which is typically the turnover-limiting (TOL) step, (iii) rearrangement of the tetrahedral orthoester intermediate with respect to which O-atoms interact most closely with the $[Al]$ -center, and, finally, (iv) ring-opening ester bond cleavage (via TS2) to generate the polymer chain alkoxide terminus elongated by one unit. The same mechanism is also active for initiation, with energetic details differing somewhat depending on how closely the precatalyst $-OR$ group resembles the alkoxide terminus of the growing polymer (from the standpoint of assessing structure-activity relationships, modeling initiation can be more efficient as it avoids the complexities associated with long, flexible growing polymer chains).

Scheme 2.4 Coordination-insertion mechanism of simple lactones (TOL = turnover-limiting). © American Chemical Society



Despite the coordination-insertion mechanism being widely accepted for ROTEP, there have been contradictory observations that are not readily explicable. Varying rate of polymerization as

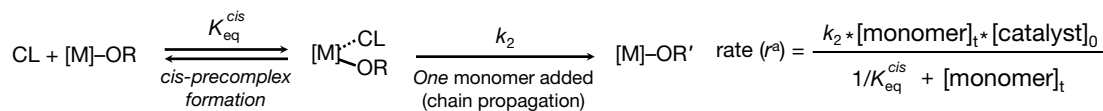
a consequence of variations in the steric and electronic features of the substituents on the ancillary ligands, as described in section 2.1.6, raise intriguing questions on the relative importance and balance between the monomer binding, and the nucleophilicity of the alkoxide group in this regard.^{39,50,51}

2.1.8 Kinetic Model for ROP of ϵ -Caprolactone

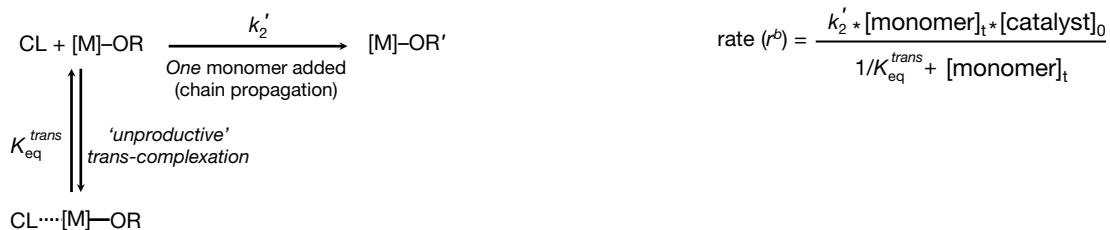
During kinetic studies of ϵ -caprolactone polymerization catalyzed by (Salen)Al(OR) complex, a saturation behavior[‡] is observed.⁵¹ Saturation kinetics is typically explained via the Michaelis–Menten equation⁵² given in Scheme 2.5, where a pre-equilibrium step having an equilibrium constant K_{eq} precedes the rate-determining step defined by rate-constant k_2 .

Scheme 2.5 Mechanism for ROTEP. K_{eq} is the equilibrium constant for monomer binding, k_2 is the catalytic rate constant for monomer enchainment and k_2' is the ratio of k_2 and K_{eq} .

(a) Monomer binds *cis*- to the alkoxy-group



(b) Monomer binds *trans*- to the alkoxy-group



Density functional modeling of this reaction revealed that the formation of a *cis*-precomplex (path *a*, Scheme 2.5) is unlikely, since it is ~12 kcal/mol higher in energy than the infinitely separated catalyst and monomer and hence is deemed “kinetically irrelevant”. Nevertheless, since saturation is observed, a pre-equilibrium involving the monomer and the catalyst must exist prior to the rate-limiting step. Given that the *cis*-bound precomplex is too high in energy, a modified

[‡]Saturation behavior means at relatively high substrate concentration, no considerable increase in reaction rate is observed with further increase in the substrate concentration.

mechanism for ROTEP was proposed (path *b*, Scheme 2.5) and K_{eq} now refers to the non-productive binding of the monomer *trans*- to the alkoxy-group at the Al-center.

Clearly, *trans*-binding is an unproductive pathway leading to substrate inhibition. From the *trans*-bound precomplex, the monomer has to first dissociate and then approach the alkoxide on the other face of the catalyst and form the alkoxide-inserted product *directly* via ‘concerted insertion’. Thus, efforts have been devoted towards designing ligand frameworks that would eliminate unproductive *trans*-binding of monomer. Section 2.2 demonstrates one such ligand aimed at bypassing *trans*-complexation, and possibly enhancing ROTEP rates.

2.1.9 Framework Distortion Energy (FDE) Hypothesis

As mentioned in section 2.1.6, the imine-tether of a metal salen complex can have a significant impact on its ROTEP reactivity. Report by Hormnirun et al.,³⁹ demonstrates an ~11-fold increase in the rate of *rac*-LA polymerization, when the diimine tether of the salen moiety was changed from a two-carbon linker, *L*²-salen (**235**; Figure 2.2) to a three-carbon linker, *L*³-salen (**241**; Figure 2.2). Marlier et al.⁴⁹ reported a detailed mechanistic study aimed at better understanding the fundamental basis for such rate differences caused by catalyst structure variation in the form of linker length. DFT modeling of the reactants and key TS geometries along the reaction coordinate revealed that, even though the bond matrices about the Al center of the *resting* precatalyst structures (“catalyst” in Scheme 2.4) of *L*²-salen vs. *L*³-salen complexes were significantly different, their corresponding TOL TS geometries (“TS1” in Scheme 2.4; **235**^{TS1}, **241**^{TS1} in Figure 2.2) were found to be strikingly similar. The mean unsigned deviation of Al–X bond distances in TS1 was only 0.01 Å and that for all *cis*-angles X–Al–Y was only about 3.0° (X/Y = N/O-atoms). This suggests that while each of these catalysts starts from *different* resting geometries, they all pass through an “optimal” TS1 geometry that is efficient for decreasing the free energy of activation associated with the alkoxide insertion step.

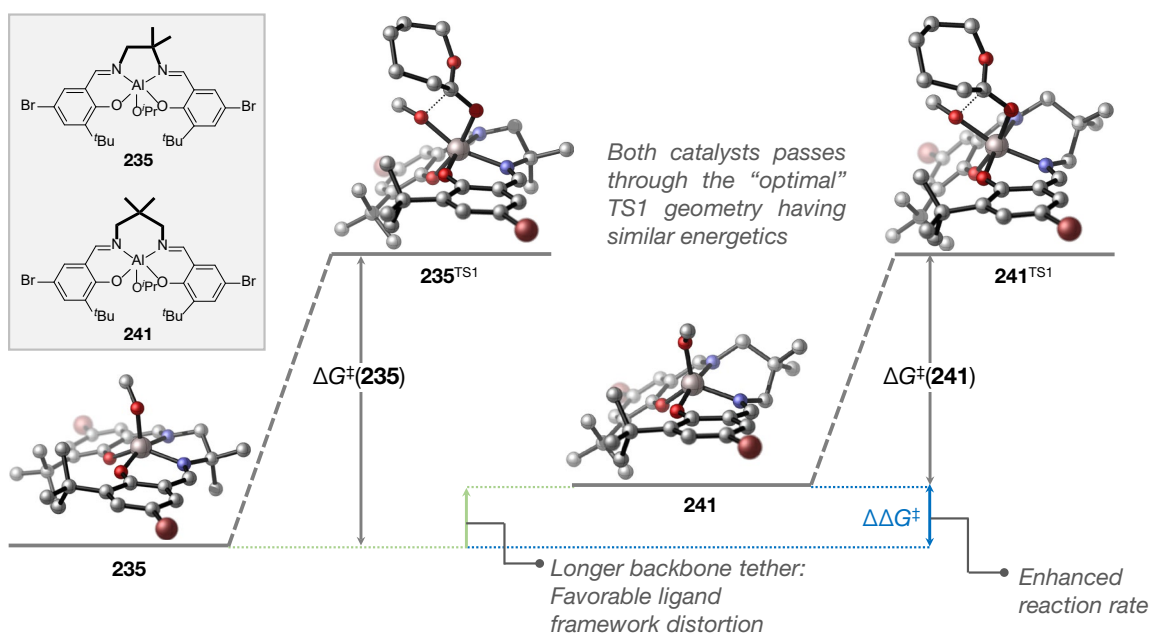


Figure 2.2 Demonstration for framework distortion energy: longer backbone tether allows favorable ligand framework distortion, which in turn decreases the activation barrier for the catalyst.

From the above analysis it can be surmised that the reactivity of a given $[M]$ -OR catalyst depends on how easily it can distort its resting precatalyst ligand framework and adopt the "optimal" TS1 geometry. This energy requirement, which quantitatively defines the framework distortion energy (FDE), was found to correlate closely with the overall activation free energy (ΔG^\ddagger) of the reaction; i.e., a catalyst with a lower FDE is associated with a lower ΔG^\ddagger value for the corresponding TS than the one with a higher FDE. For the specific case of CL polymerization with catalysts **235** and **241**, the ΔG^\ddagger (FDE) was computed to be 14.1 (15.5) and 10.3 (12.4) kcal/mol, respectively.⁵³ Given the resting precatalyst **241** is geometrically closer to its corresponding TS1 structure, as reflected in its lower FDE, it is expected to be associated with a lower ΔG^\ddagger value and consequently with a faster ROTEP rate.⁴⁹

In practice, FDE can be computed by taking the difference in the electronic energies of two frozen ligand frameworks: one derived by the removal of the alkoxy group of the optimized "resting" precatalyst and the other by removing both the alkoxy and CL from the optimized TS1 (Figure 2.3). We anticipate that this relatively simple approach for estimating the ligand FDE will have a broader utility for predicting the reactivity of metal alkoxide catalysts for cyclic ester ROTEP reactions. Rapid screening of hypothetical $[M]$ -OR catalysts may in principle be

accomplished by computing the energy for the latter structures by first imposing a frozen set of geometric parameters about the metal center for all putative TS structures and then simply relaxing the remaining geometric degrees of freedom, thereby obviating the need for specific TS structure *optimizations*, although the utility of this simplified approach will perform degrade as explored ligand sets increase in diversity.⁴⁷

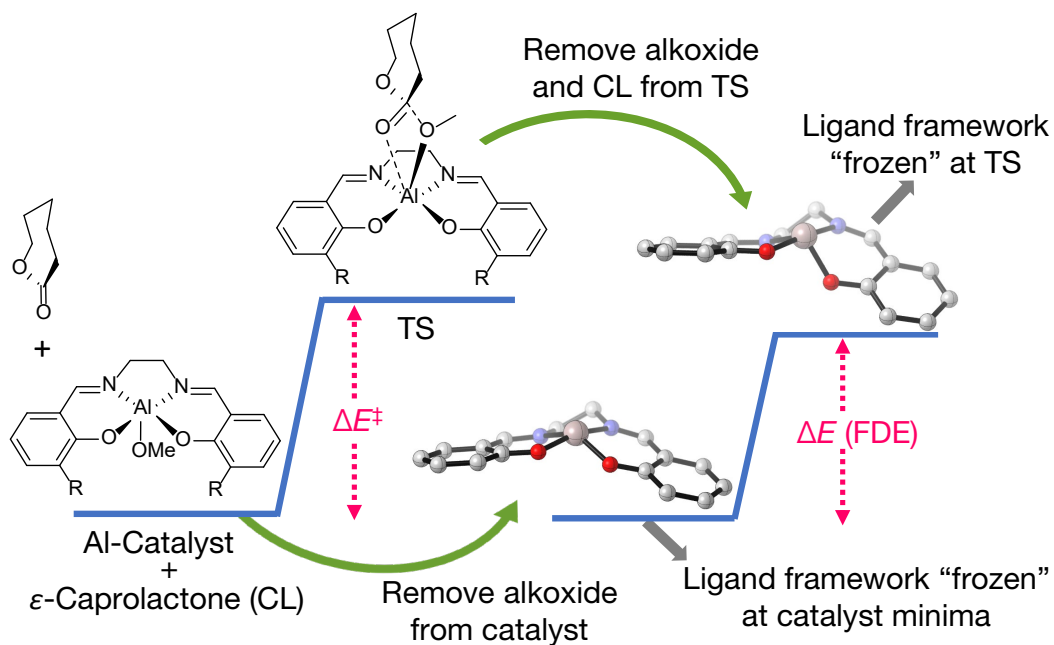


Figure 2.3 Schematic for calculating framework distortion energy.

2.2 Modeling Slow Polymerization of ϵ -Caprolactone Using Al(TMTAA) Catalyst

2.2.1 Introduction

Understanding the mechanism(s) of the ring-opening transesterification polymerization (ROTEP) of lactones by metal alkoxide complexes is a key prerequisite for the rational design of catalysts for the synthesis of sustainable polymers.⁵⁴ In recent studies, we were able to dissect the paradigm coordination–insertion mechanism into monomer binding equilibrium (K_{eq}) and insertion (k) steps through the observation of saturation kinetics in the ROTEP of ϵ -caprolactone (CL) by aluminum salen complexes (Scheme 2.5).^{49,50b,51,55} In one case, we hypothesized that the observed kinetics were affected by unproductive, inhibitory binding of monomer *trans* to the metal alkoxide moiety.⁴⁹ Inhibition was supported by theoretical calculations, which identified a *trans*-bound intermediate as a low-energy stationary point. Reasoning that if such *trans*-binding could be prevented, inhibition would be obviated and the ROTEP rate would be increased, we considered how ligand modifications might be implemented that would hinder unproductive monomer coordination. Simple strategies of increasing the steric bulk of salens generally affect interactions *cis* to the metal alkoxide bond and prevent catalyst dimerization but do not necessarily preclude unproductive binding, thus leading us to consider alternative ligand designs.⁵⁶

As one strategy, we hypothesized that a metal alkoxide complex supported by a tetradentate ancillary ligand whereby the *trans* position to the metal alkoxide bond is sterically inaccessible to the monomer yet would retain a five-coordinate geometry, allowing for the formation of octahedral rate-limiting transition-state geometry, would potentially result in high reactivity toward ROTEP. The nonplanar structure of tetramethyl-5,7,12,14-dibenzo-1,4,8,11-tetraaza[14]annulene (TMTAA) in aluminum complexes offered promise because of its demonstrated tendency to induce protrusion of the metal center ~ 0.54 Å above the ligand donor plane, thus disfavoring *trans* coordination of a sixth ligand.⁵⁷ Similar metal protrusions have been observed with porphyrins in metal– μ -oxo–metal⁵⁸ and metal alkyl⁵⁹ complexes. Additionally, controlled reactivity of aluminum alkoxide porphyrin complexes toward the polymerization of CL indicated the promise of high reactivity in the similar ligand environment provided by

TMTAA.⁶⁰ While aluminum chloride complexes of both TMTAA and porphyrins have been used to control steric bulk around the catalytic center for epoxide ring-opening polymerizations,⁶¹ we found no examples of the use of TMTAA–aluminum complexes for the catalytic ROTEP of cyclic esters. Herein, we report the synthesis and characterization of (TMTAA)AlOEt and its exploration as a catalyst for ROTEP of CL. Surprisingly, this five-coordinate aluminum alkoxide is a very sluggish catalyst, a “negative” result, but one from which we were able to learn valuable lessons through further analysis of the reaction mechanism and associated potential energy surface using density functional theory (DFT).

2.2.2 Results and Discussions

2.2.2.1 Experimental Results

Reaction of the known⁶¹ compound (TMTAA)AlCl with NaOEt at 70 °C in tetrahydrofuran yielded (TMTAA)AlOEt (**227**, 84%), which was characterized by ¹H and ¹³C NMR spectroscopy and X-ray crystallography. The monomeric, five-coordinate complex adopts a square-pyramidal geometry at the Al center ($\tau = 0.02$, where $\tau = 0$ is square pyramidal and $\tau = 1$ is trigonal bipyramidal)⁶² with the metal center displaced 0.51 Å above a plane created by the N atoms of the annulene ring (Figure 2.4). The displacement of the Al atom and the geometry of the puckered annulene ring closely resembles those of other aluminum complexes reported previously.^{57,60} Polymerizations of CL using complex **227** were performed in duplicate with fixed concentrations of CL ($0.8\text{ M} < [\text{CL}]_0 < 2\text{ M}$) and catalyst ($8\text{ mM} < [\mathbf{227}]_0 < 20\text{ mM}$) in toluene-*d*₈ at 110 °C. The concentration versus time data for the CL polymerization were fit to the first-order rate expression of $rate = k_{obs}[\text{CL}]$, where k_{obs} is the rate constant for polymer propagation. From this analysis, k_{obs} was determined to be $3.6(5) \times 10^{-4}\text{ min}^{-1}$, which corresponds to $t_{1/2} = 1920\text{ min}$.

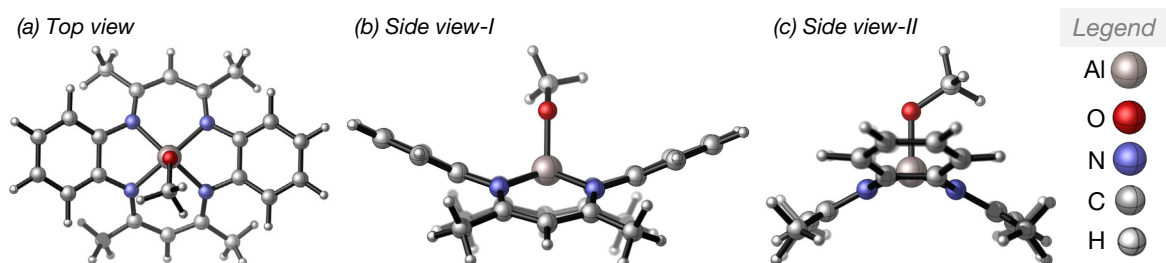


Figure 2.4 Puckered geometry of the (TMTAA)Al(OMe) complex.

In order to provide context to the rate of ROTEP of CL with **227**, it is helpful to analyze ROTEP rates for other reported aluminum alkoxide and alkyl complexes. The selected complexes shown in Figure 2.5 showcase the range of rates observed. While a comparison of the rates between complexes under different conditions can be problematic, an approximate comparison can be made through calculated $t_{1/2}$ values from reported experimental rate constants. Of this selection, **230**⁴⁹ ($t_{1/2}$ = 0.006 min) and **231**⁶³ ($t_{1/2}$ = 10 min) represent, on average, some of the faster rates reported for aluminum complexes, while **232**⁶³ ($t_{1/2}$ = 104 min) and **233**⁶⁴ ($t_{1/2}$ = 332 min) are some of the slower catalysts. Note that the range of $t_{1/2}$ values is over ~ 5 orders of magnitude just for this selection. Complex **227** polymerizes CL ~ 6 times slower than **233** (for **227**, $t_{1/2}$ = 1920 min). We are unaware of any reports of catalysts with rates as slow as **227**. With so many aluminum alkyl and alkoxide complexes polymerizing CL within shorter time frames, we sought to investigate through computation what causes **227** to be particularly inactive toward ROTEP of CL.

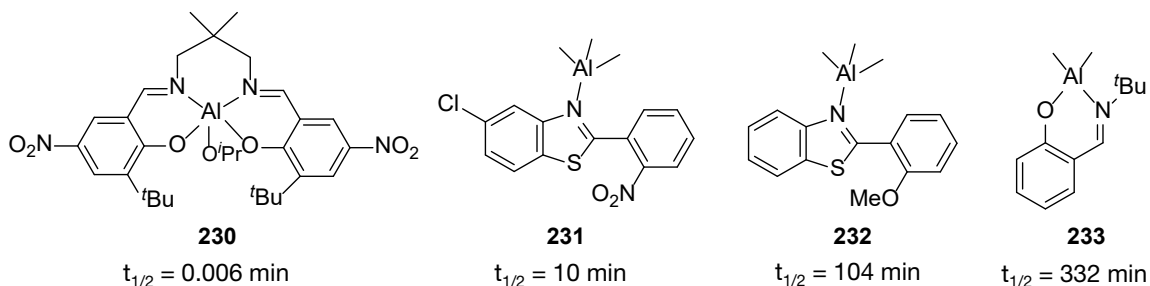


Figure 2.5 Selected aluminum complexes representing the range of rates reported for ROTEP of CL. © American Chemical Society

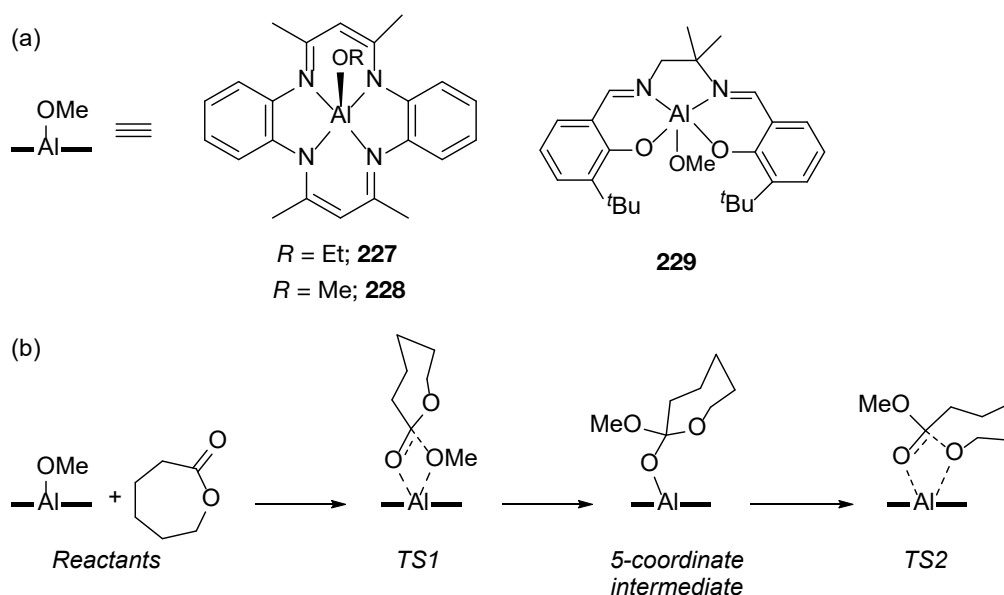
2.2.2.2 Computational Modeling

To gain insight into the inactivity of **227** in catalyzing CL homopolymerization, DFT was employed, and the energetics of key intermediates and transition-state (TS) structures involved during CL-to-PCL conversion were determined.⁶⁵ For computational efficiency, the original aluminum ethoxide complex (**227**, [Al]–OEt) was modeled as an aluminum methoxide (**228** [Al]–OMe; Scheme 2.6(a)). Owing to the geometry of the TMTAA ligand and the displacement of the Al atom above the donor ligand plane in **228** (Figure 2.4), we hypothesized that CL would not bind the Al center in a *trans* fashion. Indeed, we could not locate an energy minimum on the

potential energy surface involving CL bound *trans* to the [Al]–OMe bond (other than trivial van der Waals complexes having no atoms within the bonding distance of the “open” Al site). In this respect, our initial design goal was successful, and we expected **228** to show improved catalytic activity compared to, say, aluminum salen complexes like **229**,^{49,51} where inhibitive *trans* binding reduces the activity (Scheme 2.6(a)).

Further analysis of the potential energy surface, however, revealed that the 333 K free energy of activation (ΔG^\ddagger) associated with the TS structure for nucleophilic attack of methoxide at the carbonyl C atom of CL [turnover-limiting (TOL) step; TS1 in Scheme 2.6(b)] was quite high (30.5 kcal/mol; Figure 2.6; cf. 14.9 kcal/mol for **229**) consistent with the sluggish activity of **228**.

Scheme 2.6 (a) (TMTAA)Al-alkoxide complex and Al(Salen) Complex (b) Key stationary points along the CL ROTEP reaction coordinate



In addition to there being no stationary point(s) corresponding to binding of CL *trans* to the initiating alkoxide, neither could we find any initial six-coordinate precomplexes with CL bound to aluminum *cis* to the alkoxide, as has been seen in some other aluminum alkoxide complexes^{49,50b,51} (there is a simple van der Waals complex having a 333 K free energy 2.5 kcal/mol above the separated reactants, but because such a species is kinetically irrelevant, we do not consider it further). This suggests a concerted encounter/insertion mechanism followed by ring-opening for polymer initiation and propagation, as detailed in Scheme 2.6(b) and Figure 2.6.

To explain the high activation free energy associated with the TOL step, we assessed the “framework distortion energy”⁴⁹ associated with **228**, which measures the energy required to distort a “resting” precatalyst structure to its corresponding TS structure in the absence of reacting ligands. Thus, the framework distortion energy is computed as the difference in the electronic energies of the frozen cationic aluminum-ligand complexes derived from the removal of methoxy from optimized **228** and methoxy and CL from optimized TS1. The value computed for **228** is 22.6 kcal/mol, which may be compared to 18.3 kcal/mol for **229**.⁴⁹

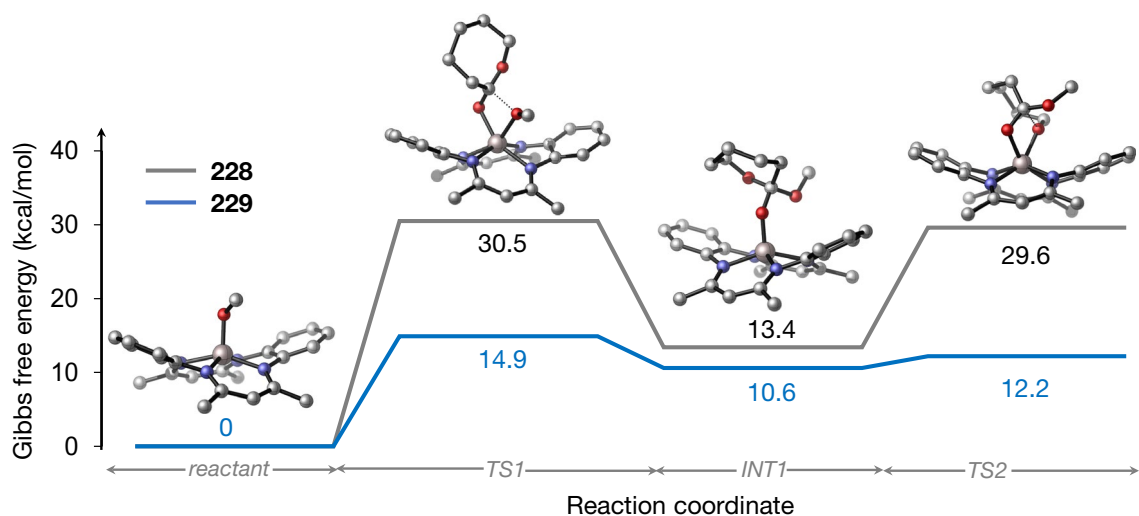


Figure 2.6 Comparison of the reaction coordinates for 333 K CL ROTEP catalyzed by **228** (grey line) and **229** (blue line).⁵¹ All values were computed at the SMD(toluene)//M06-2X/6-311+G(d,p)//M06-L/6-31+G(d,p) level.^{66,103,104,105}

While the difference in these two framework distortion energies is considerably smaller than the difference in the activation free energies, we assign the remainder of the very high free energy of activation for **228** to the failure of the TMTAA ligand distortion that *does* occur to adequately open a reactive site at the Al atom. Thus, in our prior analysis of the framework distortion energies,⁴⁹ we found that, for a series of eight aluminum salen complexes, all of the equivalent valence bond angles subtended at aluminum in the TOL TS structures were identical to within about 2°. Moreover, the X–Al–Y angles for all pairs of *cis* atoms X and Y derived from the salen ligands were between 85 and 95°; *i.e.*, the geometries in the TS structures were rendered very nearly octahedral when considering the addition of reacting methoxide and CL carbonyl O atoms.

By contrast, in TS1 for **228**, the ligand is unable to distort sufficiently to support such an octahedral geometry (one relevant N–Al–N angle is 125.7°), thereby exposing relatively little of the Al atom to the approaching CL and forcing the nucleophilic attack to proceed with limited activation of the carbonyl. Evidently, though, the energy penalty to *further* distort the TMTAA ligand exceeds the additional catalytic energy lowering that would be associated with a better exposed Al atom.⁶⁷

2.2.3 Conclusion

In summary, we learned a key lesson through the study of the slow catalyst **227**. Our work suggests that for future catalyst design, attention must be paid not only to eliminating inhibitory *trans* binding opportunities, but also to constructing ligand frameworks with sufficient flexibility that approximately octahedral TS structures can be accessed at low energetic cost.

2.3 Effects of Sterically Induced Ligand Framework Distortion on ROTEP of Cyclic Esters

2.3.1 Introduction

Ring-opening transesterification polymerization (ROTEP) of cyclic esters catalyzed by metal alkoxide complexes is an attractive route toward the sustainable production of biodegradable polymers.^{39,49,50b,51,68–70} With the ultimate aim of designing more efficient catalysts, a mechanistic understanding of these reactions has been sought through variation of the supporting ligand and metal ion.^{41,49,51,71} Particular focus has been placed on aluminum alkoxide complexes bound to salen or related imine phenoxide ligands largely because of their ready synthesis, their modest and thus conveniently monitored ROTEP rates, the ease with which steric and electronic influences can be studied through ligand structural variation, and the high degree of molecular weight control that they exhibit. For example, previous studies^{49,51} of single-site (salen)AlOR catalysts **234–236** (having 1,2-diamine tether; L^2) and **240–242** (having 1,3-diamine tether; L^3) (Figure 2.7), having different remote substituents ($X = \text{OMe}, \text{Br}, \text{NO}_2$), showed that the rates of ROTEP of ϵ -caprolactone (CL) were enhanced by electron-withdrawing groups (NO_2, Br over OMe) and longer tether length (L^3 over L^2).

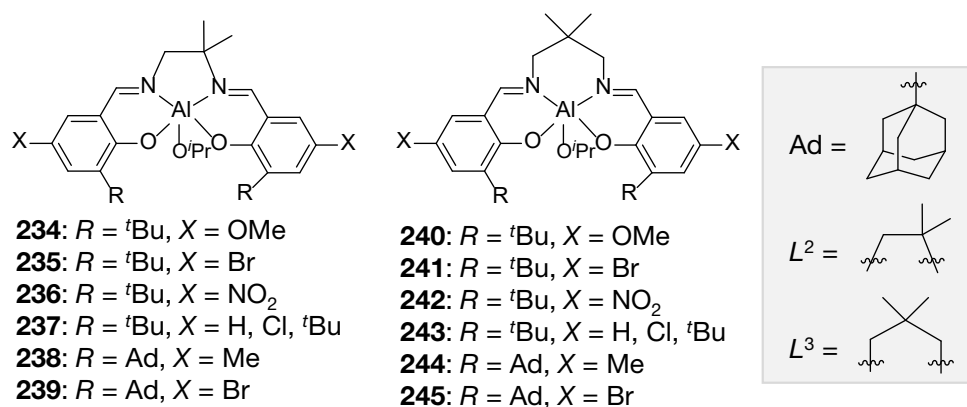


Figure 2.7 (salen)Al catalysts studied in polymerizations of cyclic esters. This work focuses on **239** and **245**.

Detailed computational analysis revealed that catalysts having longer backbone tethers (e.g., L^3 compared to L^2) adopt “resting state” geometries that are closer to trigonal-bipyramidal (tbp) and thus more readily able to distort to the rate-limiting octahedral transition-state (TS)

geometry at low energetic cost. A similar analysis focusing on the cost of distortion to the optimal octahedral TS structure rationalized the extremely low activity of a TMTAA-based aluminum catalyst for CL polymerization, which requires almost 10 days for >90% conversion.⁷² Here, the rigid, near-square-pyramidal (sp) TMTAA-ligand framework strongly resists such distortion.

These observations of such a structure–activity relationship led us to hypothesize that similar distortions of the precatalyst geometry and increased ROTEP rates might be imposed by enhancing the steric profile of the *o*-aryl substituents (*R*). Previous studies of ROTEP of *rac*-lactide (LA) by catalysts **237** and **243** revealed *slower* rates for *R* = *X* = ^tBu than for smaller H or Cl units, but substituents larger than ^tBu were not examined.³⁹ In other work, catalysts **238** and **244** having *o*-adamantyl (Ad) groups but different linker lengths exhibited essentially identical rates of ROTEP of LA, but comparisons to derivatives with ^tBu groups were not drawn, preventing comparative assessment of the steric effect of the Ad groups on ROTEP rates.^{41,71d} To address this issue and test the postulate that *ortho* substituents larger than ^tBu would enhance the rate of ROTEP of CL through favorable framework distortion, we targeted **239** and **245** for synthesis, ROTEP kinetics studies, and mechanistic evaluation via computation. As described in more detail below, comparisons to the ^tBu analogues **235** and **241** revealed a significant rate increase for the *L*² linker system that was indeed correlated with significant geometric distortion of the starting catalyst structure by the Ad groups, but a much smaller effect was seen for the already *tbp*-like system with the longer *L*³ linker. Our results and accompanying theoretical evaluation further illustrate the range of the framework distortion analysis model as a means to evaluate and design metal alkoxide complexes as ROTEP catalysts.

2.3.2 Results and Discussions

2.3.2.1 Experimental Results: Catalyst Synthesis and Characterization

The Ad-substituted salicylaldehydes used to make proligands to support catalysts **239** (*L*² linker) and **245** (*L*³ linker) were prepared analogously to previously reported procedures.^{49,51,73} Single crystals of both **239** and **245** formed during the metalation reactions, enabling their X-ray structures to be determined. The complexes are mononuclear with geometries intermediate

between the sp and ttp extremes, as reflected by τ_s values of 0.63 (**239**) and 0.81 (**245**) (where values of 0 and 1 are associated with the idealized sp and ttp geometries, respectively).⁶² These values are similar to those for the ^tBu-substituted variants **235** (0.52) and **241** (0.84),^{49,51} with the larger value for **239** compared to **235** suggesting enhanced twisting of the L^2 -salen backbone by the bulkier Ad groups in the former. These structural differences are further explored by density functional theory (DFT) calculations below.

2.3.2.2 Experimental Results: Polymerization Kinetics

The rates of polymerization of CL by catalysts **239** and **245** were determined by monitoring ¹H NMR spectroscopy of the reaction mixture. Global fits to first-order, second-order, and saturation (Michaelis–Menten⁵²) rate equations were attempted. Poor fits to first- and second-order rate laws contrasted with excellent fits to saturation kinetics, which provided K_{eq} and k_2 values (see section 2.1.8 for a discussion on rate law for ROTEP kinetics). It is evident that the polymerization rates for **239** and **245** are faster than those for **235** and **241** (Figure 2.8). Notably, the differences in the k_2 values for catalysts with the same linker lengths are significantly larger for **235** versus **239** (L^2 linker; >5 orders of magnitude difference) than for **241** versus **245** (L^3 linker; ~2 orders of magnitude difference). In other words, the effect of replacing the ^tBu group by an Ad group is larger for the L^2 -salen systems (**235** and **239**) than for the L^3 -salen complexes (**241** and **245**). In order to understand these differences and their structural bases, we turned to DFT calculations.

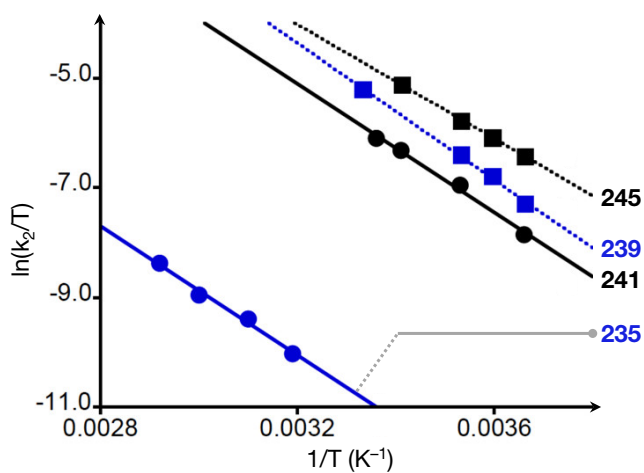


Figure 2.8 Eyring plots of $\ln(k_2/T)$ versus $1/T$ for **235** (blue circles), **241** (black circles), **239** (blue squares), and **245** (black squares). Data for **235** and **241** are from refs 51 and 49, respectively, and those for **239** and **245** are from this work. © American Chemical Society

2.3.2.3 Computational Studies

To gain further insight into the experimentally observed trend in the polymerization rates, DFT modeling of the key stationary points on the relevant potential energy surfaces was undertaken. For computational efficiency, the isopropoxy group of the precatalyst was truncated to a methoxy group, [Al]–OMe.

The Ad group is similar to the ^tBu group in terms of having a quaternary carbon attached to the aryl ring, but the remaining alkyl fragment is a polycyclic cage in the Ad case, as opposed to three methyl groups in the ^tBu case. To assess this change in the steric profile, we computed the fractional buried volume ($\%V_{\text{Bur}}$) for each catalyst, a descriptor that quantitatively characterizes the steric environment associated with the catalytic pocket.⁷⁴ To compute $\%V_{\text{Bur}}$, a sphere having a particular van der Waals radius is centered on the active site of the catalyst—in this case, the aluminum atom. The percentage volume of the sphere that overlaps with the volume of other van der Waals spheres placed on ligand atoms, each having their own characteristic radius, is $\%V_{\text{Bur}}$.⁷⁵ For complexes **235**, **241**, **239**, and **245**, the $\%V_{\text{Bur}}$ values for a 5 Å metal radius are computed to be very similar: 54.1, 55.0, 55.0, and 56.7%, respectively, confirming that the *ortho* substituent does not explicitly block the approach to the active site (see section 2.3.4.2 for details with other radii).

Table 2.2 Geometric index τ_5 , activation parameters, framework distortion energies (FDE), and activation free energies (ΔG^\ddagger) through TS1 for catalysts **235**, **241**, **239**, and **245**.^a

catalyst	τ_5 exp.	τ_5 theo.	ΔH^\ddagger ^b	ΔS^\ddagger ^b	ΔG^\ddagger_{298} ^b	$\Delta G^\ddagger_{(\text{TS1})}$ ^c	FDE ^c
235 ^d	0.52	0.35	11.5(3)	30(2)	20.4(7)	14.1	15.5
239	0.63	0.67	12.4(5)	16(1)	17.2(5)	11.2	10.0
241 ^e	0.84	0.77	10.4(4)	24(1)	17.6(5)	10.3	12.4
245	0.81	0.79	10.3(2)	22(1)	16.9(3)	10.2	11.0

^aSMD(toluene)//M06-2X/6-311+G(d,p)//M06-L/6-31+G(d,p). Energies in kcal mol⁻¹; entropy in cal K⁻¹ mol⁻¹.

^bDetermined from the linear fits in Figure 2.8 using the Eyring equation. ^cDetermined from computation. ^dRef. 51.

^eRef. 49.

Although there is not much change in the accessible volume across the various precatalysts, the close proximity of the *ortho*-substituting groups to one another, particularly in the L^2 -salen system, is such that the ligand framework distorts and deviates more from planarity in the Ad case than *t*Bu. This can be quantified by the geometry index, τ_5 , which is calculated to be 0.35 for **235** but 0.67 for **239**.^{51,76} The L^3 -salen system, with its longer linker, is significantly distorted toward a *tbp* geometry with *either* substituent, as measured by theoretical τ_5 values of 0.77 and 0.79 for **241** and **245**, respectively (Table 2.2). Because the turnover-limiting transition-state structure (TS1) (Scheme 2.4 and Figure 2.9) involves an octahedral coordination geometry, the energetic cost required to distort the more *tbp* **239** to an octahedral geometry quantified by the “framework distortion energy” (FDE; see section 2.1.9 for details) is reduced compared to that of **235**.^{77,78}

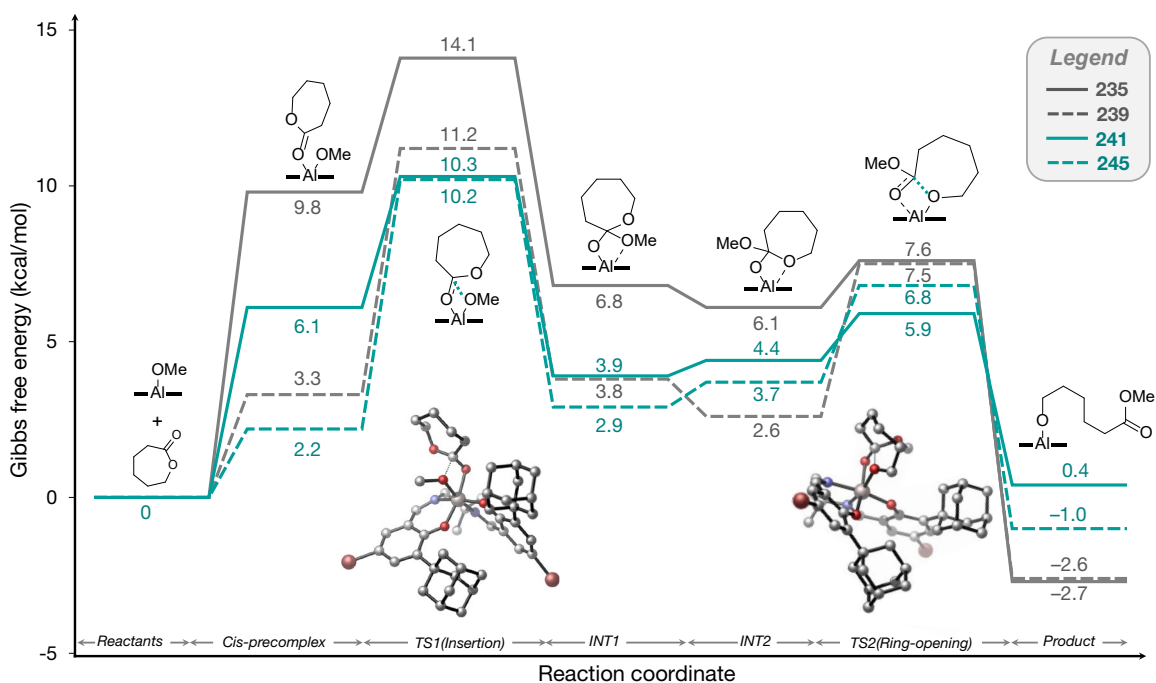


Figure 2.9 Standard-state free energies (kcal/mol) at the SMD(toluene)//M06-2X/6-311+G(d,p)//M06-L/6-31+G(d,p) level of theory for CL ring-opening relative to the infinitely separated precatalyst and monomer with line drawings of relevant stationary points, and 3D-diagram of the TS structures. Solid lines refer to *t*Bu substituted catalysts (**235** and **241**), while dotted lines refer to the corresponding Ad-substituted catalysts (**239** and **245**).

Consistent with the large geometric distortion associated with the Ad group, **239** compared to **235** has a FDE lower by 5.5 kcal/mol and a correspondingly lower free energy of activation associated with TS1 [$\Delta G^\ddagger(\text{TS1})$; lower by 2.9 kcal/mol; Table 2.2]. These results are entirely

consistent with the experimental rate acceleration observed for **239** compared to **235**. For the L^3 -salen system, by contrast, the FDE and associated $\Delta G^\ddagger(\text{TS1})$ values vary by substantially smaller values (Table 2.2), with the latter suggesting that no significant difference in the rates should be expected for **245** compared to **241**, again in close agreement with the experimental results.

2.3.3 Conclusion

Through the synthesis, structural characterization, and study of the kinetics of CL polymerization of complexes **239** and **245**, comparisons to previously reported complexes **235** and **241** were enabled that focused on the effect of changing the size and shape of the *ortho* substituents on the supporting ligand. The new Ad-substituted systems exhibited saturation kinetics, with differences in the overall rate being primarily due to disparities in the values of the rate constants k_2 , the temperature dependencies of which were analyzed by the Eyring equation. Importantly, the Ad-substituted systems **239** and **245** exhibited faster CL polymerization rates than the corresponding ones with *o*-^tBu groups (**235** and **241**), with larger effects for the complexes having the less flexible and shorter ligand backbone linker. A detailed computational study revealed that increased steric repulsion between *ortho* groups in the aryloxide ligand for models of **239** and **245** results in a significant difference in the reactant geometries, such that the FDEs to reach the TS geometry are reduced. This prediction of an enhancement in the polymerization rate with a structural change from ^tBu to Ad *ortho* substitution is consistent with the detailed kinetic analyses. While the sensitivity to substitution is large for the related catalysts **235** and **239**, which have significantly different computed FDE and $\Delta G^\ddagger(\text{TS1})$ values, it is less pronounced for catalysts **241** and **245**, which both have relaxed catalyst geometries already well characterized as *tbp*-like, leading to more *similar* FDE and $\Delta G^\ddagger(\text{TS1})$ values. Using theory to assess the hypothetical catalyst geometries and FDEs should prove useful in ongoing design efforts with respect to maximizing activity.

2.3.4 Appendix

2.3.4.1 Computational Details

All calculations were performed using the Gaussian 09 program package.¹⁰³ Molecular geometries were optimized using the M06-L¹⁰⁴ density functional with the Pople basis set 6-31+G(d,p).^{66a}

Vibrational frequency calculations were performed at the same level of theory to confirm the nature of each stationary point, and to compute relevant partition functions for the prediction of thermochemical quantities at 298.15 K. Low frequency vibrational modes below 50 cm^{-1} were replaced with a value of 50 cm^{-1} in partition-function calculations. Single-point electronic energies were then calculated using the M06-2X^{104b} functional ($E_{\text{M06-2X}}$) with the 6-311+G(d,p)^{66b} basis set. Best-estimate of free energies G were then obtained by summing M06-L/6-31+G(d,p) thermal contributions with M06-2X electronic energies, $E_{\text{M06-2X}}$. All calculations were performed including the effects of SMD¹⁰⁵ continuum solvation model using solvent parameters for toluene ($\epsilon=2.3741$). Coulomb integrals were evaluated using an automatically generated density fitting basis set to speed calculations. Two-electron integral integrations employed an ultrafine grid in all cases. An increased integral accuracy was used by setting the cut-off at 10^{-11} . Buried volume ($\%V_{\text{Bur}}$) was computed using the SambVca 2.0 tool.⁷⁵ Atomic radii were selected to be Bondi radii scaled by 1.17.⁷⁹ All coordination spheres were centered at the metal atom. A mesh spacing of 0.10 was chosen for numerical integration, while hydrogen atoms were not considered for the calculation.

2.3.4.2 Buried Volume and Steric Map

For computing buried volume ($\%V_{\text{Bur}}$), a sphere centered on the metal atom of a catalyst is considered, the volume of which corresponds to the space about the metal center that may be occluded by different ligand atoms prior to coordination of substrates. For typical metal complexes, the metal-ligand bond distances generally fall within 2.0–2.5 Å. Thus, in order to account for the space that roughly encompasses the van der Waals volume of donor atoms coordinated to the metal center, a first coordination sphere of radius 3.5 Å may be sufficient to describe reactivity and has proven to be useful for rationalizing a large number of experimental data.⁷⁵ In our calculation, however, we considered a first coordination sphere of 5 Å around the metal atom so as to include the *ortho*-aryloxy substituents (although results with a radius of 3.5 Å show an identical (lack of any) trend). Results are also shown with a coordination sphere of radius 7.5 Å, to amplify the difference in the *t*-butyl and the adamantyl group.

Table 2.3 Buried volumes ($\%V_{Bur}$) computed for the catalysts using different radius of the coordination sphere.

r (Å)	$\%V_{Bur}$			
	235	239	241	245
3.5	66.4	66.0	67.7	67.8
5.0	54.1	55.0	55.0	56.7
7.5	26.8	31.9	27.8	33.0

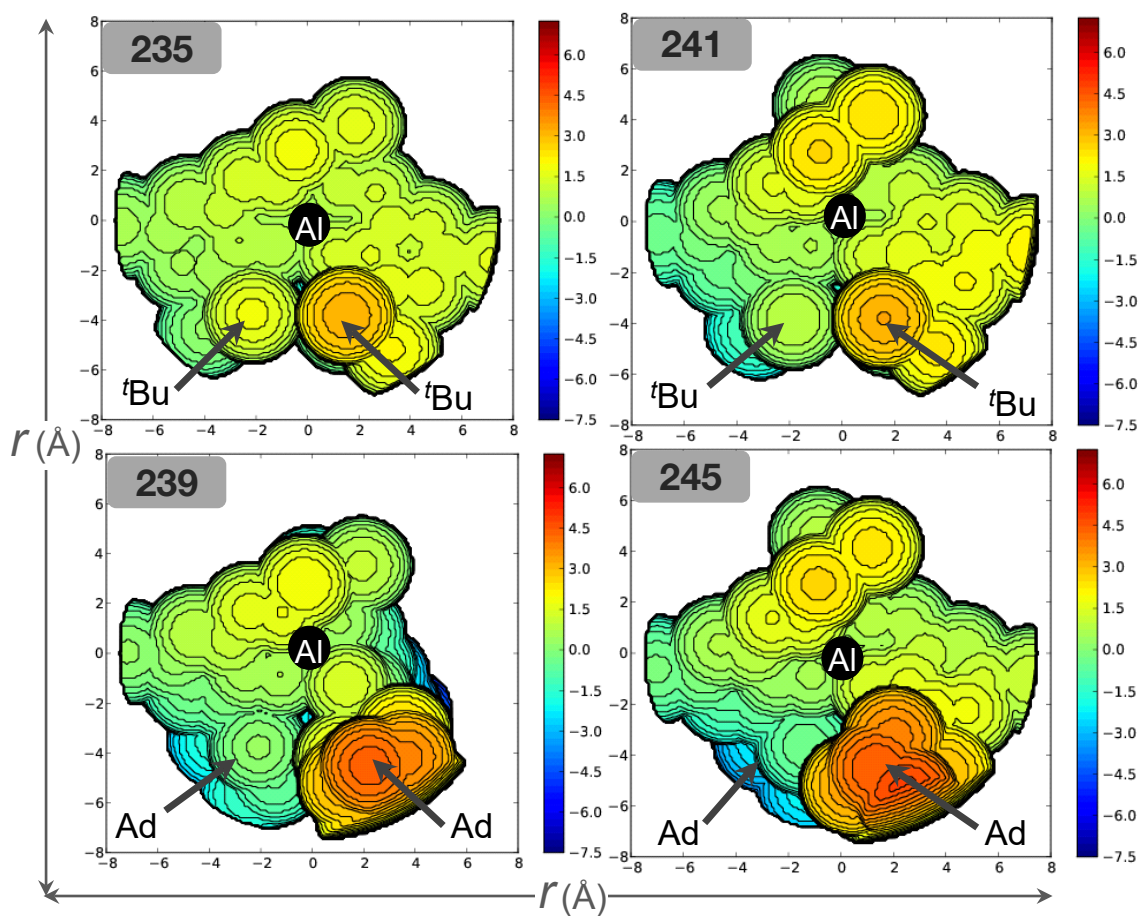


Figure 2.10 Steric maps for the four catalysts explored, using a coordination sphere of radius 7.5 Å. The map shows that both the *ortho*-substituents are quite far from the catalytic pocket.

2.4 Fast Ligand Screening Using FDE Model and Identification of an Aluminum Indolide/Schiff-Base Complex for ϵ -Caprolactone Polymerization

2.4.1 Introduction

Conversion of biomass-derived cyclic esters to aliphatic polyesters offers an attractive approach for sustainable polymer production.⁸⁰ A key synthetic approach is ring-opening transesterification polymerization (ROTEP) catalyzed by metal alkoxide complexes.⁸¹ Among the plethora of such complexes that have been studied for such purposes, salen-based aluminum complexes are especially popular because of their high Lewis acidity, low toxicity, and high tunability, allowing systematic exploration of steric/electronic factors on ROTEP rates, molecular weight control, and selectivities.^{37,82}

Over the past decade, experiment and theory combined have made significant progress with respect to elucidating the details of ROTEP mechanisms.^{48,49,51} The “coordination-insertion” pathway (Scheme 2.4) described in section 2.1.7.2 is now well-established as the preferred propagation route. Better understanding of the working mechanism of ROTEP reaction has allowed clear identification of factors that are crucial for reactivity. Ligand structure and coordination environment are two such key factors that determine the reactivity of a given ROTEP catalyst. For example, an 11-fold rate increase during *rac*-lactide (LA) polymerization was observed using a longer backbone tether for an Al-salen catalyst, and this finding was expanded upon in later work with ϵ -caprolactone (CL).^{39,49} Conversely, increased rigidity in the catalyst backbone—engineered using aryl-fused tethers rather than alkyl tethers—resulted in decreased rates of LA polymerization.⁴¹ In other recent work, an Al(TMTAA) complex of was found to be an especially sluggish catalyst for CL polymerization, which was attributed to the high rigidity of the TMTAA ligand that made it energetically costly to reach the octahedral transition-state (TS) structure associated with the TOL step (see section 2.2 for details).⁷² Given the significant influence that the ligand framework can have on polymerization rate, the development of efficient computational approaches to screen alternative ligands for activity has the potential to speed experimental testing through the prioritization of synthetic targets.

The Framework Distortion Energy (FDE; see section 2.1.9 for details) hypothesis^{49,53,78,83,84} can be a useful tool for just such screenings. The FDE descriptor rationalizes structure-activity variations for series of catalysts where the geometries of the TOL TS structures are all similar, at least with respect to coordination about the active site. In this work, we report a systematic investigation of ligands screened using the FDE model with the goal of identifying catalysts predicted to have comparable or higher ROTEP rates than previously achieved for the polymerization of CL. In addition to FDE, we analyze structural variations in precatalysts as reflected by the geometry index τ_5 (for a pentacoordinate atom, values of τ_5 range from 0 to 1 as the local coordination environment varies from square pyramidal (sp) to trigonal bipyramidal (tbp)),⁶² and also electronic structure variations associated with different coordinating heteroatoms in the ligand framework. As a result of the screening, the synthesis of one catalyst predicted to have promise was undertaken, and its catalytic activity for CL polymerization was evaluated.

2.4.2 Results and Discussions

2.4.2.1 Summary of Computational Screening

The ROTEP of CL is notably rapid for complex **246** (Figure 2.11) relative to other Al catalysts.^{53,83} The mechanistic details associated with catalysis by **246** have been explored using density functional theory, with $\Delta G^\ddagger(\text{TS1})$ and FDE computed to be 7.8 and 12.7 kcal/mol, respectively, at the SMD(CH₂Cl₂)/M06-2X-D3/6-311+G(d,p)//M06-L/6-31+G(d,p) level of theory (see section 2.4.4 for full computational details).⁸³ We therefore set as our goal, with respect to *in silico* screening of alternative catalysts, to identify ligands predicted to lead to still lower values of $\Delta G^\ddagger(\text{TS1})$ and/or FDE than those computed for **246**.

Our first design efforts focused on modification of the parent system **246** through the introduction of additional tethers, of varying length, bridging other atoms of the salen moiety (identified as P_n , Q_n and R_n in Figure 2.11, where n refers to the number of methylene units in the tether). Our goal was to constrain the pre-catalyst to a geometry more closely resembling the corresponding TS1 structure, thereby reducing FDE. However, extensive surveys of frameworks

247–249 for varying values of n failed to identify any with FDE or $\Delta G^\ddagger(\text{TS1})$ values less than those for **246**. See Appendix, section 2.4.4.4 for a summary of the results encompassing these systems.

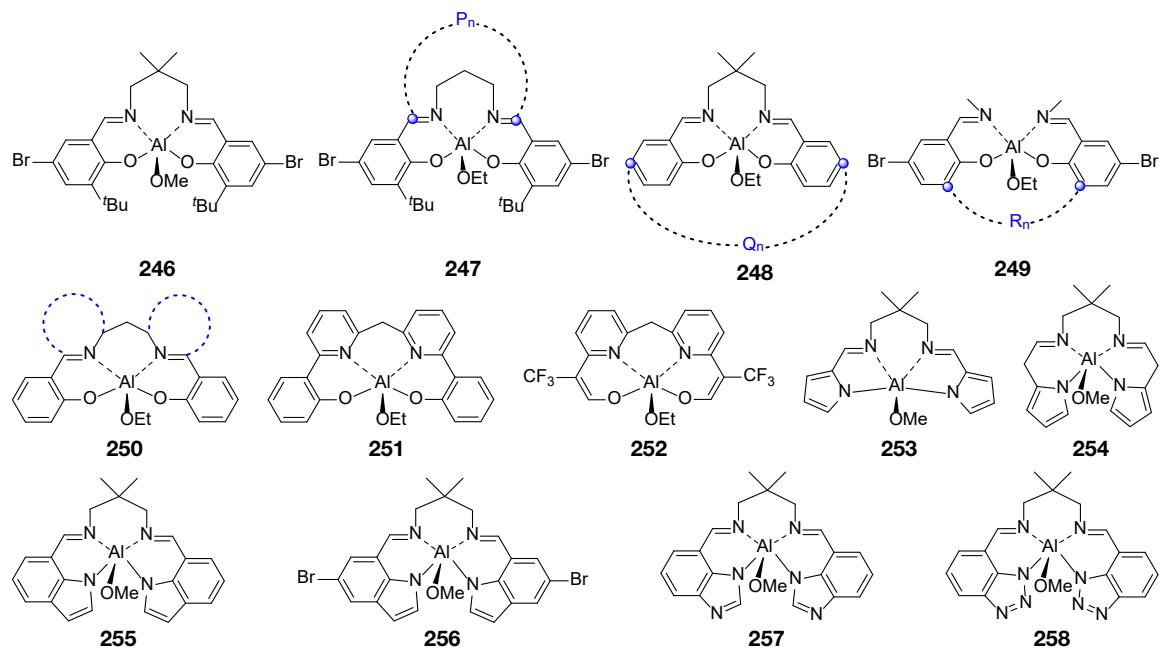


Figure 2.11 (a) Parent salen catalyst and modifications with additional alkyl tethers. (b) Pyridine-based systems as a sidearm modification to salen. (c) Pyrrole/indole-based $\{N,N,N,N\}$ -complexes. © American Chemical Society

As favorable constraints on the pre-catalyst geometries were not achieved with additional tethers, we turned next to explore incorporation of the imine functionality of the salen ligand into pyridine moieties (**251** and **252**, Figure 2.11). In this instance, the goal was to tune both the steric and electronic aspects of the catalyst, with the hypothesis being that the pyridines would modulate the Lewis acidity of the metal center through their π -donor character while simultaneously reducing steric demand associated with the overall tether. Interestingly, both **251** and **252** are predicted to be potentially active for CL homopolymerization with $\Delta G^\ddagger(\text{TS1}) \sim 6.5$ kcal/mol and FDE ~ 10.5 kcal/mol, which values are indeed below those computed for **246**. However, we concluded that the ligands themselves and their assembly about the catalytic center were likely to pose significant synthetic challenges, and on that basis, we decided instead to explore further modifications in the ligand framework, and in particular to evaluate the replacement of O donors with N alternatives (**253–258**, Figure 2.11). Complex **254** with its bis(pyrrolide) Schiff-base

ligand was reported previously.⁸⁵ In contrast to the half-salen systems reported by Lee et al.,⁸⁶ where a five-membered-ring chelate of the ligand at Al leads to faster catalysis during CL polymerization than a six-membered one, we predict **254** to be significantly faster than **253** for the same reaction (Table 2.4). The larger ligand arm of **254** permits it to adopt the octahedral geometry of the TOL TS1 more readily, as reflected by its FDE of 8.5 kcal/mol compared to 12.2 kcal/mol for **253**.

Table 2.4 Computed geometry indices (τ_5), activation free energies (ΔG^\ddagger ; kcal/mol), framework distortion energies (FDE, kcal/mol), and key bond lengths (\AA) for N_4 -donor systems.^a

Catalyst	τ_5	ΔG^\ddagger (TS1)	FDE	r_1 (Al-OMe)	r_2 (Al-O=C)
246	0.71	7.8	12.7	1.765	1.926
253	0.42	10.6	12.2	1.756	1.908
254	0.75	5.5	8.5	1.762	1.912
255	0.80	7.6	11.6	1.772	1.937
256	0.79	6.8	11.1	1.771	1.929
257	0.80	6.2	11.9	1.764	1.917
258	0.84	4.7	12.6	1.755	1.908

^a Calculations performed at the SMD(CH₂Cl₂)/M06-2X-D3/6-311+G(d,p)//M06-L/6-31+G(d,p) level of theory.

We also explored changing the pyrrolide functionality to indolide (**255**), *para*-bromindolide (**256**), benzimidazolide (**257**), and benzotriazolide (**258**). Table 2.4 further compares key energetic and structural parameters for catalysts **246** and **253–258**. We observe that the $\Delta G^\ddagger(\text{TS1})$ values for **254–258** are all low, implying rapid ROTEP rates, and a comparison of structures and energetics for **246** vs. **255** (Figure 2.12) suggests the ligand system of the latter to have significant potential. In addition, when the indolide ligands in **255** are modified to make them less electron donating, either by introducing bromo-substituents (**256**) or by introducing additional *N*-atoms in the five-membered ring (**257** and **258**), the catalyst is predicted to be more Lewis acidic, as judged by a shortening of both r_1 , the metal–alkoxide bond distance in the catalyst and r_2 , the metal–carbonyl bond distance in TS1, and there are corresponding improvements in

predicted catalytic activity as judged by decreasing values of $\Delta G^\ddagger(\text{TS1})$. Interestingly, there is considerably less variation in the predicted FDE, which is consistent with the relatively limited variation in τ_5 predicted for the pre-catalyst structures. Put differently, with τ_5 values already so close to 1.0, additional acceleration must be achieved by tuning of the overall electronic structure toward enhanced Lewis acidity.

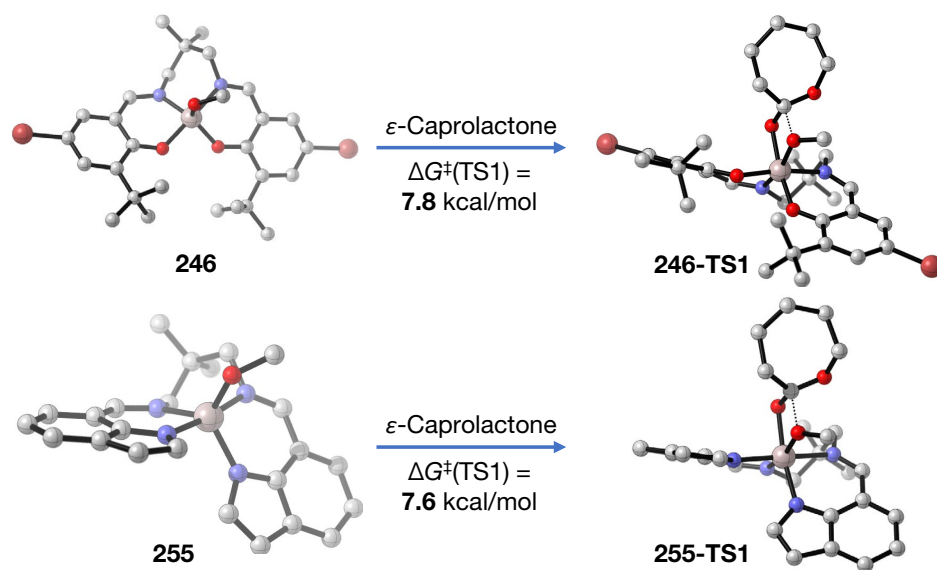


Figure 2.12 Optimized structures for **246** and **255** and their corresponding turnover-limiting TS structures for CL polymerization. © American Chemical Society

2.4.2.2 Experimental Results

Given the computational prediction of good activity for **255** coupled with its perceived synthetic accessibility, the benzyloxy analog of the catalyst (**255'**) was synthesized. The X-ray structure of **255'** revealed a mononuclear, 5-coordinate complex with a distorted tbp geometry (τ_5 value of 0.87). The overall geometry is similar to that calculated for methoxy analogue **255** (τ_5 value of 0.80).

The kinetics for the polymerization of CL were measured by mixing pre-catalyst **255'**, internal standard (bis-*para*-trimethylsilylbenzene) and monomer (targeting concentrations of 0.007 M, 0.004 M and 2.0 M, respectively, in CD_2Cl_2) and monitoring the loss of monomer and gain in polymer via ^1H NMR spectroscopy at 300 K. The relative merits of both 1st order and saturation (Michaelis-Menten) kinetic fits were unclear. In an independent test of the importance of

monomer coordination (implicit in the saturation fits), we examined the ^1H NMR spectra of solutions of **255'** in the presence of variable concentrations (0.005-1.5 M) of γ -butyrolactone (BL, not easily ring-opened due to lack of ring strain).⁸⁷ Only slight changes in the chemical shifts of the peaks associated with **255'** were observed, and these were consistent with the solvent polarity changes due to the added BL, i.e., we saw no evidence for binding of BL to the complex. We thus conclude that if CL binding occurs, it must be quite weak, and that the simpler pseudo-1st order fits of the kinetic data are preferable for obtaining useful rate constants. The fits yielded an averaged first-order rate constant (k_{obs}) of $4.1 \times 10^{-4} \text{ s}^{-1}$. While theoretical computation would suggest that **255'** (by analogy to **255**) should be about as reactive as **246** for ROTEP of CL, experimentally we observed it to be 5.5-fold slower (times to reach 95% conversion are 20 min for **246** and 110 min for **255'**, under equivalent conditions of $[\text{CL}]_0 = 2 \text{ M}$, $[\text{cat}]_0 = 7 \text{ mM}$, 300K). Such a discrepancy—roughly 1 kcal/mol at 298 K—is, however, well within the error one might expect for a DFT-based model, and suggests that framework distortion energy can indeed be a practical descriptor for estimating the ROTEP activity of hypothetical future catalysts, at least with respect to prioritizing (i) more complete computational characterization of reaction paths (e.g., **258**, where a relatively low FDE is associated with a $\Delta G^\ddagger(\text{TS1})$ value that is 3.1 kcal/mol lower than that for **246**) and (ii) promising targets for synthetic realization.

2.4.3 Conclusions

In summary, we have explored new aluminum based ROTEP catalysts *in silico* by means of DFT calculations and verified the proposed FDE model by synthesizing and evaluating one such hypothetical catalyst, predicted to offer high ROTEP activity, experimentally. While additional tethers on the salen moiety in the form of P_n , Q_n and R_n series of catalysts did not prove useful in lowering either the calculated FDE, or the ΔG^\ddagger of the TOL TS1, ligand sidearm modification with pyridine donors showed promise by modulating both the overall steric and electronic features of the catalyst. An alternative modification, involving the replacement of all O-donors with N-counterparts, provided a new class of ROTEP pre-catalysts having highly distorted tbp geometries—a feature that generally promotes ROTEP catalysis. Indeed, the synthesized variant **255'** polymerized CL rapidly, consistent with theoretical predictions. In line with prior CL-

ROTEP studies,^{39,50a,51} electron withdrawing groups on the five-membered ring of the supporting ligand of **255** show promise for even faster catalysts in the form of **256–258**. Agreement within one order of magnitude was observed when theory, using predicted $\Delta G^\ddagger(\text{TS1})$ values, was compared to experiment for the specific case of the ROTEP rates of **246** vs. **255**. Using the FDE model to screen hypothetical catalysts prior to subsequent more complete computational evaluation—and ultimate experimental realization—continues to hold promise for future catalyst design in suitably related systems.

2.4.4 Appendix

2.4.4.1 Computational Details

All calculations are performed at the density functional theory level as implemented in the Gaussian 09 electronic structure program suite.¹⁰³ Geometry optimizations are carried out at the M06-L^{104a} level of theory using the double zeta 6-31+G(d,p)^{66a} basis set for all atoms, except for *bromo*-substituted structures where the SDD⁸⁸ pseudopotential and its associated basis set has been used. Coulomb integrals are evaluated using an automatically generated density fitting basis set to speed up the relevant calculations. The grid used for numerical integration in DFT was set to “ultrafine”. The natures of all stationary points are verified by calculation of quasi-harmonic vibrational frequencies. All vibrational frequencies below 50 cm⁻¹ are replaced with values of 50 cm⁻¹. Zero-point vibrational energies and thermal contributions to electronic energy are determined from the computed partition functions at 298.15 K. For better estimate to Gibbs free energies, single point electronic energies are computed using the M06-2X^{104b} functional with the 6-311+G(d,p)^{66b} basis set at the M06-L optimized geometries and the resulting electronic energies are summed with thermal free energy contributions computed at the M06-L/6-31+G(d,p) level. For complex **246** and {N,N,N,N}-complexes **253–258**, Grimme’s D3 dispersion correction term^{19b} has been used for electronic energy calculation at the M06-2X-D3/6-311+G(d,p) level. All reported structures are optimized using the self-consistent reaction field (SCRF) approach with SMD¹⁰⁵ continuum solvation model with the solvent parameters for toluene or dichloromethane (DCM) depending on the reaction ($\epsilon(\text{toluene}) = 2.374$, and $\epsilon(\text{DCM})=8.93$), unless otherwise stated.

2.4.4.2 Sensitivity of Density Functionals in Reactivity of **246** vs. **255**

To test dependence of ΔG^\ddagger values on the choice of density functionals, we added thermal free energy contributions computed at the M06-L/6-31+G(d,p)/SMD(CH₂Cl₂) level of theory to electronic energies computed using the M06-2X-D3, PBE0-D3(BJ)^{19d,89} and ω B97X-D⁹⁰ functionals to predict absolute Gibbs free energies, employing the 6-311+G(d,p) basis set (SDD pseudopotential⁸⁸ and its associated basis was used for the Br-atom in **246**). The results are summarized in Table 2.5. Briefly, while the absolute ΔG^\ddagger values change for the different DFT functionals, the overall trend is similar, *i.e.*, we predict **255** to be similar or just slightly faster than **246** in terms of reactivity for ROTEP of CL.

Table 2.5 Comparison of activation free energies (kcal/mol) required for the turnover-limiting (TOL) TS1 during ROTEP of ϵ -caprolactone (CL) using catalysts **246** and **255** using different density functionals.^a

catalyst	Single-point electronic energy method ^b		
	M06-2X-D3	PBE0-D3(BJ)	ω B97X-D
246	7.8	11.0	12.3
255	7.6	9.9	11.5

^a Geometry optimization and frequency calculation is done at M06-L/6-31+G(d,p)/SMD(CH₂Cl₂). ^b Method/6-311+G(d,p) basis set including SMD(CH₂Cl₂) solvation

2.4.4.3 Variation of ΔG^\ddagger (TS1) as a Function of CL Orientation

Four distinct orientations of CL are possible in the TOL TS1 structure originating from a given catalyst: two separate orientations with respect to the ligand donor atoms that are *trans* to coordinated CL, and in each of these two cases, the CL ester oxygen can be found in two possible locations, leading to a total of four possible coordination environments in TS1. These conformers are identified in Figure 2.13 as I, II, III, and IV. All four orientations along the relevant potential energy surface (PES) are explored in accordance with Scheme 2.4. The detailed orientation effect of CL on the free energy of activation through TS1 for catalysts **246** and **255** is shown in Figure 2.13 and the results are summarized in Table 2.6. The table shows that the orientation III is the most favored pathway.

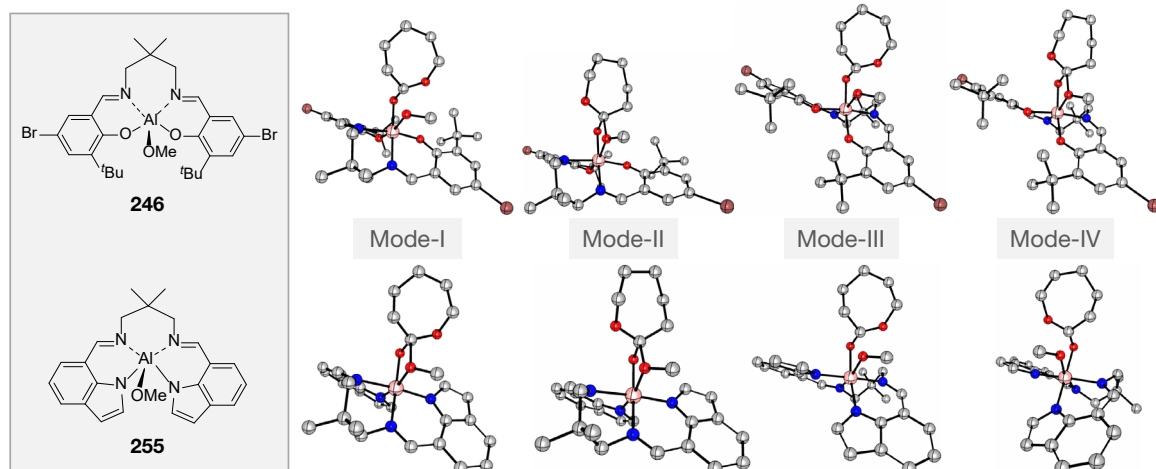


Figure 2.13 Effect of CL orientation on TS1 for catalyst **246** and **255**.

Table 2.6 Gibbs free energies in kcal/mol computed at SMD(CH₂Cl₂)/M06-2X-D3/6-311+G(d,p) |SDD(Br)//M06-L/6-31+G(d,p)|SDD(Br) level of theory.

CL-Orientation	$\Delta G^\ddagger(\text{TS1})$	
	catalyst 246	catalyst 255
I	9.2	7.8
II	10.9	9.0
III	7.8	7.6
IV	10.2	8.8

2.4.4.4 Bridging Tether Design: P_n , Q_n , R_n Series and Pyridine-Based Catalysts

As discussed in the text, we propose catalysts with P_n chain where the additional tether links two imine carbon atoms by a simple alkyl chain, and n refers to the number of methylene units in the tether. By similar modifications at the *para*- and *ortho*-aryloxy position of the aryl moiety, we generated Q_n and R_n chain, respectively, as illustrated in Figure 2.14(a). Their precatalyst structural variation in terms of geometry index τ_5 and reactivity in terms of free energy of activation of the TOL TS, $\Delta G^\ddagger(\text{TS1})$ and framework distortion energy (FDE) is reported in Table 2.7 (entries 1–10). The studied pyridine-based catalysts are shown in Figure 2.14 (b), and their geometry indices along with associated energetics for ROTEP of CL are presented in Table 2.7 (entries 11–15).

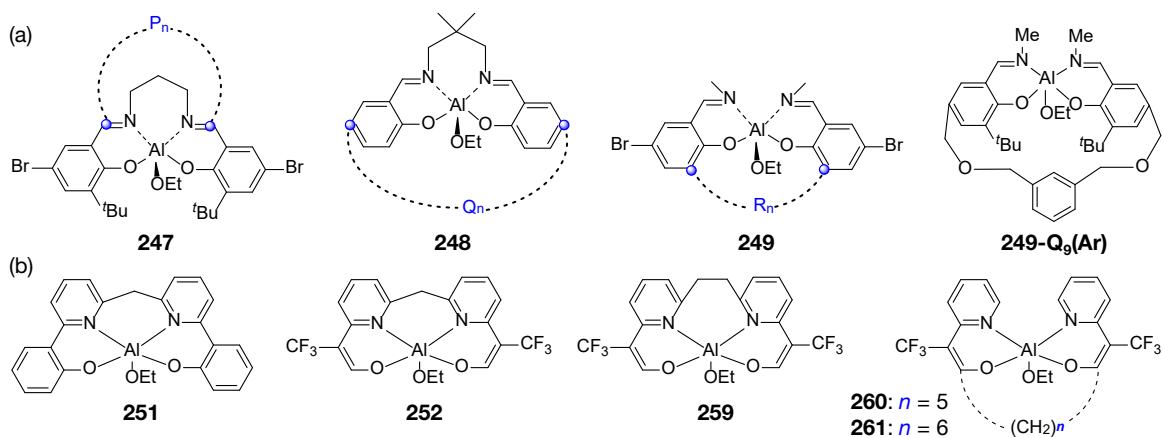


Figure 2.14 (a) Catalyst design for bridging linkers. P_n , Q_n , and R_n chains. (b) Proposed pyridine-based Al-catalysts.

Table 2.7 Catalysts in P_n , Q_n and R_n series (entries 1–10) and pyridine-based catalysts (entries 11–15) with their computed^a geometry indices, activation free energies^b and framework distortion energies^b.

entry	catalyst	τ_5	$\Delta G^\ddagger(\text{TS1})$	FDE
1	247 - P_3	0.28	24.3	19.8
2	247 - P_5	0.60	15.5	12.4
3	247 - P_6	0.65	13.9	11.0
4	247 - P_7	0.65	19.1	10.6
5	248 - Q_9	0.30	21.2	12.8
6	248 - Q_{10}	0.62	18.5	13.0
7	249 - R_3	0.70	12.9	10.6
8	249 - R_4	0.74	11.8	9.9
9	249 - R_5	0.73	11.1	10.0
10	249 - $Q_9(\text{Ar})$	0.68	10.6	9.0
11	251	0.74	6.5	10.3
12	252	0.78	6.2	10.7
13	259	0.55	8.5	9.2
14	260	0.70	7.2	7.6
15	261	0.67	8.9	10.0

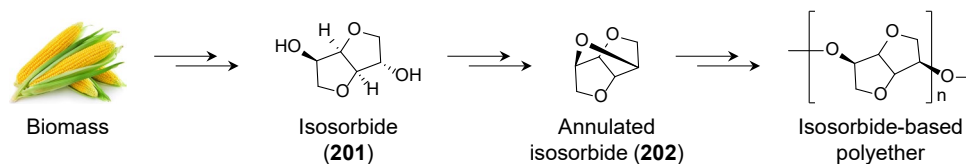
^aComputed at SMD(toluene)/M06-2X/6-311+G(d,p)//M06-L/6-31+G(d,p) level of theory. ^bkcal/mol.

2.5 Mechanistic Investigation of Isosorbide-Based Polyether Synthesis

2.5.1 Introduction

Isosorbide is an inexpensive sugar derived from sorbitol and has been studied in polymers for nearly half a century. Its rigid structure can impart high glass transition temperatures (T_g) into materials, which exhibit excellent properties including good optical clarity and strong resistance to UV, heat, impact, and abrasion.⁹¹ These properties make isosorbide an interesting, sustainable candidate for a wide variety of applications such as packaging, electronic displays, and biomedical applications (e.g. drug formulations, tissue engineering).^{91,92} Most notably, a copolycarbonate from isosorbide (marketed as Durabio™) is currently used for automobile parts as well as touchscreen electronics.⁹³ Until recently, isosorbide has been incorporated into materials almost entirely via step-growth polymerization (SGP).⁹¹ However, step-growth processes are energy intensive and the high temperature conditions often lead to thermo-oxidation of the materials, which easily become discolored from degradation.⁹¹ SGP can also restrict the molar mass and architectural control that can be achieved, especially for isosorbide due to the low reactivity of its secondary alcohols.⁹⁴ Nevertheless, the ability to control polymerization of this feedstock would be transformative for building new and unique sustainable polymers.

Scheme 2.7 Biomass derived monomer isosorbide and its annulation.



As mentioned in section 2.1.3, ring-opening polymerization (ROP) of cyclic monomers offers greater control over polymer architecture/property when compared to a step-growth mechanism, and thus we envisioned annulation of the biomass derived isosorbide monomer (**201**, Scheme 2.7), followed by its ROP. Among various possibilities (carbonate, acetal, anhydride etc.), we hypothesized that annulation of **201** in the form of a cyclic ether (1,4:2,5:3,6-trianhydro-D-mannitol, **202**) would impart sufficient ring-strain thereby facilitating subsequent ROP (Scheme 2.7). This work thus reports an enzyme-catalyzed, regioselective synthesis of an annulated

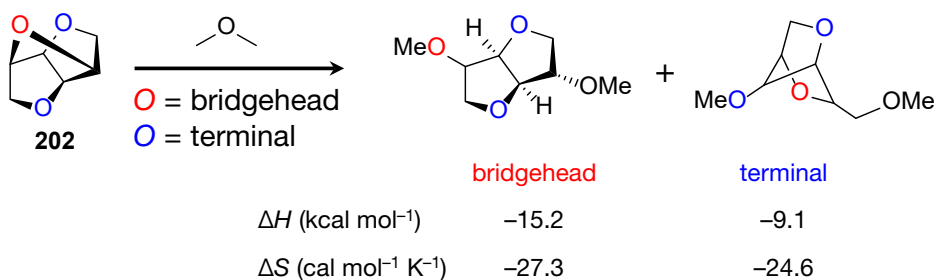
isosorbide derivative (**202**) and mechanistic insights into its cationic and quasi-zwitterionic ROP leading to the first platform for designer polymer architectures from isosorbide. High-throughput screening and density functional theory (DFT) calculations have proven to be invaluable tools for understanding the polymerization. Catalytic ROP of **202** has been achieved via initiation of a highly strained, activated epoxide, which induces selectivity for ring-opening of this complex cyclic ether. Moreover, the polymerization is selectively directed towards different macromolecular architectures through simple variations in reaction conditions.

2.5.2 Results and Discussions

2.5.2.1 Isosorbide Ring-Strain

There are several examples of very well-defined polyethers synthesized by ROP, *e.g.* ethylene oxide, oxetane, and tetrahydrofuran, but other polyethers are harder to obtain as the corresponding monomers do not have sufficient ring-strain.⁹⁵ Despite its perceived ring-strain, attempts to polymerize the isosorbide-derived trianhydrohexitol (**202**) have been largely unsuccessful to this point.⁹⁶ To first investigate if sufficient ring-strain was present in **202**, we employed DFT calculations using an isodesmic reaction (Scheme 2.8) using the computation protocol described in section 2.5.4. The two distinct ethers present in **202** have significantly different ring-strain enthalpies (ΔH): $\Delta H = -15.2$ kcal mol⁻¹ for the bridgehead ether and -9.1 kcal mol⁻¹ for the terminal ethers. The greater ring-strain observed in the bridgehead ether – compared to the *cis*-fused terminal ethers – is likely due to the highly distorted conformation of the newly annulated ring.

Scheme 2.8 Isodesmic reaction used for ring-strain computation.

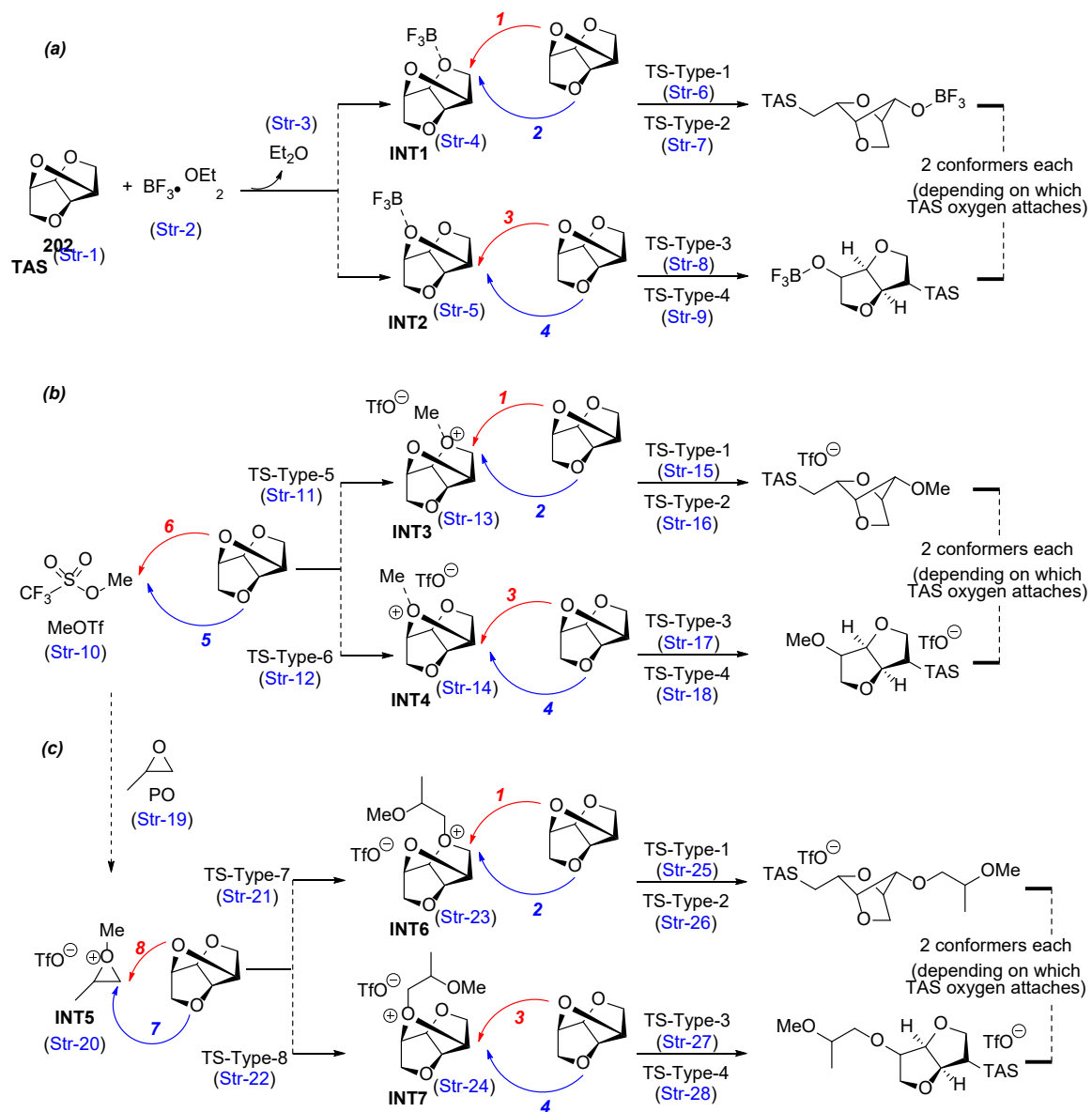


2.5.2.2 Ring-Opening Energetics using MeOTf and BF₃OEt₂ Initiators

To demonstrate **202** could undergo ROP, polymerization studies of **202** were carried out

experimentally utilizing cationic ring-opening polymerization (cROP) using MeOTf as initiator. Because **202** is constructed from three strained five-membered ethers, multiple ring-opening events could take place during polymerization

Scheme 2.9 Possible pathways for the ring-opening of **202** using (a) $\text{BF}_3 \bullet \text{OEt}_2$, (b) MeOTf alone, and (c) MeOTf in combination with PO initiator.



DFT calculations reinforced this hypothesis: For the ring-opening of **202**, Table 2.8 shows that for both MeOTf and $\text{BF}_3 \bullet \text{OEt}_2$ initiators, the free energy of activation (ΔG^\ddagger) requirement for the ring-opening event is very similar for all four pathways considered (Scheme 2.9) and spanned

a window of only 3.4 kcal mol⁻¹ (entry 1 and 2; Table 2.8). We note, however, that BF₃OEt₂ slightly favors the terminal ring-opening (route 1 and 2) whereas MeOTf favors the bridgehead ring-opening (route 3 and 4).

Table 2.8 Ring-opening energetics of **202** with BF₃OEt₂, MeOTf and MeOTf/PO initiator.^a

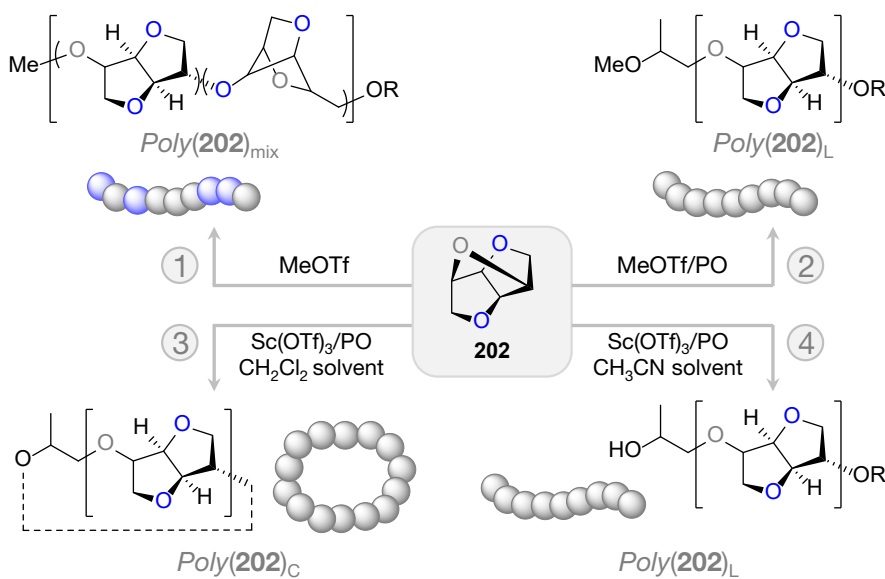
catalyst	ΔG_1^\ddagger	ΔG_2^\ddagger	ΔG_3^\ddagger	ΔG_4^\ddagger
BF ₃ OEt ₂	29.0	28.1	30.8	30.2
MeOTf	30.4	32.1	29.1	28.7
MeOTf/PO	17.6	20.3	16.7	17.8

^aGibbs free energies (kcal mol⁻¹) at 298.15 K are computed in accordance with Scheme 2.9 at M06-2X/6-311+G(d,p)/SMD(CH₂Cl₂)/M06-L/6-31+G(d,p)/SMD(CH₂Cl₂) level of theory.

2.5.2.3 Ring-Opening Selectivity Induced by Propylene Oxide

To improve selectivity, we sought to design a system that would produce greater disparity between various ring-opening events. Activation of an epoxide to form a highly strained oxonium initiating species was envisioned to potentially increase the kinetic gap between bridgehead and terminal ring-opening events (Scheme 2.10).

Scheme 2.10 Cationic ring-opening polymerization of **202**. (1) MeOTf initiator alone causes both bridgehead and terminal ring-opening; (2) MeOTf/PO induces selectivity towards bridgehead ring-opening; Sc(OTf)₃/PO in (3) low- ϵ solvent (CH₂Cl₂) prefers cyclic polymer formation, while (4) high- ϵ solvent (CH₃CN) favors linear polymer.



Thus, the reactivity bias could be shifted toward propagation through the bridgehead ether as both kinetics and thermodynamics of ring-opening would be favored. Specifically, we were interested in employing $\text{Sc}(\text{OTf})_3$ and propylene oxide (PO) for polymerization of **202** as this system has exhibited successful cROP of tetrahydrofuran.⁹⁷ This approach is also beneficial from a sustainability aspect since $\text{Sc}(\text{OTf})_3$ is catalytic and recyclable.⁹⁷

Scheme 2.11 Detailed mechanistic consideration for ring-opening of **202**, with key stationary points identified on the relevant potential energy surface using (a) $\text{Sc}(\text{OTf})_3$ catalyst alone and (b) $\text{Sc}(\text{OTf})_3/\text{PO}$ catalytic system.

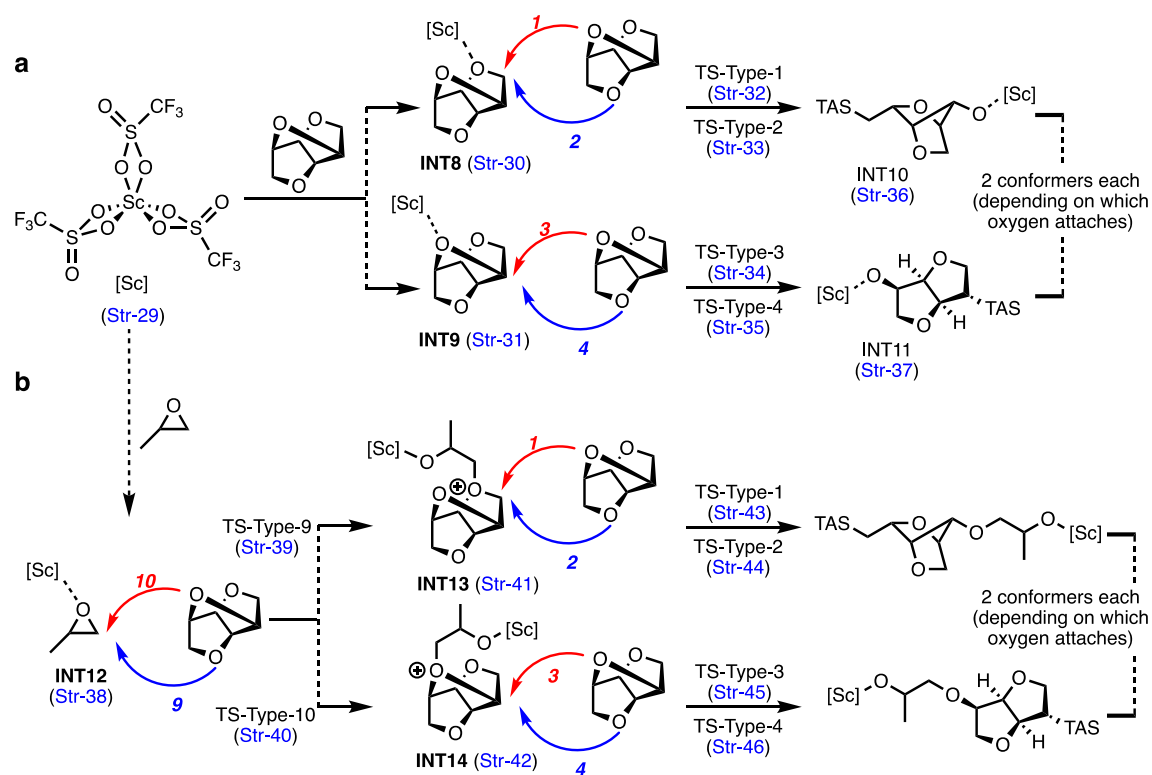


Table 2.9 Ring-opening energetics of **202** using $\text{Sc}(\text{OTf})_3$ in the absence and presence of PO initiator.^a

catalyst	ΔG_1^\ddagger	ΔG_2^\ddagger	ΔG_3^\ddagger	ΔG_4^\ddagger
$\text{Sc}(\text{OTf})_3$	28.9	27.0	30.4	27.8
$\text{Sc}(\text{OTf})_3/\text{PO}$	29.7	27.5	24.2	23.0

^aGibbs free energies (kcal mol^{-1}) at 298.15 K are computed in accordance with Scheme 2.11 at M06-2X/6-311+G(d,p)/SMD(CH_2Cl_2)/M06-L/6-31+G(d,p)/SMD(CH_2Cl_2) level of theory.

This refined catalytic system was then computationally modeled via DFT. Using $\text{Sc}(\text{OTf})_3$ alone, the ring-opening energetics did not vary much from MeOTf (Table 2.9 entry 1 vs. Table 2.8 entry 2). Introduction of the PO initiator, however, makes the ring-opening process more favorable (lowering of the activation barrier by $\sim 4.0 \text{ kcal mol}^{-1}$), with the bridgehead ring-opening becoming particularly favored over its terminal analog. This suggests that epoxide PO plays a key role in inducing selectivity during ring-opening. Note that while the absolute ring-opening energetics remain similar in the $\text{Sc}(\text{OTf})_3/\text{PO}$ case compared to the bare $\text{Sc}(\text{OTf})_3$ one, the differential stability of the preceding intermediate during homo-propagation causes a *net* difference in the overall activation barrier (Figure 2.15). Clearly, **INT13** is $\sim 2.5 \text{ kcal mol}^{-1}$ lower in free energy than the corresponding **INT14**, which can be attributed to steric factors. Indeed, the terminal experiences less steric crowding from the $[\text{Sc}]$ center, making it energetically lower than the bridgehead variant, and in the process, the effective barrier height for terminal ring-opening is increased (Table 2.9: ΔG^\ddagger_2 vs $\Delta G^\ddagger_3 = 27.5$ vs. $24.2 \text{ kcal mol}^{-1}$).

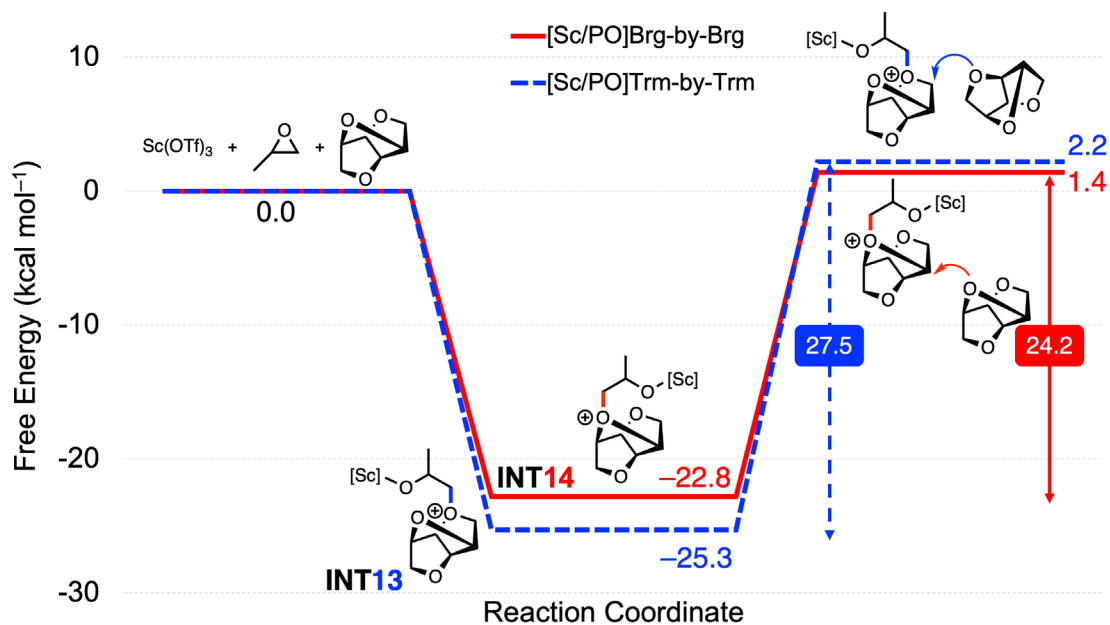


Figure 2.15 Relative ring-opening energetics of $\text{Sc}(\text{OTf})_3$ - and $\text{Sc}(\text{OTf})_3/\text{PO}$ -initiated polymerization of **202**.

2.5.2.4 Lowering of Activation Barrier with PO Initiator

To understand why presence of an epoxide lowers the activation barrier, we probed the partial charges (Q_{CMS}) of various atoms in the propagating species using the CM5 model (Figure 2.16).⁹⁸ In the presence of PO, the α -carbon has increased cationic character, presumably due to the stronger C–O bond than Sc–O bond,⁹⁹ resulting in a more electrophilic chain-end.

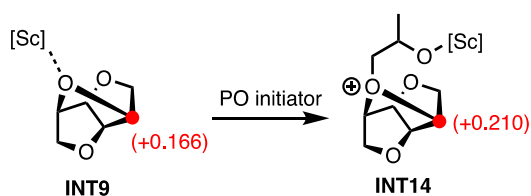


Figure 2.16 Computed CM5 partial charges on α -carbon involved during the ring-opening of **202**. **INT9** is the intermediate formed after the monomer coordinates to $\text{Sc}(\text{OTf})_3$ via the bridgehead oxygen atom. **INT14** is the corresponding intermediate when the PO initiator is used. See Scheme 2.11 for details on how they are formed.

2.5.2.5 Polymer Architecture Control Exploiting Solvent Dielectric Constant

Catalytic polymerization of **202** was explored experimentally with $\text{Sc}(\text{OTf})_3$ and PO (Scheme 2.10, bottom). Polymerizations conducted in dichloromethane yielded cyclic polymers ($\text{Poly}(\mathbf{202})_{\text{C}}$; Scheme 2.10(3)), while similar reaction in acetonitrile showed only linear chains ($\text{Poly}(\mathbf{202})_{\text{L}}$) with an alkoxy or hydroxyl end group. This observation can be rationalized by the quasi-zwitterionic nature of the active chains initiated by $\text{Sc}(\text{OTf})_3$ and PO. Due to the poor ability of solvents with low dielectric constant (ϵ) e.g. dichloromethane to solvate ions, the chain ends are likely in close proximity to neutralize the charge, increasing the probability of backbiting reactions that result in the formation of cyclic polymers.¹⁰⁰ The high ϵ of acetonitrile enhances solvation of the ions and allows for more charge separation. DFT calculations support this hypothesis as the ring-opened PO, while coordinated to $\text{Sc}(\text{OTf})_3$, possesses significant anionic character ($Q_{\text{O,CM5}} = -0.617$). Thus, backbiting may occur once a sufficient degree of polymerization is reached due to the slow propagation kinetics with respect to cyclization.

2.5.2.6 Effect of Counterion Mobility on Kinetic Barriers

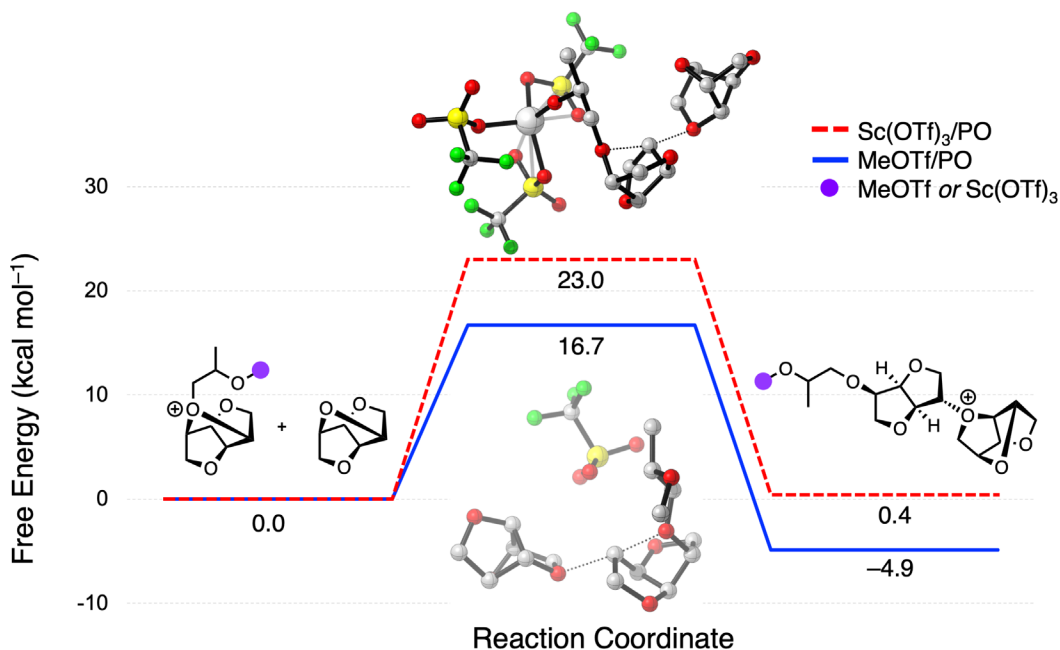


Figure 2.17 Relative ring-opening energetics of MeOTf/PO- and Sc(OTf)₃/PO-initiated polymerization of **202**.

An analogous monotonic polymerization was also conducted by activating PO with MeOTf to form the initiating species (Scheme 2.10(2)). Overall, the conversion of **202** with MeOTf/PO was also found experimentally to be higher (15% at 298 K) compared to Sc(OTf)₃/PO-initiated ROP under similar conditions. We attribute this in part to the difference in counterion mobility: the triflate is free in the case of MeOTf and coordinated in the case of Sc(OTf)₃. During the ring-opening process, significant charge separation is observed by DFT in both the oxonium propagating center as well as the partially cationic α -carbon. These charges can be partially compensated by the free triflate counterion in the MeOTf system, which drastically lowers the activation barrier ($\Delta\Delta G^\ddagger = 6.3$ kcal mol⁻¹; Figure 2.17). Modelled ring-opening transition state structure shows a free triflate ion close to the charge separated site in case of MeOTf, whereas, the counterion is always attached to the metal center in the Sc(OTf)₃ case.

2.5.3 Conclusion

In summary, the first platform for designer polymer architectures from isosorbide via ROP is presented. The annulated isosorbide derivative **202** was prepared requiring minimal-to-no

purification. We have demonstrated its cationic ring-opening polymerization (cROP) and enabled a significant increase in conversion by first activating an epoxide. Quasi-zwitterionic conditions with $\text{Sc}(\text{OTf})_3/\text{PO}$ permit control over macromolecular architecture to yield cyclic or linear polymers. Ongoing efforts are aimed at further enhancement of the kinetic favorability of polymerization, increasing monomer conversion, and developing various copolymer compositions and architectures. Understanding cROP of this derivative will allow for the study of isosorbide-based polyethers – a relatively unexplored class of materials – and more generally, be useful for controlling the selectivity and polymerization of other complex cyclic ethers.

2.5.4 Appendix

2.5.4.1 Computation Protocol

To compute various thermodynamic parameters associated with the ring-strain of monomer, an isodesmic reaction scheme has been used (Scheme 2.8). All reactant monomers and ring-opened products involved there in, have been subjected to a detailed conformer analysis using Schrödinger's MacroModel package,¹⁰¹ employing the Monte Carlo Multiple Minimum (MCOMM) searching protocol using Merck Molecular Force Field (MMFFs) forcefield.¹⁰² All conformers within 15 kcal mol⁻¹ of the global minima were selected for further analysis using density functional theory (DFT), where conformers within 2 kcal mol⁻¹ of the global minimum were included in the final Boltzmann weighting. Ring-strain parameters are then reported as a Boltzmann average of relevant conformers. DFT calculations are performed using Gaussian 09 program package.¹⁰³ Geometry optimizations are carried out at M06-L level of theory¹⁰⁴ using double zeta 6-31+G(d,p) basis set⁶⁶ for all atoms. Coulomb integrals are evaluated using an automatically generated density fitting basis set. An “ultrafine” grid has been used for numerical integration, along with an integral accuracy of 10⁻¹¹. Natures of all stationary points are verified by vibrational frequency calculation at the same level of theory. Low frequency vibrational modes below 50 cm⁻¹ are replaced with a value of 50 cm⁻¹ while computing vibrational partition functions. Zero-point vibrational energies and thermal contributions to electronic energy are determined from the computed partition functions at 298.15 K. For better estimate to Gibbs free energies, single point electronic energies are computed using M06-2X functional¹⁰⁴ with the 6-

311+G(d,p) basis set⁶⁶ at the M06-L optimized geometries and are summed to thermal free energy contributions computed at M06-L/6-31+G(d,p) level of theory. Partial charges are calculated from the final M06-2X densities using Charge Model 5 (CM5).⁹⁸ All reported structures are optimized using the self-consistent reaction field (SCRF) approach with SMD continuum solvation model¹⁰⁵ with the solvent parameters for dichloromethane (CH₂Cl₂) ($\epsilon = 8.93$).

Chapter 3

Site-selective Benzylic C–H Functionalization: Azidation and Etherification

Synopsis. Site-selective functionalization of benzylic C–H bonds is very attractive in drug discovery, chemical biology, and materials synthesis. While C–H functionalization methods allow for efficient synthesis of target molecules, the availability of multiple C–H bonds within a given molecule, however, introduces the challenge of site selectivity. This chapter discusses our collaborative effort in understanding the mechanism of selective functionalization (azidation and etherification) of benzylic C–H bonds using copper catalysts in combination with N-fluorobenzenesulfonimide (NFSI). Detailed mechanistic study employing density functional theory suggests a radical-polar crossover pathway, providing a basis for the observed lack in enantioselectivity.

3.1 Site-Selective Copper-Catalyzed Azidation of Benzylic C–H Bonds¹⁰⁶

3.1.1 Introduction

C–H functionalization methods improve the efficiency of target molecule syntheses¹⁰⁷ and expand the scope of accessible structures.¹⁰⁸ The large number of C–H bonds within an individual molecule, however, introduces the challenge of site selectivity.^{107,109,110} Recent efforts to develop methods for C(sp³)–H azidation¹¹¹ reflect the versatility of azides in drug discovery, chemical biology, and materials synthesis.¹¹² Azides represent effective ammonia surrogates,¹¹³ they are readily converted into *N*-heterocycles, including triazoles, tetrazoles, and pyrroles,^{114,115} and they provide access to important bioactive molecules (Figure 3.1; A and B).¹¹⁶

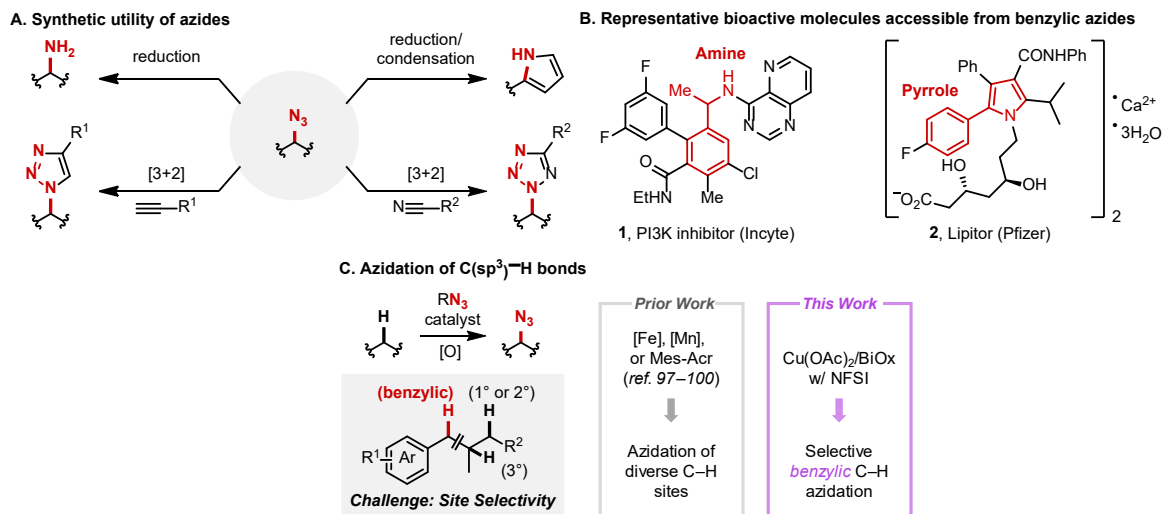


Figure 3.1 Azides are important intermediates in organic syntheses (A) and medicinal chemistry (B) and are ideally prepared by direct azidation of sp³ C–H bonds (C). NFSI, *N*-fluorobenzenesulfonimide. Mes-Acr, 9-mesityl-10-alkylacridinium catalyst. © American Chemical Society

Advances in C–H azidation include iron-^{117,118} and manganese-catalyzed,¹¹⁹ and photochemical^{120,121} methods that enable the use of diverse C–H substrates as the limiting reagent; however, the issue of site selectivity has been only partially addressed. Mechanisms of these methods likely involve radical intermediates that feature high selectivity for tertiary aliphatic C–H bonds in the presence of primary and secondary C–H bonds; however, selectivity for benzylic over aliphatic positions is relatively low¹²⁰ or has not been investigated. Benzylic and heterobenzylic C–H bonds are ubiquitous in bioactive molecules, and site-selective

functionalization of such positions could have broad impact. We^{122,123} and others¹²⁴ have recently demonstrated that copper catalysts in combination with *N*-fluorobenzenesulfonimide (NFSI) enable selective functionalization of benzylic C–H bonds. We envisioned that a similar approach could be used to achieve C–H azidation with high benzylic site-selectivity (Figure 3.1C).¹²⁵ Here, we demonstrate this transformation and provide fundamental insights into the reaction. Comparison of the site-selectivity of this Cu-catalyzed reaction with other C–H azidation methods highlights the unique benzylic selectivity of the method, and the synthetic utility is demonstrated via preparation of important target molecules.

3.1.2 Results and Discussion

3.1.2.1 Experimental Results

Initial reaction optimization efforts used 1-ethylnaphthalene **3a** and TMSN₃ as coupling partners. An initial attempt with previously reported benzylic C–H cyanation conditions¹²² led to the desired product, but with low conversion and yield (6%, entry 1, Table 3.1). Increasing the temperature to 50 °C and using nitromethane as the solvent significantly increased the yield of **4a** (entries 2 and 3, Table 3.1). Cu^I and Cu^{II} acetate salts were the most effective catalyst precursors (entries 3 and 6), and Cu(OAc)₂ was selected because it led to higher yields, and its air-stability facilitated handling. Testing the reaction in the absence of **L1** highlighted the importance of an ancillary ligand (entry 7). Screening of other ligands showed that improved yields could be obtained with 2,2'-bioxazoline (BiOx) ligands (e.g., 85% yield with **L4**, entry 10). Further screening led to the optimized conditions in entry 11, affording 93% yield of azide **4a**. No enantioselectivity was observed, even when using a single enantiomer of the chiral ligand. This result prompted us to undertake several efforts to probe the reaction mechanism.

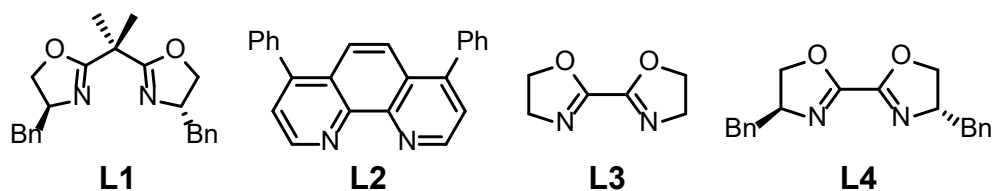
Cu^I-mediated reductive activation of NFSI generates an imidyl radical that promotes hydrogen-atom transfer (HAT) from the benzylic C–H bond.¹²³ The resulting benzyl radical can react with a Cu^{II}-azide species to afford the benzyl azide. Under simulated catalytic conditions in the absence of benzylic substrate, Cu^IOAc, **L2**, NFSI, and TMSN₃ generate a dimeric Cu^{II}-azide complex, characterized by X-ray crystallography (Figure 3.2 A). Addition of Gomberg's dimer,¹²⁶

which readily dissociates into two trityl radicals, to a solution of this complex generated trityl azide in 91% yield (Figure 3.2 B).^{127,128} This stoichiometric reaction was complemented by a catalytic reaction with triphenylmethane, which led to the benzyl azide in 66% yield.

Table 3.1 Reaction Optimization^a

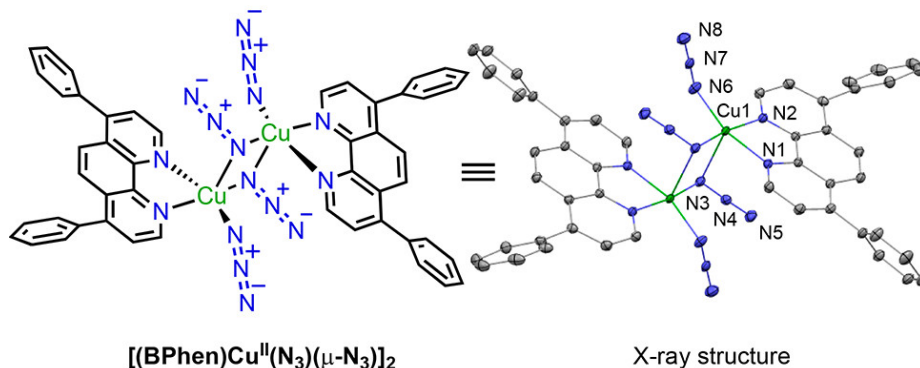
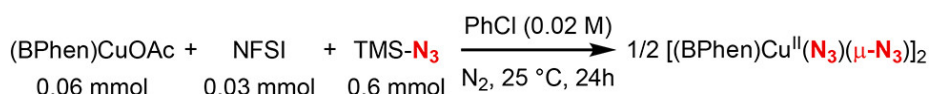


entry	catalyst (mol%), ligand (mol%)	NFSI (equiv.)	TMS-N ₃ (equiv.)	yield ^b (%)
1	CuOAc (10), L1 (10) (room temp., solv = benzene) ¹²²	1.5	3.0	6
2	CuOAc (10), L1 (10) (solv = benzene)	1.5	3.0	51
3	CuOAc (10), L1 (10)	1.5	3.0	55
4	CuI (10), L1 (10)	1.5	3.0	31
5	Cu(acac) ₂ (10), L1 (10)	1.5	3.0	42
6	Cu(OAc) ₂ (10), L1 (10)	1.5	3.0	62
7	Cu(OAc) ₂ (10) (no ligand)	1.5	3.0	15
8	Cu(OAc) ₂ (10), L2 (10)	1.5	3.0	37
9	Cu(OAc) ₂ (10), L3 (10)	1.5	3.0	69
10	Cu(OAc) ₂ (10), L4 (10)	1.5	3.0	85
11	Cu(OAc)₂ (2.0), L4 (4.0)	2.5	3.6	93^c



^a 0.4 mmol 1-ethylnaphthalene (**3a**). ^b NMR yield, ext. std. = mesitylene. ^c Isolated yield.

A. Synthesis of $[(\text{BPhen})\text{Cu}^{\text{II}}(\text{N}_3)(\mu\text{-N}_3)]_2$



B. Reaction of $[(\text{BPhen})\text{Cu}^{\text{II}}(\text{N}_3)(\mu\text{-N}_3)]_2$ with Gomberg's dimer

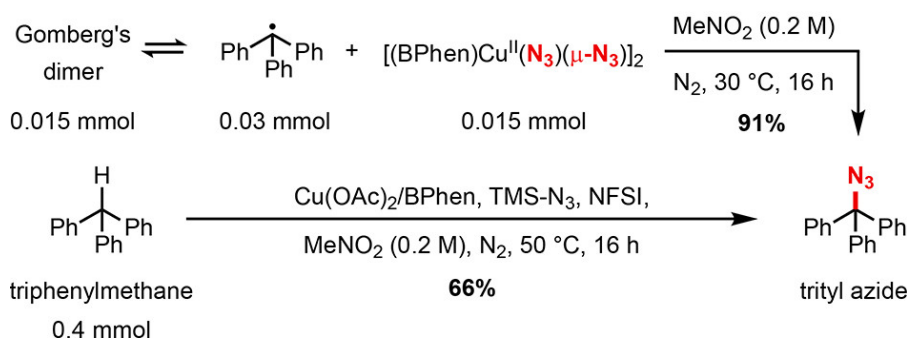


Figure 3.2 (A) Synthesis and crystal structure of $[(\text{BPhen})\text{Cu}^{\text{II}}(\text{N}_3)(\mu\text{-N}_3)]_2$ (hydrogen atoms and chlorobenzene molecule omitted for clarity). (B) Reaction of $[(\text{BPhen})\text{Cu}^{\text{II}}(\text{N}_3)(\mu\text{-N}_3)]_2$ with Gomberg's dimer (6 mol% $\text{Cu}(\text{OAc})_2/\text{BPhen}$, 3.6 equiv. TMSN_3 , 2.5 equiv. NFSI). © American Chemical Society

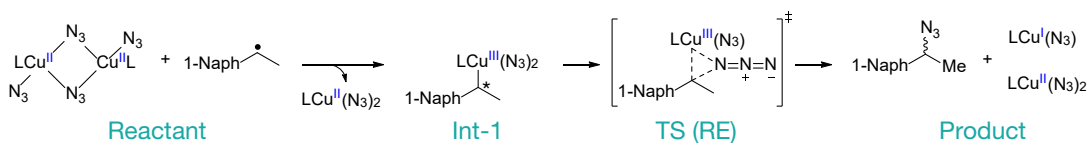
3.1.2.2 Computational Studies

Seminal studies by Kochi suggest several possible pathways for C–N bond formation, as depicted in Figure 3.3A.¹²⁹ In Path I, the benzyl radical adds to a Cu^{II} center to generate a benzyl- Cu^{III} species that can undergo C–N reductive elimination.^{122,129a} Path II includes a series of pathways involving radical attack at a terminal or bridging azide ligand, either at the proximal or distal N-atom of the azide.^{129b–d} Finally, Path III involves one-electron oxidation of the benzyl radical by Cu^{II} to generate the corresponding cation, which can then react readily with an azide nucleophile.^{123,129e–f} Density functional theory calculations were performed to assess relevant structures and their associated energies in these pathways (M06-L/basis-II/SMD(MeNO_2)/B3LYP-D3(BJ)/basis-I level of theory: Basis-I = 6–31G(d,p) for non-

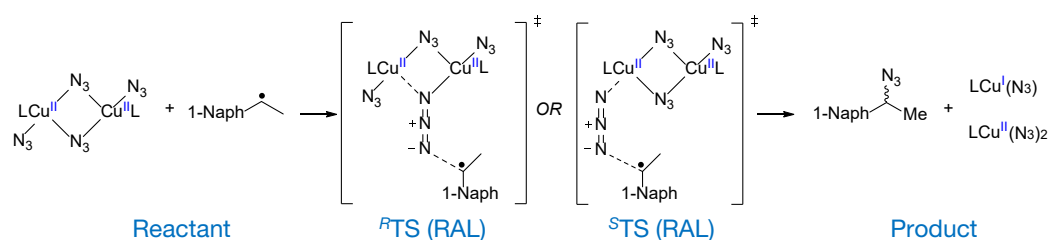
metals; SDD basis and pseudopotential¹³³ for Cu. Basis-II = def2-TZVP for non-metals, def2-TZVP basis and SDD pseudopotential for Cu; see Section 9 in Supporting Information for details).

A. Three plausible reaction pathways

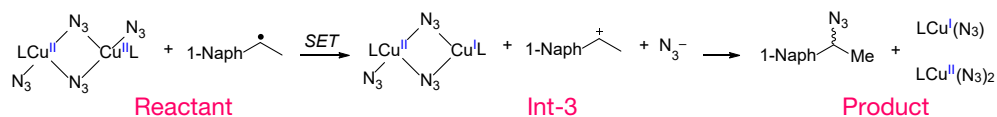
Path-I: Radical Addition to Cu/Reductive Elimination (RE)



Path-II: Radical Addition to N₃ Ligand (RAL)



Path-III: Radical Polar Crossover



B. Calculated energetics for reaction pathways

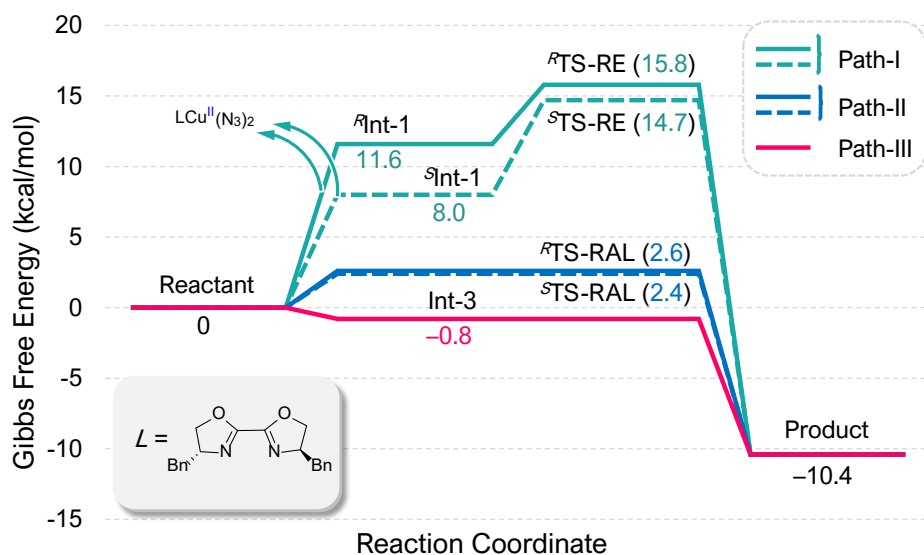


Figure 3.3 Three proposed pathways for azidation of the benzyl radical (A), and simplified energy diagrams comparing the three pathways (B) (Gibbs free energies computed at 298.15 K with the M06-L/basis-II/SMD(MeNO₂)/B3LYP-D3(BJ)/basis-I level of theory).

The energy diagrams in Figure 3.3B highlight the most favorable energies identified for Paths I–III for the reaction of the benzyl radical of 1-ethylnaphthalene and **L4**-ligated Cu^{II}-dimer. The results show that radical addition to Cu^{II}, followed by C–N reductive elimination from **Int-1** has the highest energy among the different mechanisms (Figure 3.3B). Radical addition to an azide ligand proceeds with much lower barrier. The pro-*R* face favors addition to a bridging azide while the pro-*S* favors addition to a terminal azide: $\Delta G^\ddagger = 2.6$ and 2.4 kcal/mol for ^{*R*}**TS2** and ^{*S*}**TS2**, respectively. In both cases, radical addition is favored at the distal *N*-atom of the azide ligand (see Figure 3.6 for energies of all paths). Computational analysis of the electron-transfer pathway leveraged the experimental redox potential measured for [(BPhen)Cu^{II}(N₃)(μ-N₃)₂] (–0.16 V vs. Fc^{0/+}) and reported potentials for the benzyl radicals of ethylbenzene and isopropylbenzene ($E^\circ_{R^+|R^\bullet} = -0.01$ and -0.22 V vs. Fc^{0/+}).¹³⁰ Using these values as benchmarks, calculated redox potentials for [(**L4**)Cu^{II}(N₃)(μ-N₃)₂] and the benzyl radical of **3a** reveal that oxidation of the radical by the Cu^{II}-dimer is thermodynamically favorable ($\Delta G^\circ = -0.8$ kcal/mol) (see section 3.1.4.3 and 3.1.4.4 for details).

The small calculated energy difference between Paths II and III, and the absence of an electron-transfer rate constant, prevent clear distinction between these two paths on the basis of computational studies; however, both are predicted to afford little or no enantioselectivity.¹³¹ Experimental data providing some support for Path III was obtained from catalytic azidation of 4-Ph-cumene. The benzylic azidation product was obtained in a 2:1 ratio with a vicinal diazide byproduct. Control experiments suggest the diazidation arises from an *α*-methylstyrene intermediate (see ref. 106 for details). These results are most consistent with a radical-polar crossover mechanism, in which the benzyl cation can react with an azide nucleophile or lose a proton to generate an alkene, which undergoes subsequent 1,2-diazidation.

3.1.2.3 Experimental Site-Selectivity Studies

Efforts were then made to explore the site-selectivity of this method relative to other C–H azidation methods (Figure 3.4). Three substrates incorporating both secondary benzylic and tertiary aliphatic C–H bonds were selected: isobutylbenzene **3b**, isopentylbenzene **3c**, and ibuprofen methyl ester **3d**. Use of the Cu/NFSI catalytic conditions at 30 °C led to azidation yields

of 48%, 71%, and 62%, respectively, with benzylic:tertiary (B:T) selectivity, ranging from 11:1–30:1. No azidation was observed at the tertiary benzylic position adjacent to the ester group in **3d**. This result probably reflects both steric inhibition and a polarity mismatch in reaction with the sulfonimidyl radical. These results may be compared with analogous data from three other C–H azidation methods, including photochemical,¹²⁰ Mn-catalyzed,¹¹⁹ and Fe-catalyzed^{117–118} reactions (II–IV, Figure 3.4). The site-selectivity for **3b** and **3d** were reported previously with method II and exhibit a B:T ratio of ~ 1:1.¹²⁰ Independent testing of **3c** revealed tertiary C–H azidation. Mn(salen)Cl with PhIO (method III)¹¹⁹ also exhibits good selectivity for benzylic azidation: B:T = 4.6:1, 4.6:1, and 14:1, respectively, for **3b**, **3c**, and **3d**, although these reactions were operationally more challenging and led to lower yields (28–48%) than Cu/NFSI. The Fe(OAc)₂/I^{III}-azide system (method IV)^{117–118} showed relatively low B:T selectivity with **3b–3d** (1:1–2.5:1). Collectively, the data in Figure 4 demonstrate that benzylic C–H bonds are not necessarily the most reactive sites in radical C–H functionalization reactions. (For “Scope of Benzylic C–H Azidation of Alkylarenes” see ref. 106)

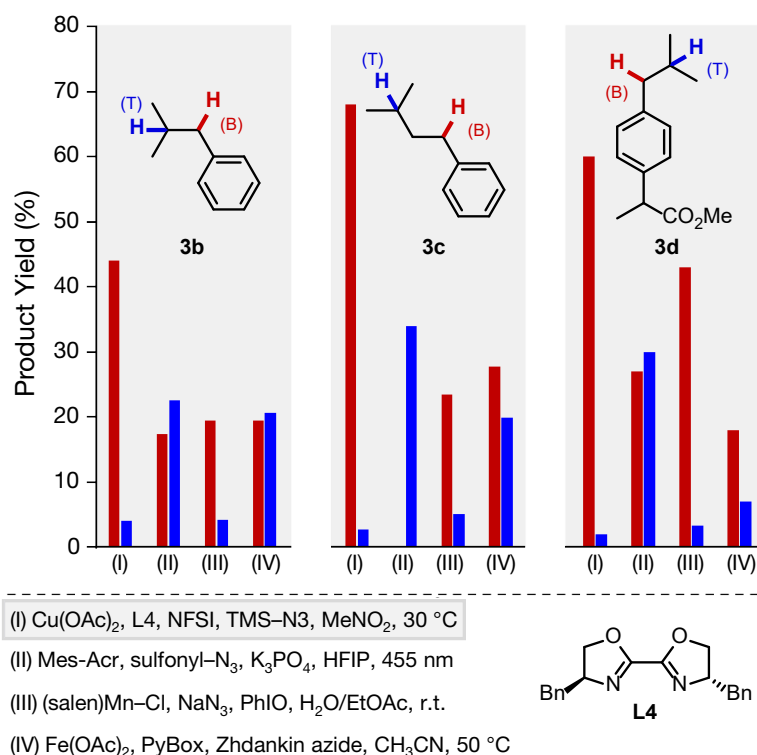


Figure 3.4 Azidation site selectivity with different catalytic methods (see for ref. 106 details). Standard condition for method I; substrate (0.4 mmol), Cu(OAc)₂ (2.0 mol%), BiOx (4.0 mol%), TMSN₃ (3.6

equiv.), NFSI (2.5 equiv.), 0.2 M MeNO₂, 30 °C, 24 h for **3b**, 48 h for **3c** and **3d**. © American Chemical Society

3.1.3 Conclusion

The results described herein show that a copper-based catalytic system composed entirely of commercially available components enables selective benzylic C–H azidation with broad scope. The reaction is initiated by hydrogen-atom transfer, followed by reaction of the benzylic radical with a Cu^{II}-azide intermediate. Experimental and computational data are most consistent with a radical-polar crossover pathway involving a benzylic cation. The unique combination of good yields, diverse functional group compatibility, and high benzylic site-selectivity make this method well-suited for the incorporation of primary amines and azide-derived heterocycles (pyrroles, triazoles, and tetrazoles) into pharmaceutical and agrochemical building blocks, intermediates, and existing bioactive molecules.

3.1.4 Appendix

3.1.4.1 Computational Methods

For all computed structures, density functional theory calculations are performed with the Gaussian 16 (rev. C.01) electronic structure program suite.¹⁰³ Geometries of all stationary points are optimized in the *gas phase* at the B3LYP-D3(BJ)/basis-I level of theory,^{19d,20,132} where *basis-I* comprises the 6-31G(d,p) basis⁶⁶ for non-metals and the Stuttgart/Dresden effective core potential with its associated basis set (SDD) for Cu.¹³³ For numerical integration in DFT, “ultrafine” grid is chosen together with the default integral accuracy set at 10⁻¹². Vibrational frequency calculations were performed at the same level of theory to ensure natures of all stationary points. Frequencies below 50 cm⁻¹ were replaced by a value of 50 cm⁻¹ in the vibrational partition function when computing thermal contributions to free energies (1 atm pressure, T = 298.15K). For better estimate to Gibbs free energies, single point electronic energies were recomputed using M06-L/basis-II level of theory^{104a} (*basis-II*: the def2-TZVP basis¹³⁴ for non-metals and def2-TZVP basis/SDD pseudo potential for Cu). Solvation effects were included employing the SMD continuum solvation model¹⁰⁵ with solvent parameters for nitromethane ($\epsilon = 36.562$).

For the series of reactions (Figure 3.3A; Path-II) of the doublet benzylic radical with the triplet $[\text{LCu}^{\text{II}}(\text{N}_3)_2]_2$ dimer, yielding a benzylic azide product and the $\text{LCu}^{\text{I}}(\text{N}_3)$ species, both having closed shell singlet electronic structures, along with the doublet $[\text{LCu}^{\text{II}}(\text{N}_3)_2]$ monomer species, the corresponding transition-state (TS) structures were located on the broken-symmetry (BS) surface. In those cases, the spin-projection scheme of Yamaguchi et al.^{135,211} was used for obtaining approximate spin-projected electronic energies of the lower-spin states using equation (3.1). Redox potentials of various species were also computed (at 298.15 K) using the above-mentioned protocol. For the redox transformation: $\text{O}(\text{sol}) + n\text{e}^-(\text{g}) \rightarrow \text{R}(\text{sol})$, standard reduction potential has been computed using equation (3.2).

$$E_{\text{AP}}^{\text{LS}} = E^{\text{HS}} + (E_{\text{BS}}^{\text{LS}} - E^{\text{HS}}) \times \frac{\langle \hat{S}^2 \rangle_{\text{exact}}^{\text{HS}} - \langle \hat{S}^2 \rangle_{\text{exact}}^{\text{LS}}}{\langle \hat{S}^2 \rangle^{\text{HS}} - \langle \hat{S}^2 \rangle_{\text{BS}}^{\text{LS}}} \quad (3.1)$$

Where, E = electronic energy, BS = broken (spin) symmetry, AP = approximate (spin) projection, LS = low-spin, HS = high-spin.

$$E_{\text{O|R}}^0 = \frac{G^0(\text{O,sol}) - G^0(\text{R,sol})}{n_e F} - E_{\text{reference}}^0 \quad (3.2)$$

Where, $n_e = 1$, F is the Faraday constant. We first report *absolute* reduction potentials of various species setting $E_{\text{reference}}^0$ at 0 V. Corresponding values vs. the $\text{Fc}^{0/+}$ reference were then calculated using an empirical correction factor accounting for experimentally available redox data, as detailed in Section 3.1.4.3.

3.1.4.2 Electronic Structure of the $[\text{LCu}^{\text{II}}(\text{N}_3)_2]_2$ Dimer and Analysis of the Dimer/Monomer Equilibria

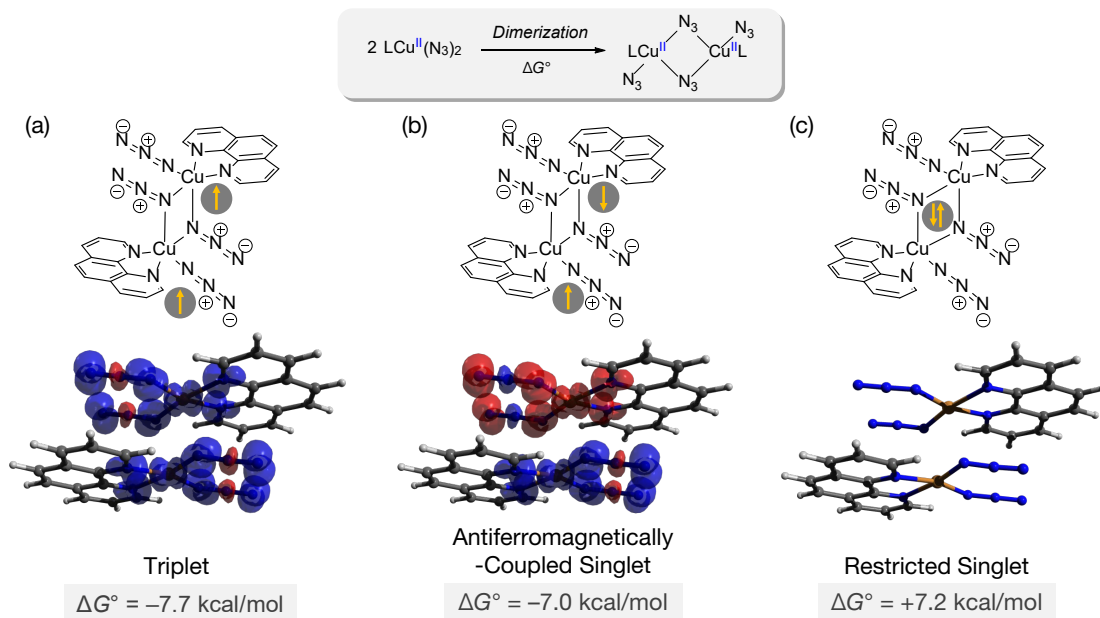


Figure 3.5 Gibbs free energy change (kcal/mol) due to dimerization. Calculations done at 298.15 K at M06-L/basis-II/SMD(MeNO₂)/B3LYP-D3(BJ)/basis-I level of theory.

Electronic structure of the experimentally isolated $[\text{LCu}^{\text{II}}(\text{N}_3)_2]_2$ dimer ($L = \text{BPhen}$ experimentally and $L = \text{Phen}$ computationally) was probed at the DFT level. Dimerization in the triplet electronic state was found to be energetically most favorable, the triplet dimer being ~ 7.7 kcal/mol lower in free energy relative to the corresponding infinitely separated monomers. When the ligand is switched to the chiral BiOx* (**L4**) ligand, however, the dimer stabilization is reduced to only ~ 2.0 kcal/mol.

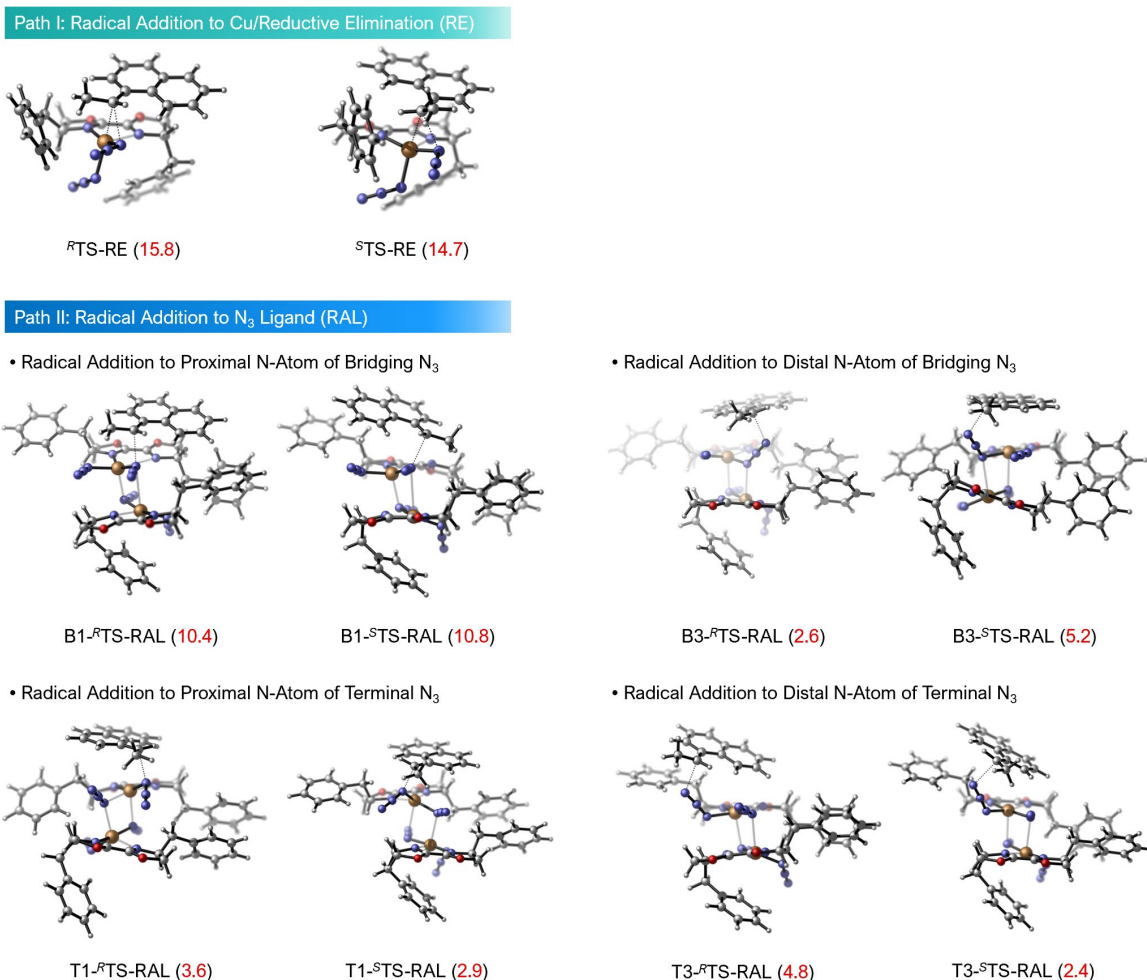
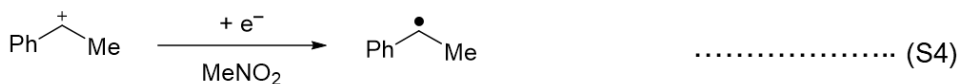


Figure 3.6 Optimized transition-state (TS) structures leading to product formation via reductive elimination (RE) and direct radical addition to the azide ligand (RAL) for both pro-*R* and pro-*S* faces of the benzylic radical derived from 1-ethylnaphthalene. Gibbs free energies of activation (ΔG^\ddagger ; kcal/mol) of the respective TS structures are included in parenthesis. Gibbs free energies are reported at 298.15 K calculated at M06-L/basis-II/SMD(MeNO₂)/B3LYP-D3(BJ)/basis-I level of theory. “RE” implies reductive elimination (Path-I). The prefix “B3-” implies that the reaction is happening at the distal *N*-atom of the bridging azide group. Similarly, “T1-” prefix means that it is the proximal *N*-atom of the terminal azide group.

3.1.4.3 Computed Reduction Potentials

Accurate computational prediction of standard reduction potentials for copper-containing compounds using density functional methods can sometimes prove challenging.¹³⁶ In this work, we have computed absolute reduction potentials for various species and used two sets of correction factors, $f(\text{Cu})$ [= 3.706 V] for copper-based complexes and $f(\text{Org})$ [= 4.487 V] for organic species, to convert computed reduction potentials into values relative to the Fc|Fc^+

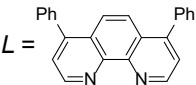
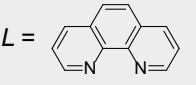
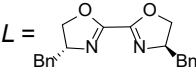
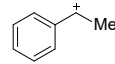
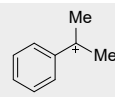
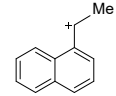
reference used experimentally. The values of the correction factors are taken as those required to map the computed absolute reduction potentials for $[\text{LCu}^{\text{II}}(\text{N}_3)_2]_2$ ($L = \text{BPhen}$) dimer species and ethylbenzene cation to their experimental values (Figure 3.7 and Table 3.2). Thus, reported values for *other* copper-containing or organic molecules rely on computation to predict a *variation* from the reference compounds, not a first-principles reduction potential.



Specifically, using the reaction in eq S3 and $L = \text{BPhen}$, the absolute reduction potential for $\text{Cu}^{\text{II}}/\text{Cu}^{\text{I}}$ system was calculated to be 3.544 V at the M06-L/basis-II/SMD(nitromethane)//B3LYP-D3(BJ)/basis-I level of theory (298.15 K). Experimentally, the corresponding value versus the $\text{Fc}|\text{Fc}^+$ reference potential was determined to be -0.162 V. Thus, we have used $f(\text{Cu}) = (3.544 + 0.162)$ V = 3.706 V for computing reduction potentials of all copper-based complexes.

Similarly, the reaction in eq S4 was used to determine the correction factor, $f(\text{Org})$. The absolute reduction potential for the $\text{R}^+|\text{R}^\bullet$ couple ($R = \text{PhCHMe}$) was computed to be 4.477 V at 298.15 K, while the corresponding experimental value was determined to be -0.01 V.¹³⁷ Thus, we have used $f(\text{Org}) = (4.477 + 0.01)$ V = 4.487 V for computing reduction potentials of the other organic radicals. Note that in both cases, the correction factor f needs to be **subtracted** from the computed absolute reduction potential to obtain values relative to the $\text{Fc}|\text{Fc}^+$ reference.

Table 3.2 Calculated (vs $\text{Fc}^{0/+}$), and experimental (vs $\text{Fc}^{0/+}$) reduction potentials (V) of various species at 298.15 K using reaction schemes (eqs S3 and S4).

$f(\text{Cu}) = 3.706 \text{ V}$			
$[\text{LCu}^{\text{II}}(\text{N}_3)_2]_2$ Species	$E^\circ (\text{Cu}^{\text{II}} \text{Cu})^a$ absolute, V	$E^\circ (\text{Cu}^{\text{II}} \text{Cu})$ vs $\text{Fc}^{0/+}$, V	$E^\circ (\text{Cu}^{\text{II}} \text{Cu})$ [exp] vs $\text{Fc}^{0/+}$, V
$L = $ 	3.544	-0.162	-0.162 ^b
$L = $ 	3.482	-0.223	N.A.
$L = $ 	3.642	-0.063	N.A.
$f(\text{Org}) = 4.487 \text{ V}$			
R^+ Species	$E^\circ (R^+ R^{\bullet})^a$ absolute, V	$E^\circ (R^+ R^{\bullet})$ vs $\text{Fc}^{0/+}$, V	$E^\circ (R^+ R^{\bullet})$ [exp] vs $\text{Fc}^{0/+}$, V
	4.477	-0.01	-0.01 ^c
	4.254	-0.233	-0.22 ^c
	4.391	-0.096	N.A.

3.1.4.4 Thermodynamics of Radical Polar Crossover Pathway

Using the reduction potentials presented in Table 3.2, Gibbs free energy change (ΔG°) for the oxidation of the R^\bullet radical ($R = 1\text{-Naph}(\text{CH})\text{Me}$) by the Cu^{II} dimer yielding the R^+ cation can be calculated as follows:

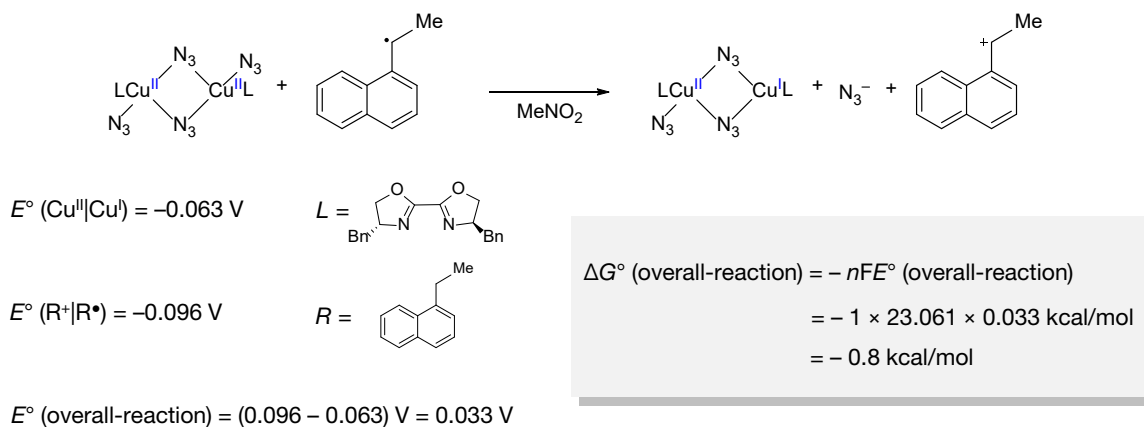


Figure 3.7 Derivation of Gibbs free energy change (ΔG°) for the oxidation of the 1-Naph-CH(\bullet)Me radical by the Cu^{II} -dimer yielding the corresponding benzylic cation. Reduction potentials were obtained from Table 3.2.

3.2 Copper-Catalyzed Benzylic Etherification via Radical Relay Enabled by Redox Buffering

3.2.1 Introduction

Medicinal chemistry efforts in the pharmaceutical industry rely on efficient synthetic methods to prepare molecules with diverse chemical structures and compositions. Coupling methods that unite molecular fragments from two large pools of substrates, such as amide coupling and palladium-catalyzed cross coupling, are among the most important and widely used reaction classes in this domain.^{138,139} The prevalent use of sp^2 -hybridized coupling partners (i.e., aryl, vinyl, acyl electrophiles), however, constrains the topological diversity of molecules that may be accessed and, in many cases, leads to molecules with less desirable physicochemical and other pharmaceutical properties. These limitations have contributed to a growing demand for cross-coupling methods involving sp^3 -hybridized carbon atoms to access molecules with more three-dimensional character.^{140,141}

$C(sp^3)$ -H bonds adjacent to aromatic and heteroaromatic rings are ubiquitous in key pharmacophores, and methods for selective cross coupling of benzylic C-H bonds and other versatile substrate partners (e.g., arylboronic acids, amines, alcohols, Figure 3.8(a)) could have a transformative influence on drug discovery. Such reactions would present a wealth of opportunities for elaboration of simple building blocks and pharmaceutical intermediates, as well as late-stage functionalization of drug molecules.¹⁴² The comparatively low bond strength of benzylic C-H bonds makes them intrinsically reactive and provides a potential basis for high site selectivity in complex molecules bearing many other C-H bonds. Benzylic sites are also notorious metabolic hot spots in pharmaceuticals, and their selective substitution has important pharmacological implications.¹⁴³

In recent years, a number of methods have been developed for intermolecular functionalization of $C(sp^3)$ -H bonds that show good site-selectivity, even in the absence of a directing group. Some of the most effective are those that replace the hydrogen atom of a C-H bond with a small fragment, for example, oxygenation,¹⁴⁴ amination,¹⁴⁵⁻¹⁴⁷ carbene insertion,¹⁴⁸ halogenation,^{149,150} and various pseudohalogenation reactions.¹⁵¹⁻¹⁵⁴ Complementary advances

have been made in methods for site-selective functionalization of low-cost feedstock molecules, such as alkylarenes,^{155,156} tetrahydrofuran,^{157,158} or simple hydrocarbons^{159–161} that use excess C–H substrate relative to the oxidant and/or functionalization reagent. Collectively, these precedents do not incorporate the characteristics typically associated with "cross coupling" reactions. The most effective cross-coupling methods, such as the Suzuki-Miyaura¹⁶² and Buchwald-Hartwig^{163,164} reactions, have a number of common traits: (a) the most valuable coupling partner is used as the limiting reagent, in ideal cases approaching a 1:1 stoichiometry of the two coupling partners, (b) both coupling partners draw from a diverse pool of readily (ideally commercially) available reagents, and (c) the reactions exhibit broad tolerance of the steric, electronic and functional-group properties of both coupling partners.

Benzyl ethers are prominent motifs in pharmaceuticals and bioactive molecules (Figure 3.8(b)). Alcohols represent an abundant class of building blocks that are widely used as partners in other coupling reactions, including classical methods, such as the Williamson ether synthesis,¹⁶⁵ in addition to modern catalytic methods.^{163–166} Precedents for the direct oxidative coupling of benzylic C–H bonds and alcohols, however, are confined to electron-rich arenes^{167–169} such as those capable of undergoing hydride transfer to DDQ (2,3-dichloro-5,6-dicyano-1,4-benzoquinone). C–H cleavage via hydrogen-atom transfer (HAT) should be much less sensitive to electronic effects relative to pathways initiated by electron or hydride transfer,¹⁷⁰ which directly generate cationic intermediates. Thus, we postulated that a "radical relay" strategy¹⁵¹ could provide the basis for selective, broad-scope cross coupling of benzylic C–H bonds and alcohols, using the C–H substrate as the limiting reagent (Figure 3.8(c)). This reaction could be initiated by Cu^I-mediated activation of an oxidant, such as *N*-fluorobenzenesulfonimide (NFSI), which generates an *N*-centered radical capable of promoting HAT from the benzylic C–H bond. The resulting Cu^{II} species is then available to mediate coupling of the benzylic radical with the alcohol coupling partner (Figure 3.8(c)). Here, we show¹²³ that radical-relay cross coupling of benzylic C–H bonds with alcohols is made possible by in situ reductive activation of the catalyst. The latter concept not only provides the basis for successful reactivity in the present reactions, but also sets the stage for development of other benzylic C–H cross-coupling methods.

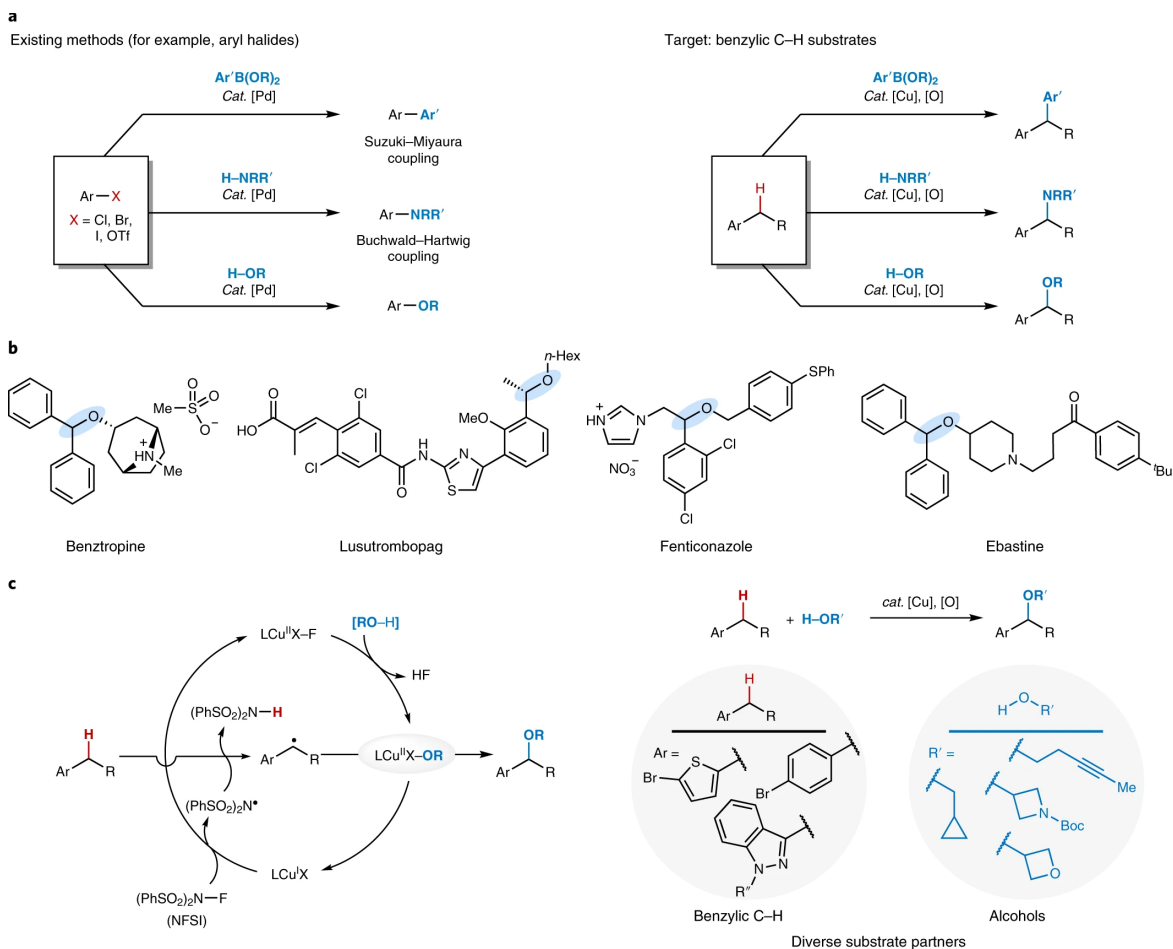


Figure 3.8 Cross-coupling reactions of benzylic C–H bonds and alcohols via a radical relay pathway. (a) Conceptual similarity between traditional cross-coupling reactions of aryl halides and the targeted benzylic C–H functionalization reactions. (b) Important examples of existing drug molecules containing benzylic ether moieties. (c) Proposed radical relay mechanism for benzylic C–H etherification enabling the coupling of two diverse pools of substrates. © Springer Nature

3.2.2 Results

3.2.2.1 Identifying the Redox Buffer Effect

Recent examples of radical relay Cyanation,¹⁵¹ arylation,¹⁷¹ and related functionalization of benzylic C–H bonds^{172–174} provided a starting point for this investigation. We anticipated that reaction conditions similar to these precedents could lead to effective benzylic etherification (Figure 3.9(a)). Attempted coupling of 4-ethylbiphenyl and methanol, however, led to negligible yield of the benzylic ether **4** with little conversion of the substrate or NFSI (Figure 3.9(a)). The good product yields observed from analogous cyanation and arylation reactions indicate that the coupling partner can have a major influence on the reaction outcome. We postulated that the

coupling partner could influence the reactive form of the Cu catalyst. Stoichiometric experiments probing the reaction of Cu^{II} with the different coupling partners revealed that TMSCN and ArB(OH)₂ induce rapid reduction of Cu^{II} to Cu^I, resulting in the formation of cyanogen¹⁷⁵ and biaryl.¹⁷⁶ In contrast, MeOH does not reduce Cu^{II} under these conditions (Figure 3.9(b)).

These observations indicate that the mechanism in Figure 3.8(c) is overly simplified and needs to be modified to explain successful reaction with certain coupling partners, but not with others. The modified mechanism in Figure 3.9(b) retains reaction of Cu^I (**A**) with NFSI to initiate catalysis. This step generates Cu^{II} (**B**) and a nitrogen-centered radical, •NSI (Figure 3.9(c), left cycle). The latter species can either undergo a productive reaction with the benzylic C–H bond, or it can react with a second equivalent of Cu^I, quenching the radical and forming a second Cu^{II} species (**B'**; Figure 3.9(c), right cycle). Experimental observations suggest that NFSI rapidly oxidizes all of the Cu^I to Cu^{II} when the reaction is initiated, but that certain coupling partners, such as TMSCN or ArB(OH)₂, are capable of reducing Cu^{II} to regenerate Cu^I during the course of the reaction (right cycle, red arrow). The Cu^I generated in this manner will react with NFSI to generate •NSI in the absence of a large pool of Cu^I, thereby supporting productive HAT from the benzylic substrate. MeOH does not readily reduce Cu^{II}, and the Cu catalyst will accumulate as a Cu^{II} species, such as **B** or **B'**. The inability of Cu^{II} to react with NFSI under such conditions will cause the reaction to stall. These mechanistic considerations suggested that a reductant could be identified as a "redox buffer", leading to controlled regeneration of Cu^I during the reaction. To test this hypothesis, several reductants were investigated as additives in the etherification reaction with MeOH, including phosphites, silanes, hydrazines, and sodium ascorbate. Promising reactivity was observed with dimethylphosphite [(MeO)₂P(O)H], and a representative time course of the reaction in Figure 3.9(d) illustrates the effect of this additive. In the absence of phosphite, the reaction proceeds to <10% conversion of 4-ethylbiphenyl, while inclusion of 0.5 equiv of (MeO)₂P(O)H leads to high conversion within 5 h at room temperature, generating the benzyl methyl ether in 52% yield (unoptimized). The latter reaction mixture exhibits a blue-green color (cf. Figure 3.9(b)), implicating a Cu^{II} catalyst resting state; however, the results are consistent with the ability of phosphite to serve as a redox buffer (Figure 3.9(c)).¹⁷⁷ This

hypothesis was probed further with a series of UV-visible and EPR experiments, in which reduction of Cu^{II} to Cu^I by dimethyl phosphite was clearly indicated.

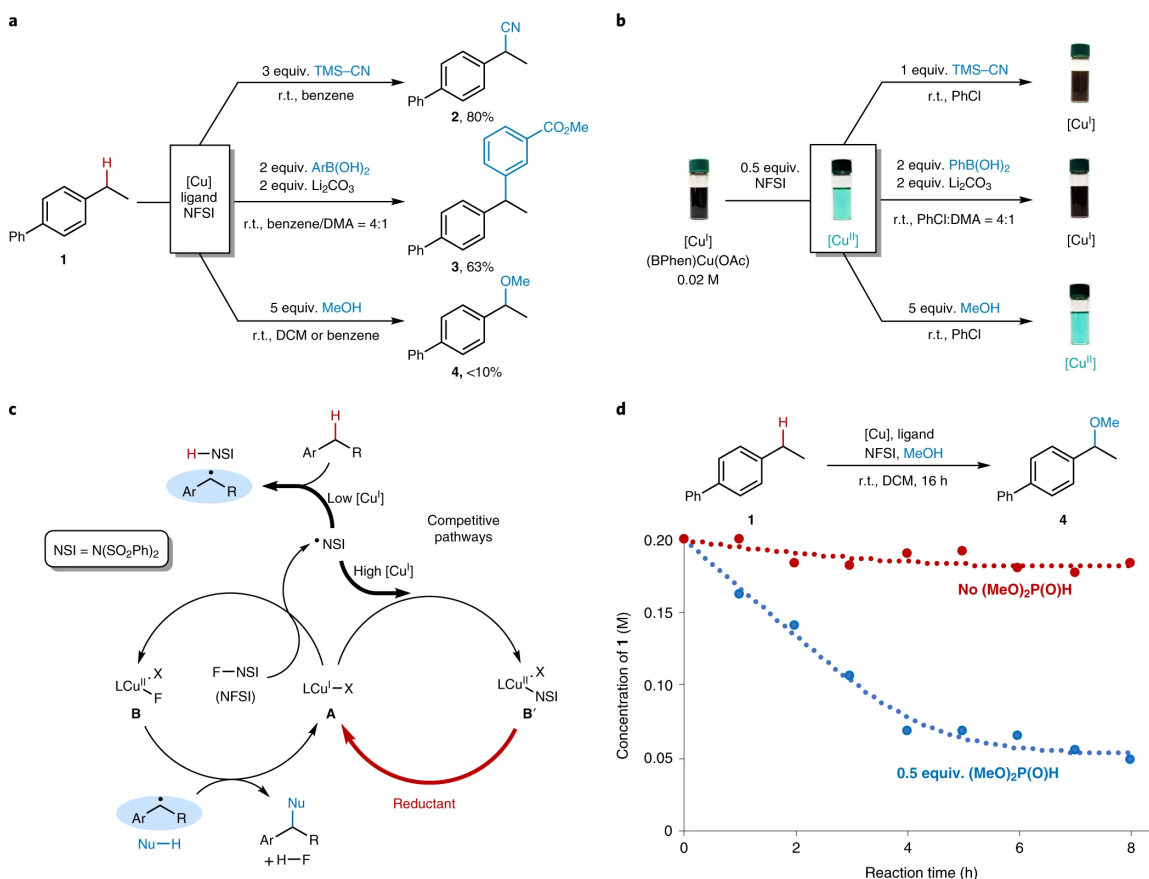


Figure 3.9 Cu-catalyzed benzylic C-H functionalization with NFSI as the oxidant. (a) Cu-catalyzed benzylic C-H functionalization reactions.^{151,171} (b) Changes in the Cu redox state between +1 (brown) and +2 (blue-green) upon addition of NFSI to a solution of the Cu^I catalyst precursor, followed by addition of cross-coupling partners. (c) Modified radical relay mechanism (cf. Figure 3.8(c)) to account for quenching of the •NSI by Cu^I and regeneration of Cu^I by a reducing substrate or additive. (d) Reaction time course for benzylic etherification conducted in the absence (red) and presence of 0.5 equiv. of dimethylphosphite (blue). Reaction conditions: 4-ethylbiphenyl (0.2 mmol), NFSI (0.4 mmol), MeOH (1.0 mmol), CuCl (0.02 mmol), 2,2'-bioxazoline (0.02 mmol), DCM (1 mL), room temperature. © Springer Nature

3.2.2.2 Reaction Development

These preliminary results provided the basis for further reaction optimization, and the oxidative coupling of ethylbenzene and methanol was tested with different solvents, ancillary ligands, Cu sources, and reaction temperatures. A number of monodentate and bidentate ligands were evaluated, and the unsubstituted 2,2'-bioxazoline (biox) ligand led to the best product yields. Use

of chiral ligand derivatives did not lead to enantioselectivity under these conditions (see below for further discussion).^{151,178} Inclusion of hexafluoroisopropanol (HFIP) as a co-solvent with dichloromethane (DCM:HFIP = 4:1) led to higher yields and significantly increased the reaction rate, allowing the reaction to proceed at lower temperature (40 °C). The activating effect of HFIP suggests that it may enhance the reactivity of the •NSI radical, for example, by hydrogen-bonding to the sulfonyl groups.¹⁷⁹ Under these conditions, reactions of ethylbenzene and 4-ethylbiphenyl, which are electronically similar, generated the 1-methoxyethylbenzene and 4-(1-methoxyethyl)biphenyl in 80% and 88% yield, respectively (Figure 3.10). Use of ethylarenes bearing electron-donating versus electron-withdrawing substituents exhibited variable results, with yields ranging from 10–67% (Figure 3.10, red bars); however, the modular nature of the reaction conditions enabled straightforward optimization of these yields by applying intuitive principles. For example, the electron-rich 4-methoxyethylbenzene is more reactive under the standard conditions and undergoes full conversion with the generation of considerable unidentified side products. Use of milder conditions, including removing the co-solvent HFIP (which enhances reactivity) and lowering the temperature from 40 °C to room temperature, led to formation of the desired product in 80% yield. Substrates bearing electron-withdrawing substituents are somewhat less reactive, as evident from incomplete conversion of the starting material under the original conditions. In these cases, the product yield was improved by raising the reaction temperature to 50 °C and/or increasing the Cu catalyst loading to 20 mol %. After applying these variations, the product yields ranged from 66–88%. Only the 4-cyano derivative, which is very electron deficient, retained a low yield (10%) after attempted optimization.

The good results obtained here with electronically differentiated substrates may be rationalized by the HAT C–H activation mechanism. Previous reports of benzylic etherification initiated by hydride or single-electron transfer directly generate cationic intermediates and are typically only effective for electron-rich substrates.^{167–169} Loss of a neutral hydrogen atom is much less susceptible to electronic effects.¹⁷⁰

The broad tolerance of arene electronic properties is complemented by nearly exclusive site selectivity for benzylic over tertiary C–H bonds. Isobutylbenzene and ibuprofen methyl ester have

been used previously to probe selectivity for benzylic versus tertiary C–H activation in photoredox-based azidation¹⁵⁰ and nitrene insertion^{146,180} reactions. Approximately 1:1 product ratios were observed in the reported reactions with these substrates (Figure 3.10(b)). Recognizing that the selectivity depends on the mechanism and reagent involved in the C–H cleavage step, we tested these substrates in the present oxidative coupling conditions with methanol. Exclusive reaction at the benzylic position was observed with both substrates (Figure 3.10(b)), affording 72% and 67% yield of the two methyl ethers, respectively. Complementary experiments with toluene, ethylbenzene, and cumene reveal preferential reactivity at secondary benzylic positions.

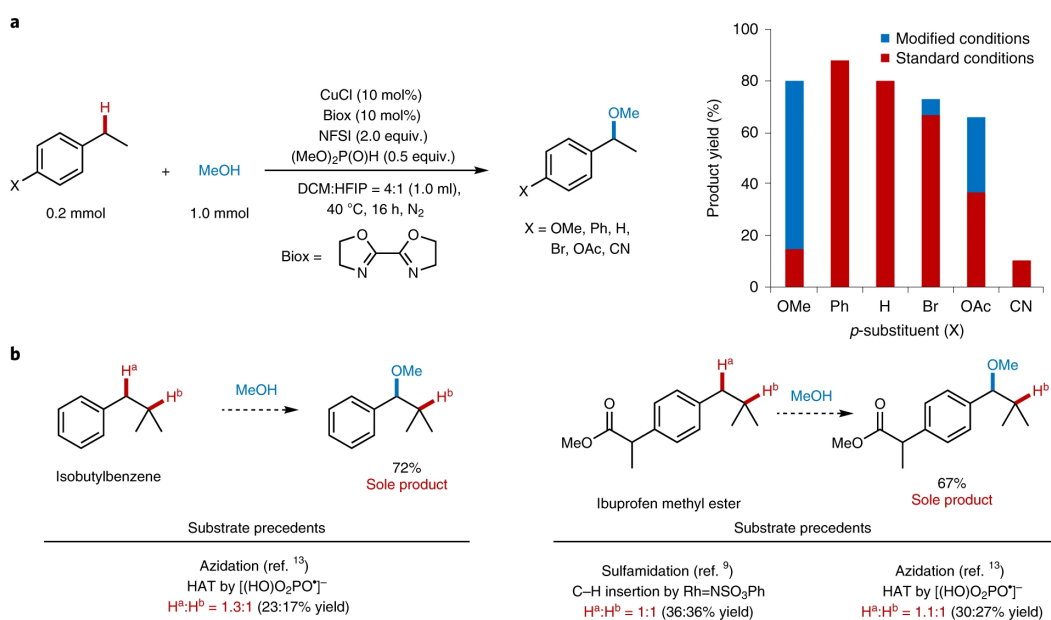


Figure 3.10 Electronic effects and site selectivity observed in the oxidative coupling of ethylarenes and methanol. (a) Results observed from the reaction under standard (red) and individually optimized (blue) conditions (¹H NMR yields with CH₂Br₂ as the internal standard. Modified conditions: X = OMe: 20 mol % Cu/biox in DCM at r.t.; X = Br: 5 mol % Cu/biox; X = OAc: 20 mol % Cu/biox at 50 °C. (b) Analysis of benzylic versus tertiary site selectivity observed in etherification of isobutylbenzene and ibuprofen methyl ester. © Springer Nature

3.2.2.3 Computational Analysis of the Proposed Mechanism

The catalytic mechanism proposed in Figure 3.9 was analyzed by density functional theory (DFT) methods to probe the energetics of individual reaction steps, with a particular focus on the competing pathways involving the •NSI and benzylic radical intermediates, and to gain further insights into C–O bond formation (Figure 3.11). The following computation methods were employed in this effort: M06-

L/basis-II/SMD($\epsilon = 10.6$)/B3LYP-D3(BJ)/basis-I/SMD($\epsilon = 10.6$) level of theory (basis-I = 6-31G(d,p) for non-metals and SDD basis and pseudopotential for Cu; basis-II = def2-TZVP for non-metals, def2-TZVP basis and SDD pseudopotential for Cu (see ref. 123 for details).

The reaction of NFSI with (biox)Cu^I(Cl) is computed to be highly favorable ($\Delta G^\circ = -15.2$ kcal/mol), generating •NSI and (biox)Cu^{II}(Cl)(F).¹⁸¹ Subsequent reaction of •NSI with a second equivalent of Cu^I is even more favorable ($\Delta G^\circ = -27.5$ kcal/mol), generating (biox)Cu^{II}(Cl)(NSI) (Figure 3.11, red pathway). This sequence is consistent with the experimental observations in Figure 3.9(b) which show rapid formation of Cu^{II} species upon addition of NFSI to solutions of Cu^I. We then evaluated the energetics of •NSI reactivity with the benzylic C–H bond of ethylbenzene. This HAT reaction, which forms a benzylic radical and H–NSI is also strongly favored ($\Delta G^\circ = -17.0$ kcal/mol) and exhibits an activation free energy (ΔG^\ddagger ; cf. **TS-2**) of +9.6 kcal/mol.

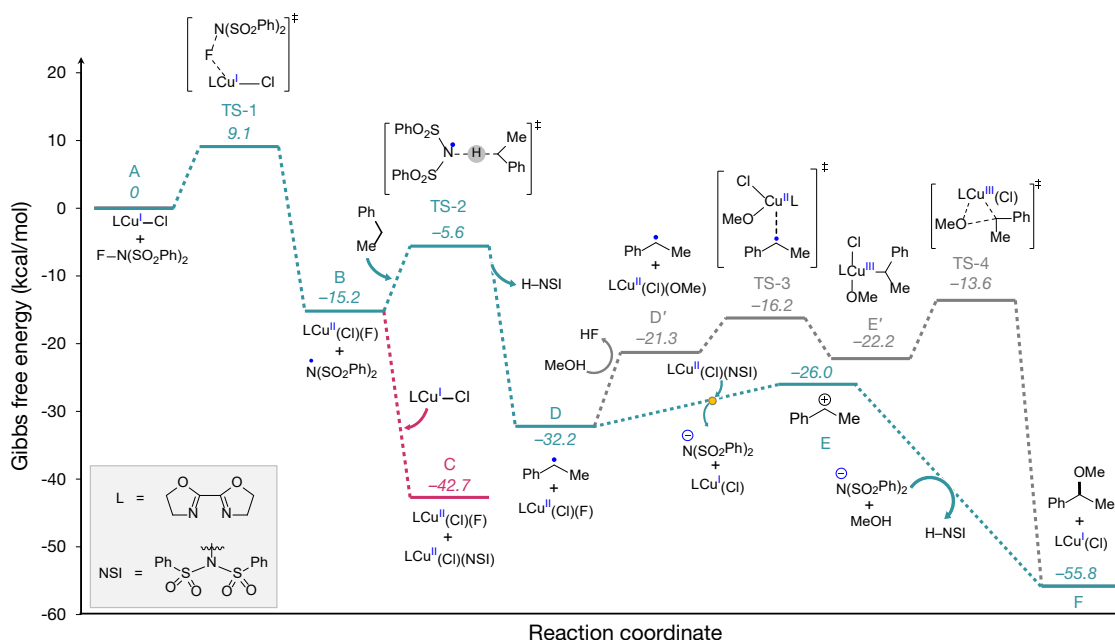


Figure 3.11 Calculated reaction pathways and energy landscape for (biox)Cu^I/NFSI-mediated methoxylation of ethylbenzene. (Gibbs free energies at 313.15 K; computed at M06-L/basis-II/SMD($\epsilon = 10.6$)/B3LYP-D3(BJ)/basis-I/SMD($\epsilon = 10.6$) level of theory).

Two possible pathways were considered for product formation. The first features benzylic radical addition to Cu^{II} and C–O bond formation via reductive elimination from an organocopper(III) intermediate (Figure 3.11, grey pathway), while the second features a radical-

polar crossover pathway^{182,183} in which C–O bond formation involves reaction of the alcohol with a benzylic cation (Figure 3.11, green pathway). The former pathway requires incorporation of a methoxide ligand into the Cu^{II} coordination sphere, and the calculations indicate that substitution of fluoride is favored over chloride. The resulting process, which affords (biox)Cu^{II}(Cl)(OMe) and HF, is endergonic ($\Delta G^\circ = +10.9$ kcal/mol). Addition of the benzylic radical to the Cu^{II} species proceeds with a small kinetic barrier (**TS-3**, $\Delta G^\ddagger = +5.1$ kcal/mol) to form the benzylcopper(III) species **E'** in a nearly ergoneutral process ($\Delta G^\circ = -0.9$ kcal/mol). Subsequent C–O reductive elimination yields the methoxylated product via **TS-4**, which represents the highest energy species along this pathway (+18.6 kcal/mol relative to **D**). The alternative pathway for C–O bond formation involves one-electron oxidation of the benzylic radical by (biox)Cu^{II}(Cl)(NSI) to afford a benzylic cation. This electron-transfer step is only moderately uphill (**E**, $\Delta G^\circ = +6.2$ kcal/mol), and the resulting cation can undergo a highly favorable reaction with methanol to produce the methoxylated product (**F**, $\Delta G^\circ = -29.8$ kcal/mol).

The organocopper(III) pathway aligns with the pathway proposed for Cu/NFSI-mediated cyanation of benzylic C–H bonds, which proceeds with high enantioselectivity.¹⁵¹ The computational results in Figure 3.11, however, favor the radical-polar crossover pathway for the etherification reaction, and this conclusion is further supported by several additional observations. The methoxylation reaction generates racemic products, even when chiral biox ligands are used. Deuterium kinetic isotope effect experiments conducted with PhEt and PhEt-*d*₁₀ reveal the presence of a small, but significant, primary KIE (competition experiment: KIE = 2.1; independent rate measurement: KIE = 1.7). These results are consistent with the radical-polar crossover pathway, which shows that the HAT step has the highest barrier. In contrast, C–O reductive elimination is calculated to be the rate-limiting step in the organocopper(III) pathway, and a negligible KIE is expected for this step.

For details regarding the “Synthetic scope and utility” of this method, see reference 123.

3.2.3 Conclusions

Collectively, these results demonstrate a new class of highly selective, non-directed C–H cross coupling reactions that create opportunities for efficient synthesis of novel molecules and diversification of chemical structures, ranging from simple aromatic and heteroaromatic building blocks to complex pharmacophores and existing drug molecules. Prominent features of these reactions include good product yields, the ability to use the benzylic substrate as the limiting reagent, high benzylic site selectivity, and access to a broad substrate scope with respect to both reaction partners. Mechanistic insights set the stage for these results by revealing that traditional reaction conditions lead to accumulation of the catalyst in an inactive Cu^{II} state, and the key breakthrough arose from identification of dialkylphosphites as effective in situ reductants that convert Cu^{II} into catalytically active Cu^{I} during the course of the reaction. Further mechanistic studies support a catalytic pathway involving radical-polar crossover initiated by HAT from the benzylic C–H site. This pathway is noteworthy because HAT exhibits a weak dependence on substrate electronic properties that allows for broad substrate scope, and the subsequent trapping of the benzylic cation by alcohols is similarly promiscuous, allowing for broad scope among alcohol coupling partners. Overall, it is likely that the "redox buffering" strategy will not be unique to this reaction class and allow for the discovery and development of other radical relay C–H cross-coupling methods with widespread impact and utility in medicinal chemistry and organic synthesis.

Chapter 4

X–H (X = C, O) Bond Activation

Using Biomimetic, High-Valent Copper(III) Complexes

Synopsis. Exploring C–H activation reactions in light hydrocarbons is of special interest as it has the potential to address challenges in fuel liquefaction. As possibly biomimetic species, small-molecule mononuclear copper(III) hydroxo-, peroxy-, and benzoate species have been shown to activate X–H (X = C, O) bonds. Such reactivity can be characterized as a hydrogen atom transfer (HAT) or a concerted proton-coupled electron transfer (cPCET). The distinction between these two mechanisms is important as they can have implications in the reaction rate: cPCET reactions are typically faster compared to HAT cases. This chapter demonstrates the use of state-of-the-art theoretical tools to distinguish these mechanisms for different reagent/substrate combinations and delineates the coupled nature of proton and electron transfer from the substrate to different copper-oxygen species which can be exploited for strategic tuning of reactivity and selectivity toward various substrate X–H (X = C, O) bonds.

4.1 Mechanisms for X–H (X = C, O) Bond Activation by Mononuclear Copper(III) Cores: HAT or cPCET?

4.1.1 Introduction

Copper is a key-element in several enzymes that oxidize a variety of organic substrates.¹⁸⁴ Exploiting such reactivity for the controlled oxidation of light hydrocarbons is of special interest as it has the potential to address challenges in fuel liquefaction.¹⁸⁵ Integral to understanding the reactivity of copper-based catalysts is the identification of reactive intermediates involved in the oxidative process.¹⁸⁶ Towards this end, mononuclear, formally Cu(III) cores supported by a tridentate dianionic ligand (*N,N'*-bis(2,6-diisopropylphenyl)-2,6-pyridinedicarboxamide, L²⁻)^{186c,187} and derivatives¹⁸⁸ have been prepared as possible synthetic analogs of various putative copper-oxygen enzyme intermediates. The reactivity of selected [LCu(III)–Y] species (Y = OH, **401**; Y = OOCm, **402**; Cm = cumyl/*α,α*-dimethylbenzyl; Figure 4.1) for hydrogen-atom abstraction (HAA) involving substrate X–H (X = C, O) bonds has been studied. For instance, **401** undergoes rapid HAA from substrates with weak C/O–H bonds,^{187b,c} while **402** exhibits more limited reactivity towards similar substrates.^{187d,e} Such differential reactivities dependent on the reactive ligand Y prompted us to explore in further detail how varying Y influences HAA reactions.

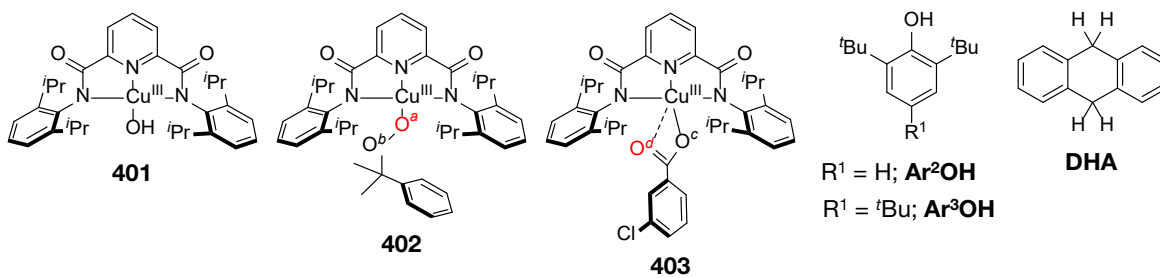


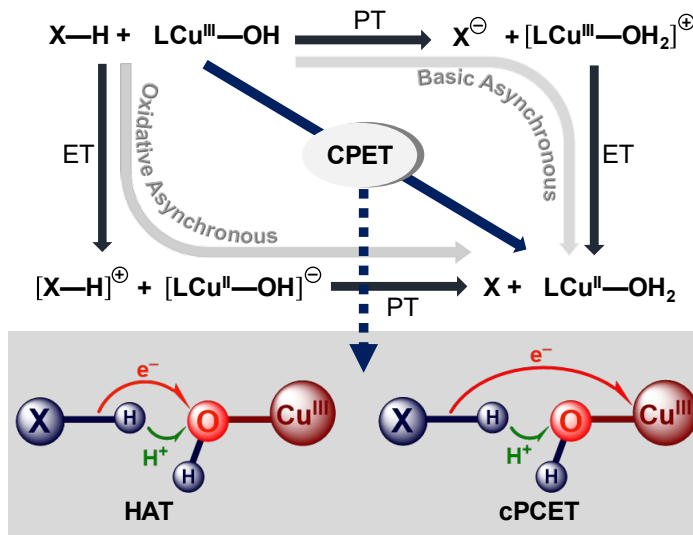
Figure 4.1. Two organic substrates, DHA and ArⁿOH ($n = 2$ in theoretical studies, $n = 3$ in experimental studies), used in this study together with three [LCu(III)–Y] complexes. The *α,α*-dimethylbenzyl group in **402** is abbreviated as “Cm” and the *meta*-chlorophenyl group in **403** is referred to as “Ar¹”. © American Chemical Society

Transition-metal carboxylates are an additional class of compounds known for C–H bond functionalization.¹⁸⁹ Use of formally Cu(III)-carboxylates for this purpose, however, is unprecedented.¹⁹⁰ We report here the synthesis of a [Cu(III)–O₂CAr¹]²⁺ core, **3**, (Ar¹ = *meta*-chlorophenyl), supported by the same L²⁻ ligand as in **401** and **402**. We systematically compare

the HAA reactivities of **401**, **402**, and **403**, towards the weak C–H bond in 9,10-dihydroanthracene (DHA) and the O–H bond in 2,4,6-tri-*tert*-butylphenol (Ar³OH). We also apply a suite of computational techniques to gain insight into the underlying mechanistic details of these various HAA processes involving DHA and 2,6-di-*tert*-butylphenol (Ar²OH, which removes the para *t*-butyl group of Ar³OH for computational convenience).

X–H bond activation by a [Cu(III)–Y]²⁺ core formally involves the net transfer of both a proton (H⁺) and an electron (e⁻), i.e., the net transfer of a hydrogen atom. The mechanistic details with respect to “how” these transfers occur, however, can be complex, and a detailed understanding of reactivity and selectivity is critical if principles are sought for the design of new systems having tailored reactivity. Mechanistic behavior can, in principle, span a continuum of character, but discussion in terms of extremes offers heuristic value. Thus, one pair of contrasting limits for proton-coupled electron transfer involves (a) a *concerted* proton and electron transfer (CPET) process,¹⁹¹ in which the electron and the proton are transferred in a single elementary step and (b) a *step-wise* process that includes the generation of a (reactive) intermediate: either proton transfer first, followed by electron transfer (PT/ET), or vice versa (ET/PT).¹⁹²

Scheme 4.1. Stepwise (ET/PT or PT/ET) vs. CPET pathways for X–H bond activation by a representative Cu(III) species (**401**). Two key variations of CPET reaction, namely HAT and cPCET are also shown. © American Chemical Society



CPET reactions themselves can also be discussed in terms of extremes, namely: (a) hydrogen-atom transfer (HAT) and (b) concerted proton-coupled electron transfer (cPCET). The

nomenclature HAT generally describes CPET reactions where the electron and proton travel “together” between the same donor/acceptor sites, whereas the term cPCET is used to describe cases where the proton and electron are transferred in a single elementary step but they transfer between different donor and acceptor sites (Scheme 4.1).¹⁹²⁻¹⁹⁵ Distinction of a cPCET reaction coordinate can also be made with regards to how closely the *concerted* reaction approaches the limiting step-wise paths (Scheme 4.1, edges) and invokes “asynchronicity” in e⁻/H⁺ transfer.^{193,194b} Accordingly, concerted asynchronous HAA reactions displaying a more PT-like character in the transition-state is referred to as a *basic* asynchronous cPCET mechanism, while those having a more ET-like character is usually designated as being *oxidatively* asynchronous.^{196,197a}

HAA reactions following a CPET pathway avoid the formation of possible high-energy intermediates associated with elementary ET or PT,¹⁹² but within the paradigm of CPET itself, it remains non-trivial to distinguish HAT from cPCET mechanisms, because both proceed as elementary processes with identical reactants and products.¹⁹⁸ In this regard, modern computational techniques can be powerful tools for characterization of a CPET reaction coordinate.^{195,197,199} In this work, we apply multiple such diagnostic models to reveal that both HAT and cPCET mechanisms are associated with X–H bond (X = C, O) activation by [Cu(III)–Y]²⁺ cores, with the particular mechanism varying as a function of the reactive ligand Y and the nature of the X–H substrate itself.

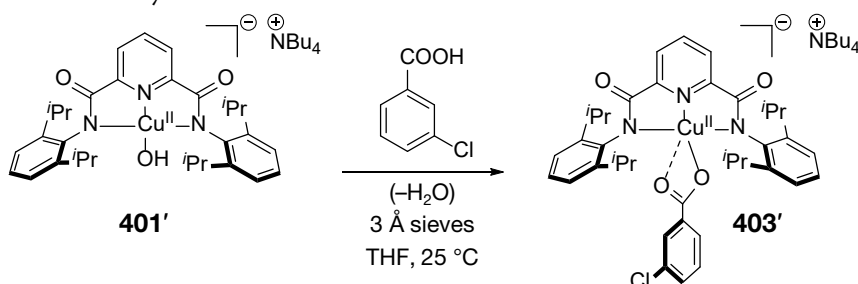
4.1.2 Experimental Results

4.1.2.1 Synthesis and Characterization of LCu(III)O₂CAr¹.

Reaction of a solution of [NBu₄][LCu(II)OH]^{187a} (**401'**) in tetrahydrofuran (THF) with *meta*-chlorobenzoic acid in the presence of 3 Å molecular sieves yielded teal-green [NBu₄][LCu(II)O₂CAr¹] (**403'**) (Scheme 4.2). The X-ray structure (X-ray crystallography performed on an analogous NEt₄⁺ salt) revealed a four-coordinate copper center with a distorted square-planar geometry (geometry index, $\tau_4 = 0.19$; Figure 4.2).²⁰⁰ The ⁻O₂CAr¹ moiety is bound via one oxygen atom in the equatorial position at a short distance (1.929(3) Å) and via the second oxygen in the axial position at a longer distance (2.516(3) Å). Disregarding the latter weak interaction, the overall geometry and Cu–N distances for **403'** are similar to those of **401'** and

$[\text{NBu}_4][\text{LCu(II)OOCm}]$, **402'**.^{187d} However, the Cu–O distance is ~ 0.1 Å longer in **403'** than in **401'** and **402'**, perhaps due to charge delocalization in the carboxylate moiety.

Scheme 4.2. Synthesis of $[\text{NBu}_4][\text{LCu(II)O}_2\text{CAr}^1]$, **403'**, starting from $[\text{NBu}_4][\text{LCu(II)OH}]$, **401'**. © American Chemical Society



Cyclic voltammetry measurements were performed with **403'** in THF at 25 °C, where a reversible process was observed having half wave potential, $E_{1/2} = 0.228$ V vs. Fc/Fc^+ . This redox couple is ~ 0.3 V higher than previously reported $\text{LCu}^{\text{II}}/\text{LCu}^{\text{III}}$ redox couples supported by anionic ligands (**401'**/**401'**^{187a,c} = -0.074 V vs. Fc/Fc^+ ; **402'**/**402'**^{187d} = -0.154 V vs. Fc/Fc^+) and ~ 0.5 V lower than for $[\text{LCu}^{\text{II}}(\text{THF})]^{+0}$ (0.735 V vs. Fc/Fc^+) that features a neutral THF ligand.^{187c} These results suggest that a stronger oxidant than those used for **401'** or **402'** is required to generate **403** chemically, and we chose acetyl ferrocenium tetrakis(3,5-bis(trifluoromethyl)-phenyl)borate, $[\text{AcFc}][\text{BAr}^{\text{F}}_4]$, which has $E_{1/2} = 0.270$ V vs. Fc/Fc^+ in CH_2Cl_2 .²⁰¹

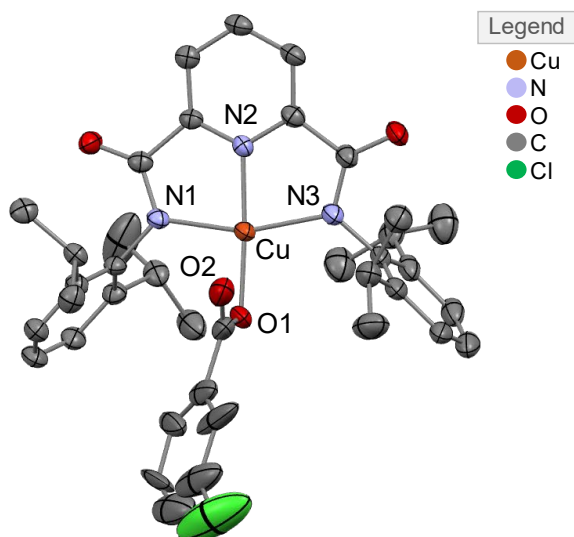


Figure 4.2 X-ray crystal structure of anionic **403'** with the NEt_4 cation and H atoms omitted for clarity.

UV-Vis spectroscopy was used to monitor the one-electron oxidation of **403'** by $[\text{AcFc}][\text{BAr}^{\text{F}}_4]$. Upon addition of the oxidant at $-80\text{ }^\circ\text{C}$ in THF, two major features appeared. The growth of these features maximized after one equivalent of $[\text{AcFc}][\text{BAr}^{\text{F}}_4]$ had been added. The final spectrum of the intense blue solution contains a shoulder at 491 nm ($\epsilon = 5,000\text{ M}^{-1}\text{ cm}^{-1}$) and features at 650 nm ($\epsilon = 13,000\text{ M}^{-1}\text{ cm}^{-1}$) and 830 nm ($\epsilon = 10,500\text{ M}^{-1}\text{ cm}^{-1}$). While the observation of these spectral features is clearly indicative of formation of a formally Cu(III) complex (**403**),^{187a-d,188} the transitions themselves are significantly red-shifted compared to those observed for **401** (540 nm, $\epsilon = 11,500\text{ M}^{-1}\text{ cm}^{-1}$) and **402** (507 nm, $\epsilon = 13,000\text{ M}^{-1}\text{ cm}^{-1}$; 578 nm, $\epsilon = 12,000\text{ M}^{-1}\text{ cm}^{-1}$; 690 nm, $\epsilon = 9,000\text{ M}^{-1}\text{ cm}^{-1}$).¹⁸⁷ The oxidation of **403'** is chemically reversible at $-80\text{ }^\circ\text{C}$ in THF, as evident from the experiments using repeated additions of oxidant ($[\text{AcFc}][\text{BAr}^{\text{F}}_4]$) and reductant (Fc^*). Further corroborating the formulation of **403**, the oxidized solution is EPR silent. Once generated, **403** is sufficiently stable at $-80\text{ }^\circ\text{C}$ to perform reactivity studies, but decays slowly via an ill-defined process ($t_{1/2} \sim 40\text{ min}$).

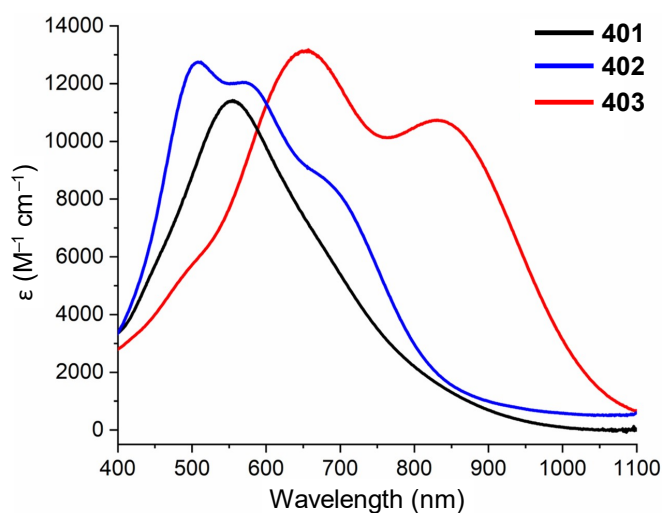


Figure 4.3. Overlay of UV-Vis spectra of LCu(III)OH (**401**, black), LCu(III)OOCm (**402**, blue) and $\text{LCu(III)O}_2\text{CAr}^1$ (**403**, red), in THF at $-80\text{ }^\circ\text{C}$. © American Chemical Society

4.1.2.2 Experimental Reactivity Studies.

The reactions of THF solutions of **401** and **403** (0.1 mM, both generated with 1 equiv $[\text{AcFc}][\text{BAr}^{\text{F}}_4]$) with excess (50 equiv) Ar^3OH (O–H bond-dissociation free energy, BDFE = 77.1 kcal mol⁻¹)¹⁹² at $-80\text{ }^\circ\text{C}$ were compared.²⁰² Consumption of **401** and **403** was indicated by decay of their UV-Vis features; no such reaction was observed in the previous investigation of **402**.^{187d}

Analysis of the product solutions after reactions of both **401** and **403** with Ar³OH by EPR spectroscopy revealed a signal at $g \sim 2$ assigned to Ar³O[•] (~80% yield for **401**^{187b}, ~20% yield for **403**, a low yield for which we have no clear explanation).²⁰³ In addition to the organic radical, UV-Vis data support formation of a Cu(II) species we tentatively assign as LCu(II)(THF) on the basis of comparison to previously reported data.^{187c} The kinetics for the reactions were followed by monitoring the decay of the reactant UV-Vis spectral features. The resulting data were fit globally using a second order reaction model via ReactLab KINETICS;²⁰⁴ the resulting rate constants shown in Table 4.1 are averages of triplicate measurements. The reaction of Ar³OH with **403** ($k_2 = 3(1) \times 10^{-1} \text{ M}^{-1} \text{ s}^{-1}$) was two orders of magnitude slower than with **401** ($k_2 = 2(1) \times 10^1 \text{ M}^{-1} \text{ s}^{-1}$) under the same reaction conditions. We explore possible rationales for this difference via theory below.

Table 4.1 Experimental second order rate constants (k_2 , $\text{M}^{-1} \text{ s}^{-1}$) for HAA from Ar³OH^a and DHA^b with complexes **401–403**.

species	Ar ³ OH	DHA
401	$2(1) \times 10^1$	$4.2(9) \times 10^1$
402	<i>no rxn.</i>	<i>no rxn.</i>
403	$3(1) \times 10^{-1}$	$1.1(4) \times 10^{-1}$

^a Measured at $-80 \text{ }^\circ\text{C}$ in THF. ^b Measured at $-25 \text{ }^\circ\text{C}$ in 1,2-DFB.

The reactivity of **403** with C–H bonds was also explored by examining the kinetics of reactions with DHA (BDFE = 76 kcal mol⁻¹).¹⁹² No reaction was observed in the previous investigation of **402** with 200 equiv DHA at $-25 \text{ }^\circ\text{C}$ in 1,2-difluorobenzene (1,2-DFB).^{187d} Upon treatment of **403** with excess DHA (200 equiv) at $-80 \text{ }^\circ\text{C}$ in THF, no enhancement of the rate of decay of **403** was observed. We then prepared **401** and **403** at higher temperature ($-25 \text{ }^\circ\text{C}$) in 1,2-DFB, a solvent that is less susceptible than THF to attack by **401** at that temperature. The UV-Vis spectrum of **403** in 1,2-DFB at $-25 \text{ }^\circ\text{C}$ (prepared with 1 equiv [AcFc][BAr^F₄], $t_{1/2} \sim 20$ min) revealed slightly red-shifted features (two major features appearing at 670 and 850 nm, respectively) compared to the analogous spectrum in THF. Treatment of the DFB solution of **403** with DHA (200 equiv) at $-25 \text{ }^\circ\text{C}$ revealed a sluggish decay of the reactant UV-Vis features and the growth of features due to anthracene (358 and 378 nm);²⁰⁵ in a similar experiment using 10 equiv

DHA, 0.6 equiv of anthracene was identified after workup and GC/MS analysis. The kinetic data were fit to a second order rate law, yielding $k_2 = 1.1(4) \times 10^{-1} \text{ M}^{-1} \text{ s}^{-1}$ (Table 4.1).²⁰⁶ The reaction of **401** with DHA under the same conditions revealed $k_2 = 4.2(9) \times 10^1 \text{ M}^{-1} \text{ s}^{-1}$, which is within error of the previously reported value.^{187c} Thus, the rate of reaction of **403** with DHA is ~ 2 orders of magnitude slower than that of **401**. In summary, distinct differences in the rates of reactions of **401**, **402** and **403** with Ar³OH and DHA were observed. Overall, **401** reacts the fastest in the presence of O–H or C–H bonds, followed by **403**, which is followed by unreactive **402**.

4.1.3 Computational Results

4.1.3.1 Computed Spectra

TD-DFT calculations were carried out for all three compounds **401–403** at the PBE0-D3(BJ)/basis-III/SMD(THF) level of theory on the B3LYP/basis-I optimized geometries to better understand the experimentally observed UV-Vis spectral features. A qualitative picture of the electronic transitions was obtained by examining the KS orbitals, which, as Stowasser and Hoffmann have pointed out, are a good basis for qualitative interpretation of molecular orbitals and moreover have energy orderings consistent with more rigorous levels of theory.²⁰⁷ Accordingly, the calculations indicated that the *N*-arylamide functionality of the L²⁻ ligand should be viewed as an extended π system with Lewis basicity concentrated in distinct regions, namely, the amide π -system and the aryl π -clouds (cf. the HOMO–5 and HOMO of **403**, Figure 4.4). In every case, calculations suggest that pairs of low energy excitations into the lowest unoccupied molecular orbital (LUMO), which includes substantial Cu $d_{x^2-y^2}$ amplitude (Figure 4.4), are best described as ligand-to-metal charge transfer (LMCT) but coming as *combinations* from these two portions of the ligand, with varying degrees of aryl π versus amide π depending on the specific excitation. With respect to the red-shifted features for the benzoate case, this is entirely consistent with the more positive standard reduction potential for **403** ($E_{1/2} = 228 \text{ mV}$ vs. Fc/Fc⁺) compared to that of **401** and **402** (-74 mV and -154 mV vs. Fc/Fc⁺, respectively).¹⁸⁷ Put differently, the Cu atom in **403** is more electrophilic, which is manifested in the orbital energies for **401** compared to **403**: the HOMO energies are similar (within 0.07 eV), but the LUMO in **403** is much lower in energy (by ~0.40 eV), leading to the observed redshift (Table 4.2).

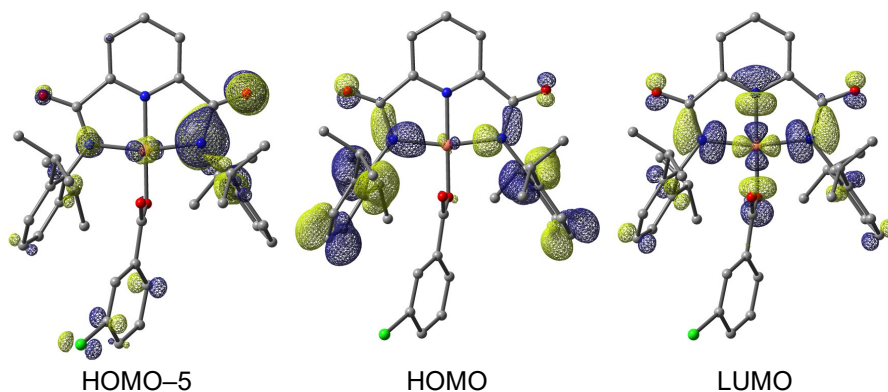


Figure 4.4. Spectroscopically relevant highest occupied molecular orbital (HOMO) and HOMO-5, together with the lowest unoccupied molecular orbital (LUMO) for complex **403**. © American Chemical Society

Table 4.2. Most intense molecular excitation energies computed^a for different Cu(III) complexes. Experimental excitation energies are provided in parentheses for comparison.

species	orbital energy (eV)		excitation energies (eV)
	HOMO	LUMO	
401	-6.49	-3.59	2.24 (2.30)
402	-6.36	-3.72	1.78 (1.76), 2.06 (2.14), 2.80 (2.48)
403	-6.42	-3.99	1.63 (1.49), 1.90 (1.91), 2.65 (2.53)

^aTD-DFT calculations performed at PBE0-D3(BJ)/basis-III/SMD(THF)//B3LYP-D3(BJ)/basis-I level of theory.

4.1.3.2 Unraveling Reactive Sites for HAA.

For complex **401**, there is no ambiguity that the hydrogen atom from the substrate is transferred to the O-atom of the -OH functionality. For **402**, by contrast, both the O-atom of the peroxy-moiety proximal to Cu (O^a) as well as the O-atom bonded to the cumyl benzylic position (O^b) may in principle be active (Figure 4.1). Similarly, for **403**, HAA can occur at the carboxylate oxygen proximal to Cu (O^c) or at the more distal carbonyl O-atom (O^d) (Figure 4.1). To determine the active sites for HAA, we have characterized the reactivity at all four of these sites.

For **402**, O^a is clearly the preferred site for HAA: computed activation free energies are lower by ~13 kcal/mol for Ar²OH and ~6 kcal/mol for DHA compared to site O^b (Table 4.3). This trend is consistent with what would be expected based on alternative Cu-based product stabilities, i.e., a copper-coordinated cumyl hydroperoxide versus a copper-oxo-coordinate cumyl alcohol, and indeed, the overall free energies of reaction (ΔG°) for the **402**/DHA pair are computed to be 3.9

and 18.6 kcal/mol at sites O^a and O^b, respectively (Figure 4.9). On the contrary, HAA in **403** takes place preferentially at the distal site O^d, with free energies of activation lower by 8.7 and 4.5 kcal/mol for Ar²OH and DHA, respectively, compared to reactivity at O^c (Table 4.3). This preference may also be attributed to product stability, with reaction at O^d leading to coordination of the more Lewis basic carbonyl of the product carboxylic acid to copper (Figure 4.9 and Figure 4.10), but there may certainly also be some degree of steric influence (O^d being more accessible), particularly with the bulkier Ar²OH substrate.

Table 4.3 Free energies of activation (ΔG^\ddagger , kcal/mol) calculated for different reactive sites O^a, O^b, O^c, or O^d with Ar²OH and DHA substrates.[§]

species	Ar ² OH	DHA
	ΔG_{193}^\ddagger	ΔG_{248}^\ddagger
402 (O ^a)	8.0	16.8
402 (O ^b)	21.2	23.2
403 (O ^c)	11.6	19.0
403 (O ^d)	2.9	14.5

[§]SMD(solvent)/B3LYP-D3(BJ)/basis-II//B3LYP-D3(BJ)/basis-I at 193.15 K for Ar²OH and 248.15 K for DHA.

4.1.3.3 Comparative Reactivity with Ar²OH and DHA.

Considering only lowest energy pathways, the calculated free energies of activation for **401–403** reacting with substrates Ar²OH and DHA are presented in Table 4.4. For both substrates, we compute the reactivity order to be **401**>**403**>**402**, which agrees with the experimentally observed trends (see Table 4.1 for comparison). Greater basicity of the hydroxyl group in **401** that results in a strong O–H BDFE in the product Cu(II) aqua complex and thus a strong thermodynamic driving force plays a key role towards its highest reactivity. As the basicity of a carboxylate is low, the (perhaps surprisingly) higher reactivity of **403** than that of **402** can be attributed to its better oxidizing power as gauged by their respective $E_{1/2}$ values. Moreover, as discussed in more detail below, the higher reactivity of **403** may also be ascribed to a significant asynchronicity along the proton and electron transfer coordinates, since asynchronous transfer of H⁺/e⁻, together with other competing factors, has been demonstrated²⁰⁸ to lower HAA activation barriers in other circumstances.

Table 4.4 Computed[§] free energies of activation (ΔG^\ddagger , kcal/mol) for HAA from Ar²OH and DHA with complexes **401–403**.

species	Ar ² OH	DHA
	ΔG_{193}^\ddagger	ΔG_{248}^\ddagger
401	2.6	7.0
402 (O ^a)	8.0	16.8
403 (O ^d)	2.9	14.5

[§]SMD(solvent)/B3LYP-D3(BJ)/basis-II//B3LYP-D3(BJ)/basis-I level of theory at 193.15 K for Ar²OH and at 248.15 K for DHA.

4.1.3.4 Mechanistic Diagnostics: Component of Dipole Moment Along the IRC.

Having demonstrated a good correspondence between computed free energies of activation and experimentally measured rate constants, we may proceed to analyze the evolving electronic structures of the reacting partners along their respective reaction coordinates in order to better characterize the nature of the various reactions. As discussed above, in a cPCET process, the proton and electron travel between different donor/acceptor sites. Given the opposite charges of these particles, varying degrees of separation must affect the overall dipole moment, and in particular the component of the dipole moment projected on the reaction coordinate vector, i.e., the X–H–Y axis.^{199a} For an HAT mechanism, however, only a very small change in the projected dipole moment would be expected as the separation of the electron from the proton is never large.¹⁹⁹ Note that by focusing on the projection of the dipole moment onto the reaction coordinate (and its variation), quantitatively complicating factors associated with the magnitude and relative alignment of the *overall* dipole moment with the reaction coordinate are eliminated.

Evolutions of the relevant components of the dipole moment along the reaction coordinate for HAA from Ar²OH and DHA with complexes **401–403** are shown in Figure 4.5. The changes in the projected dipole moment for reactions of **401–403** with Ar²OH (solid lines) range from 6 to nearly 25 D, consistent with the polar character of the O–H bonds involved and a cPCET process. By contrast, for **401** and **402**, HAA from DHA (dashed lines) proceeds with changes in the projected dipole moment of less than 5 D, consistent with a more ‘true’ HAT process. Results for **403**, however, are in striking contrast to those for **401** and **402**: The change in the projected dipole moment for reaction with DHA is almost identical to that for reaction with Ar²OH. This

suggests a clear change in mechanism for HAA from DHA across the three [LCu(III)–Y] species: For Y=OH and OOCm an HAT pathway is followed, while for Y=O₂CAr¹ the mechanism is cPCET.

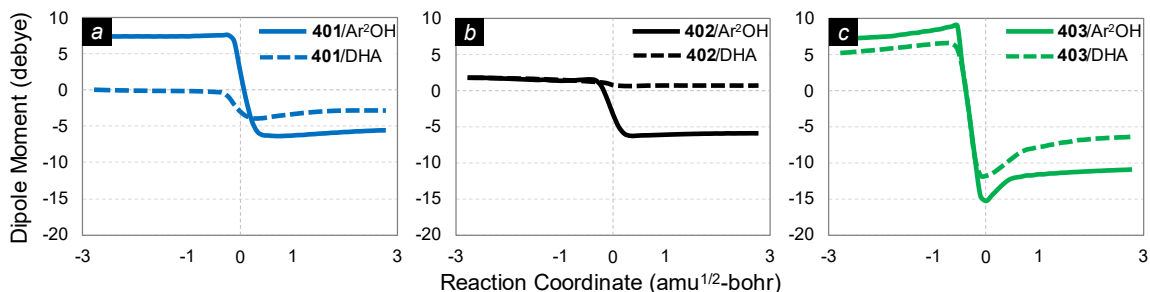


Figure 4.5. Evolution of the total dipole moment vector (Hirshfeld) projected along the axis of H-atom abstraction. (a), (b), and (c) corresponds to HAA reactivity of complexes **401** (blue), **402** (black), and **403** (green) respectively. Solid lines are used for the Ar²OH substrate, while dashed lines represent the DHA substrate. © American Chemical Society

4.1.3.5 Mechanistic Diagnostics: Intrinsic Bond Orbital Analysis.

In order to further characterize the HAA mechanism, we have employed the IBO localization scheme of Knizia and coworkers.^{195,209} It has been demonstrated that changes in IBOs along a given reaction coordinate closely track the ‘curly arrows’ generally used to explain bond-making/bond-breaking reaction mechanisms and, in the particular case of HAA reactions, for analyzing the nuances of HAT versus cPCET.^{195,210} Illustrative examples are shown in Figure 4.6, where evolutions of IBOs for α - and β -electrons of X–H bond along the intrinsic reaction coordinate have been carefully assessed to understand relevant charge flow. Figure 4.6(a-c) shows evolution of the IBOs for the activated C–H bond during HAA from DHA by **401**. In this simplest case, it is clear that along the reaction coordinate, the α -IBO (Figure 4.6(b), purple lobe) transforms from a C–H bond in DHA to an O–H bond in [LCu(II)–OH₂] as the electron follows the proton, while the β -IBO (Figure 4.6(c), green lobe) evolves from being a C–H bond to a semi-localized radical on the monohydroanthracene product. This electronic redistribution exemplifies a ‘true’ HAT mechanism as shown in Figure 4.7(a).

A similar analysis for the reaction of **401** with Ar²OH is shown in Figure 4.6(d-f). Evolution of the β -IBO of the O–H bond is shown in Figure 4.6(e), and the corresponding α -IBO evolves almost identically. Since *both* the α - and β -IBOs of the original O–H bond remain on the aryloxy

substrate along the H-coordinate, the electron transfer must take place from another IBO to complete the overall HAA (recalling that this is a concerted reaction). As shown in Figure 4.6(f), in the vicinity of the TS-geometry, it is a β -IBO of the aryl π -cloud of Ar²OH that evolves into a copper $d_{x^2-y^2}$ orbital. As the transfer of the proton and electron involve different donor/acceptor centers, this process is best described as a cPCET pathway, as indicated with curly arrows in Figure 4.7(b).

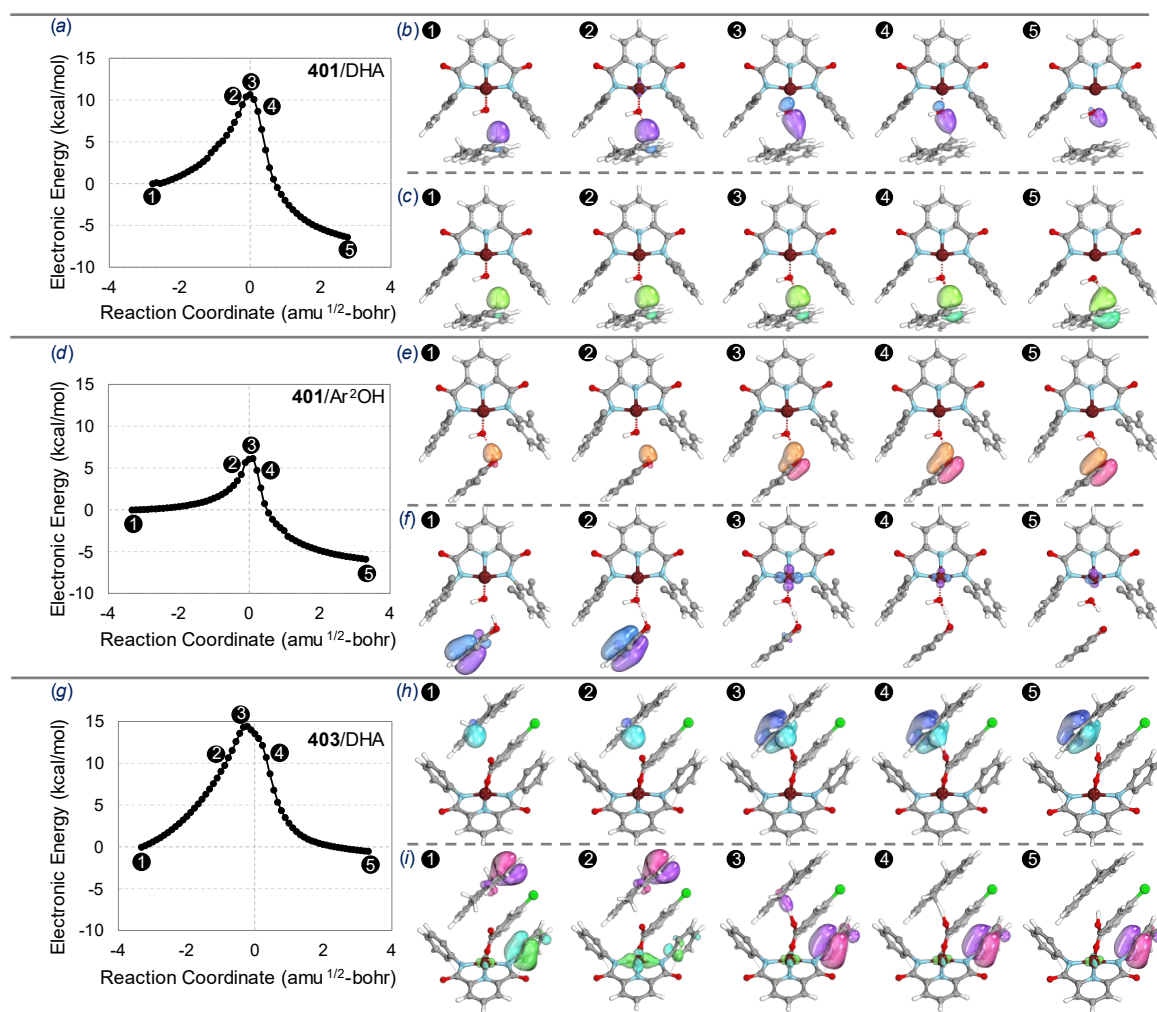


Figure 4.6. Plots of the change in electronic energies (computed at UB3LYP-D3(BJ)/basis-I level) along the intrinsic reaction coordinate (IRC/amu^{1/2}-bohr) for (a) **401/DHA**, (d) **401/Ar²OH** and (g) **403/DHA** pairs. Intrinsic bond orbital (IBO) transformations of the C–H bond along the IRC are shown in (b) purple (α -IBO) and (c) green (β -IBO). Changes in the O–H β -IBO for **401/Ar²OH** are shown in (e), while (f) shows changes in the β -IBO of the π -electron density of the aryl ring that eventually ends up on the Cu-atom. Transformation of the C–H β -IBO for **403/DHA** is presented in (h), which again stays on the DHA moiety. Changes in two β -IBOs corresponding to the π -density of DHA (blue-green) and that

of diisopropylphenyl moiety of the ligand (pink-orange) are represented simultaneously in (i). IBO transformations indicate that the density on DHA is transferred to the Cu-center through a ligand-assisted pathway. In all cases, isopropyl groups of the ligand and tert-butyl groups of the Ar²OH substrate are omitted for clarity. © American Chemical Society

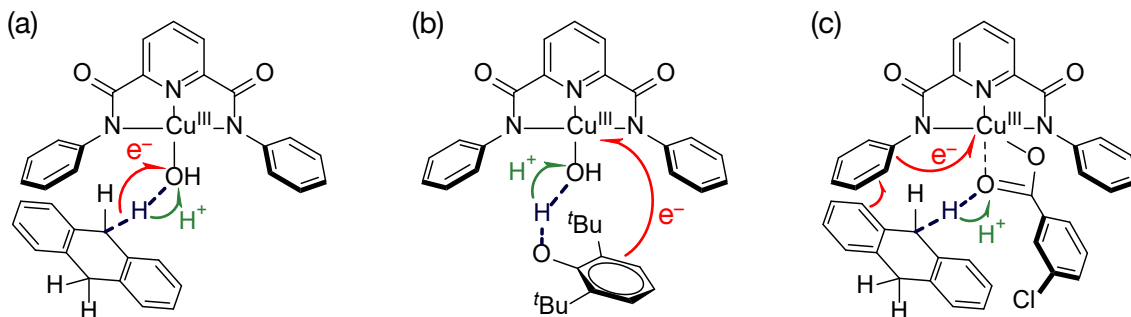


Figure 4.7. Electron flow during HAA from (a) **401**/DHA, (b) **401**/Ar²OH, and (c) **403**/DHA. © American Chemical Society

Continuing with the IBO analysis, a scenario similar to **401**/Ar²OH is present for the reaction of **403** with DHA, i.e., both α - and β -IBOs of the C–H bond remain on the hydrocarbon substrate (Figure 4.6(h) for β -IBO). Interestingly, a β -IBO of DHA π -density is found to evolve into a Cu $d_{x^2-y^2}$ orbital through a ligand-assisted pathway (Figure 4.6(i)), that is, density in a ligand π -IBO flows to Cu concomitantly with density from a DHA π -IBO flowing to the ligand itself. While this π – π communication adds an additional layer of complexity with respect to detail, the overall electron flow makes it clear that the reaction of **403** with DHA is best described as a cPCET mechanism (Figure 4.7(c)), consistent with the conclusions drawn from analysis of projected dipole moment changes discussed above. IBO transformations of the remaining pairs: **402**/DHA resembles data shown in Figure 4.6(b–c), while those of **402**/Ar²OH, and **403**/Ar²OH pairs are similar to those presented in Figure 4.6(e–f) (see ref. 211 for details). The net conclusion from these analyses is that **401**–**403** all react with Ar²OH via a cPCET mechanism, **401** and **402** react with DHA via an HAT mechanism, but **403** instead abstracts a H-atom from DHA following the cPCET pathway.

In regard to details within the paradigm of a cPCET process, a varying degree of asynchronicity in H⁺/e⁻ transfer is possible during the concerted event, which can have a significant impact on the reaction rate. Hence, it is informative to be able to quantify the extent to which transfer of proton and electron coupled. A simple way of achieving this is to calculate the

asynchronicity factor (η), a thermodynamic parameter introduced by Srncic and coworkers for describing the relative contributions of two competing factors dictating a net HAA process: the acidity constant (pK_a) and the redox potential.²⁰⁸ In cases where acidobasic contributions are more important, a negative value of η is expected, while a positive value of η indicates a more dominant role of the redox potential.^{196,208} For instance, it has been demonstrated recently that C–H bond activation by a Co(III)–oxo species with various hydrocarbons occurs via a *basic* asynchronous concerted pathway, where a H^+ is transferred to the acceptor-site prior to e^- transfer (cf. Scheme 4.1).¹⁹⁶ Concomitantly, the asynchronicity factor was computed to be *negative* in this case. The **403**/DHA reactivity revealed here, by contrast, is concerted, but we compute it to be *oxidatively* asynchronous as we compute a *positive* value for η (+626 and +933 mV for reactions with Ar^2OH and DHA, respectively; Table 4.5).

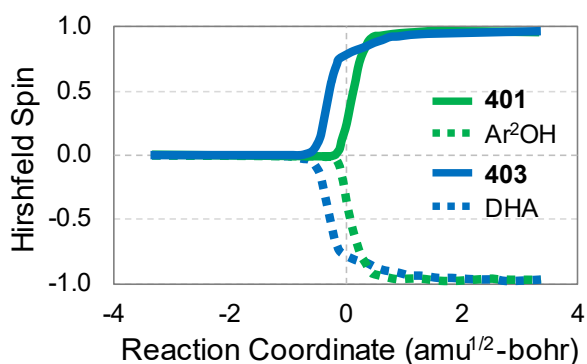


Figure 4.8 Changes in the Hirshfeld spin-population for **401**/ Ar^2OH (green) and **403**/DHA (blue), along their respective cPCET reaction coordinates. Solid lines represent total spin on Cu-complexes (Fragment^{Cu}), while dotted lines reflect the total spin on organic substrates (Fragment^{Sub}). At the start of the reaction, both Fragment^{Cu} and Fragment^{Sub} are closed-shell systems, thus the total spin on both fragments starts from zero. At/near the TS, single electron transfer leads to local spin on both fragments. © American Chemical Society

A better visual picture of the oxidative asynchronicity in **403**/DHA could be obtained by examining Figure 4.6(i2), which shows the electron-transfer event occurring at a point along the reaction coordinate where the H^+ is still primarily on the DHA fragment, consistent with an asynchronous cPCET mechanism having a more ET-like character in the TS. A comparative analysis of the cPCET mechanisms in **401**/ Ar^2OH and **403**/DHA is provided in Figure 4.8, where evolution of the Hirshfeld spin population along the H-coordinate for both systems is plotted. Interestingly, for **3**/DHA, the spin-density on the Cu-fragment starts increasing (and, that of the

DHA moiety starts decreasing) well before the TS is reached—indicating early transfer of the electron from the substrate. This transfer is advanced even when comparing to the cPCET case of **401**/Ar²OH, where a similar change in density begins to appear only in close vicinity to the TS, in spite of the more polar character of the O–H bonds involved. This variation may presumably again be attributed to the substantially more positive standard reduction potential of **403** compared to **401** and **402**.

4.1.4 Conclusions

A new [Cu(III)–Y]²⁺ species with Y = O₂CAr¹ (**403**) has been prepared and characterized. Its reactivity towards X–H bond (X = C, O) activation has been studied and compared to that of two analogous [Cu(III)–Y]²⁺ cores with Y = OH (**401**) and OOCm (**402**) supported by the same L²⁻ ligand. Systematic comparison of reactivity with a given substrate across the series (Y = OH, OOCm, and O₂CAr¹) has enabled us to discern the contribution of the acceptor Y-group towards the complex's X–H bond functionalization reactivity. One key finding is that **403** is a better oxidant than **402** owing to the weaker carboxylate donor, which makes the Cu-center in **403** more electrophilic, and this in turn makes benzoate **403** more reactive than alkylperoxo **402**. On the other hand, the greater basicity of the hydroxide moiety in **401** contributes significantly towards its highest reactivity.

There are other mechanistic differences as well: detailed examination of X–H bond activation by **401**–**403** indicates variations in the synchronicity of concerted proton and electron transfer (CPET), ranging from quite asynchronous to the near-perfect synchronicity of true hydrogen-atom transfer, with reaction coordinates sensitive to both reactive ligand Y and substrate. Measurement of the dipole moment component projected on the H-donor/acceptor axis¹⁹⁹ proves one efficient means to assess relative synchronicity. Analysis of intrinsic bond orbitals^{195,209,210} enables direct visualization of electron flow along reaction coordinates, and has been used here to resolve a mechanistic dichotomy within the paradigm of CPET reactions. For Y = OH and OOCm, reactions with 9,10-dihydroanthracene are found to proceed by hydrogen-atom transfer, while reactions with a bulky phenol are found to proceed instead by concerted

proton-coupled electron transfer. For $Y = O_2CAr^1$, by contrast, *both* reactions are found to proceed by concerted proton-coupled electron transfer, with a high degree of oxidative asynchronicity, driven in part by the greater oxidizing power of the Cu(III) species. Such a detailed mechanistic picture delineating the coupled nature of proton and electron transfer from the substrate to different copper-oxygen species should be of broader relevance in HAA catalysis and can be exploited for strategic tuning of reactivity and selectivity toward various substrate X–H bonds.

4.1.5 Appendix

4.1.5.1 Reactivity of 402 and 403 Towards DHA: Site O^a vs. O^b and O^c vs. O^d

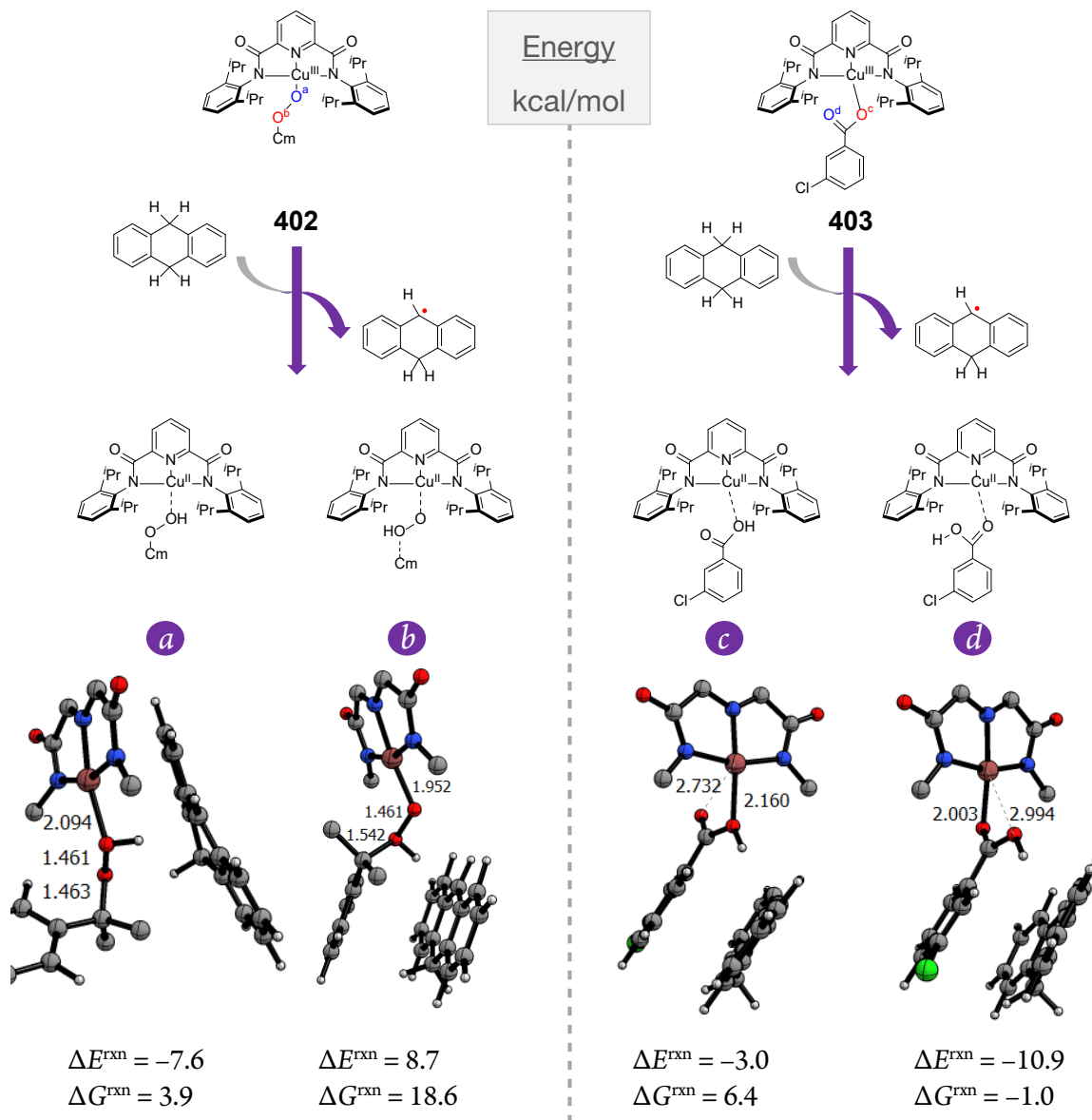


Figure 4.9 Computed change in electronic energy (ΔE^{rxn}) and Gibbs free energy (ΔG^{rxn}) leading to product formation, upon HAA from the DHA substrate. Energies are in kcal/mol computed at B3LYP/basis-II/SMD($\epsilon = 13.6$)/B3LYP/basis-I level of theory. Clearly, Products formed at sites 'a' and 'd' are thermodynamically more stable.

4.1.5.2 Reactivity of 402 and 403 Towards Ar²OH: Site O^a vs. O^b and O^c vs. O^d

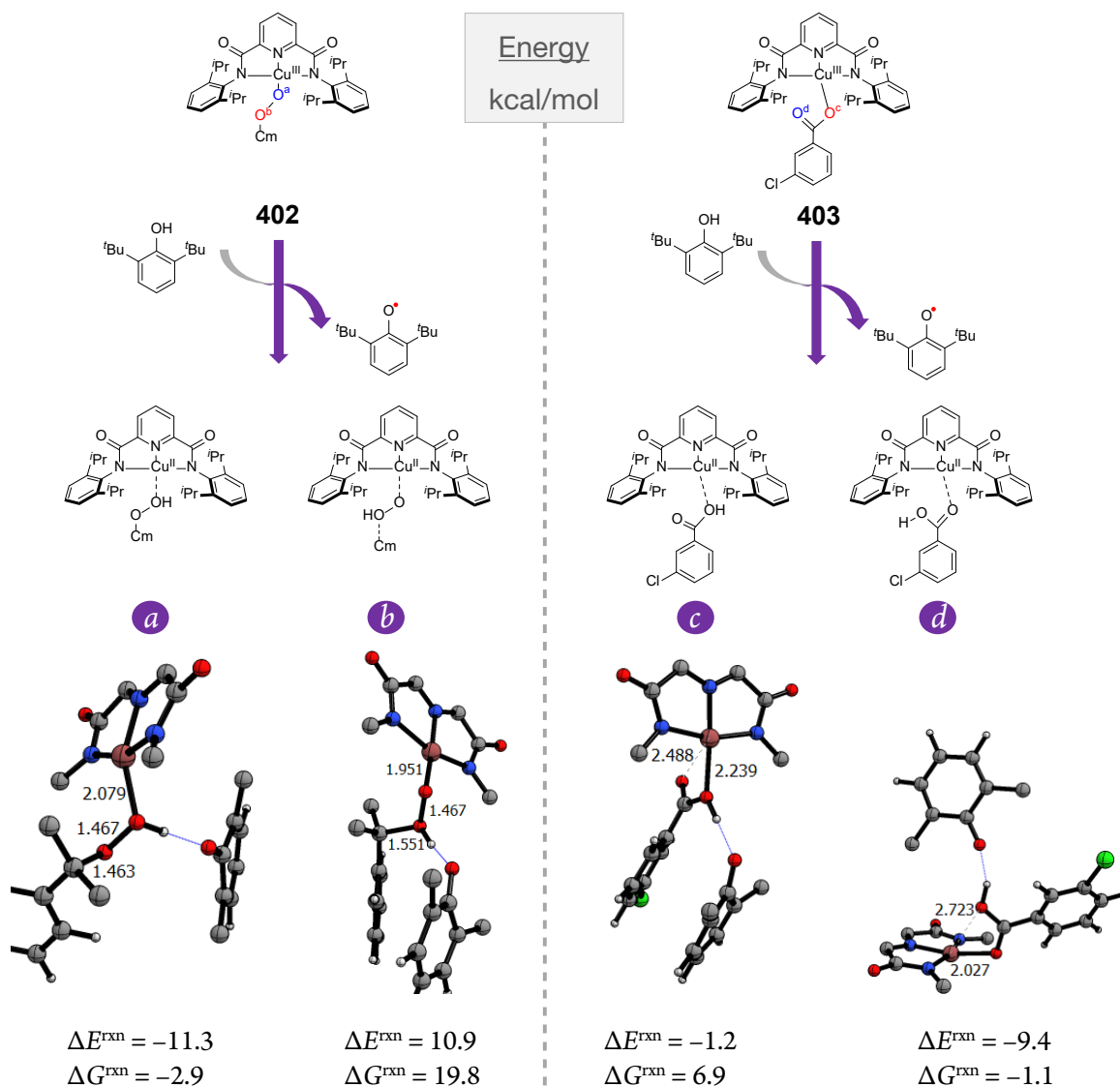


Figure 4.10 Computed change in electronic energy (ΔE^{rxn}) and Gibbs free energy (ΔG^{rxn}) leading to product formation, upon HAA from the Ar²OH substrate. Energies are in kcal/mol computed at B3LYP/basis-II/SMD($\epsilon = 7.4$)/B3LYP/basis-I level of theory. Clearly, Products formed at sites 'a' and 'd' are thermodynamically more stable.

4.1.5.3 Computation Protocol.

Geometry optimization and frequency calculations are done at the density functional theory (DFT) level as implemented in the Gaussian 09 and Gaussian 16 electronic structure program suite.¹⁰³ Geometry optimizations are done in the gas-phase using the B3LYP density functional¹³²

calculations including Grimme's three-body dispersion term (D3)¹⁹ and Becke-Johnson (BJ) damping.^{19d,20} For gas-phase geometry optimizations and vibrational frequencies, Pople's split-valence 6-31G(d) basis set^{66a} was used for light atoms and the Stuttgart/Dresden effective core potential with its associated basis set (SDD)¹³³ was used for Cu (basis-I). Improved electronic energies were computed from single-point calculations using the triple-zeta def2-TZVP basis set²¹² for non-metals and SDD for Cu (basis-II). An experimentally relevant solvent reaction field was included in single-point calculations employing the SMD continuum solvation model¹⁰⁵ using solvent parameters for THF ($\epsilon = 7.4$) in the case of reactions with Ar²OH and for cyclopentanone ($\epsilon = 13.6$, chosen to best mimic experimental 1,2-DFB ($\epsilon = 13.8$)) in the case of DHA. For time-dependent density functional theory (TD-DFT) calculations, the PBE0 density functional^{89a} together with the def2-TZVP basis set for non-metals and the def2-TZVPP basis and SDD pseudo-potential for Cu was used (basis-III).

Although a seemingly technical computational detail, it is critical to note that all HAA reactions studied here involve closed-shell organic molecules and formally Cu(III) complexes ($3d^8$) as reactants, which are themselves also well-described by closed-shell singlet electronic states. Along all reaction coordinates, however, the reacting partners evolve into individual open-shell doublets (an organic radical and a formally Cu(II) ($3d^9$) species). Thus, within the single-determinantal Kohn–Sham (KS) DFT formalism, all reaction paths must at some point evolve on a broken-symmetry (BS) singlet potential energy surface (PES), characterized by KS determinants having $M_s = 0$ but $\langle S^2 \rangle$ values greater than 0 (and approaching 1 with increased separation of the radical partners).²¹³ We found that for all cases studied here, the crossing to the BS singlet PES occurs prior to reaching the transition-state (TS) structure for CPET. Thus, all TS structures were optimized at the unrestricted level of theory using the BS formalism (BS-UDFT), which takes the static correlation of the open-shell singlet into account in a cost-effective way.²¹⁴ Since the BS-UDFT determinant is contaminated by higher spin-states^{214,215} (triplet in this case), an approximate spin-projection scheme proposed by Yamaguchi et al.²¹⁶ was used to spin-purify the final electronic energies. For systems involving singlet/triplet states this is given by:

$$E_{AP}^{\text{Singlet}} = E^{\text{Triplet}} + \frac{2(E_{BS}^{\text{Singlet}} - E^{\text{Triplet}})}{\langle \hat{S}^2 \rangle_{\text{Triplet}} - \langle \hat{S}^2 \rangle_{BS}^{\text{Singlet}}} \quad (1)$$

Where, E = electronic energy, BS = broken (spin) symmetry, AP = approximate (spin) projection, LS = low-spin, HS = high-spin.

For analyzing reaction path, intrinsic reaction coordinate (IRC) calculations were carried out using the HPC algorithm.²¹⁷ Hirshfeld population analysis²¹⁸ was performed at each point on the IRC to obtain information about dipole moment and spin-density. For orbital localization using the intrinsic bond orbital (IBO) scheme, single-point calculations were re-performed along the IRCs using the electronic structure code ORCA 4.0.1.2.²¹⁹ The B3LYP/G functional along with D3(BJ) correction and def2-SVP²²⁰ basis for non-metals, def2-TZVP²²⁰ for Cu were also used. SCF convergence tolerance was set to “TightSCF”. Calculations were speed-up by using the RIJCOSX approximation using the def2/J universal Coulomb-fitting basis sets.²²¹ DFT integration grid and the accuracy of the COSX grid in RIJCOSX calculations was set to Grid5 and GridX5 respectively. IBOs were generated using IboView program²²² with “iboexp = 2”.

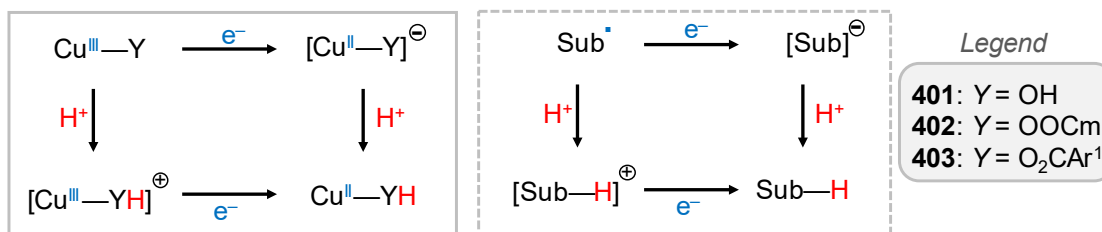
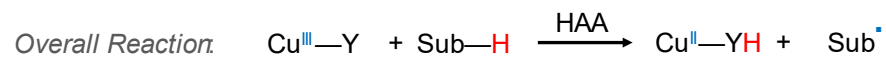
4.1.5.4 Asynchronicity Factor

In order to quantify the asynchronicity in the electron and proton transfer in the concerted HAA process, we have computed the asynchronicity factor (η) proposed by Srnec and coworkers.²⁰⁸ η has been computed for HAA from both Ar²OH and DHA (Table 4.5) by all three complexes **401**–**403**, according to Scheme 4.3, which is based on the original work reported in ref. 208. In all cases, we calculate a positive value for η , which indicates asynchronicity in favor of electron-transfer.

Table 4.5 Calculated asynchronicity factors (η) in mV.

species	η (mV)	η (mV)
	substrate = Ar ² OH; T = 193.15 K	substrate = DHA; T = 248.15 K
401	45	350
402	329	642
403	626	933

Scheme 4.3 Species relevant for computing asynchronicity factor. $G(\text{species})$ refers to the Gibbs free energy of the relevant species. $[\text{Sub}^\bullet]$ refers to the usual radical product after HAA, $[\text{SubH}^\oplus]$ is the substrate structure, either DHA or Ar^2OH oxidized by 1-electron, and $[\text{Sub}^-]$ is the substrate structure after deprotonating the acidic proton from the X-H bond.



$$\text{Asynchronicity Factor } (\eta) = \frac{1}{\sqrt{2}} [-G(\text{Cu}^{\text{II}}\text{Y}^-) + G(\text{Sub}^-) + G(\text{Cu}^{\text{III}}\text{YH}^\oplus) - G(\text{SubH}^\oplus)] \quad \dots\dots\dots (2)$$

4.2 Carboxylate Electronic Effects on the PCET Reactivity of $[\text{CuO}_2\text{CR}]^{2+}$ Cores

4.2.1 Introduction

With the ultimate aim of using mechanistic understanding to inform the development of more efficient and selective oxidation catalysts, copper complexes relevant to postulated catalytic intermediates have been targeted for detailed study.^{186b-c,223} Species with $[\text{CuO}]^+$, $[\text{CuOH}]^{2+}$, $[\text{CuO}_2]^+$, and $[\text{CuOOR}]^{+/2+}$ cores have garnered particular attention because of their hypothesized role as oxidizing intermediates in synthetic systems^{185b,224} and in enzymes.^{184,225} Studies of complexes with such cores aim to unravel structure/reactivity relationships. For example, in previous work we prepared formally Cu(III) complexes LCuOH ($L = \text{bis}(2,6\text{-diisopropylphenyl carboxamido})\text{pyridine}$ and derivatives; Figure 4.11), defined their structural and spectroscopic attributes, and examined their hydrogen-atom abstraction (HAA) reactivity with C–H and O–H bonds in organic substrates.^{187a-c,187e,226} Rapid rates for these reactions were rationalized by the formation of a strong O–H bond in the product, $\text{LCu}(\text{OH}_2)$, and the effects of changing the electron-donating properties of the supporting ligand L^{2-} were evaluated through variation of substituents on the aryl rings or reducing the pyridine moiety. Also, the HAA reactions of LCuOH and $[\text{LCuO}_2]^-$ with a series of *para*-substituted phenols were compared, revealing intriguing differences in mechanisms traversed as the properties of the phenol substrates were varied.^{187b,e} These differences were traced to divergent thermodynamic properties of the two cores supported by the same ligand L^{2-} .

More recently,²¹¹ we prepared a new formally Cu(III) complex LCuO_2CR ($R = -\text{C}_6\text{H}_4(\text{m-Cl})$; Figure 4.11) and compared its rates of reactions with 9,10-dihydroanthracene (DHA) and 2,4,6-tri-*t*-butylphenol (TTBP) to those of LCuOH and $\text{LCuOOC}(\text{Me}_2)\text{Ph}$.^{187d,190} Differences in the rates of HAA reactions were observed ($\text{LCuOH} > \text{LCuO}_2\text{CR} \gg \text{LCuOOC}(\text{Me}_2)\text{Ph}$), and these differences were rationalized by invoking changes in the mechanisms followed. Importantly in the current context, the reactions of LCuO_2CR ($R = -\text{C}_6\text{H}_4(\text{m-Cl})$) were found via theory to involve a concerted, yet asynchronous PCET process, with the proton migrating to the carbonyl oxygen atom that is likely not (or only weakly) bound to the copper ion, well after the electron is transferred to the copper center. Such a process represents an example of site-separated PCET,

which has attracted significant attention, in part because it is likely to be important in biological contexts.^{191,192,227}

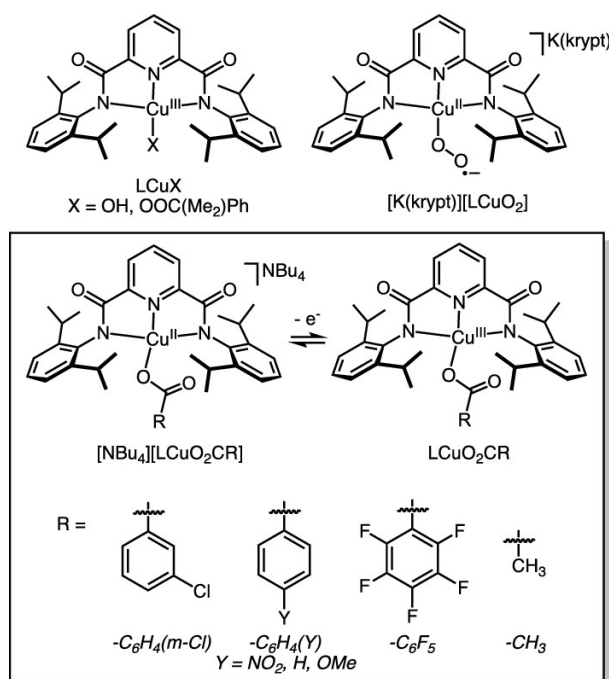


Figure 4.11 Copper complexes supported by L^{2-} (focus of this work in box). © American Chemical Society

Intrigued by the novel mechanistic findings for LCuO_2CR ($R = -\text{C}_6\text{H}_4(m\text{-Cl})$), we sought to probe the effects of changing R . Specifically, we asked how varying R might influence the structural, spectroscopic, redox, and reactivity properties of the $[\text{CuO}_2\text{CR}]^{2+}$ core and its precursor $[\text{CuO}_2\text{CR}]^+$. Herein we report the results of such studies,²²⁸ which provide fundamental chemical insights, including into how thermodynamic attributes influence reactivity of formally Cu(III) species.

4.2.2 Experimental Studies: Reactivity of $[\text{Cu}^{\text{III}}\text{O}_2\text{CR}]^{2+}$ Complexes.

We examined the reactions of $\text{LCu}^{\text{III}}(\text{O}_2\text{CR})$ (all R except $-\text{C}_6\text{H}_2(\text{tPr})_3$) with TTBP in order to evaluate trends in reactivity with relatively weak O–H bonds. In all cases, reactions were indicated by a decay of the UV-Vis spectroscopic features associated with $\text{LCu}^{\text{III}}(\text{O}_2\text{CR})$ and observation of the aryloxy radical by EPR spectroscopy.²¹¹ Second-order rate constants (k_2) for the reactions of $\text{LCu}^{\text{III}}(\text{O}_2\text{CR})$ with TTBP (THF, -80°C) are listed in Table 4.6. A clear trend in k_2 with the

electron donating properties of R is seen for the reactions with TTBP, which is illustrated in a plot of $\log k_2$ vs. $E_{1/2}$ for the $[\text{LCu}^{\text{III,II}}(\text{O}_2\text{CR})]^{0/-}$ couple in Figure 4.12. These plots show that the more electron withdrawing R, the more oxidizing the complex, and the faster the rate of reaction with TTBP.

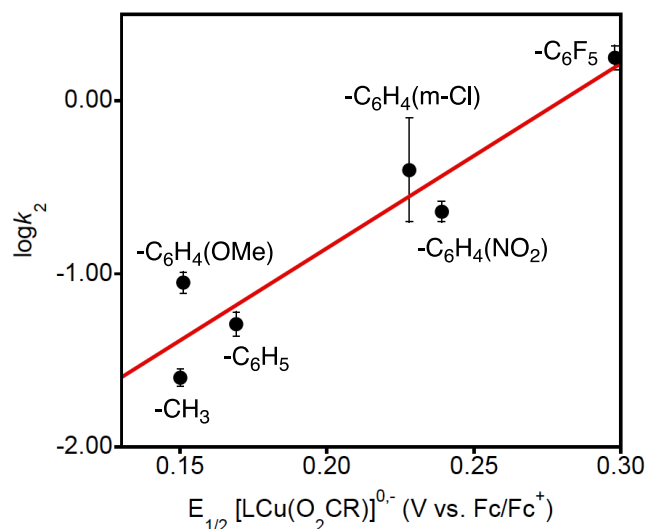


Figure 4.12 Plot of $\log k_2$ for the reaction of $\text{LCu}^{\text{III}}\text{O}_2\text{CR}$ with TTBP at -80°C in THF vs. $E_{1/2}$ for the $[\text{LCu}(\text{O}_2\text{CR})]^{0/-}$ couple. Red line is linear fit to $\log k_2 = 10.7 \times E_{1/2} - 2.98$, $R^2 = 0.90$. © American Chemical Society

4.2.3 Computational Reactivity Trend

To gain insight into the experimentally characterized variation in reactivity as a function of the substituents on the benzoates in $\text{LCu}^{\text{III}}\text{O}_2\text{CR}$ described above, density functional modeling of the PCET reaction coordinate was undertaken at the B3LYP-D3(BJ)/basis-II/SMD(THF)//B3LYP-D3(BJ)/basis-I level of theory^{19d,20,105,132} (basis-I: 6-31G(d)^{66a} for light atoms and SDD¹³³ for Cu; basis-II: def2-TZVP²¹² basis for non-metals and SDD for Cu) along the broken-symmetry singlet potential energy surface. Table 4.6 displays computed free energies of activation (ΔG^\ddagger) for reactions of the indicated complexes with the substrate 2,6-di-*t*-butylphenol (DTBP, lacking the third *t*-butyl group of TTBP for computational expediency). In fair agreement with the experimentally observed trend, increased electron-withdrawing ability of R correlates with an increase in the PCET rate, as quantified by the general decrease (within the error of DFT) in the computed ΔG^\ddagger values (Table 4.6).

In related work,²¹¹ we have demonstrated that the reaction of $\text{LCu}^{\text{III}}(\text{O}_2\text{C}_6\text{H}_4(m\text{-Cl}))$ with DTBP proceeds via a concerted proton-coupled electron transfer pathway having a high degree of oxidative asynchronicity, meaning that the transition-state (TS) structure for the concerted event has more electron-transfer like character. Similar asynchronicity in electron/proton transfer may also be invoked for all the N,N',N'' -carboxylates described herein, with the degree of asynchronicity increasing as the electron-withdrawing ability of R gradually increases (recall that the asynchronicity is *oxidative* in nature, and the Cu center systematically becomes more oxidizing). Along with other influencing factors, such increasing asynchronicity in electron/proton transfer has been documented to lower the free energy barrier of a concerted PCET process,²⁰⁸ so increased PCET reaction rates with more electron-withdrawing R is anticipated.

Table 4.6 Second-order rate constants (k_2) for reactions of $[\text{LCu}^{\text{III}}(\text{O}_2\text{CR})]$ with the indicated substrates and computed^a ΔG^\ddagger and other parameters for the reactions of $[\text{LCu}^{\text{III}}\text{O}_2\text{CR}]$ with DTBP.

R	exp rate (TTBP ^b) ($\text{M}^{-1}\text{s}^{-1}$)	ΔG^\ddagger (kcal/mol)	Cu–O1 (Å)	TS Cu–O1 (Å)	$\langle S^2 \rangle^c$
C_6F_5	1.8(4)	2.3	1.868	1.984	0.853
$\text{C}_6\text{H}_4(\text{NO}_2)$	0.23(3)	3.7	1.864	1.966	0.827
$\text{C}_6\text{H}_4(m\text{-Cl})^d$	0.3(1)	2.9	1.859	1.956	0.817
C_6H_5	0.052(8)	7.9	1.861	1.948	0.730
$\text{C}_6\text{H}_4(\text{OMe})$	0.09(1)	7.2	1.860	1.943	0.700

^aSMD(THF)/B3LYP-D3(BJ)/basis-II//B3LYP-D3(BJ)/basis-I level of theory at 193.15 K.

^bTHF, -80°C . ^cCalculated at the UB3LYP-D3(BJ)/basis-I level of theory. ^dref. 211.

Furthermore, we note that with increasing electron-withdrawing nature of R , the cleavage of the Cu–O1 bond in individual TS structures (Figure 4.13) becomes easier, facilitating formation of the product Cu^{II} species. Thus, while the equatorial Cu–O1 bond length in the Cu^{III} reagent remains similar across the series (variation of ~ 0.009 Å, Table 4.6), it varies significantly in the respective TS structures (variation of ~ 0.041 Å, Table 4.6, Figure 4.13). This interpretation is supported by comparison of the computed values of the $\langle S^2 \rangle$ operator, which gradually increase towards unity with increasing electron-withdrawing ability of R , consistent with increased separation of the developing radical loci in the products. The significant computational challenges

associated with the broken-symmetry approach in the region of the transition-state suggests that the quantitative variation as a function of substituent may not be particularly accurately predicted, but the consistency of the qualitative variation with experiment suggests that the observed variations in geometric and electronic structures as a function of substituent are likely germane to the reactivity differences.

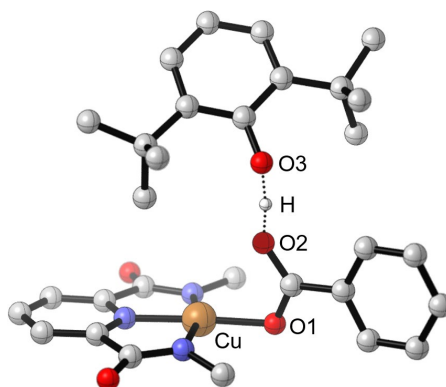


Figure 4.13 Representative transition-state structure for the reaction of $\text{LCu}^{\text{III}}\text{O}_2\text{CC}_6\text{H}_5$ with DTBP. H-atoms and the 2,6-diisopropylphenyl groups on the L^{2-} ligand are omitted for clarity. Selected distances (\AA): Cu–O1, 1.948; Cu–O2, 2.699; O2–H, 1.178; H–O3, 1.211. © American Chemical Society

It is informative to compare the trends in $\text{LCu}^{\text{III}}(\text{O}_2\text{CR})/\text{TTBP}$ reactivity to similar studies of the reactions of copper-oxygen species (supported by L^{2-} and related ligands) with phenols or DHA.^{187b,187e,188a} Reactions of $\text{LCu}^{\text{III}}\text{OH}$ with a series of *para*-substituted phenols ($^X\text{ArOH}$, $X = \text{NO}_2, \text{CF}_3, \text{Cl}, \text{H}, \text{Me}, \text{OMe}, \text{NMe}_2$) showed a general trend of increasing rate with more electron rich substrates (greater electron donating substituents, lower $E_{1/2}$, higher $\text{p}K_a$), albeit with outliers for the most electron poor phenols (e.g. $X = \text{NO}_2$).^{187b} These and other results were interpreted to indicate that these reactions involved concerted proton-coupled electron transfer, but with asynchronicity favoring ET ($X = \text{NMe}_2$) or favoring PT ($X = \text{OMe}, \text{Me}, \text{H}, \text{Cl}$).^{187b,187e} The rates of these reactions are significantly faster than those of $\text{LCu}^{\text{III}}(\text{O}_2\text{CR})$ with TTBP, but the trends are analogous, with faster rates exhibited by the most electron-poor, oxidizing reagents ($^X\text{ArOH}$ or $\text{LCu}^{\text{III}}(\text{O}_2\text{CR})$, respectively). In other work,^{188a} the reactivity of $[\text{CuOH}]^{2+}$ cores supported by derivatives of L^{2-} with perturbed electron donating capabilities was probed by incorporating $-\text{NO}_2$ groups at the *para* positions of the 2,6-diisopropylaryl rings ($^{\text{NO}_2}\text{L}^{2-}$, electron poor) or hydrogenating the central pyridine ring to generate a piperidine donor ($^{\text{pip}}\text{L}^{2-}$, electron rich). The

observed trend in rates of PCET with DHA $^{\text{NO}_2}\text{LCuOH} > \text{LCuOH} > ^{\text{pip}}\text{LCuOH}$ were rationalized by the same trend in product bond dissociation enthalpies (BDEs), which in turn resulted from greater influences of the ligand changes on redox potential than on hydroxide basicity. For the reactions of LCuO_2CR , the trend in rate of reaction with TTBP is also dominated by the effect of R on the redox potential, as the rate increases as $E_{1/2}$ increases and the basicity of the (free) carboxylate ion decreases. However, in these reactions the trend in rates does not correlate with the free carboxylic acid O–H BDEs, which notably are essentially identical for $R = -\text{NO}_2$ and $-\text{OMe}$ (107.1 and 106.8 kcal mol⁻¹, respectively).²²⁹ We speculate that the absence of such a thermodynamic rationale reflects asynchronicity of the PCET reaction and/or perturbation of the BDEs through interactions of the carboxylate ion or product carboxylic acid with the copper ion (effects that we have not measured).

4.2.4 Conclusions

A series of complexes $[\text{NBu}_4][\text{LCu}^{\text{II}}(\text{O}_2\text{CR})]$ ($R = -\text{C}_6\text{F}_5, -\text{C}_6\text{H}_4(\text{NO}_2), -\text{C}_6\text{H}_5, -\text{C}_6\text{H}_4(\text{OMe}), -\text{CH}_3, \text{and } -\text{C}_6\text{H}_2(^i\text{Pr}_3)$) were prepared and characterized, and compared to the data for the complex with $R = -\text{C}_6\text{H}_4(m\text{-Cl})$.²¹¹ All adopted structures featuring N,N',N'' -coordination of the supporting L^{2-} ligand, except for the case where $R = -\text{C}_6\text{H}_2(^i\text{Pr}_3)$, in which the supporting ligand isomerized to N,N',O -coordination as revealed by X-ray crystallography and UV-Vis and EPR spectroscopy. Chemical oxidations of these complexes at $-80\text{ }^\circ\text{C}$ in THF or $-25\text{ }^\circ\text{C}$ in DFB resulted in the formation of $\text{LCu}^{\text{III}}(\text{O}_2\text{CR})$, which exhibited appropriate LMCT features in their UV-Vis spectra. These features as well as the rates of the reactions of $\text{LCu}^{\text{III}}(\text{O}_2\text{CR})$ with the O–H bond in TTBP correlated well with the electron donating/withdrawing nature of R, as revealed by a logarithmic plot of the second order rate constant for the reaction with TTBP vs. the $[\text{LCu}^{\text{III,II}}(\text{O}_2\text{CR})]^{0-} E_{1/2}$ (Figure 4.12). DFT calculations corroborated the experimentally observed reactivity trend during H-atom abstraction from 2,6-di-*t*-butylphenol by N,N',N'' -complexes. A systematic increase in the reaction rate is observed with increasing electron withdrawing nature of R, quantified by, within error, a gradual decrease in the computed ΔG^\ddagger values, attributable to a gradual increase in the degree of asynchronicity in electron/proton transfer. Taken together, the evidence supports oxidatively asynchronous proton-coupled electron

transfer pathways for the reactions of $\text{LCu}^{\text{III}}(\text{O}_2\text{CR})$ with the hindered phenol, with the oxidizing power of the complexes being predominant in controlling the reaction rate.

Chapter 5

Structure and Reactivity of Metal–Organic Framework-Supported Single-Site Catalysts

Synopsis. Heterogeneous catalysts synthesized by anchoring catalytically active species over metal–organic frameworks (MOFs), which themselves are a class of porous crystalline material consisting of inorganic nodes connected via organic linkers arranged in three-dimensional networks, has garnered significant interest in the last decade. High energy efficiency and atom economy make this class of material highly attractive for industrial applications. However, given the complexity of the material, a detailed structure–activity correlation is hard to obtain experimentally. Thus, in this final chapter of the thesis, I have summarized our current efforts in identifying the local structure of the catalytically active species in MOF-based single-site catalysts. Moreover, by modeling the catalytic reaction pathway (e.g., selective oxidation of benzyl alcohol to benzaldehyde), we have identified the factors dictating catalytic performance and prescribed strategies for improving their activity. Two specific cases are discussed: in the first case vanadium oxo species is anchored over MOF ($\text{VO}_x@MOF$) and in the second one Pd^{II} is deposited over acid modified MOF-support ($\text{Pd}@MOF$).

5.1 Structure and Reactivity of MOF-Supported Single-Site Heterogeneous VO_x Catalyst

5.1.1 Introduction

A traditional approach to heterogeneous catalysis involves anchoring catalytic moieties (atoms, ions, clusters, or complexes) on metal-oxide or silica supports, and this often leads to an uneven distribution of catalytic sites. Moreover, spontaneous sintering often results in catalyst deactivation. One strategy to prevent detrimental self-association in heterogeneous materials is to immobilize the active species at well-separated sites in a structurally regular porous support. Isolated single-site heterogeneous catalysts installed onto robust solid supports constitute a class of materials having atom economy and energy efficiency, and they are highly attractive for industrial applications.^{230–233}

Among various possible active species, vanadium oxide (VO_x) is especially interesting because it is naturally abundant and moderately nontoxic and has shown high catalytic performance for various redox processes, including epoxidation of olefins and oxidation of hydrocarbons and alcohols.²³⁴ Effort has been devoted to determining the catalytic active sites and understanding the mechanism of the oxidation processes in order to find structure–activity correlations.²³⁵ Such correlations, however, are most likely for uniform and well-defined active sites, which are often elusive when traditional heterogeneous support materials are used.

Metal–organic frameworks (MOFs)—a class of porous crystalline materials consisting of inorganometallic nodes connected by multidentate organic linkers arranged in three-dimensional networks—are promising supports owing to their large specific surface area^{231,236,237} and their potential for hosting structurally similar, well-isolated active species without agglomeration or adsorbates or “cross-talk” between sites.^{231,232} Moreover, the pore openings of MOFs can provide easy access of reactant molecules to the active centers,²³⁸ while structural periodicity may promote a uniform distribution of catalytic sites throughout the support material. Accordingly, an important goal of our work is to study MOF nodes as supports for size-selected well-defined oxide clusters,²³⁹ and in the present article we report on MOF-supported VO_x (V-MOF) catalysts.

Examples of VO_x species immobilized over MOF-supports include a report by Nguyen et al.,²⁴⁰ where the authors installed $\text{V}^{(\text{V})}$ species on the zirconium oxide nodes of UiO-66 MOF to generate a thermally stable single-site heterogeneous UiO-66-V catalyst that demonstrated good catalytic activity for oxidative dehydrogenation of cyclohexene to benzene. Bulánek et al. reported efficient oxidative dehydrogenation of ethanol using VO_x incorporated into the MIL-101(Cr) MOF.²⁴¹ Cui et al.²³⁷ and Otake et al.²⁴² incorporated $\text{V}^{(\text{V})}$ ions into MOFs by metalating the hydroxyl groups on the zirconium oxide and hafnium oxide nodes of Zr-NU-1000 and Hf-MOF-808 via solvothermal deposition in MOFs (SIM), yielding Zr-NU-1000-V and Hf-MOF-808-V, respectively. High catalytic performance of these two systems was reported for selective oxidation of benzyl alcohol to benzaldehyde, and this encouraged us to carry out the study presented here, which involves detailed computational exploration of various V-MOF structures and possible pathways for catalytic oxidation. Specifically, the present study has three main purposes:

- 1) Identify the local structure of the catalytically active species.
- 2) Model the catalytic pathway towards selective oxidation of benzyl alcohol to benzaldehyde.
- 3) Understand the factors dictating catalytic performance, e.g. the node topology or/and nature of the metal oxide species at the node.

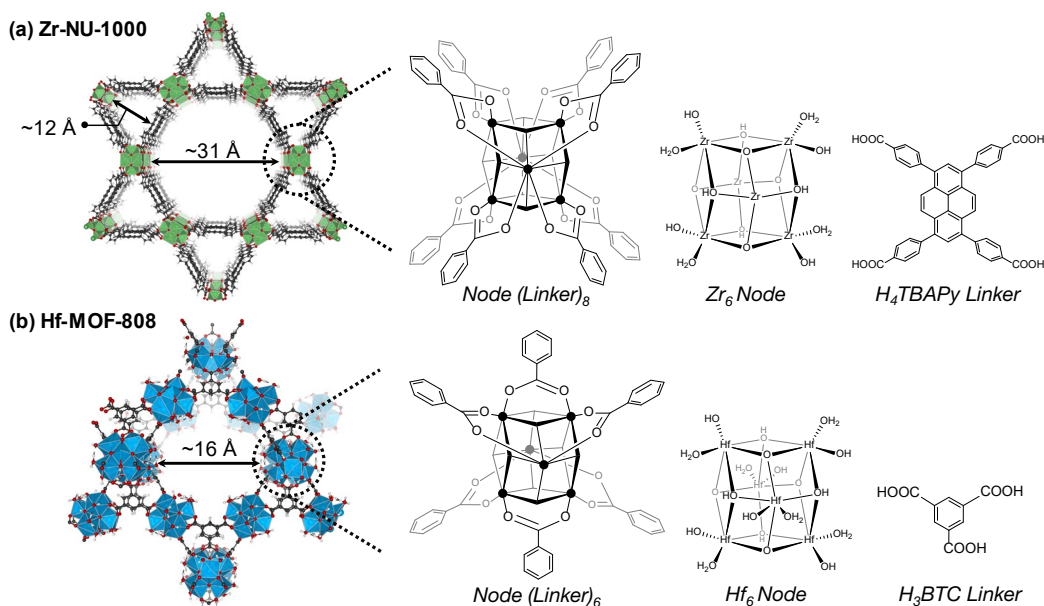
5.1.2 Structural Features of the Support and V-MOFs.

Key structural features of the Zr-NU-1000 and Hf-MOF-808 supports are highlighted in Scheme 5.1. One difference between these supports is that in Zr-NU-1000, eight of the H_4TBPpy (1,3,6,8-(*p*-benzoic acid)pyrene) linkers are so oriented that two of the six $\text{Zr}^{(\text{IV})}$ ions are connected to four linkers making them coordinatively saturated, and hence are not available for post synthetic modification. In contrast, each of the six $\text{Hf}^{(\text{IV})}$ centers in Hf-MOF-808 are bridged via two H_3BTC (benzene-1,3,5-tricarboxylic acid) linkers, while simultaneously coordinating one hydroxyl group and one aqua group each, making all six $\text{Hf}^{(\text{IV})}$ centers available for VO_x deposition via SIM.

Important structural elements of the V-MOFs were obtained by Otake et al.²⁴² using (i) X-ray photoelectron spectroscopy, which indicated oxidation of the $\text{V}^{(\text{IV})}$ precursor, vanadyl acetylacetonate ($\text{O}=\text{V}(\text{acac})_2$), into $\text{V}^{(\text{V})}$ during deposition over MOF nodes, and (ii) inductively

coupled plasma optical emission spectrometry, which suggested, on average, *one* vanadium species per node of Hf-MOF-808-V and Zr-NU-1000-V. Single-crystal X-ray diffraction analyses of both V-MOF samples revealed the presence of multiple crystallographically nonequivalent single-Hf-MOF vanadium sites. The positional disorder of vanadium sites was attributed to a varied degree of hydration of VO_x species; however, IR spectroscopic measurements did not offer a clear picture of the catalytic site. Therefore, we modeled various V-MOF structures, and compared their IR spectral signatures with the experimentally available IR features,²⁴² to decipher information related to the local structure of the catalytically active site.

Scheme 5.1 MOF nodes in (a) Zr-NU-1000 and (b) Hf-MOF-808. (left) One node and associated linkers except that the actual H₄TBAPy (1,3,6,8-(p-benzoic acid)pyrene) and H₃BTC (benzene-1,3,5-tricarboxylic acid) linkers are truncated to benzoate in this schematic. (middle) One node without linkers. (right) A linker. © American Chemical Society



5.1.3 Computation protocol

5.1.3.1 Methods for Exploring V-MOF Structures

To better understand the structure and reactivity of the vanadia-incorporated species, density functional calculations were performed on model structures. Cluster models for Zr-NU-1000 and Hf-MOF-808 were obtained from previously reported^{243,244} periodic calculations by keeping the carbon atoms of the linkers frozen to maintain structural rigidity of the MOF. All cluster models were optimized using the *Gaussian 16* electronic structure program.¹⁰³ Structure searches were

performed using a cluster model in which the linkers were truncated to benzoates. Geometry optimization and frequency calculations were performed using the M06-L density functional^{104a} with basis-I, where basis-I denotes def2-SVP²²⁰ for non-metals, def2-TZVP²²⁰ for V and def2-TZVP with a SDD²⁴⁵ effective core potential (ECP) for Zr and Hf atoms. Zero-point and thermal contributions to Gibbs free energies were computed at this level of theory and added to single-point electronic energies computed with a larger basis set called basis-II: def2-TZVP for non-metals, def2-TZVPP²²⁰ for V and def2-TZVPP with a SDD ECP for Zr and Hf atoms. IR spectral features were also calculated by M06-L/basis-I with frequencies scaled by a factor of 0.958.²⁴⁶

5.1.3.2 Methods for Reactivity Studies

To study the reaction mechanism for selective oxidation of benzyl alcohol to benzaldehyde, the clusters with benzoate linkers were truncated to acetates in all cases. Along the reaction path, in accordance with previous reports describing alcohol oxidation by supported VO_x catalysts,²⁴⁷ transition-state (TS) structure corresponding to the turnover-limiting (TOL) hydrogen-atom abstraction (HAA) step was found to be biradicaloid in nature. Therefore, we allowed the density-functional Slater determinants to break spin symmetry when the restricted-spin solution was unstable. In such cases, the spin-projection scheme of Yamaguchi et al.²⁴⁸ was used to obtain spin-state energies of the lower-spin states, because the broken-symmetry determinant is a mixture of spin states (see Supporting Information for details). Note that for reactivity studies, we have used the M06 exchange–correlation functional,^{104b} which is a hybrid meta functional with 27% Hartree-Fock (HF) exchange, since local functionals tend to predict very late TS structures with high barriers, while hybrid functionals with high % HF exchange predict much earlier TS structures with low barriers for systems involving broken spin-symmetry.²⁴⁹

5.1.4 Modeling VO_x Attachment to the MOF Node

In order to understand the manner in which the VO_x species are immobilized on the surface of the support material and explain the effect of the support on the reactivity of the catalyst,²⁵⁰ we first attempted to identify the local structures of the catalytically active species under operating conditions. Based on literature precedence^{234a,250,251} of alumina/silica/ceria/zirconia-supported

VO_x catalysts, six possible modes of V^(V) attachment to the MOF node were considered, as shown in Figure 5.1.

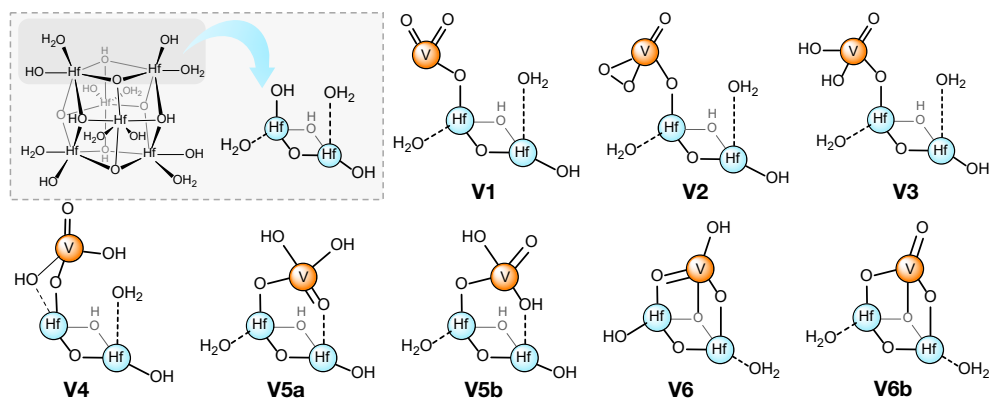


Figure 5.1 Node of Hf-MOF-808, with a focus on the site responsible for chemisorption of VO_x (inset). Possible modes for the deposition of a formally V^(V) species over the MOF-808 node. © American Chemical Society

The di-oxo structure V1 is generally dismissed in the literature based on X-ray absorption analyses and vibrational spectroscopic measurements.²⁵² A simple di-oxo V^(V) model compound (HO)(O)₂V...OH₂ was computed (see Appendix; Figure 5.7, line F7), and it shows IR features due to symmetric and anti-symmetric V=O stretching band at 1040 and 1055 cm⁻¹ respectively; however, only one relevant peak could be observed in this region in the experimental vibrational spectra (at ~1040 cm⁻¹; Figure 5.3b).

The oxo-peroxo structure V2, usually referred to in the literature as the “umbrella structure”,²⁵³ has been widely debated. Such an oxo-peroxo vanadia species is found in vanadium haloperoxidase (VHPO) enzymes,²⁵⁴ and it has been confirmed in VHPO mimics by Waidmann et. al. and Palmajumder et. al.²⁵⁵ However, for both hydrated and dehydrated vanadia catalysts anchored over silica supports, such a structure is not possible,^{251b,256} and hence it is not considered in detail here (see Appendix; Figure 5.7, line V2 for spectral data of such a structure).

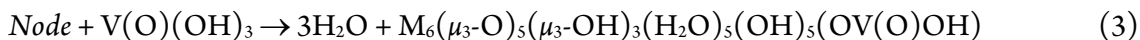
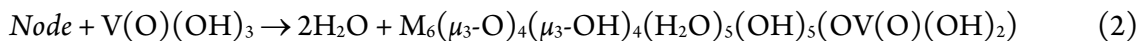
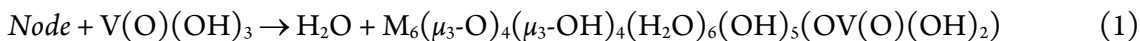
Structure V3 can be regarded as a hydrated form of V2, and its various structures are explored in detail below. V4 is a slightly dehydrated form of V3, where one of the V–OH groups replaces one of the Hf-bound H₂O molecules from the node and forms a chelated VO_x species.

V5 differs from V4 by the fact that the V=O bond coordinates to the adjacent Hf-center in the bridging mode, replacing a H₂O molecule. The V6 structure is a dehydrated form of V5, where the second V–OH group coordinates to the μ-hydroxo group of the node, analogous to pyramidal type structures generally invoked in silica/ceria-supported vanadia chemistry.^{234a} The other variant of V6, the usual “tripod” model where the remaining V–OH group condenses with the Hf–OH group forming another V–O–Hf bond, conformer V6b, was found to be higher in energy than V6, and is discussed only in the Supporting Information (see Appendix; Figure S.6).

5.1.5 Results and Discussions

5.1.5.1 Free Energies

Gibbs free energies (ΔG°) of the reaction yielding V-MOF starting from the bare-MOF were calculated for anchoring modes V3-V6 based on the following reaction schemes:



where *Node* is $M_6(\mu_3-O)_4(\mu_3-OH)_4(H_2O)_6(OH)_6$, with $M = Zr/Hf$ for Zr-NU-1000 and Hf-MOF-808, respectively.

Relative stabilities of these various conformers are reported in Figure 5.2, which shows that structure V3 with V attached by one bridging oxo is the most favorable for the Hf-MOF-808 support. On the other hand, the structure V5 with V attached by two bridging oxo ligands is found to be the most favored Zr-NU-1000-V conformer. This result, however, is in clear contrast with cases where VO_x species is deposited over hydrated (001) and (101) crystal surfaces of tetragonal zirconia, in which case, the most stable vanadia conformer is found to be the one where the OV(OH)₃ species is anchored to two Zr surface-ions as well as one surface oxygen ion, analogous to the V6-NU1000 (Figure 5.2) conformer.^{251a} This finding further demonstrates that flat crystal surfaces and small clusters of the same oxide stabilize catalytically active oxide species differently.

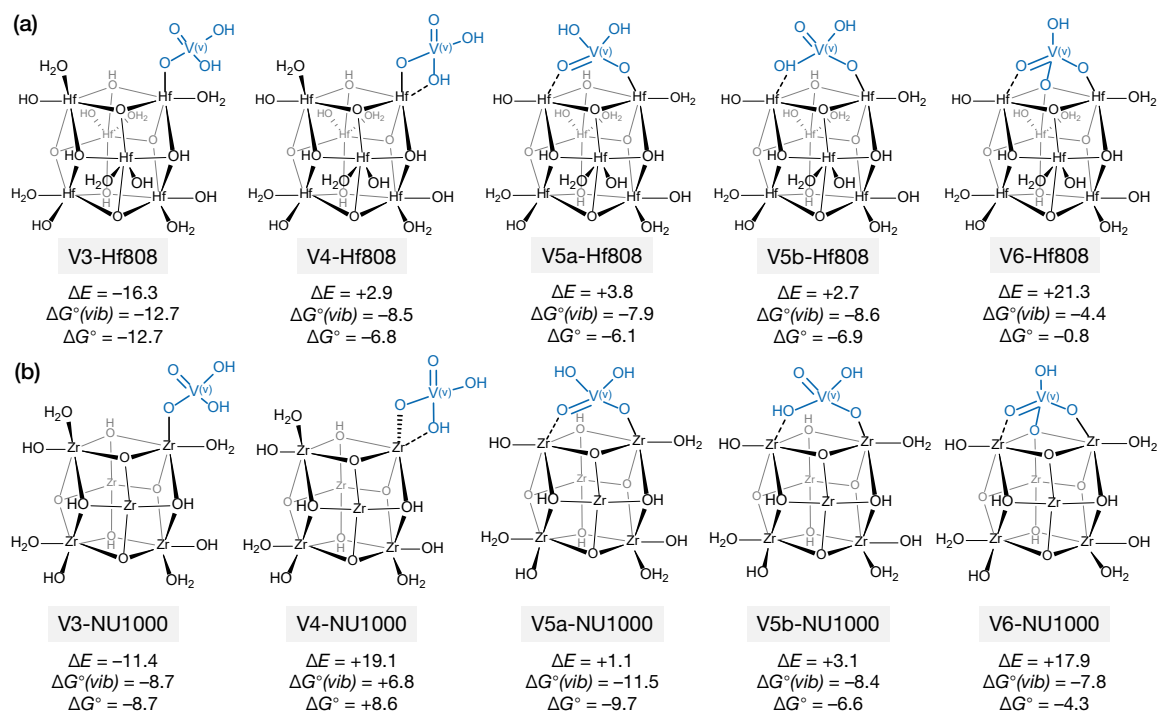


Figure 5.2. Gibbs free energies of reaction (in the condensed phase, $\Delta G^\circ(\text{vib})$, where translational and rotational degrees of freedom of the released H_2O molecule(s) were not allowed, and in the gas phase, ΔG° , considering all degrees of freedom of all species; kcal/mol) at 298.15 K with a standard state of 1 atm for various structures of V-MOFs: (a) Hf-MOF-808-V and (b) Zr-NU1000-V, calculated by M06-L/basis-II//M06-L/basis-I. Electronic energies (ΔE) and Gibbs free energies of reaction are calculated in accordance with eq. 1–3, and thus, the number of water molecules (n) released as a result of $\text{OV}(\text{OH})_3$ deposition over bare MOF node are: $n = 1$ (V3), $n = 2$ (V4, V5a, V5b), $n = 3$ (V6). © American Chemical Society

5.1.5.2 Computed IR Spectral Data

Vibrational spectral features of all model structures shown in Figure 5.1 were investigated to facilitate comparison with experimental structural information. Figure 5.3 presents a series of IR spectra computed for the bare Hf-MOF-808 support and various Hf-MOF-808-V structures, together with experimental IR data²⁴² to simplify comparison. For the bare MOF, the calculated broad peak at $940\text{--}950\text{ cm}^{-1}$ (feature *a*) is due to O–H bending modes of H_2O molecules coordinated to Hf-centers that are hydrogen bonded to Hf–OH groups. Two peaks at $\sim 980\text{--}990\text{ cm}^{-1}$ (*b*) and $\sim 1100\text{--}1120\text{ cm}^{-1}$ (*c*) can be attributed to anti-symmetric and symmetric stretching of the carboxylate group of benzoate linkers, respectively. Finally, the small feature at $\sim 1190\text{ cm}^{-1}$ (*d*) is due to C–H rocking modes of the benzene ring of the benzoate linker.

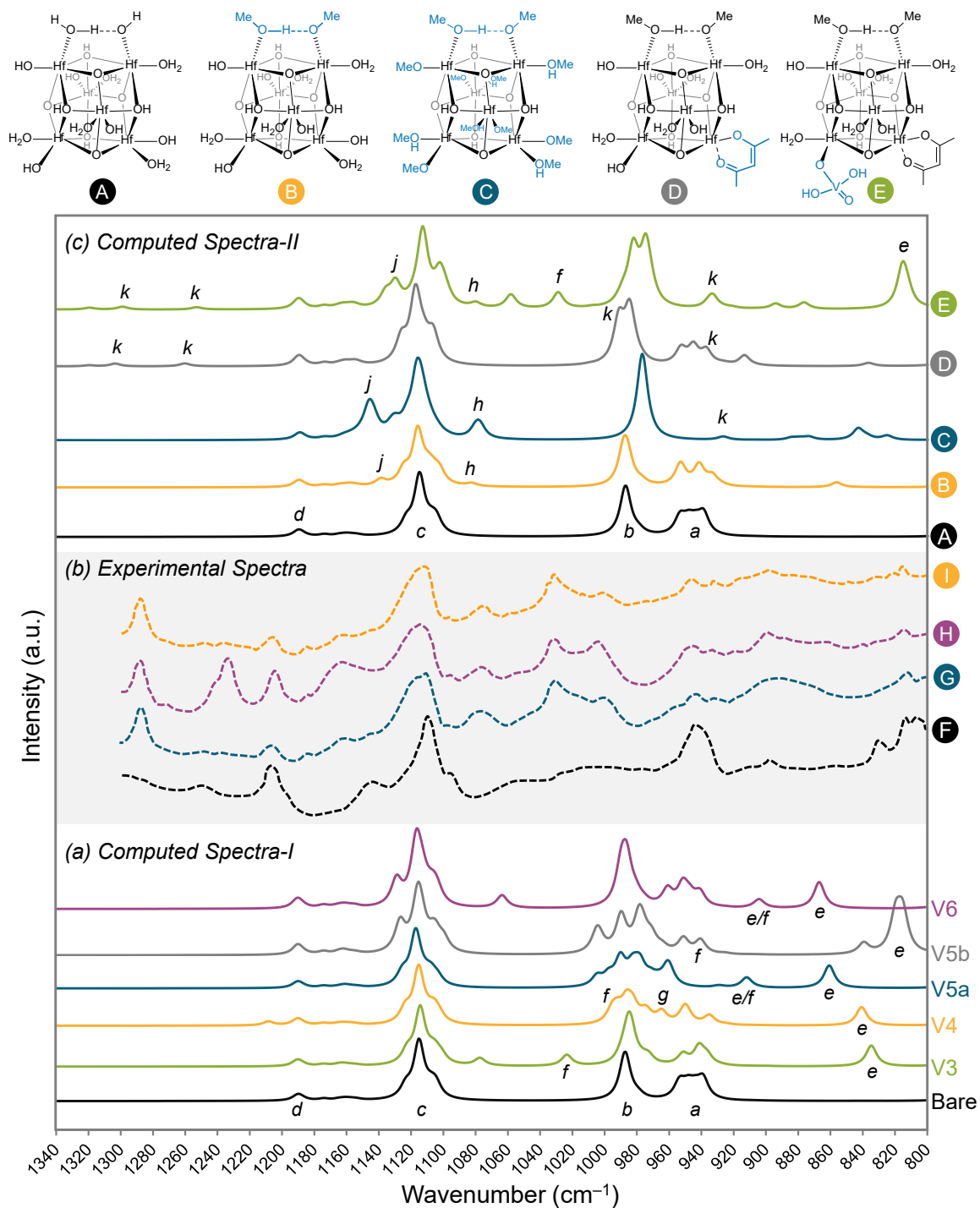


Figure 5.3. (a) Computed IR spectra for the bare Hf-MOF-808 support and various V-MOF structures shown in Figure 5.2a: a, O–H bending modes of H₂O molecules coordinated to Hf centers; b and c, anti-symmetric and symmetric stretching of the carboxylate group of benzoate linkers coordinating Hf₆ cluster, respectively; d, C–H rocking modes of benzoate linkers; e, Hf–O–V stretching modes; f, V=O stretching modes; g, O–H bending modes of hydrogen bonded V–OH. (b) Experimental IR spectra (F–I) in the 800–1300 cm⁻¹ region as reported in ref. 242: (F) bare Hf-MOF-808 at room temperature; (G) Hf-MOF-808-V at room temperature; (H) Hf-MOF-808-V at room temperature, cooled after treating the sample

with heat at 125 °C; (I) Hf-MOF-808-V at room temperature after heating in the presence of humid air. (c) Computed IR spectra (A–E) of bare Hf-MOF-808 (A) and vanadia-deposited Hf-MOF-808-V conformers having various other species (e.g. MeOH, –OMe, acetylacetonate ligand from V^(IV) precursor, VO_x species) available to coordinate to the metal ions at the node under reaction conditions; these species are represented by their line-drawn structures at the top of the figure (A–E, each having the benzoate linker): h, C–O stretching modes of coordinated methanol; j, CH₃ bending modes of coordinated methoxy groups; k, features due to coordinated acetylacetonate ligand. © American Chemical Society

The Hf–O–V stretching modes are calculated at ~850–900 cm⁻¹; this is feature *e* in Figure 5.3, and it is much narrower than the broad peak at ~900 cm⁻¹ found experimentally (Figure 5.3b, line G), thus suggesting the presence of a distribution of closely related V-MOF structures under experimental conditions.

Feature *f* at ~1000 cm⁻¹ in Figure 5.3, was assigned experimentally²⁴² to Hf–O–V out-of-phase bending modes, but this is inconsistent with our calculations, which indicate that this feature is due to V=O stretching modes of some of the structures (e.g. V4).

The transition at 1030 cm⁻¹ was attributed experimentally²⁴² solely to the coordinated acetylacetonate ligand from the vanadium precursor; however, we note that conformer V3 with one bridging oxo, which is thermodynamically the most favorable Hf-MOF-808-V structure, shows an intense peak in this region (*f*) due to V=O stretching modes.

While features at even higher wavenumbers (1080, 1160, 1240 cm⁻¹) were attributed²⁴² to V–O or V=O stretching modes, we were not able to find features above 1040 cm⁻¹ that can be ascribed to such modes. Hence, we considered coordination of other species available under the reaction condition, and the results are shown in Figure 5.3c. In particular, since Hf-MOF-808-V samples were prepared using methanol as solvent,²⁴² we considered methanol binding to the node by replacing water molecules, and we replaced –OH groups at the node with –OMe groups, since such methanolysis has been reported previously for Zr-NU-1000 and Zr-UiO-66 MOFs.²⁵⁷ Figure 5.3c shows that features (*h* and *j*) at 1080 and 1140 cm⁻¹ are due to both methanol and the methoxy groups, and are likely present at the active site of the catalyst.

5.1.5.3 Reaction Mechanism on Zr-NU-1000

Since the V5a-NU1000 conformer (Figure 5.2) was computed to be the most favored Zr-NU-1000-V species thermodynamically, we next explored the mechanism of the selective oxidation of benzyl alcohol (BnOH) to benzaldehyde (PhCHO) using V5a-NU1000 as the catalyst, and the results are in Figure 5.4. The first step involves chemisorption of the BnOH substrate onto the V-MOF catalyst, which can occur either at the V–OH bond of the VO_x species (site V), or over the M–OH (M = Hf or Zr) bond of the node (site S), resulting either a V–OBn/M–OH (green path) or a V–OH/M–OBn (blue path) pair respectively.²⁵⁸ The resulting chemisorbed INT1 is a closed-shell singlet species. Next, a hydrogen-atom is transferred from the methylene group of INT1 to the vanadyl bond (V=O) to generate a triplet biradical intermediate (INT2) with an open-shell V^(IV) species and a resonance-stabilized organic radical. The transition state (TS2) connecting INT1 to INT2 is calculated as a broken-symmetry determinant having $M_s = 0$ but $\langle S^2 \rangle$ greater than 0.^{247,211} The corresponding spin-restricted solution is 1.4 kcal/mol higher in energy ($\Delta G^\ddagger = 32.4$ vs. 33.8 kcal/mol). The analogous TS on the triplet surface is much higher in energy ($\Delta G^\ddagger = 63.1$ kcal/mol) and is not relevant for discussing reactivity.

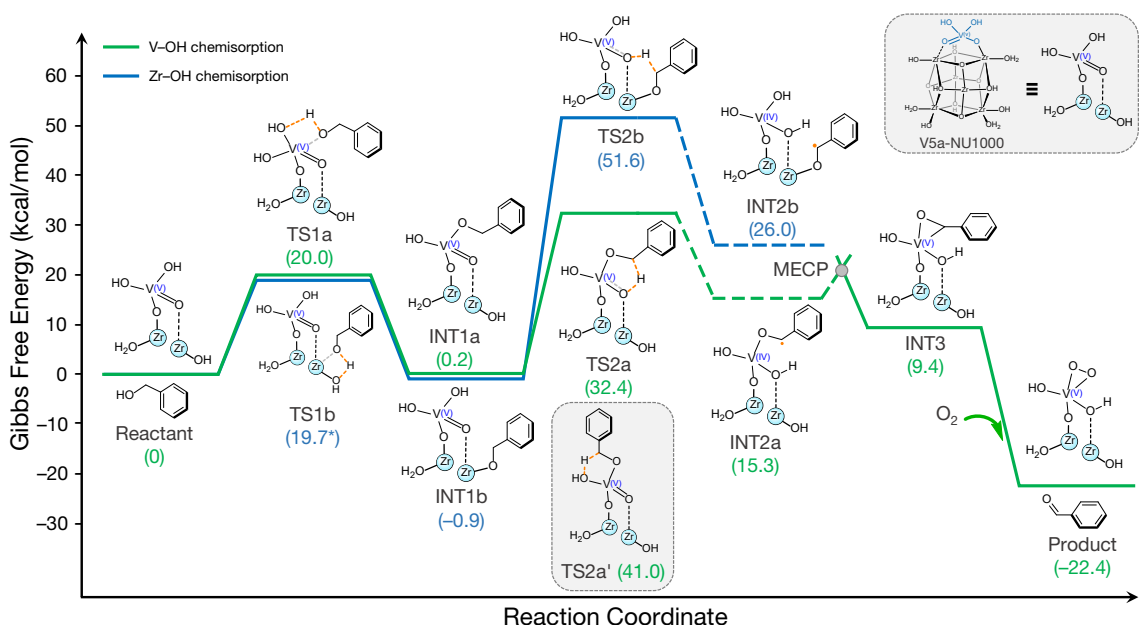


Figure 5.4. Standard-state free energies and free energies of activation (kcal/mol) calculated by M06/basis-II//M06/basis-I for oxidation of benzyl alcohol to benzaldehyde. The green line describes alcohol chemisorption at a V–OH bond and subsequent benzyl C–H bond activation, and the blue line represents reactivity via chemisorption at a Zr–OH bond. The singlet intermediates (INT1a/1b) are spin-

symmetry stable, but the transition-state structures TS2a/2a'/2b are calculated as broken-symmetry singlets, and INT2a/2b are triplets. Note that for TS1b geometry, not all convergence criteria were met, and the energy is an estimated upper bound. The minimum energy crossing point (MECP) between INT2a (triplet) and INT3 (singlet) was not located. © American Chemical Society.

The two radical centers on INT2 then recombine to yield a $V^{(V)}$ intermediate involving a V–O–C metallacycle (INT3). Finally, two-electron reduction of the vanadia center releases benzaldehyde while generating a transient $V^{(III)}$ species which is readily reoxidized by molecular oxygen into a cyclic $V^{(V)}$ -peroxo intermediate (Product).

Figure 5.4 demonstrates that passage through TS2 is the turnover-limiting (TOL) step of the overall catalytic cycle. It also shows that for Zr-NU-1000-V, HAA at site V (green path; TS2a) is more favorable than at site S (blue path; TS2b) by ~ 20 kcal/mol. To determine whether the V–OH bond or the vanadyl V=O bond preferentially abstracts the H-atom (TOL step), we explored both possibilities (TS2a and TS2a', respectively). Figure 5.4 shows that abstraction by the vanadyl group is preferred to that by the V–OH group by ~ 8.6 kcal/mol.

Table 5.1. Computed Free Energies of Activation (ΔG^\ddagger , kcal/mol) for HAA from Benzylic Position of the Substrate at Two Adsorption Sites Using Various V-MOF Catalysts.^a

V-MOF Structure	ΔG^\ddagger for C–H Activation	
	V-adsorbed (Site V)	Support adsorbed (Site S)
V2 (Hf-MOF-808)	39.1	42.3
V3 (Hf-MOF-808)	35.1	41.9
V4 (Hf-MOF-808)	40.8	43.5
V5 (Hf-MOF-808)	38.5	32.2
V6 (Hf-MOF-808)	43.5	36.9
V5 (Zr-NU-1000)	32.4	52.5
V5 (Zr-MOF-808)	40.9	32.1

^aM06/basis-II//M06/basis-I level at 298.15 K.

Comparing the results presented in Table 5.1, we note that the MOF architecture has a greater influence over the specific V-MOF's catalytic activity, rather than the identity of the metal (M) constituting the M_6 cluster of the node. Consistently, within the MOF-808 architecture, both V5 (Hf-MOF-808-V) and V5 (Zr-MOF-808-V) conformers have similar activation barrier for the turn-over-limiting C–H activation step, $\Delta G^\ddagger \sim 32$ kcal/mol, and both prefer a mechanism where

the substrate adsorbs over the M–OH bond ($M = \text{Hf}, \text{Zr}$) of the MOF-support in the first step. On the other hand, when the MOF support was changed to a whole different architecture in Zr-NU-1000, the preferred route for substrate oxidation occurs via adsorption over the V–OH bond of the vanadium site.

5.1.5.4 IBO Analysis for C–H Activation on Zr-NU-1000: HAT vs. cPCET.

We then examined the question of whether the TOL C–H activation process involves a hydrogen-atom transfer (HAT) pathway or a concerted proton-coupled electron transfer (cPCET) route, since a difference in mechanism could be associated with a significant difference in the observed rate of the reaction.²¹¹ We note that the nomenclature classifying an HAA process as HAT or cPCET is not unique, but here we use the label HAT for a process in which an electron and a proton from the C–H bond travel to the same acceptor site, whereas a cPCET mechanism involves them ending on different acceptor centers. Typically, a cPCET reaction is faster than a synchronous HAT process.

To distinguish these alternatives, we used the intrinsic bond orbital (IBO) localization scheme²⁵⁹ and followed the relevant charge flow along the minimum energy path (MEP) through TS2a at site V; this procedure has been used previously to distinguish these cases.^{211,260} Panel *a* of Figure 5.5 shows the electronic energy (including nuclear repulsion) along the MEP, and panel *b* shows the evolution of the IBOs. Panel *b* shows that as the proton is transferred from the C–H bond in $\text{V}^{(\text{V})}\text{--OBn}$ to the vanadyl oxygen atom, the acceptor site for the electron is the $\text{V}^{(\text{V})}$ ion, and this transfer forms a $\text{V}^{(\text{IV})}\text{--OH}$ bond. This result is summarized schematically in panel *c* of Figure 5.5. We conclude that the TOL step in the C–H activation mechanism is best described as a cPCET process. This is in agreement with the cPCET characterization of the activation of the methanol C–H bond at single vanadia sites supported on flat ceria surfaces.^{247b} The same cPCET mechanism is also followed for HAA via both TS2b and TS2a' (ref. 261).

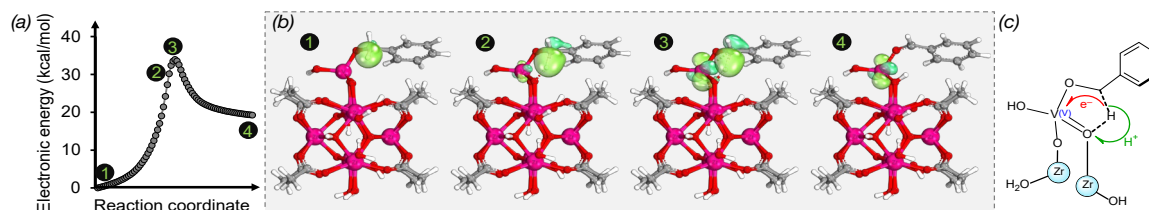


Figure 5.5. (a) Change in electronic energy (computed by spin-unrestricted M06/basis-I) along the minimum energy path through TS2a for hydrogen-atom abstraction from the methylene group of the chemisorbed benzyl alcohol. (b) Intrinsic bond orbitals of the C–H bond corresponding to the calculations in panel a. (c) A simplified representation of the proton and electron transfer process. © American Chemical Society.

5.1.6 Conclusions

A systematic search for structures of vanadia-deposited MOF (V-MOF) was performed, and key structures are reported for both Zr-NU-1000-V and Hf-MOF-808-V. Their IR spectra was computed and compared to experimentally collected²⁴² IR data. Their catalytic pathways for selective oxidation of benzyl alcohol to benzaldehyde were reported. The main results of this study can be summarized as:

- 1) The local structure of the vanadia anchored at the node of the MOF includes some methanol and the methoxy groups that correspond to the IR features measured experimentally. This computational study thus shows for the first time a local structure of the V-MOF catalyst that is compatible with all structural information available experimentally.
- 2) The catalytic activity of vanadia anchored at the MOF is highly dependent on the topology of the supporting node. While Zr-NU-1000 favors selective oxidation of benzyl alcohol yielding benzaldehyde via chemisorption at a V–OH bond, Hf-MOF-808 and Zr-MOF-808 prefer activation of the substrate via chemisorption at a Hf–OH or Zr–OH bond of the support. These results suggest that the MOF architecture is more important in controlling catalysis by V-MOFs rather than the identity of the metal on the node.
- 3) By using localized bond orbitals and following their transformation along the reaction coordinate, we obtained a detailed picture of the electron flow during the turnover-limiting C–H bond activation process. In all of the cases studied, we characterize this as a concerted proton-coupled electron transfer (cPCET) process.

The insight obtained in this study can be exploited for strategic tuning of reactivity and selectivity of V-MOF catalysts by changing the nature of the support material either by using a different MOF architecture or by using different metals on the node, although the former will likely have a greater impact on the catalytic performance.

5.1.7 Appendix

5.1.7.1 Detailed Exploration of Conformers for Hf-MOF-808-V Having Acetate Linker

An in-depth exploration of Hf-MOF-808-V conformers were undertaken using the acetate linkers. The mechanism of VO_x -species attachment to the node is explained in Figure 5.6.

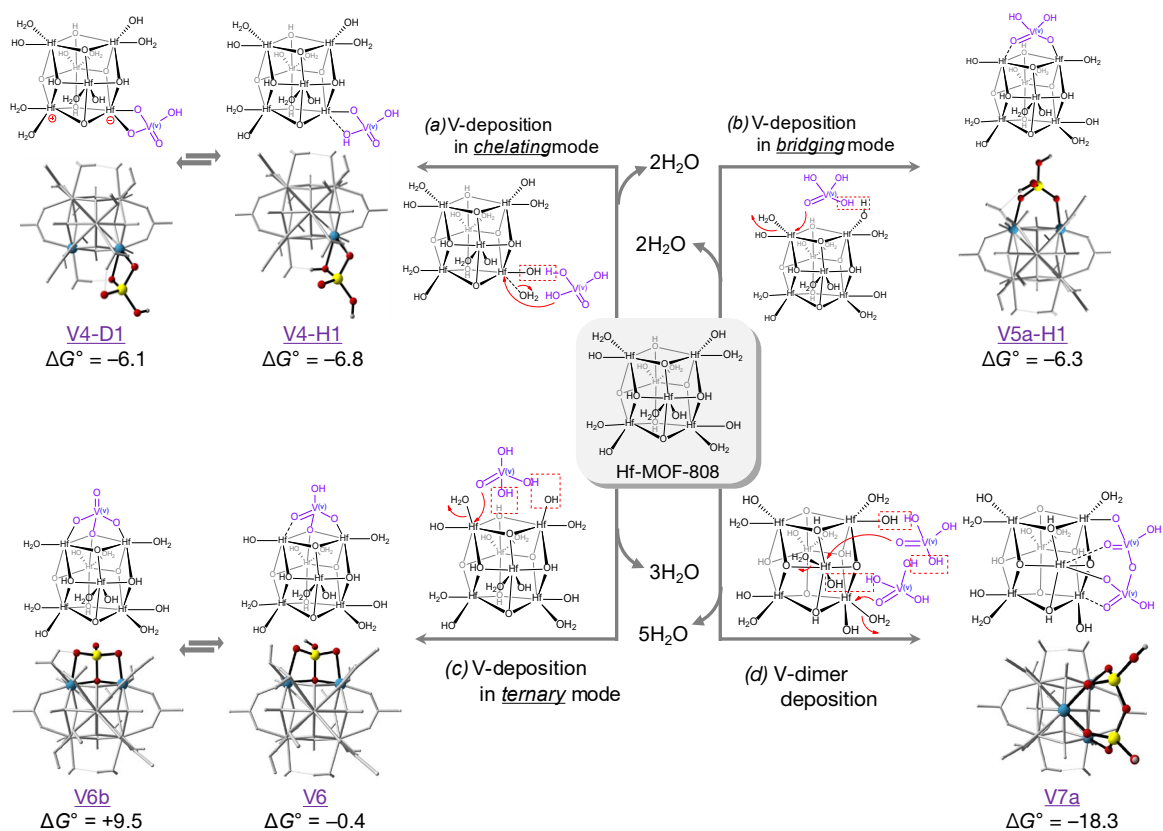


Figure 5.6 Key modes for VO_x deposition on Hf-MOF-808 (**acetate** linker), along with their computed reaction free energies. Gibbs free energies are reported in kcal/mol computed at M06-L/basis-II//M06-L/basis-I level of theory at 298.15K.

5.1.7.2 IR Spectral Data

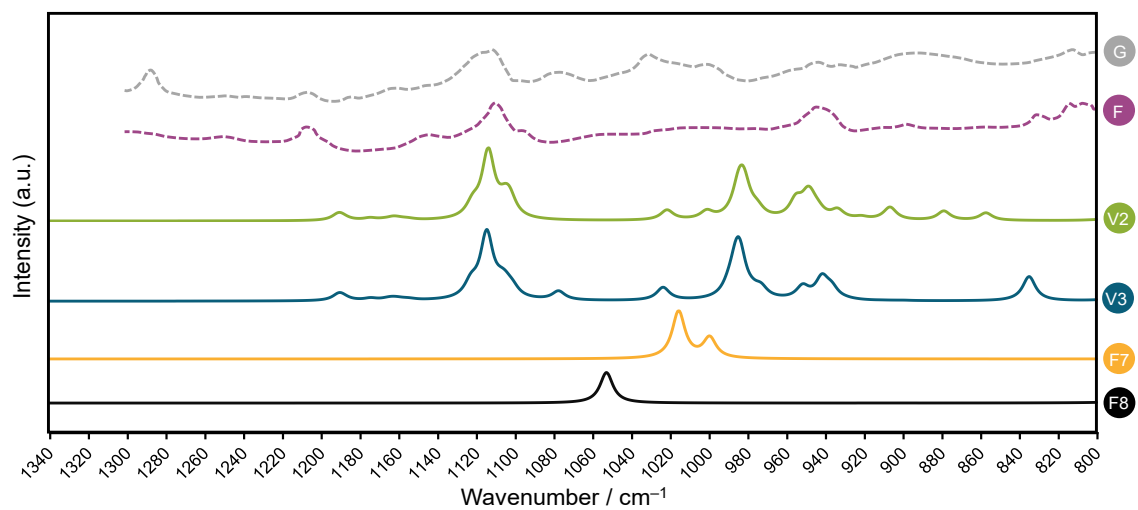


Figure 5.7 Computed IR data for model vanadium dioxo (F7) and mono-oxo (F8) species, Hf-MOF-808-V conformers V2 and V3, compared against experimental IR spectra of bare Hf-MOF-808 (H) and Hf-MOF-808-V (G) at room temperature. Note that M06-L/basis-I vibrational frequencies were scaled by a factor of 0.958.

5.2 Enhanced Activity of Heterogeneous Pd(II) Catalysts on Acid Functionalized MOFs

5.2.1 Introduction

Single-site heterogeneous catalysts (SSHCs) supported on solid substrates have helped develop strategies for designing efficient catalysts by facilitating the determination of the location of active sites and the mechanism of catalytic cycles.^{232,238,262} Because SSHCs largely improve atom economy and energy efficiency, some SSHCs have already been synthesized on an industrial scale and commercialized.²⁶³ Recently, SSHCs supported on acidic oxides have received significant attention as a result of their unique catalyst–support interactions provided by the presence of strong Brønsted and Lewis acidic sites on the support’s surface.^{264,265a-b} For example, organometallic catalysts anchored on sulfated oxides yield ‘cationic’ metal centers which exhibit higher activities in olefin polymerization and olefin hydrogenation compared to the organometallic catalyst or oxide analogue alone.^{264a-b} Various metal oxides, including zirconia,²⁶⁴ iron oxide,^{265a} alumina^{265b-c} and titania,^{265c,266a} have been acidified by sulfation or phosphation to support SSHCs.

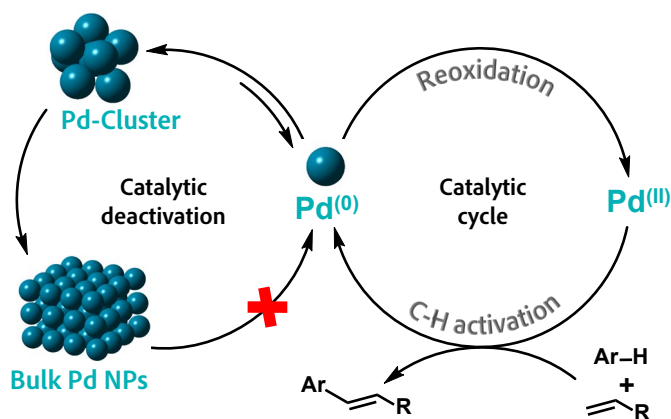
Porous metal oxide scaffolds are particularly attractive because the potential grafting sites within the material are also accessible, and this results in more active sites per gram of the catalyst.^{266b-d} However, porous metal oxides lack structural tunability as a result of the harsh synthetic conditions (high temperatures and pressures), and the anchored catalyst species can be challenging to characterize owing to ill-defined pore structures of the metal oxide support.

Due to their uniformity, metal–organic frameworks (MOFs), which are infinite coordination networks of metal ions or inorganometallic clusters bridged through organic linkers, have been utilized as support materials^{264–267} to allow for observation of anchored SSHCs through crystallographic techniques. We and others have characterized newly installed catalytic species in MOFs, which can be introduced using post-synthetic modification methods such as vapor-phase atomic layer deposition in MOFs (AIM)²⁶⁸ and solution-phase solvothermal deposition in MOFs (SIM).²⁶⁹ Akin to SIM, MOF nodes can be functionalized post-synthetically with oxyanions in solution, given that the MOF has open metal sites and is stable under acidic conditions.^{270a-b}

Zirconium-based MOFs, like MOF-808^{270c} consisting of Zr₆-oxide cluster nodes connected by benzene-1,3,5-tricarboxylate linkers, make excellent candidates for the incorporation of oxyanions. Previously, Jiang et al.^{270d} have deposited sulfate ions on the nodes of MOF-808, to create a solid-state superacid capable of performing a host of acid-catalyzed reactions. Also, while we were preparing this manuscript, an important and elegant study using sulfated MOF-808 for highly efficient isobutene dimerization catalyst was published by Yaghi and co-workers.²⁷¹

Apart from behaving as a catalyst, these coordinated oxyanions can be further utilized as anchoring sites for metal ions, such as palladium, to create SSHCs within the solid substrates.²⁷² Palladium is a great catalyst for C–H activation and C–C bond forming reactions.²⁷³ Recently, the developments in oxidative coupling reactions have provided new approaches for C–C bond formation using Pd^(II)/Pd⁽⁰⁾ catalytic cycles.²⁷⁴ In these reactions, the dissociation, and subsequent agglomeration of Pd(0), is the primary catalyst deactivation pathway (Scheme 5.2). Therefore, stabilizing the Pd(II) active sites is paramount.

Scheme 5.2 The catalytic cycle and deactivation of oxidative Heck catalyst. NPs = nanoparticles, Ar = aryl group



Herein, single crystals of phosphated and sulfated hafnium-based⁴⁴ MOF-808 (Hf-MOF-808-PO₄ and Hf-MOF-808-SO₄), were employed as heterogeneous catalyst supports for palladium oxidative coupling catalysts. The structures and properties of these MOFs were elucidated by various techniques, including infrared (IR) spectroscopy, single-crystal X-ray diffraction (SCXRD) analyses, and potentiometric acid–base titrations. Then, Pd(II) was installed on Hf-

MOF-808, Hf-MOF-808-PO₄ and Hf-MOF-808-SO₄. From X-ray photoelectron spectroscopy (XPS) measurements, acid functionalization of the MOF Hf₆-oxide nodes was found to largely improve the stability of incorporated Pd(II). SCXRD studies indicated that the palladium atoms were positioned on the nodes of the acid-ligated MOFs. Further, the presence of sulfate or phosphate improved the catalytic ability of Hf-MOF-808 in the oxidative Heck reaction, suggesting stabilization of Pd(II) by the acid sites. Our understanding of the results was enhanced by detailed electronic structure calculations employing density functional theory.

5.2.2 Results and Discussions

5.2.2.1 Phosphation and Sulfation of Hf-MOF-808

Phosphoric and sulfuric acid functionalizations of the nodes of Hf-MOF-808 were performed by soaking the parent MOF in diluted H₃PO₄ and H₂SO₄ solutions, respectively. Inductively coupled plasma optical emission spectroscopy (ICP-OES) measurements indicated 2.4 phosphorous and 2.4 sulfur atoms per Hf₆-oxide node for Hf-MOF-808-PO₄ and Hf-MOF-808-SO₄, respectively. In addition, the infrared (IR) spectra showed vibrational bands characteristic of phosphate and sulfate groups in the respective MOFs. Furthermore, the oxyanion locations were successfully determined by SCXRD measurements as illustrated in Figure 5.8(a–d), which showed that Hf-MOF-808-PO₄ and Hf-MOF-808-SO₄ are isostructural. The phosphate and sulfate groups were observed on the bridging positions of the Hf₆-oxide node with average P–O(node) and S–O(node) distances of 1.57 and 1.70 Å, respectively. These phosphated and sulfated MOFs were then used as heterogeneous supports to see if they alter the property and functionality of an incorporated catalytic site.

Palladium was incorporated inside Hf-MOF-808, Hf-MOF-808-PO₄ and Hf-MOF-808-SO₄ using the SIM method. Palladium acetate was dissolved in dichloromethane solution containing the MOFs. Striking color changes were observed; Hf-MOF-808 changed from a white to dark brown powder (Pd@Hf-MOF-808 here after), while Hf-MOF-808-PO₄ and MOF-808-SO₄ changed from white to dark-reddish color (hereafter labeled Pd@Hf-MOF-808-PO₄ and Pd@Hf-MOF-808-SO₄). The dark color of Pd@Hf-MOF-808 indicates the formation of Pd nanoparticles

(NPs) during Pd-SIM process. Transmission electron microscopy (TEM) images of Pd@Hf-MOF-808 verified the presence of Pd NPs inside and outside of MOF crystals. No evidence of NP formation was found in the oxyanion functionalized MOFs. ICP results of these Pd-SIM MOFs indicated the incorporation of approximately 2 palladiums per MOF node without leaching of phosphate or sulfate groups.

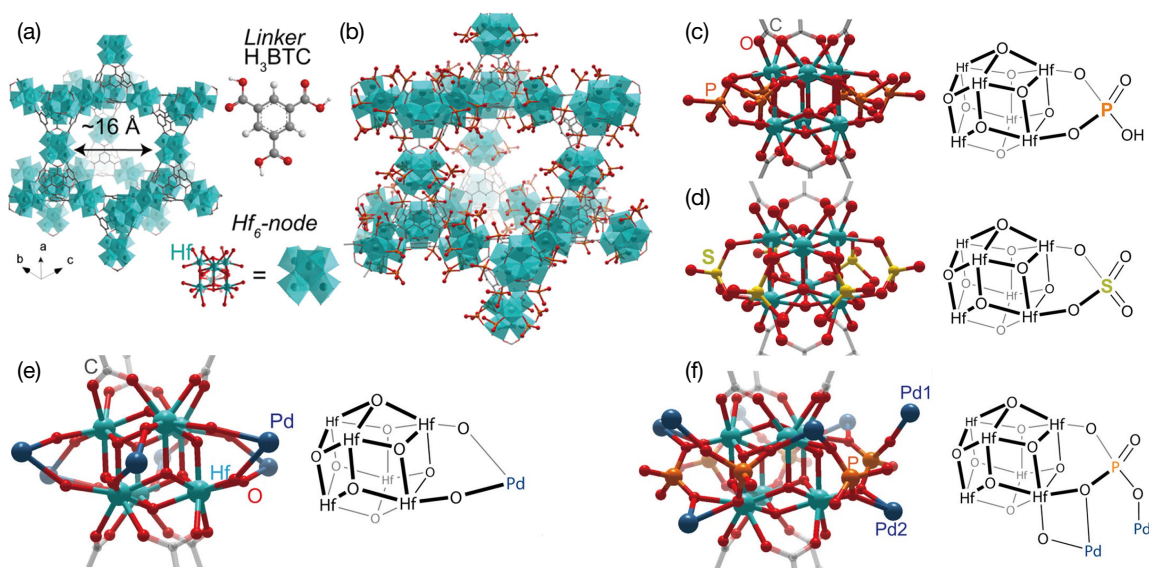


Figure 5.8 (a) Crystal structures (100 K) of Hf-MOF-808 and (b,c) the crystal structures after phosphation and (d) sulfation. Occupancies of SO_4 and PO_4 are 40% (2.4 S and 2.4 P per Hf_6 node). (e,f) Crystal structures of Pd(II) sites incorporated in MOFs at 100 K. Representation of the Pd(II) site on the node of Pd@Hf-MOF-808 (e) and representation of two different Pd(II) sites on the node of Pd@Hf-MOF-808- PO_4 (f). © American Chemical Society

To determine the oxidation states of Pd species inside the MOFs, XPS measurements were performed which showed two components corresponding to the presence of both Pd(0) and Pd(II) species. This result is consistent with the TEM evidence of nanoparticle formation during the sample preparation, as well as, the presence of Pd(II) at the grafting sites on the MOF nodes. For Pd@Hf-MOF-808- PO_4 and Pd@Hf-MOF-808- SO_4 , the binding energies of Pd 3d levels showed single-component Pd(II) species. Interestingly, with increasing palladium content, the Hf 4f binding energies in Pd@Hf-MOF-808- SO_4 remained unaffected, implying that the Pd(II) resides on the sulfate sites. Meanwhile, gradual shifts were observed for the Hf 4f binding energies on Pd@Hf-MOF-808 and Pd@Hf-MOF-808- PO_4 , implying there is an interaction between the incorporated Pd(II) sites and the oxygen directly bound to the Hf-node. In the Raman spectra,

the intensities of P=O and S=O stretching vibration modes become weaker after Pd-SIM, suggesting that the Pd(II) species are coordinated on oxyanions on MOF nodes for Pd@Hf-MOF-808-PO₄ and Pd@Hf-MOF-808-SO₄.

To further understand the Pd(II) sites in the MOFs, SCXRD analyses were conducted (Figure 5.8). For Pd@Hf-MOF-808, a single-ion Pd(II) site was observed bridging between two terminal oxygens on adjacent Hf atoms on the node (Figure 5.8e). The Pd(II) site was disordered between two crystallographically equivalent positions with Pd–O distances of 2.27 Å. In addition to palladium, acetate was observed to coordinate to the Hf₆-oxide node, replacing a pair of terminal aqua and hydroxyl groups. In the case of Pd@Hf-MOF-808-PO₄, several different binding motifs were present compared to those in Pd@Hf-MOF-808 (Figure 5.8f). One Pd(II) site was observed on the chelating position (Pd1) with Pd–O distance of 2.25 Å and the other Pd(II) site was observed on the phosphate oxygen (Pd2) with 1.91 Å. Here, the crystallographically determined Pd amount (0.9 Pd per Hf₆-oxide node) is less than half of the ICP result (2.2 Pd per Hf₆-oxide node), implying that the incorporated palladium ions are disordered in several sites around sulfates with small occupancies.

5.2.2.2 Stability of the Coordinated Pd(II) Species in an H₂ Atmosphere

As described previously, Pd nanoparticles formed during the preparation of Pd@Hf-MOF-808. In contrast, in the cases of the phosphated and sulfated MOFs, Pd@Hf-MOF-808-PO₄ and Pd@Hf-MOF-808-SO₄, only Pd(II) sites were successfully incorporated, and there was no significant decomposition to Pd(0) nanoparticles. These results suggest the improved stability of Pd(II) on the acid functionalized MOFs over the parent Hf-MOF-808. To test this stability, the Pd-SIM MOFs sat under a 2% H₂ atmosphere for 12 hours, and Pd(II) reduction was monitored by XPS measurements. Less Pd(II) reduced to Pd(0) in Pd@Hf-MOF-808-PO₄ and Pd@Hf-MOF-808-SO₄ compared to the result for Pd@Hf-MOF-808. This result can be rationalized by the existence of the weak conjugate bases electrostatically interacting and stabilizing Pd(II) on the nodes of the acid functionalized MOFs as reported previously with the sulfated oxides.^{264a–b,266a}

5.2.2.3 Catalytic Reactions

Having confirmed the presence and the improved stability of Pd(II) sites in the acid functionalized MOFs, we expected higher Pd(II) catalytic activity in these MOFs as compared to the parent MOF. In the oxidative Heck reaction, Pd(II) is the catalytic active species for carbon-carbon bond formation. Specifically, the C–H alkylation reaction of 2-phenylphenol (**501**) with ethyl acrylate was chosen as the model reaction (Figure 5.9).²⁷⁵ The reaction was performed in a suspension of the MOFs (5 mol% of Pd to the substrate **501**) as the catalyst, Cu(II)/O₂ as the oxidizing agent, and 2-methylbutanol as the solvent. As shown in the reaction time profiles (Figure 5.9), Pd@Hf-MOF-808-PO₄ and Pd@MOF-808-SO₄ show higher yields and faster conversions than when using Pd@Hf-MOF-808, as predicted from Pd(II) stability studies. The loss of catalytic activity over time was observed in all Pd-SIM MOF reactions because of nanoparticle formation. These nanoparticles likely block the pore apertures in MOFs, resulting in no activity when the MOF is recycled, despite the persistence of some Pd(II) sites observed by XPS spectra. Turnover frequencies (TOFs) of these catalysts under differential conditions (10 % conversion) were calculated to be 0.06 ± 0.01 h⁻¹ for Pd@Hf-MOF-808, 0.33 ± 0.03 h⁻¹ for Pd@Hf-MOF-808-SO₄, and 0.93 ± 0.02 h⁻¹ for Pd@Hf-MOF-808-PO₄. The acid functionalizations of the MOF resulted in more than 5-fold (Pd@Hf-MOF-808-SO₄) and 15-fold (Pd@Hf-MOF-808-PO₄) rate enhancements compared to bare Pd@Hf-MOF-808.

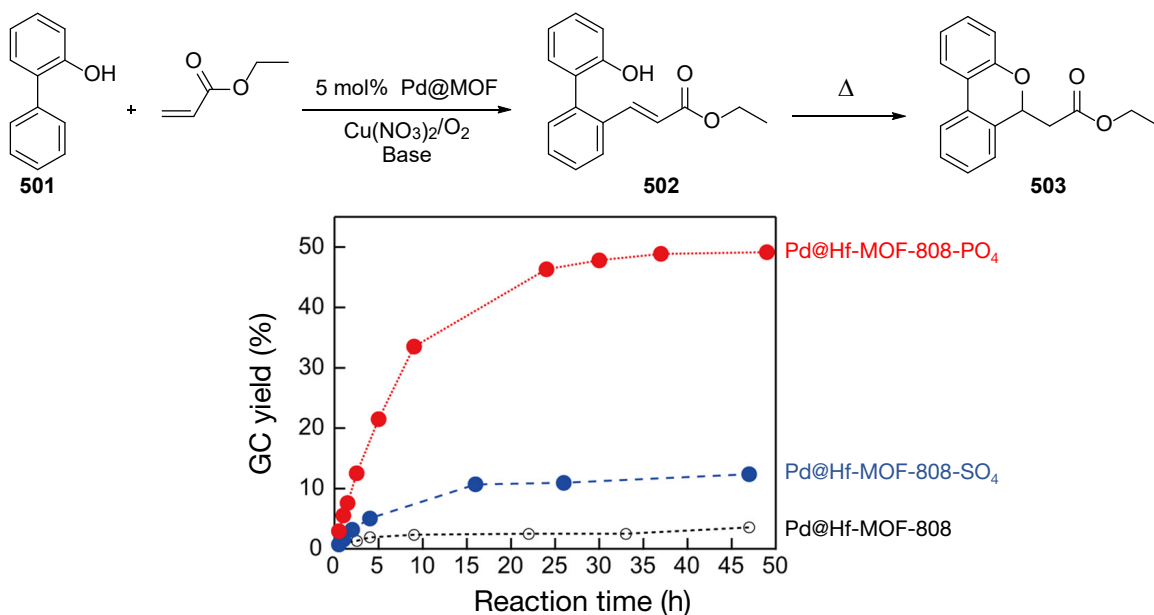
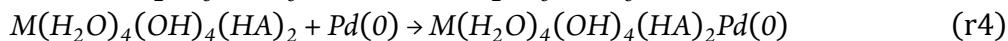
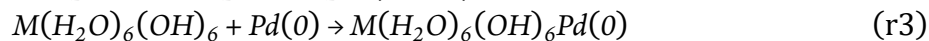
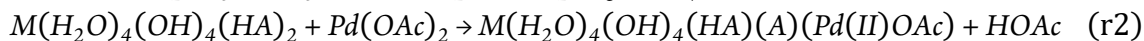
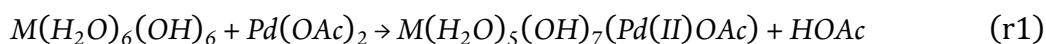


Figure 5.9 Reaction scheme of the C–H activation reaction of 2-phenylphenol (**501**) with ethyl acrylate to form (**502**) along with reaction time profiles for the catalytic formation of **502**. Black open circles, blue filled circles, and red filled circles represent the reaction time profiles for Pd@Hf-MOF-808, Pd@Hf-MOF-808-SO₄, and Pd@Hf-MOF-808-PO₄, respectively. © American Chemical Society

5.2.2.4 Computational Characterization

To further probe the effects of phosphate and sulfate functionalization on the relative stability of Pd-SIM MOF-808, we performed density functional calculations of the energies of relevant reactants and possible reactive intermediates. We consider the overall energetics for the following four reactions:



where $M = Hf_6(\mu_3-O)_4(\mu_3-OH)_4$ and $A = HPO_4^{2-}$ or SO_4^{2-} . We investigated all possible structures of the products of (r1)–(r4) and of the reactants of (r2) and (r4). The lowest-energy conformers of the reactants of (r2) and (r4) are named PO₄-2,5-3,5 and SO₄-1,1-4,4-C and are expected to be the dominant structures for Hf-MOF-808-SO₄ and Hf-MOF-808-PO₄; these structures are shown in Figure 5.10. Our detailed study shows (see ref 244) that in addition to these key conformers, other low-energy structures may also be present, particularly if the distribution of structures is not fully equilibrated during the acidification process.

Starting from the two lowest-energy structures for the phosphate and sulfate acidified species, we have calculated the reaction free energies for the depositions of Pd(OAc)₂ and Pd(0) at all possible sites and compared these with the analogous lowest free energies of reaction on unmodified Hf-MOF-808. The reaction energies for the most favorable processes and their corresponding structures are given in Figure 5.10. We note, again, that while the lowest-energy isomer is shown in Figure 5.10, there are other isomers within an energy range that may well be accessible under kinetic conditions, and indeed the siting of the Pd atoms in the various Pd(OAc)-decorated structures spanning that accessible energy range is consistent with the multiple positions identified in the crystal structure of phosphate acidified Hf-MOF-808. Thus, while the

Pd(II)@PO₄-2,5-3,5-o5o5 structure shown in Figure 5.10 has the Pd atom in a position consistent with crystallographic site 2, several relatively low-energy structures are also possible (see ref 244) where the Pd atom is in a position consistent with crystallographic site 1.

Returning to thermodynamic considerations, the reaction free energy for the deposition of Pd(OAc)₂ on Hf-MOF-808 is -5.2 kcal/mol for the Pd(II)@H₂O-1,2 conformer (-3.2 kcal/mol for the Pd(II)@H₂O-1,2 conformer), which is, to within the expected error of the model, essentially equal to that on Hf-MOF-808-SO₄ (-4.9 kcal/mol) and that on Hf-MOF-808-PO₄ (-4.0 kcal/mol). Interestingly, the deposition of Pd(OAc)₂ on Hf-MOF-808-PO₄ is exergonic (-8.3, -3.2, -2.5, -4.0 kcal/mol) for all the possible conformers of Hf-MOF-808-PO₄,²⁴⁴ while this deposition is endergonic (6.5, 6.0, 4.3 kcal/mol) for most conformers of Hf-MOF-808-SO₄, the only exception being the -4.9 kcal/mol value just noted for the SO₄-1,1-4,4-C conformer shown in Figure 5.²⁴⁴

The Gibbs free energy for Pd(0) binding on Hf-MOF-808 is -26.0 kcal/mol, which is much less favorable than predicted for Hf-MOF-808-SO₄ (-36.4 kcal/mol) or Hf-MOF-808-PO₄ (-40.4 kcal/mol). This suggests that the dominant role of the acidic groups in fostering increased catalyst lifetime may be to stabilize adsorbed Pd(0), thereby slowing down the diffusion of Pd atoms to form Pd nanoparticles.

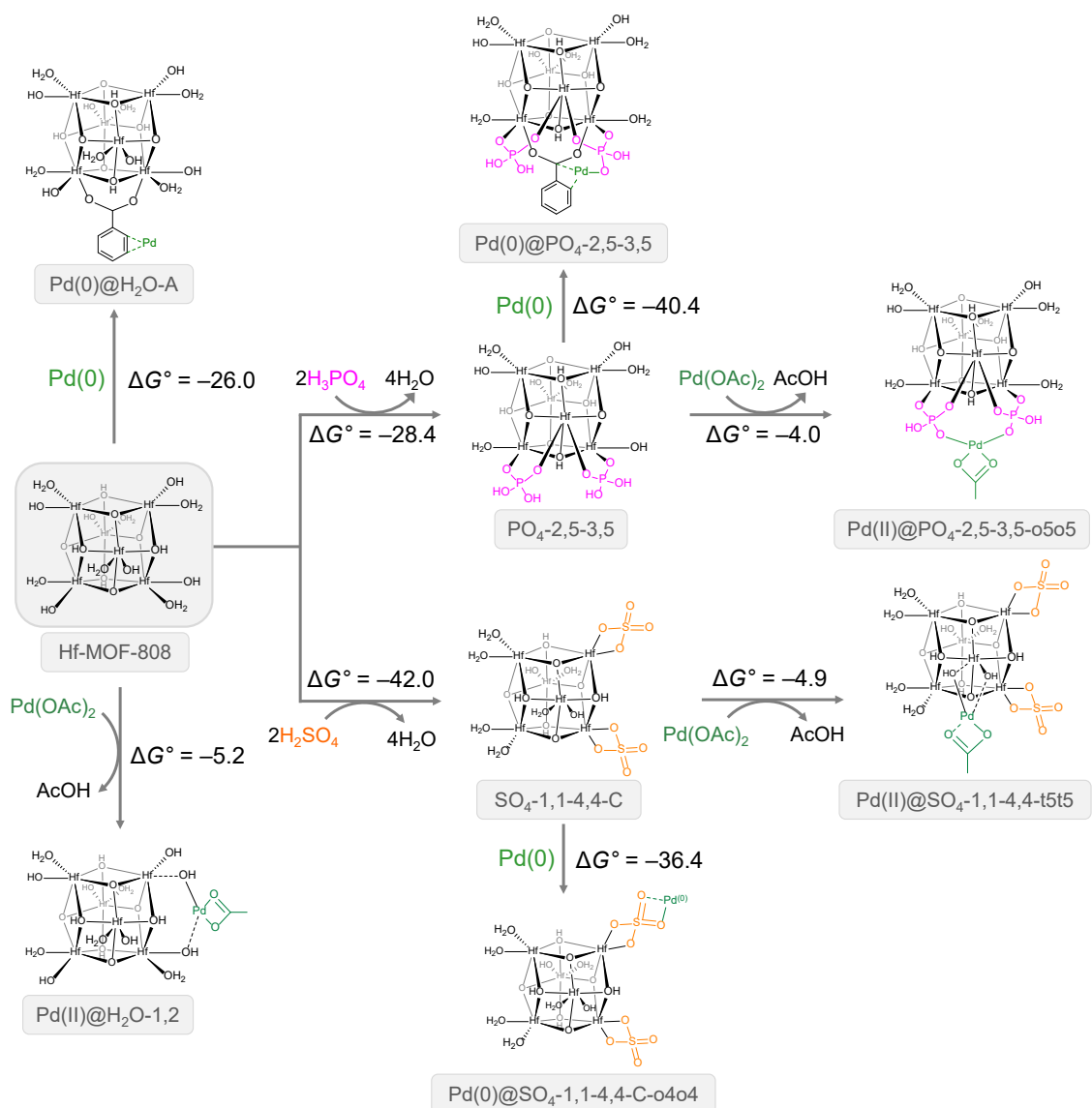


Figure 5.10 The reaction network for the formation of Pd(II)@Hf-MOF-808 and Pd(0)@Hf-MOF-808 with or without phosphate or sulfate modification. The Gibbs free energies of reaction ΔG° (kcal/mol) are calculated at 298.15 K, with standard state of 1 atm for gases and 1 M for solutes and including the solvation effect of dichloromethane. In compound names, we use the shorthand SO_4 , PO_4 , and H_2O for Hf-MOF-808- SO_4 , Hf-MOF-808- PO_4 , Hf-MOF-808, respectively.

5.2.3 Conclusion

The acid functionalized MOFs, Hf-MOF-808- PO_4 and Hf-MOF-808- SO_4 have been synthesized and investigated for their ability to serve as catalyst supports of a Pd(II) SSHC. The structures of single-ion Pd(II) sites incorporated in as-synthesized, phosphated and sulfated Hf-MOF-808 were characterized through XPS, vibrational spectroscopies, single-crystal structural analyses, and

quantum mechanical calculations. In the case of Hf-MOF-808, the Pd(II) was observed directly coordinated to the Hf₆-oxide node. In contrast, the Pd(II) coordination motifs in the phosphate functionalized MOF were drastically different. Stability tests of these Pd(II) sites under an H₂ atmosphere revealed that phosphate and sulfate groups on the node improved the stability of Pd(II) sites as compared to the bare MOF. These stabilized Pd(II) sites in Hf-MOF-808-PO₄ and Hf-MOF-808-SO₄ showed better catalytic activity in the oxidative Heck reaction, where Pd(II) is the catalytic active site. The density functional calculations also suggest that the node functionalization increases the catalyst lifetime compared to that of the pristine MOF by reducing the mobility of Pd(0) atoms that can otherwise agglomerate into unreactive nanoparticles when generated as part of the catalytic cycle. These findings provide insights on the design and methodology to creating more efficient catalysts. Our ongoing work focuses on utilizing these acid functionalized MOFs as catalyst support for other catalytic reactions, including olefin polymerization and hydrogenation.

Bibliography

- (1) Mardirossian, N.; Head-Gordon, M. Thirty Years of Density Functional Theory in Computational Chemistry: An Overview and Extensive Assessment of 200 Density Functionals. *Mol. Phys.* **2017**, *115*, 2315–2372.
- (2) Cramer, C. J. *Essentials of Computational Chemistry: Theories and Models, 2nd Edition*; Wiley, 2004.
- (3) (a) Hartree, D. R. The Wave Mechanics of an Atom with a Non-Coulomb Central Field. Part II. Some Results and Discussion. *Math. Proc. Cambridge Philos. Soc.* **1928**, *24*, 111–132. (b) Hartree, D. R. The Wave Mechanics of an Atom with a Non-Coulomb Central Field. Part III. Term Values and Intensities in Series in Optical Spectra. *Math. Proc. Cambridge Philos. Soc.* **1928**, *24*, 426–437.
- (4) Levine, I. N. *Quantum Chemistry*, 7th ed.; Pearson, 2013.
- (5) Slater, J. C. The Theory of Complex Spectra. *Phys. Rev.* **1929**, *34*, 1293–1322.
- (6) (a) Roothaan, C. C. J. New Developments in Molecular Orbital Theory. *Rev. Mod. Phys.* **1951**, *23*, 69–89. (b) Roothaan, C. C. J. Self-Consistent Field Theory for Open Shells of Electronic Systems. *Rev. Mod. Phys.* **1960**, *32*, 179–185.
- (7) (a) Thomas, L. H. The Calculation of Atomic Fields. *Math. Proc. Cambridge Philos. Soc.* **1927**, *23*, 542–548. (b) Fermi, E. Un Metodo Statistico per La Determinazione Di Alcune Priorieta Dell'atome'. *Rend. Accad. Naz. Lincei* **1927**, *6*, 602–607.
- (8) Hohenberg, P.; Kohn, W. Inhomogeneous Electron Gas. *Phys. Rev.* **1964**, *136*, B864–B871.
- (9) Kohn, W.; Sham, L. J. Self-Consistent Equations Including Exchange and Correlation Effects. *Phys. Rev.* **1965**, *140*, A1133–A1138.
- (10) Koch, W.; Holthausen, M. C. *A Chemist's Guide to Density Functional Theory*, 2nd ed.; Wiley-VCH, 2001.
- (11) Parr, R. G.; Yang, W. *Density-Functional Theory of Atoms and Molecules*; Oxford University Press, New York, 1989.
- (12) Vosko, S. H.; Wilk, L.; Nusair, M. Accurate Spin-Dependent Electron Liquid Correlation Energies for Local Spin Density Calculations: A Critical Analysis. *Can. J. Phys.* **1980**, *58*, 1200–1211.
- (13) Shakerzadeh, E. Theoretical investigations of interactions between boron nitride nanotubes and drugs, in *Boron Nitride Nanotubes in Nanomedicine*, ed. Ciofani, G.; Mattoli, V. Elsevier, **2016**, ch. 4, pp. 59–77.
- (14) Burke, K.; Perdew, J. P.; Wang, Y. Derivation of a Generalized Gradient Approximation: The PW91 Density Functional. In *Electronic Density Functional Theory*; Springer US: Boston, MA, 1998; pp 81–111.
- (15) Perdew, J. P.; Burke, K.; Ernzerhof, M. Generalized Gradient Approximation Made Simple. *Phys. Rev. Lett.* **1996**, *77*, 3865–3868.
- (16) Staroverov, V. N.; Scuseria, G. E.; Tao, J.; Perdew, J. P. Comparative Assessment of a New Nonempirical Density Functional: Molecules and Hydrogen-Bonded Complexes. *J. Chem. Phys.* **2003**, *119*, 12129.
- (17) (a) Grimme, S. Accurate Description of van Der Waals Complexes by Density Functional Theory Including Empirical Corrections. *J. Comput. Chem.* **2004**, *25*, 1463–1473. (b) Grimme, S. Density Functional Theory with London Dispersion Corrections. *Wiley Interdiscip. Rev. Comput. Mol. Sci.* **2011**, *1*, 211–228. (c) Grimme, S.; Hansen, A.; Brandenburg, J. G.; Bannwarth, C. Dispersion-Corrected Mean-Field Electronic Structure Methods. *Chem. Rev.* **2016**, *116*, 5105–5154.
- (18) Grimme, S. Dispersion interaction and chemical bonding. In *The Chemical Bond: Chemical Bonding Across the Periodic Table*, eds Frenking, G, Shaik S, **2014**, Wiley-VCH, Hoboken, NJ, pp 477–500.

-
- (19) (a) Grimme, S. Semiempirical GGA-Type Density Functional Constructed with a Long-Range Dispersion Correction. *J. Comput. Chem.* **2006**, *27*, 1787–1799. (b) Grimme, S.; Antony, J.; Ehrlich, S.; Krieg, H. A Consistent and Accurate Ab Initio Parametrization of Density Functional Dispersion Correction (DFT-D) for the 94 Elements H-Pu. *J. Chem. Phys.* **2010**, *132*, 154104. (c) Grimme, S. Density Functional Theory with London Dispersion Corrections. *Wiley Interdiscip. Rev. Comput. Mol. Sci.* **2011**, *1*, 211–228. (d) Grimme, S.; Ehrlich, S.; Goerigk, L. Effect of the Damping Function in Dispersion Corrected Density Functional Theory. *J. Comput. Chem.* **2011**, *32*, 1456–1465.
- (20) Johnson, E. R.; Becke, A. D. A Post-Hartree-Fock Model of Intermolecular Interactions: Inclusion of Higher-Order Corrections. *J. Chem. Phys.* **2006**, *124*, 174104.
- (21) Zhao, Y.; Truhlar, D. G. Density Functionals with Broad Applicability in Chemistry. *Acc. Chem. Res.* **2008**, *41*, 157–167.
- (22) Staudinger, H. Über Polymerisation. *Ber. Dtsch. Chem. Ges. B* **1920**, *53*, 1073–1085.
- (23) Hillmyer, M. A.; Tolman, W. B. Aliphatic Polyester Block Polymers: Renewable, Degradable, and Sustainable. *Acc. Chem. Res.* **2014**, *47*, 2390–2396.
- (24) Arbaoui, A.; Redshaw, C. Metal Catalysts for ϵ -Caprolactone Polymerisation. *Polym. Chem.* **2010**, *1*, 801–826.
- (25) Peplow, M. The Plastics Revolution: How Chemists Are Pushing Polymers to New Limits. *Nature* **2016**, *536*, 266–268.
- (26) (a) Mühlaupt, R. Green Polymer Chemistry and Bio-Based Plastics: Dreams and Reality. *Macromol. Chem. Phys.* **2013**, *214*, 159–174. (b) Vilela, C.; Sousa, A. F.; Fonseca, A. C.; Serra, A. C.; Coelho, J. F. J.; Freire, C. S. R.; Silvestre, A. J. D. The Quest for Sustainable Polyesters - Insights into the Future. *Polym. Chem.* **2014**, *5*, 3119–3141.
- (27) Thakur, V. K.; Thakur, M. K.; Raghavan, P.; Kessler, M. R. Progress in Green Polymer Composites from Lignin for Multifunctional Applications: A Review. *ACS Sustain. Chem. Eng.* **2014**, *2*, 1072–1092.
- (28) Odian, G. *Principles of Polymerization*, 4 Edition.; Wiley-Interscience, 2004.
- (29) Williams, C. K. Synthesis of Functionalized Biodegradable Polyesters. *Chem. Soc. Rev.* **2007**, *36*, 1573–1580.
- (30) Jérôme, C.; Lecomte, P. Recent Advances in the Synthesis of Aliphatic Polyesters by Ring-Opening Polymerization. *Adv. Drug Deliv. Rev.* **2008**, *60*, 1056–1076.
- (31) Kiesewetter, M. K.; Shin, E. J.; Hedrick, J. L.; Waymouth, R. M. Organocatalysis: Opportunities and Challenges for Polymer Synthesis. *Macromolecules* **2010**, *43*, 2093–2107.
- (32) Ober, C. K.; Cheng, S. Z. D.; Hammond, P. T.; Muthukumar, M.; Reichmanis, E.; Wooley, K. L.; Lodge, T. P. Research in Macromolecular Science: Challenges and Opportunities for the Next Decade. *Macromolecules* **2009**, *42*, 465–471.
- (33) Saxon, D. J.; Nasiri, M.; Mandal, M.; Maduskar, S.; Dauenhauer, P. J.; Cramer, C. J.; LaPointe, A. M.; Reineke, T. M. Architectural control of isosorbide-based polyethers via ring-opening polymerization. *J. Am. Chem. Soc.* **2019**, *141*, 5107–5111.
- (34) Duda, A.; Penczek, S. Thermodynamics, Kinetics, and Mechanisms of Cyclic Esters Polymerization. In *Polymers from Renewable Resources*; ACS Symposium Series; American Chemical Society, 2001; Vol. 764, pp 13–160.
- (35) (a) Iida, M.; Araki, T.; Teranishi, K.; Tani, H. Effect of Substituents on Stereospecific Polymerization of β -Alkyl- and β -Chloroalkyl- β -Propiolactones. *Macromolecules* **1977**, *10*, 275–284. (b) Gross, R. A.; Zhang, Y.; Konrad, G.; Lenz, R. W. Polymerization of β -Monosubstituted- β -Propiolactones Using Trialkylaluminum-Water Catalytic Systems and Polymer Characterization. *Macromolecules* **1988**, *21*, 2657–2668.

-
- (36) Dechy-Cabaret, O.; Martin-Vaca, B.; Bourissou, D. Controlled Ring-Opening Polymerization of Lactide and Glycolide. *Chem. Rev.* **2004**, *104*, 6147–6176.
- (37) MacDonald, J. P.; Shaver, M. P. Aluminum Salen and Salan Polymerization Catalysts: From Monomer Scope to Macrostructure Control. In *Green Polymer Chemistry: Biobased Materials and Biocatalysis*; ACS Symposium Series; American Chemical Society, 2015; Vol. 1192, pp 10–147.
- (38) Vincens, V.; Le Borgne, A.; Spassky, N. Aluminium Complex of a Schiff's Base as New Initiator for Oligomerization of Heterocycles. *Makromol. Chemie. Macromol. Symp.* **1991**, *47*, 285–291.
- (39) Hormnirun, P.; Marshall, E. L.; Gibson, V. C.; Pugh, R. I.; White, A. J. P. Study of Ligand Substituent Effects on the Rate and Stereoselectivity of Lactide Polymerization Using Aluminum Salen-Type Initiators. *Proc. Natl. Acad. Sci.* **2006**, *103*, 15343–15348.
- (40) Gregson, C. K. A.; Blackmore, I. J.; Gibson, V. C.; Long, N. J.; Marshall, E. L.; White, A. J. P. Titanium-Salen Complexes as Initiators for the Ring Opening Polymerisation of *rac*-Lactide. *Dalton Trans.* **2006**, *99*, 3134–3140.
- (41) Agatemor, C.; Arnold, A. E.; Cross, E. D.; Decken, A.; Shaver, M. P. Aluminium Salophen and Salen Initiators in the Ring-Opening Polymerisation of *rac*-Lactide and *rac*- β -Butyrolactone: Electronic Effects on Stereoselectivity and Polymerisation Rates. *J. Organomet. Chem.* **2013**, *745–746*, 335–340.
- (42) Zintl, M.; Molnar, F.; Urban, T.; Bernhart, V.; Preishuber-Pflügl, P.; Rieger, B. Variably Isotactic Poly(hydroxybutyrate) from Racemic β -Butyrolactone: Microstructure Control by Achiral Chromium(III) Salophen Complexes. *Angew. Chemie Int. Ed.* **2008**, *47*, 3458–3460.
- (43) Hormnirun, P.; Marshall, E. L.; Gibson, V. C.; White, A. J. P.; Williams, D. J. Remarkable Stereocontrol in the Polymerization of Racemic Lactide Using Aluminum Initiators Supported by Tetradentate Aminophenoxide Ligands. *J. Am. Chem. Soc.* **2004**, *126*, 2688–2689.
- (44) Hancock, S. L.; Mahon, M. F.; Jones, M. D. Aluminium Salalen Complexes Based on 1,2-Diaminocyclohexane and Their Exploitation for the Polymerisation of *rac*-Lactide. *Dalt. Trans.* **2013**, *42*, 9279–9285.
- (45) Gibson, V. C.; Marshall, E. L. Metal Complexes as Catalysts for Polymerization Reactions. In *Comprehensive Coordination Chemistry II*; McCleverty, J. A., Meyer, T. J., Eds.; Elsevier: Oxford, 2003; Vol. 9, pp 1–74.
- (46) Connor, E. F.; Nyce, G. W.; Myers, M.; Möck, A.; Hedrick, J. L. First Example of N-Heterocyclic Carbenes as Catalysts for Living Polymerization: Organocatalytic Ring-Opening Polymerization of Cyclic Esters. *J. Am. Chem. Soc.* **2002**, *124*, 914–915.
- (47) Mandal, M.; Luke, A. M.; Dereli, B.; Elwell, C. E.; Reineke, T. M.; Tolman, W. B.; Cramer, C. J. “Computational prediction and experimental verification of ϵ -caprolactone ring-opening polymerization activity by an aluminum complex of an indolide/Schiff-base ligand.” *ACS Catal.* **2019**, *9*, 885–889.
- (48) Selected examples and lead references: (a) Marshall, E. L.; Gibson, V. C.; Rzepa, H. S. A Computational Analysis of the Ring-Opening Polymerization of *rac*-Lactide Initiated by Single-Site β -Diketiminato Metal Complexes: Defining the Mechanistic Pathway and the Origin of Stereocontrol. *J. Am. Chem. Soc.*, **2005**, *127*, 6048–6051. (b) Wei, J.; Riffel, M. N.; Diaconescu, P. L. Redox Control of Aluminum Ring-Opening Polymerization: A Combined Experimental and DFT Investigation. *Macromolecules*, **2017**, *50*, 1847–1861. (c) Robert, C.; Schmid, T. E.; Richard, V.; Haquette, P.; Raman, S. K.; Rager, M.-N.; Gauvin, R. M.; Morin, Y.; Trivelli, X.; Guérineau, V.; del Rosal, I.; Maron, L.; Thomas, C. M. Mechanistic Aspects of the Polymerization of Lactide Using a Highly Efficient Aluminum(III) Catalytic System. *J. Am. Chem. Soc.*, **2017**, *139*, 6217–6225. (d) Jitonnorn, J.; Molloy, R.; Punyodom, W.; Meelua, W. Theoretical Studies on Aluminum Trialkoxide-Initiated Lactone Ring-Opening Polymerizations: Roles of Alkoxide Substituent and Monomer Ring Structure. *Comput. Theor. Chem.* **2016**, *1097*, 25–32.
- (49) Marlier, E. E.; Macaranas, J. A.; Marell, D. J.; Dunbar, C. R.; Johnson, M. A.; DePorre, Y.; Miranda, M. O.; Neisen, B. D.; Cramer, C. J.; Hillmyer, M. A.; Tolman, W. B. Mechanistic Studies of ϵ -Caprolactone

Polymerization by (Salen)AlOR Complexes and a Predictive Model for Cyclic Ester Polymerizations. *ACS Catal.* **2016**, *6*, 1215–1224.

- (50) (a) Nomura, N.; Ishii, R.; Yamamoto, Y.; Kondo, T. Stereoselective Ring-Opening Polymerization of a Racemic Lactide by Using Achiral Salen- and Homosalen-Aluminum Complexes. *Chem. – A Eur. J.* **2007**, *13*, 4433–4451. (b) Ding, K.; Miranda, M. O.; Moscato-goodpaster, B.; Ajellal, N.; Breyfogle, L. E.; Hermes, E. D.; Schaller, C. P.; Roe, S. E.; Cramer, C. J.; Hillmyer, M. A.; Tolman, W. B. Roles of Monomer Binding and Alkoxide Nucleophilicity in Aluminum-Catalyzed Polymerization of ϵ -Caprolactone. *Macromolecules* **2012**, *45*, 5387–5396.
- (51) Miranda, M. O.; Deporre, Y.; Vazquez-Lima, H.; Johnson, M. A.; Marell, D. J.; Cramer, C. J.; Tolman, W. B. Understanding the Mechanism of Polymerization of ϵ -Caprolactone Catalyzed by Aluminum Salen Complexes. *Inorg. Chem.* **2013**, *52*, 13692–13701.
- (52) Johnson, K. A.; Goody, R. S. The Original Michaelis Constant: Translation of the 1913 Michaelis–Menten Paper. *Biochemistry* **2011**, *50*, 8264–8269.
- (53) Macaranas, J. A.; Luke, A. M.; Mandal, M.; Neisen, B. D.; Marell, D. J.; Cramer, C. J.; Tolman, W. B. Sterically induced ligand framework distortion effects on catalytic cyclic ester polymerizations. *Inorg. Chem.* **2018**, *57*, 3451–3457.
- (54) (a) Arbaoui, A.; Redshaw, C. Metal Catalysts for ϵ -Caprolactone Polymerisation. *Polym. Chem.* **2010**, *1*, 801–826. (b) Kiesewetter, M. K.; Shin, E. J.; Hedrick, J. L.; Waymouth, R. M. Organocatalysis: Opportunities and Challenges for Polymer Synthesis. *Macromolecules* **2010**, *43*, 2093–2107. (c) Wu, J.; Yu, T. L.; Chen, C. T.; Lin, C. C. Recent Developments in Main Group Metal Complexes Catalyzed/Initiated Polymerization of Lactides and Related Cyclic Esters. *Coord. Chem. Rev.* **2006**, *250*, 602–626. (d) Dechy-Cabaret, O.; Martin-Vaca, B.; Bourissou, D. Controlled Ring-Opening Polymerization of Lactide and Glycolide. *Chem. Rev.* **2004**, *104*, 6147–6176.
- (55) Selected other examples of CL polymerization by aluminum salen or related complexes: (a) Pepels, M. P. F.; Bouyahyi, M.; Heise, A.; Duchateau, R. Kinetic investigation on the catalytic ring-opening (co)polymerization of (macro)lactones using aluminum salen catalysts. *Macromolecules* **2013**, *46*, 4324–4334. (b) Huang, H.-C.; Wang, B.; Zhang, Y.-P.; Li, Y.-S. Bimetallic aluminum complexes with cyclic β -ketiminato ligands: the cooperative effect improves their capability in polymerization of lactide and ϵ -caprolactone. *Polym. Chem.* **2016**, *7*, 5819–5827. (c) Kan, C.; Ma, H. Copolymerization of l-lactide and ϵ -caprolactone catalyzed by mono- and dinuclear salen aluminum complexes bearing bulky 6,6'-dimethylbiphenyl-bridge: random and tapered copolymer. *RSC Adv.* **2016**, *6*, 47402–47409. (d) Pappalardo, D.; Annunziata, L.; Pellecchia, C. Living ring-opening homo- and copolymerization of ϵ -caprolactone and L- and D,L-lactides by dimethyl(salicylaldiminato)aluminum compounds. *Macromolecules* **2009**, *42*, 6056–6062.
- (56) (a) Nomura, N.; Ishii, R.; Akakura, M.; Aoi, K. Stereoselective Ring-Opening Polymerization of Racemic Lactide Using Aluminum-Achiral Ligand Complexes: Exploration of a Chain-End Control Mechanism. *J. Am. Chem. Soc.* **2002**, *124*, 5938–5939. (b) Aluthge, D. C.; Ahn, J. M.; Mehrkhodavandi, P. Overcoming Aggregation in Indium Salen Catalysts for Isolelective Lactide Polymerization. *Chem. Sci.* **2015**, *6*, 5284–5292. (c) Aluthge, D. C.; Yan, E. X.; Ahn, J. M.; Mehrkhodavandi, P. Role of Aggregation in the Synthesis and Polymerization Activity of SalBinap Indium Alkoxide Complexes. *Inorg. Chem.* **2014**, *53*, 6828–6836.
- (57) Goedken, V. L.; Ito, H.; Ito, T. An Unusually Stable Aluminium-Alkyl Bond: Synthesis and Reactivity Studies of the Macrocyclic Al(C₂₂H₂₂N₄)Et Complex. *J. Chem. Soc., Chem. Commun.* **1984**, *1*, 1453–1454.
- (58) Yamamoto, G.; Nadano, R.; Satoh, W.; Yamamoto, Y.; Akiba, K. Synthesis of μ -oxo-bridged group 15 element – aluminium heterodinuclear porphyrins [(oep) (Me)M–O–Al(oep)]ClO₄ (M = P, As, Sb) and X-ray crystal structure of [(oep) (Me)As–O–Al(oep)]ClO₄. *Chem. Commun.* **1997**, *4*, 1325–1326.
- (59) (a) Guillard, R.; Zrineh, A.; Tabard, A.; Endo, A.; Han, B. C.; Lecomte, C.; Souhassou, M.; Habbou, A.; Ferhat, M.; Kadish, K. M. Synthesis and Spectroscopic and Electrochemical Characterization of Ionic and σ -Bonded

- Aluminum(III) Porphyrins. Crystal Structure of Methyl(2,3,7,8,12,13,17,18-octaethylporphinato)aluminum(III), (OEP)Al(CH₃). *Inorg. Chem.* **1990**, 29, 4476–4482. (b) Guillard, R.; Barbe, J.-M.; Ibnlfassi, A.; Zrineh, A.; Adamian, V. A.; Kadish, K. M. Synthesis, Characterization, and Electrochemistry of Heteroleptic Double-Decker Complexes of the Type Phthalocyaninato-Porphyrinato-Zirconium(IV) or -Hafnium(IV). *Inorg. Chem.* **1995**, 34, 1472–1481.
- (60) Endo, M.; Aida, T.; Inoue, S. Immortal Polymerization of ϵ -Caprolactone Initiated by Aluminum Porphyrin in the Presence of Alcohol. *Macromolecules* **1987**, 20, 2982–2988.
- (61) Sugimoto, H.; Kawamura, C.; Kuroki, M.; Aida, T.; Inoue, S. Lewis Acid-Assisted Anionic Ring-Opening Polymerization of Epoxide by the Aluminum Complexes of Porphyrin, Phthalocyanine, Tetraazaannulene, and Schiff Base as Initiators. *Macromolecules* **1994**, 27, 2013–2018.
- (62) Addison, A. W.; Rao, T. N.; Reedijk, J.; van Rijn, J.; Verschoor, G. C. Synthesis, Structure, and Spectroscopic Properties of Copper(II) Compounds containing Nitrogen–Sulphur Donor Ligands; the Crystal and Molecular Structure of Aqua[1,7-bis(N-methylbenzimidazol-2'-yl)-2,6-dithiaheptane]copper(II) Perchlorate. *J. Chem. Soc., Dalton Trans.* **1984**, 1349–1356.
- (63) Huang, Y.-T.; Wang, W.-C.; Hsu, C.-P.; Lu, W.-Y.; Chuang, W.-J.; Chiang, M. Y.; Lai, Y.-C.; Chen, H.-Y. The ring-opening polymerization of ϵ -caprolactone and l-lactide using aluminum complexes bearing benzothiazole ligands as catalysts. *Polym. Chem.* **2016**, 7, 4367–4377.
- (64) Zhang, Y.; Gao, A.; Zhang, Y.; Xu, Z.; Yao, W. Aluminum complexes with benzoxazolphenolate ligands: Synthesis, characterization and catalytic properties for ring-opening polymerization of cyclic esters. *Polyhedron* **2016**, 112, 27–33.
- (65) The M06-2X/6-311+G(d,p)//M06-L/6-31+G(d,p) level (including continuum toluene solvation effects) was chosen based on the prior excellent performance of this level of theory for rationalizing experimental trends in caprolactone polymerization catalyzed by aluminum coordination compounds.
- (66) (a) Hehre, W. J.; Ditchfield, R.; Pople, J. A. Self-Consistent Molecular Orbital Methods. XII. Further Extensions of Gaussian-Type Basis Sets for Use in Molecular Orbital Studies of Organic Molecules. *J. Chem. Phys.* **1972**, 56, 2257–2261. (b) Krishnan, R.; Binkley, J. S.; Seeger, R.; Pople, J. A. Self-Consistent Molecular Orbital Methods. XX. A Basis Set for Correlated Wave Functions. *J. Chem. Phys.* **1980**, 72, 650–654. (c) Hehre, W. J. *AB INITIO Molecular Orbital Theory*; Wiley, 1986.
- (67) For completeness, we note that the predicted free energy for the final product along the reaction coordinate in Figure 2.2 for the TMTAA ligand is 7.8 kcal/mol; i.e., the overall reaction is predicted to be endergonic. While part of this may be associated with initiation being less favorable than chain-propagation, another significant issue is the underestimation of the entropy of a growing polymer chain when computed simply from application of the conventional ideal-gas, rigid-rotator, harmonic-oscillator approximation to a single product structure, as discussed previously in the following: (a) Martinez, H.; Miró, P.; Charbonneau, P.; Hillmyer, M. A.; Cramer, C. J. Selectivity in Ring-Opening Metathesis Polymerization of Z-Cyclooctenes Catalyzed by a Second-generation Grubbs Catalyst. *ACS Catal.* **2012**, 2, 2547–2556. (b) Martinez, H.; Hillmyer, M. A.; Cramer, C. J. Factors Controlling the Regio- and Stereoselectivity of the Ring-Opening Metathesis Polymerization of 3-Substituted Cyclooctenes by Monoaryloxide Pyrrolide Imido Alkylidene (MAP) Tungsten Catalysts. *J. Org. Chem.* **2014**, 79, 11940–11948.
- (68) Zhong, Z.; Dijkstra, P. J.; Feijen, J. Controlled and Stereoselective Polymerization of Lactide: Kinetics, Selectivity, and Microstructures. *J. Am. Chem. Soc.* **2003**, 125, 11291–11298.
- (69) Chisholm, M. H.; Gallucci, J. C.; Phomphrai, K. Comparative Study of the Coordination Chemistry and Lactide Polymerization of Alkoxide and Amide Complexes of Zinc and Magnesium with a β -Diiminato Ligand Bearing Ether Substituents. *Inorg. Chem.* **2005**, 44, 8004–8010.

-
- (70) Chen, H. Y.; Peng, Y. L.; Huang, T. H.; Sutar, A. K.; Miller, S. A.; Lin, C. C. Comparative Study of Lactide Polymerization by Zinc Alkoxide Complexes with a β -Diketiminato Ligand Bearing Different Substituents. *J. Mol. Catal. A: Chem.* **2011**, *339*, 61–71.
- (71) (a) Rosen, T.; Popowski, Y.; Goldberg, I.; Kol, M. Zinc Complexes of Sequential Tetradentate Monoanionic Ligands in the Ioselective Polymerization of *rac*-Lactide. *Chem. – Eur. J.* **2016**, *22*, 11533–11536. (b) Gupta, K. C.; Sutar, A. K. Catalytic Activities of Schiff Base Transition Metal Complexes. *Coord. Chem. Rev.* **2008**, *252*, 1420–1450. (c) Cozzi, P. G. Metal-Salen Schiff Base Complexes in Catalysis: Practical Aspects. *Chem. Soc. Rev.* **2004**, *33*, 410–421. (d) Cross, E. D.; Allan, L. E. N.; Decken, A.; Shaver, M. P. Aluminum Salen and Salan Complexes in the Ring-Opening Polymerization of Cyclic Esters: Controlled Immortal and Copolymerization of *rac*- β -Butyrolactone and *rac*-Lactide. *J. Polym. Sci., Part A: Polym. Chem.* **2013**, *51*, 1137–1146.
- (72) Stasiw, D. E.; Mandal, M.; Neisen, B. D.; Mitchell, L. A.; Cramer, C. J.; Tolman, W. B. Why So Slow? Mechanistic Insights from Studies of a Poor Catalyst for Polymerization of ϵ -Caprolactone. *Inorg. Chem.* **2017**, *56*, 725–728.
- (73) (a) Gademann, K.; Chavez, D. E.; Jacobsen, E. N. Highly Enantioselective Inverse-Electron-Demand Hetero-Diels-Alder Reactions of α,β -unsaturated Aldehydes. *Angew. Chem., Int. Ed.* **2002**, *41*, 3059–3061. (b) Bryliakov, K. P.; Talsi, E. P. Titanium-Salan-Catalyzed Asymmetric Oxidation of Sulfides and Kinetic Resolution of Sulfoxides with H_2O_2 as the Oxidant. *Eur. J. Org. Chem.* **2008**, *19*, 3369–3376.
- (74) Hillier, A. C.; Sommer, W. J.; Yong, B. S.; Petersen, J. L.; Cavallo, L.; Nolan, S. P. A Combined Experimental and Theoretical Study Examining the Binding of N-Heterocyclic Carbenes (NHC) to the Cp^*RuCl ($\text{Cp}^* = \eta^5\text{-C}_5\text{Me}_5$) Moiety: Insight into Stereoelectronic Differences between Unsaturated and Saturated NHC Ligands. *Organometallics* **2003**, *22*, 4322–4326.
- (75) Falivene, L.; Credendino, R.; Poater, A.; Petta, A.; Serra, L.; Oliva, R.; Scarano, V.; Cavallo, L. SambVca 2. A Web Tool for Analyzing Catalytic Pockets with Topographic Steric Maps. *Organometallics* **2016**, *35*, 2286–2293.
- (76) The agreement between theory and experiment for τ is less good for **235** than for **239**, but when a structure for **235** is computed, constraining τ to its experimental value of 0.52, the increase in energy is only 0.5 kcal/mol, suggesting that, at least in this range of the τ coordinate, the system is fairly flexible and solid-state packing effects may contribute to differences in the observed crystal and fully optimized gas-phase structures.
- (77) Although the energetics of a single cycle of propagation must be independent of the catalyst, Figure 2.9 shows small variations in net energetics as a function of the catalyst. This is because the step being studied is initiation, not propagation, and the terminal methoxy remains close enough to have different interactions with the different catalyst structures (which would be eliminated with continued chain growth).
- (78) Bickelhaupt, F. M.; Houk, K. N. Analyzing Reaction Rates with the Distortion/Interaction-Activation Strain Model. *Angew. Chem., Int. Ed.* **2017**, *56*, 10070–10086.
- (79) Bondi, A. van der Waals Volumes and Radii. *J. Phys. Chem.* **1964**, *68*, 441–451.
- (80) (a) Schneiderman, D. K.; Hillmyer, M. A. *50th Anniversary Perspective: There Is a Great Future in Sustainable Polymers*. *Macromolecules*, **2017**, *50*, 3733–3749. (b) Corma, A.; Iborra, S.; Velty, A. Chemical Routes for the Transformation of Biomass into Chemicals. *Chem. Rev.* **2007**, *107*, 2411–2502.
- (81) (a) O'Keefe, B. J.; Hillmyer, M. A.; Tolman, W. B. Polymerization of Lactide and Related Cyclic Esters by Discrete Metal Complexes. *J. Chem. Soc., Dalton Trans.* **2001**, 2215–2224. (b) Labet, M.; Thielemans, W. Synthesis of Polycaprolactone: A Review. *Chem. Soc. Rev.*, **2009**, *38*, 3484–3504. (c) Thomas, C. M. Stereocontrolled Ring-Opening Polymerization of Cyclic Esters: Synthesis of New Polyester Microstructures. *Chem. Soc. Rev.* **2010**, *39*, 165–173.
- (82) Wei, Y.; Wang, S.; Zhou, S. Aluminum Alkyl Complexes: Synthesis, Structure, and Application in ROP of Cyclic Esters. *Dalton Trans.*, **2016**, *45*, 4471–4485.

- (83) In the original article (*Inorg. Chem.* **2018**, 57, 3451), the $\Delta G^\ddagger(\text{TS1})$ and FDE for **246** were computed to be 10.3 and 12.4 kcal/mol respectively as opposed to 7.8 and 12.7 kcal/mol reported here. This is attributed to three factors: (i) CH_2Cl_2 solvation effects instead of toluene, (ii) inclusion of Grimme's D3-dispersion correction term and (iii) a more favorable orientation of the CL fragment in TS1 identified here; for details on how CL orientation affects TS1 energetics, see section 2.8.5.2.
- (84) Jin, R.; Liu, S.; Lan, Y. Distortion-Interaction Analysis along the Reaction Pathway to Reveal the Reactivity of the Alder-Ene Reaction of Enes. *RSC Adv.* **2015**, 5, 61426–61435.
- (85) (a) Du, H.; Velders, A. H.; Dijkstra, P. J.; Zhong, Z.; Chen, X.; Feijen, J. Polymerization of Lactide Using Achiral Bis(Pyrrolidene) Schiff Base Aluminum Complexes. *Macromolecules*, **2009**, 42, 1058–1066. (b) Tabthong, S.; Nanok, T.; Sumrit, P.; Kongsaree, P.; Prappai, S.; Chuawong, P.; Hormnirun, P. Bis(Pyrrolidene) Schiff Base Aluminum Complexes as Isoselective-Biased Initiators for the Controlled Ring-Opening Polymerization of *rac*-Lactide: Experimental and Theoretical Studies. *Macromolecules*, **2015**, 48, 6846–6861. (c) Rufino-Felipe, E.; Lopez, N.; Vengoechea-Gómez, F. A.; Guerrero-Ramírez, L.-G.; Muñoz-Hernández, M.-Á. Ring-Opening Polymerization of *rac*-Lactide Catalyzed by Al(III) and Zn(II) Complexes Incorporating Schiff Base Ligands Derived from Pyrrole-2-Carboxaldehyde. *Appl. Organomet. Chem.*, **2018**, 32, e4315.
- (86) Lee, C. L.; Lin, Y. F.; Jiang, M. T.; Lu, W. Y.; Vandavasi, J. K.; Wang, L. F.; Lai, Y. C.; Chiang, M. Y.; Chen, H. Y. Improvement in Aluminum Complexes Bearing Schiff Bases in Ring-Opening Polymerization of ϵ -Caprolactone: A Five-Membered-Ring System. *Organometallics*, **2017**, 36, 1936–1945.
- (87) Houk, K. H.; Jabbari, A.; Hall, H. K. Jr.; Alemán, C. Why δ -Valerolactone Polymerizes and γ -Butyrolactone Does Not. *J. Org. Chem.*, **2008**, 73, 2674–2678.
- (88) Igel-Mann, G.; Stoll, H.; Preuss, H. Pseudopotentials for Main Group Elements (IIIa through VIIa). *Mol. Phys.* **1988**, 65, 1321–1328.
- (89) Adamo, C.; Barone, V. Toward Reliable Density Functional Methods without Adjustable Parameters: The PBE0 Model. *J. Chem. Phys.* **1999**, 110, 6158.
- (90) Chai, J.-D.; Head-Gordon, M. Long-Range Corrected Hybrid Density Functionals with Damped Atom–Atom Dispersion Corrections. *Phys. Chem. Chem. Phys.* **2008**, 10, 6615–6620.
- (91) Fenouillot, F.; Rousseau, A.; Colomines, G.; Saint-Loup, R.; Pascault, J.-P. Polymers from Renewable 1,4:3,6-Dianhydrohexitols (Isosorbide, Isomannide and Isoidide): A Review. *Prog. Polym. Sci.* **2010**, 35, 578–622.
- (92) (a) Zia, K. M.; Noreen, A.; Zuber, M.; Tabasum, S.; Mujahid, M. Recent Developments and Future Prospects on Bio-Based Polyesters Derived from Renewable Resources: A Review. *Int. J. Biol. Macromol.* **2016**, 82, 1028–1040. (b) Kang, H.; Li, M.; Tang, Z.; Xue, J.; Hu, X.; Zhang, L.; Guo, B. Synthesis and Characterization of Biobased Isosorbide-Containing Copolyesters as Shape Memory Polymers for Biomedical Applications. *J. Mater. Chem. B* **2014**, 2, 7877–7886.
- (93) DURABIO-Engineering bio-sourced resin. <https://www.mcgp-global.com/en/asia/products/brand/durabiotm/>, 2016.
- (94) (a) Thiem, J.; Lüders, H. Darstellung Und Gezielte Polykondensation von Anhydroalditol-Bausteinen Aus Stärke. *Starch - Stärke* **1984**, 36, 170–176. (b) Thiem, J.; Lüders, H. Synthesis of Polyterephthalates Derived from Dianhydrohexitols. *Polym. Bull.* **1984**, 11, 365–369. (c) Noordover, B. A. J.; van Staaldouin, V. G.; Duchateau, R.; Koning, C. E.; van Benthem; Mak, M.; Heise, A.; Frissen, A. E.; van Haveren, J. Co- and Terpolyesters Based on Isosorbide and Succinic Acid for Coating Applications: Synthesis and Characterization. *Biomacromolecules* **2006**, 7, 3406–3416. (d) Kricheldorf, H. R.; Behnken, G.; Sell, M. Influence of Isosorbide on Glass-Transition Temperature and Crystallinity of Poly(Butylene Terephthalate). *J. Macromol. Sci., Part A: Pure Appl. Chem.* **2007**, 44, 679–684.
- (95) For reference, $\Delta H_{\text{EO}} = -33.4 \text{ kcal mol}^{-1}$ and $\Delta H_{\text{THF}} = -4.6 \text{ kcal mol}^{-1}$. Dubois, P.; Coulembier, O.; Raquez, J.-M. *Handbook of Ring-Opening Polymerization*; John Wiley & Sons, 2009.

-
- (96) (a) Strietholt, W. A.; Thiem, J.; Höweler, U. F. B. Synthesis and Ring-Opening Polymerization of 1,4:2,5:3,6-Trihydro-D-Mannitol and Structure Studies by MNDO Calculations. *Makromol. Chem.* **1991**, *192*, 317–331. (b) Thiem, J.; Strietholt, W. A. Ring-Opening Copolymerization of Anhydroalditols with Tetrahydrofuran. *Macromol. Chem. Phys.* **1995**, *196*, 1487–1493.
- (97) You, L.; Hogen-Esch, T. E.; Zhu, Y.; Ling, J.; Shen, Z. Brønsted Acid-Free Controlled Polymerization of Tetrahydrofuran Catalyzed by Recyclable Rare Earth Triflates in the Presence of Epoxides. *Polymer* **2012**, *53*, 4112–4118.
- (98) Marenich, A. V.; Jerome, S. V.; Cramer, C. J.; Truhlar, D. G. Charge Model 5: An Extension of Hirshfeld Population Analysis for the Accurate Description of Molecular Interactions in Gaseous and Condensed Phases. *J. Chem. Theory Comput.* **2012**, *8*, 527–541.
- (99) Luo, Y.-R. *Comprehensive Handbook of Chemical Bond Energies*; CRC Press, 2007.
- (100) Guo, L.; Lahasky, S. H.; Ghale, K.; Zhang, D. N-Heterocyclic Carbene-Mediated Zwitterionic Polymerization of *N*-Substituted *N*-Carboxyanhydrides toward Poly(*α*-Peptoid)s: Kinetic, Mechanism, and Architectural Control. *J. Am. Chem. Soc.* **2012**, *134*, 9163–9171.
- (101) Macromodel: Schrödinger Release 2018-4: MacroModel, Schrödinger, LLC, New York, NY, 2018.
- (102) (a) Halgren, T. A. Merck Molecular Force Field. I. Basis, Form, Scope, Parameterization, and Performance of MMFF94. *J. Comput. Chem.* **1996**, *17*, 490–519. (b) Halgren, T. A.; Nachbar, R. B. Merck Molecular Force Field. IV. Conformational Energies and Geometries for MMFF94. *J. Comput. Chem.* **1996**, *17*, 587–615.
- (103) (a) Frisch, M. J.; Trucks, G. W.; Schlegel, H. B.; Scuseria, G. E.; Robb, M. A.; Cheeseman, J. R.; Scalmani, G.; Barone, V.; Mennucci, B.; Petersson, G. A.; Nakatsuji, H.; Caricato, M.; Li, X.; Hratchian, H. P.; Izmaylov, A. F.; Bloino, J.; Zheng, G.; Sonnenberg, J. L.; Hada, M.; Ehara, M.; Toyota, K.; Fukuda, R.; Hasegawa, J.; Ishida, M.; Nakajima, T.; Honda, Y.; Kitao, O.; Nakai, H.; Vreven, T.; Montgomery, J. A., Jr.; Peralta, J. E.; Ogliaro, F.; Bearpark, M.; Heyd, J. J.; Brothers, E.; Kudin, K. N.; Staroverov, V. N.; Kobayashi, R.; Normand, J.; Raghavachari, K.; Rendell, A.; Burant, J. C.; Iyengar, S. S.; Tomasi, J.; Cossi, M.; Rega, N.; Millam, N. J.; Klene, M.; Knox, J. E.; Cross, J. B.; Bakken, V.; Adamo, C.; Jaramillo, J.; Gomperts, R.; Stratmann, R. E.; Yazyev, O.; Austin, A. J.; Cammi, R.; Pomelli, C.; Ochterski, J. W.; Martin, R. L.; Morokuma, K.; Zakrzewski, V. G.; Voth, G. A.; Salvador, P.; Dannenberg, J. J.; Dapprich, S.; Daniels, A. D.; Farkas, Ö.; Foresman, J. B.; Ortiz, J. V.; Cioslowski, J.; Fox, D. J. Gaussian 09, *Gaussian, Inc.*, Wallingford CT, 2009. (b) Gaussian 16, Revision A.03, Frisch, M. J.; Trucks, G. W.; Schlegel, H. B.; Scuseria, G. E. *et al.* Gaussian, Inc., Wallingford CT, 2016.
- (104) (a) Zhao, Y.; Truhlar, D. G. A New Local Density Functional for Main-Group Thermochemistry, Transition Metal Bonding, Thermochemical Kinetics, and Noncovalent Interactions. *J. Chem. Phys.* **2006**, *125*, 194101. (b) Zhao, Y.; Truhlar, D. G. The M06 Suite of Density Functionals for Main Group Thermochemistry, Thermochemical Kinetics, Noncovalent Interactions, Excited States, and Transition Elements: Two New Functionals and Systematic Testing of Four M06-Class Functionals and 12 Other Functionals. *Theor. Chem. Acc.* **2008**, *120*, 215–241.
- (105) Marenich, A. V.; Cramer, C. J.; Truhlar, D. G. Universal Solvation Model Based on Solute Electron Density and on a Continuum Model of the Solvent Defined by the Bulk Dielectric Constant and Atomic Surface Tensions. *J. Phys. Chem. B* **2009**, *113*, 6378–6396.
- (106) Suh, S.-E.; Chen, S.-J.; Mandal, M.; Guzei, I.; Cramer, C. J.; Stahl, S. S. Site-Selective Copper-Catalyzed Azidation of Benzylic C–H Bonds. *J. Am. Chem. Soc.* **2020**. (doi.org/10.1021/jacs.0c05362)
- (107) (a) Hartwig, J. F. Catalyst-Controlled Site-Selective Bond Activation. *Acc. Chem. Res.* **2017**, *50*, 549–555. (b) Stang, E. M.; White, M. C. Total Synthesis and Study of 6-Deoxyerythronolide B by Late-Stage C–H Oxidation. *Nat. Chem.* **2009**, *1*, 547–551. (c) Rosen, B. R.; Simke, L. R.; Thuy-Boun, P. S.; Dixon, D. D.; Yu, J.-Q.; Baran, P. S. C–H Functionalization Logic Enables Synthesis of (+)-Hongoquercin A and Related Compounds. *Angew. Chem., Int. Ed.* **2013**, *52*, 7317–7320.

-
- (108) Cernak, T.; Dykstra, K. D.; Tyagarajan, S.; Vachal, P.; Krska, S. W. The Medicinal Chemist's Toolbox for Late Stage Functionalization of Drug-Like Molecules. *Chem. Soc. Rev.* **2016**, *45*, 546–576.
- (109) Newhouse, T.; Baran, P. S. If C–H Bonds Could Talk: Selective C–H Bond Oxidation. *Angew. Chem., Int. Ed.* **2011**, *50*, 3362–3374.
- (110) Hartwig, J. F.; Larsen, M. A. Undirected, Homogeneous C–H Bond Functionalization: Challenges and Opportunities. *ACS Cent. Sci.* **2016**, *2*, 281–292.
- (111) Goswami, M.; de Bruin, B. Metal-Catalysed Azidation of Organic Molecules. *Eur. J. Org. Chem.* **2017**, *2017*, 1152–1176.
- (112) (a) Wang, X.; Huang, B.; Liu, X.; Zhan, P. Discovery of Bioactive Molecules from CuAAC Click-Chemistry-Based Combinatorial Libraries. *Drug Discov. Today* **2016**, *21*, 118–132. (b) El-Sagheer, A. H.; Brown, T. Click Nucleic Acid Ligation: Applications in Biology and Nanotechnology. *Acc. Chem. Res.* **2012**, *45*, 1258–1267. (c) Pickens, C. J.; Johnson, S. N.; Pressnall, M. M.; Leon, M. A.; Berkland, C. J. Practical Considerations, Challenges, and Limitations of Bioconjugation via Azide–Alkyne Cycloaddition. *Bioconjugate Chem.* **2018**, *29*, 686–701.
- (113) Gololobov, Y. G.; Kasukhin, L. F. Recent Advances in the Staudinger Reaction. *Tetrahedron* **1992**, *48*, 1353–1406.
- (114) Bräse, S.; Gil, C.; Knepper, K.; Zimmermann, V. Organic Azides: An Exploding Diversity of a Unique Class of Compounds. *Angew. Chem. Int. Ed.* **2005**, *44*, 5188–5240.
- (115) Padwa, A. Aziridines and Azirines: Monocyclic. In *Comprehensive Heterocyclic Chemistry III*; Katritzky, A. R.; Ramsden, C. A.; Scriven, E. F. V.; Taylor, R. J. K., Eds.; Elsevier Science: Oxford, 2008; Vol. 1, Chapter 1.01.6.2, pp 50–64.
- (116) (a) Li, Y.-L.; Combs, A. P.; Bicyclic Heteroaryl aminoalkyl Phenyl Derivatives as PI3K Inhibitors, International Patent 2015191677A1, Dec 17, 2015. (b) Ivanov, K. L.; Villemson, E. V.; Budynina, E. M.; Ivanova, O. A.; Trushkov, I. V.; Melnikov, M. Y. Ring Opening of Donor-Acceptor Cyclopropanes with the Azide Ion: A Tool for Construction of N-Heterocycles. *Chem. Eur. J.* **2015**, *21*, 4975–4987. (c) Kim, M.-S.; Yoo, M.-H.; Rhee, J.-K.; Kim, Y.-J.; Park, S.-J.; Choi, J.-H.; Sung, S.-Y.; Lim, H.-G.; Cha, D.-W.; Synthetic Intermediates, Process for Preparing Pyrrolylheptanoic Acid Derivatives Therefrom. International Patent 2009084827A3, July 9, 2009.
- (117) Karimov, R. R.; Sharma, A.; Hartwig, J. F. Late Stage Azidation of Complex Molecules. *ACS Cent. Sci.* **2016**, *2*, 715–724.
- (118) Sharma, A.; Hartwig, J. F. Metal-Catalysed Azidation of Tertiary C–H Bonds Suitable for Late-Stage Functionalization. *Nature* **2015**, *517*, 600–604.
- (119) Huang, X.; Bergsten, T. M.; Groves, J. T. Manganese-Catalyzed Late-Stage Aliphatic C–H Azidation. *J. Am. Chem. Soc.* **2015**, *137*, 5300–5303.
- (120) Margrey, K. A.; Czaplinski, W. L.; Nicewicz, D. A.; Alexanian, E. J. A General Strategy for Aliphatic C–H Functionalization Enabled by Organic Photoredox Catalysis. *J. Am. Chem. Soc.* **2018**, *140*, 4213–4217.
- (121) Wang, Y.; Li, G.-X.; Yang, G.; He, G.; Chen, G. A Visible-Light-Promoted Radical Reaction System for Azidation and Halogenation of Tertiary Aliphatic C–H Bonds. *Chem. Sci.* **2016**, *7*, 2679–2683.
- (122) Zhang, W.; Wang, F.; McCann, S. D.; Wang, D.; Chen, P.; Stahl, S. S.; Liu, G. Enantioselective Cyanation of Benzylic C–H Bonds via Copper-Catalyzed Radical Relay. *Science* **2016**, *353*, 1014–1018.
- (123) Hu, H.; Chen, S.-J.; Mandal, M.; Pratik, S. M.; Buss, J. A.; Krska, S. W.; Cramer, C. J.; Stahl, S. S. Copper-Catalyzed Benzylic C–H Coupling with Alcohols via Radical Relay Enabled by Redox Buffering. *Nat. Catal.* **2020**, *3*, 358–367.

- (124) (a) Ni, Z.; Zhang, Q.; Xiong, T.; Zheng, Y.; Li, Y.; Zhang, H.; Zhang, J.; Liu, Q. Highly Regioselective Copper-Catalyzed Benzylic C–H Amination by *N*-Fluorobenzenesulfonimide *Angew. Chem., Int. Ed.* **2012**, *51*, 1244–1247. (b) Zhang, W.; Chen, P.; Liu, G. Copper-Catalyzed Arylation of Benzylic C–H Bonds with Alkylarenes as the Limiting Reagents. *J. Am. Chem. Soc.* **2017**, *139*, 7709–7712. (c) Zhang, W.; Wu, L.; Chen, P.; Liu, G. Enantioselective Arylation of Benzylic C–H Bonds by Copper-Catalyzed Radical Relay. *Angew. Chem. Int. Ed.* **2019**, *58*, 6425–6429. (d) Xiao, H.; Liu, Z.; Shen, H.; Zhang, B.; Zhu, L.; Li, C. Copper-Catalyzed Late-Stage Benzylic C(sp³)–H Trifluoromethylation. *Chem* **2019**, *5*, 940–949.
- (125) Complementary C–H functionalization methods showing high benzylic site selectivity have been reported recently: (a) Clark, J. R.; Feng, K.; Sookezian, A.; White, M. C. Manganese-Catalysed Benzylic C(sp³)–H Amination for Late-Stage Functionalization. *Nat. Chem.* **2018**, *10*, 583–591. (b) Tanwar, L.; Börgel, J.; Ritter, T. Synthesis of Benzylic Alcohols by C–H Oxidation. *J. Am. Chem. Soc.* **2019**, *141*, 17983–17988.
- (126) Gomberg, M. An instance of Trivalent Carbon: Triphenylmethyl. *J. Am. Chem. Soc.* **1900**, *22*, 757–771.
- (127) Jang, E. S.; McMullin, C. L.; Käß, M.; Meyer, K.; Cundari, T. R.; Warren, T. H. Copper(II) Anilides in sp³ C–H Amination. *J. Am. Chem. Soc.* **2014**, *136*, 10930–10940.
- (128) Bower, J. K.; Cypcar, A. D.; Henriquez, B.; Stieber, S. C. E.; Zhang, S. C(sp³)–H Fluorination with a Copper(II)/(III) Redox Couple. *J. Am. Chem. Soc.* **2020**, *142*, 8514–8521.
- (129) (a) Kochi, J. K. Electron-Transfer Mechanisms for Organometallic Intermediates in Catalytic Reactions. *Acc. Chem. Res.* **1974**, *7*, 351–360. (b) Jenkins, C. L.; Kochi, J. K. I. Ligand Transfer of Halides (Chloride, Bromide, Iodide) and Pseudohalides (Thiocyanate, Azide, Cyanide) from Copper(II) to Alkyl Radicals. *J. Org. Chem.* **1971**, *36*, 3095–3102. (c) Jenkins, C. L.; Kochi, J. K. II. Kinetics of Ligand Transfer Oxidation of Alkyl Radicals. Evidence for Carbonium Ion Intermediates. *J. Org. Chem.* **1971**, *36*, 3103–3111. (d) Jenkins, C. L.; Kochi, J. K. Homolytic and Ionic Mechanisms in the Ligand-Transfer Oxidation of Alkyl Radicals by Copper(II) Halides and Pseudohalides. *J. Am. Chem. Soc.* **1972**, *94*, 856–865. (e) Kochi, J. K.; Bemis, A. Carbonium Ions from Alkyl Radicals by Electron Transfer. *J. Am. Chem. Soc.* **1968**, *90*, 4038–4051. (f) Kochi, J. K.; Bemis, A.; Jenkins, C. L. Mechanism of Electron Transfer Oxidation of Alkyl Radicals by Copper(II) Complexes. *J. Am. Chem. Soc.* **1968**, *90*, 4616–4625.
- (130) Wayner, D. D. M.; McPhee, D. J.; Griller, D. Oxidation and Reduction Potentials of Transient Free Radicals. *J. Am. Chem. Soc.* **1988**, *110*, 132–137.
- (131) Control experiments show that benzyl azides can racemize under the reaction conditions. See section 4 of the Supporting Information for details, in addition to the following reference: Ott, A. A.; Topczewski, J. J. Catalytic Racemization of Activated Organic Azides *Org. Lett.* **2018**, *20*, 7253–7256.
- (132) (a) Becke, A. D. Density-Functional Thermochemistry. III. The Role of Exact Exchange. *J. Chem. Phys.* **1993**, *98*, 5648. (b) Becke, A. D. Density-functional Thermochemistry. IV. A New Dynamical Correlation Functional and Implications for Exact-exchange Mixing. *J. Chem. Phys.* **1996**, *104*, 1040.
- (133) Dolg, M.; Wedig, U.; Stoll, H.; Preuss, H. Energy-Adjusted *Ab Initio* Pseudopotentials for the First Row Transition Elements. *J. Chem. Phys.* **1987**, *86*, 866–872.
- (134) Weigend, F.; Ahlrichs, R. Balanced Basis Sets of Split Valence, Triple Zeta Valence and Quadruple Zeta Valence Quality for H to Rn: Design and Assessment of Accuracy. *Phys. Chem. Chem. Phys.* **2005**, *7*, 3297.
- (135) (a) Yamaguchi, K.; Takahara, Y.; Fueno, T.; Houk, K. N. Extended Hartree-Fock (EHF) Theory of Chemical Reactions. *Theor. Chim. Acta* **1988**, *73*, 337–364. (b) Kitagawa, Y.; Saito, K.; Yamaguchi, K. Approximate Spin Projection for Broken-Symmetry Method and Its Application in *Symmetry (Group Theory) and Mathematical Treatment in Chemistry*; IntechOpen: Rijeka, 2018; Chapter 7, p. 121-139.
- (136) Dereli, B.; Ortuño, M. A.; Cramer, C. J. Accurate Ionization Energies for Mononuclear Copper Complexes Remain a Challenge for Density Functional Theory. *ChemPhysChem* **2018**, *19*, 959–966.

-
- (137) (a) Wayner, D. D. M.; McPhee, D. J.; Griller, D. Oxidation and Reduction Potentials of Transient Free Radicals. *J. Am. Chem. Soc.* **1988**, *110*, 132–137. (b) Pavlishchuk, V. V.; Addison, A. W. Conversion Constants for Redox Potentials Measured versus Different Reference Electrodes in Acetonitrile Solutions at 25°C. *Inorganica Chim. Acta* **2000**, *298*, 97–102.
- (138) Brown, D. G.; Boström, J. Analysis of past and present synthetic methodologies on medicinal chemistry: where have all the new reactions gone?: miniperspective. *J. Med. Chem.* **2016**, *59*, 4443–4458.
- (139) Boström, J., Brown, D. G., Young, R. J.; Keserü, G. M. Expanding the medicinal chemistry synthetic toolbox. *Nat. Rev. Drug Disc.* **2018**, *17*, 709–727.
- (140) Lovering, F., Bikker, J.; Humblet, C. Escape from flatland: increasing saturation as an approach to improving clinical success. *J. Med. Chem.* **2009**, *52*, 6752–6756.
- (141) Blakemore, D. C. *et al.* Organic synthesis provides opportunities to transform drug discovery. *Nat. Chem.* **2018**, *10*, 383–394.
- (142) Cernak, T., Dykstra, K. D., Tyagarajan, S., Vachal, P.; Krska, S. W. The medicinal chemist's toolbox for late stage functionalization of drug-like molecules. *Chem. Soc. Rev.* **2016**, *45*, 546–576.
- (143) Thompson, T. N. Optimization of metabolic stability as a goal of modern drug design. *Med. Res. Rev.* **2001**, *21*, 412–449.
- (144) White, M. C.; Zhao, J. Aliphatic C–H oxidations for late-stage functionalization. *J. Am. Chem. Soc.* **2018**, *140*, 13988–14009.
- (145) Muniz, K.; Bosnidou, A. E. Intermolecular radical C(sp³)–H amination under iodine catalysis. *Angew. Chem. Int. Ed.* **2019**, *58*, 7485–7489.
- (146) Chiappini, N., Mack, J.; Du Bois, J. Intermolecular C(sp³)–H amination of complex molecules. *Angew. Chem. Int. Ed.* **2018**, *57*, 4956–4959.
- (147) Clark, J. R., Feng, K., Sookezian, A.; White, M. C. Manganese-catalysed benzylic C(sp³)–H amination for late-stage functionalization. *Nat. Chem.* **2018**, *10*, 583–591.
- (148) Davies, H. M. L.; Morton, D. Guiding principles for site selective and stereoselective intermolecular C–H functionalization by donor/acceptor rhodium carbenes. *Chem. Soc. Rev.* **2011**, *40*, 1857–1869.
- (149) Liu, W.; Groves, J. T. Manganese catalyzed C–H halogenation. *Acc. Chem. Res.* **2015**, *48*, 1727–1735.
- (150) Margrey, K. A., Czaplyski, W. L., Nicewicz, D. A.; Alexanian, E. J. A general strategy for aliphatic C–H functionalization enabled by organic photoredox catalysis. *J. Am. Chem. Soc.* **2018**, *140*, 4213–4217.
- (151) Zhang, W. *et al.* Enantioselective cyanation of benzylic C–H bonds via copper-catalyzed radical relay. *Science* **2016**, *353*, 1014–1018.
- (152) Sharma, A.; Hartwig, J. F. Metal-catalysed azidation of tertiary C–H bonds suitable for late-stage functionalization. *Nature* **2015**, *517*, 600–604.
- (153) Huang, X.; Groves, J. T. Taming azide radicals for catalytic C–H azidation. *ACS Catal.* **2016**, *6*, 751–759.
- (154) Czaplyski, W. L., Na, C. G.; Alexanian, E. J. C–H xanthylation: A synthetic platform for alkane functionalization. *J. Am. Chem. Soc.* **2016**, *138*, 13854–13857.
- (155) Vasilopoulos, A., Zultanski, S. L.; Stahl, S. S. Feedstocks to pharmacophores: Cu-catalyzed oxidative arylation of inexpensive alkylarenes enabling direct access to diarylalkanes. *J. Am. Chem. Soc.* **2017**, *139*, 7705–7708.
- (156) Wang, Z., Zheng, Z., Xu, X., Mao, J.; Walsh, P. J. One-pot aminobenzoylation of aldehydes with toluenes. *Nat. Commun.* **2018**, *9*, 3365.

-
- (157) Shield, B. J.; Doyle, A. G. Direct C(sp³)-H cross coupling enabled by catalytic generation of chlorine radicals. *J. Am. Chem. Soc.* **2016**, *138*, 12719–12722.
- (158) Heitz, D. R., Tellis, J. C.; Molander, G. A. Photochemical nickel-catalyzed C–H arylation: synthetic scope and mechanistic investigations. *J. Am. Chem. Soc.* **2016**, *138*, 12715–12718.
- (159) Perry, I. B. *et al.* Direct arylation of strong aliphatic C–H bonds. *Nature* **2018**, *560*, 70–75.
- (160) Liu, D. *et al.* Nickel-catalyzed selective oxidative radical cross-coupling: an effective strategy for inert Csp³-H functionalization. *Org. Lett.* **2015**, *17*, 998–1001.
- (161) Tran, B. L., Li, B., Driess, M.; Hartwig, J. F. Copper-catalyzed intermolecular amidation and imidation of unactivated alkanes. *J. Am. Chem. Soc.* **2014**, *136*, 2555–2563.
- (162) Miyaura, N.; Suzuki, A. Palladium-catalyzed cross-coupling reactions of organoboron compounds. *Chem. Rev.* **1995**, *95*, 2457–2483.
- (163) Ruiz-Castillo, P.; Buchwald, S. L. Applications of palladium-catalyzed C–N cross-coupling reactions. *Chem. Rev.* **2016**, *116*, 12564–12649.
- (164) Hartwig, J. F. Transition metal catalyzed synthesis of arylamines and aryl ethers from aryl halides and triflates: scope and mechanism. *Angew. Chem. Int. Ed.* **1998**, *37*, 2046–2067.
- (165) Williamson, A. Theory of ætherification. *Philos. Mag.* **1850**, *37*, 350–356.
- (166) Enthaler, S.; Company, A. Palladium-catalysed hydroxylation and alkoxylation. *Chem. Soc. Rev.* **2011**, *40*, 4912–4924.
- (167) Chapman, L. M., Beck, J. C., Wu, L.; Reisman, S. E. Enantioselective total synthesis of (+)-psiguadial B. *J. Am. Chem. Soc.* **2016**, *138*, 9803–9806.
- (168) Maloney, D. J., Chen, S.; Hecht, S. M. Stereoselective synthesis of the atropisomers of myristinin B/C. *Org. Lett.* **2006**, *8*, 1925–1927.
- (169) Lee, B. J., Deglopper, K. S.; Yoon, T. P. Site-Selective Alkoxylation of Benzylic C–H Bonds via Photoredox Catalysis. *Angew. Chem. Int. Ed.* **2020**, *59*, 197–202.
- (170) Rafiee, M., Wang, F., Hruszkewycz, D. P.; Stahl, S. S. N-Hydroxyphthalimide-mediated electrochemical iodination of methylarenes and comparison to electron-transfer-initiated C–H Functionalization. *J. Am. Chem. Soc.* **2018**, *140*, 22–25.
- (171) Zhang, W., Chen, P.; Liu, G. Copper-catalyzed arylation of benzylic C–H bonds with alkylarenes as the limiting reagents. *J. Am. Chem. Soc.* **2017**, *139*, 7709–7712.
- (172) Ni, Z. *et al.* Highly Regioselective copper-catalyzed benzylic C–H amination by N-Fluorosulfonimide. *Angew. Chem. Int. Ed.* **2012**, *51*, 1244–1247.
- (173) Yang, H. *et al.* Silver-promoted oxidative benzylic C–H trifluoromethoxylation. *Angew. Chem. Int. Ed.* **2018**, *57*, 13266–13270.
- (174) Xiao, H. *et al.* Copper-catalyzed late-stage benzylic C(sp³)-H trifluoromethylation. *Chem* **2019**, *5*, 940–949.
- (175) Janz, G. J. Cyanogen. *Inorg. Synth.* **1957**, *5*, 43–48.
- (176) Demir, A. S., Reis, Ö.; Emrullahoglu, M. Role of copper species in the oxidative dimerization of arylboronic acids: synthesis of symmetrical biaryls. *J. Org. Chem.* **2003**, *68*, 10130–10134.
- (177) Hong, Y., Yang, D., Luo, Y., Pao, C.-W., Lee, J.-F.; Lei, A. Direct observation of reduction of Cu(II) to Cu(I) by P–H compounds using XAS and EPR spectroscopy. *Organometallics* **2016**, *35*, 1426–1429.
- (178) Zhang, W., Wu, L., Chen, P.; Liu, G. Enantioselective arylation of benzylic C–H bonds via copper-catalyzed radical relay. *Angew. Chem. Int. Ed.* **2019**, *58*, 6425–6429.

-
- (179) Colomer, I., Chamberlain, A. E. R., Donohoe, T. J. Hexafluoroisopropanol as a highly versatile solvent. *Nat. Rev. Chem.* **2017**, *1*, 0088.
- (180) Bess, E. N. *et al.* Analyzing site selectivity in Rh₂(esp)₂-catalyzed intermolecular C–H amination reactions. *J. Am. Chem. Soc.* **2014**, *136*, 5783–5789.
- (181) Haines, B. E. *et al.* Cu-Catalyzed aromatic C–H imidation with N-fluorobenzenesulfonimide: mechanistic details and predictive models. *Chem. Sci.* **2017**, *8*, 988–1001.
- (182) Murphy, J. A. The Radical-Polar Crossover Reaction. In *Radicals in Organic Synthesis* (eds. P. Renaud & M. P. Sibi) 298–315 (Wiley, 2001).
- (183) Banerjee, S., Sathyamoorthi, S., Du Bois, J.; Zare, R. N. Mechanistic analysis of a copper-catalyzed C–H oxidative cyclization of carboxylic acids. *Chem. Sci.* **2017**, *8*, 7003–7008.
- (184) Solomon, E. I.; Heppner, D. E.; Johnston, E. M.; Ginsbach, J. W.; Cirera, J.; Qayyum, M.; Kieber-Emmons, M. T.; Kjaergaard, C. H.; Hadt, R. G.; Tian, L. Copper Active Sites in Biology. *Chem. Rev.* **2014**, *114*, 3659–3853.
- (185) (a) Lee, J. Y.; Karlin, K. D. Elaboration of Copper–Oxygen Mediated C–H Activation Chemistry in Consideration of Future Fuel and Feedstock Generation. *Curr. Opin. Chem. Biol.* **2015**, *25*, 184–193. (b) Trammell, R.; D’Amore, L.; Cordova, A.; Polunin, P.; Xie, N.; Siegler, M. A.; Belanzoni, P.; Swart, M.; Garcia-Bosch, I. Directed Hydroxylation of sp² and sp³ C–H Bonds Using Stoichiometric Amounts of Cu and H₂O₂. *Inorg. Chem.* **2019**, *58*, 7584–7592.
- (186) (a) Itoh, S. Developing Mononuclear Copper–Active-Oxygen Complexes Relevant to Reactive Intermediates of Biological Oxidation Reactions. *Acc. Chem. Res.* **2015**, *48*, 2066–2074. (b) Liu, J. J.; Diaz, D. E.; Quist, D. A.; Karlin, K. D. Copper(I)-Dioxygen Adducts and Copper Enzyme Mechanisms. *Isr. J. Chem.* **2016**, *56*, 738–755. (c) Elwell, C. E.; Gagnon, N. L.; Neisen, B. D.; Dhar, D.; Spaeth, A. D.; Yee, G. M.; Tolman, W. B. Copper-Oxygen Complexes Revisited: Structures, Spectroscopy, and Reactivity. *Chem. Rev.* **2017**, *117*, 2059–2107.
- (187) (a) Donoghue, P. J.; Tehranchi, J.; Cramer, C. J.; Sarangi, R.; Solomon, E. I.; Tolman, W. B. Rapid C–H Bond Activation by a Monocopper(III)–Hydroxide Complex. *J. Am. Chem. Soc.* **2011**, *133*, 17602–17605. (b) Dhar, D.; Yee, G. M.; Markle, T. F.; Mayer, J. M.; Tolman, W. B. Reactivity of the copper(III)-hydroxide unit with phenols. *Chem. Sci.* **2017**, *8*, 1075–1085. (c) Dhar, D.; Tolman, W. B. Hydrogen Atom Abstraction from Hydrocarbons by a Copper(III)-Hydroxide Complex. *J. Am. Chem. Soc.* **2015**, *137*, 1322–1329. (d) Neisen, B. D.; Gagnon, N. L.; Dhar, D.; Spaeth, A. D.; Tolman, W. B. Formally Copper(III)–Alkylperoxo Complexes as Models of Possible Intermediates in Monooxygenase Enzymes. *J. Am. Chem. Soc.* **2017**, *139*, 10220–10223. (e) Bailey, W. D.; Dhar, D.; Cramblitt, A. C.; Tolman, W. B. Mechanistic Dichotomy in Proton-Coupled Electron-Transfer Reactions of Phenols with a Copper Superoxide Complex. *J. Am. Chem. Soc.* **2019**, *141*, 5470–5480.
- (188) (a) Dhar, D.; Yee, G. M.; Spaeth, A. D.; Boyce, D. W.; Zhang, H.; Dereli, B.; Cramer, C. J.; Tolman, W. B., Perturbing the Copper(III)–Hydroxide Unit through Ligand Structural Variation, *J. Am. Chem. Soc.* **2016**, *138*, 356–368. (b) Dhar, D.; Yee, G. M.; Tolman, W. B., Effects of Charged Ligand Substituents on the Properties of the Formally Copper(III)-Hydroxide ([CuOH]²⁺) Unit. *Inorg. Chem.* **2018**, *57*, 9794–9806.
- (189) (a) Ackermann, L. Carboxylate-Assisted Transition-Metal-Catalyzed C–H Bond Functionalizations: Mechanism and Scope. *Chem. Rev.* **2011**, *111*, 1315–1345. (b) Shi, G.; Zhang, Y. Carboxylate-Directed C–H Functionalization. *Adv. Synth. Catal.* **2014**, *356*, 1419–1442. (c) Davies, D. L.; Macgregor, S. A.; McMullin, C. L. Computational Studies of Carboxylate-Assisted C–H Activation and Functionalization at Group 8–10 Transition Metal Centers. *Chem. Rev.* **2017**, *117*, 8649–8709. (d) Afreen, F.; Mathur, P.; Rheingold, A. Oxidase Studies of Some Benzimidazole Diamide Copper(II) Complexes. *Inorganica Chim. Acta* **2005**, *358*, 1125–1134.
- (190) Such reactivity has been reported for Ni complexes: Pirovano, P.; Farquhar, E. R.; Swart, M.; McDonald, A. R. Tuning the Reactivity of Terminal Nickel(III)-Oxygen Adducts for C–H Bond Activation. *J. Am. Chem. Soc.* **2016**, *138*, 14362–14370.

-
- (191) Weinberg, D. R.; Gagliardi, C. J.; Hull, J. F.; Murphy, C. F.; Kent, C. A.; Westlake, B. C.; Paul, A.; Ess, D. H.; McCafferty, D. G.; Meyer, T. J. Proton-coupled electron transfer. *Chem. Rev.* **2012**, *112*, 4016–4093.
- (192) Warren, J. J.; Tronic, T. A.; Mayer, J. M. Thermochemistry of Proton-Coupled Electron Transfer Reagents and Its Implications. *Chem. Rev.* **2010**, *110*, 6961–7001.
- (193) Hodgkiss, J. M.; Rosenthal, J.; Nocera, D. G. The Relation between Hydrogen Atom Transfer and Proton-Coupled Electron Transfer in Model Systems. In *Hydrogen-Transfer Reactions*; Hynes, J. T., Klinman, J. P., Limbach, H.-H., Schowen, R. L., Eds.; WILEY-VCH Verlag GmbH: Weinheim, 2007; pp 503–562.
- (194) (a) Hammes-Schiffer, S. Theoretical Perspectives on Proton-Coupled Electron Transfer Reactions. *Acc. Chem. Res.* **2001**, *34*, 273–281. (b) Cukier, R. I. Theory and Simulation of Proton-Coupled Electron Transfer, Hydrogen-Atom Transfer, and Proton Translocation in Proteins. *Biochim. Biophys. Acta - Bioenerg.* **2004**, *1655*, 37–44.
- (195) Klein, J. E. M. N.; Knizia, G. cPCET versus HAT: A Direct Theoretical Method for Distinguishing X–H Bond-Activation Mechanisms. *Angew. Chemie Int. Ed.* **2018**, *57*, 11913–11917.
- (196) Goetz, M. K.; Anderson, J. S. Experimental Evidence for pKa-Driven Asynchronicity in C–H Activation by a Terminal Co(III)–Oxo Complex. *J. Am. Chem. Soc.* **2019**, *141*, 4051–4062.
- (197) (a) Usharani, D.; Lacy, D. C.; Borovik, A. S.; Shaik, S. Dichotomous Hydrogen Atom Transfer vs Proton-Coupled Electron Transfer during Activation of X–H Bonds (X = C, N, O) by Nonheme Iron-Oxo Complexes of Variable Basicity. *J. Am. Chem. Soc.* **2013**, *135*, 17090–17104. (b) Geng, C.; Weiske, T.; Li, J.; Shaik, S.; Schwarz, H. Intrinsic Reactivity of Diatomic 3d Transition-Metal Carbides in the Thermal Activation of Methane: Striking Electronic Structure Effects. *J. Am. Chem. Soc.* **2019**, *141*, 599–610.
- (198) (a) Hammes-Schiffer, S. Proton-Coupled Electron Transfer: Moving Together and Charging Forward. *J. Am. Chem. Soc.* **2015**, *137*, 8860–8871. (b) Hammes-Schiffer, S.; Stuchebrukhov, A. A. Theory of Coupled Electron and Proton Transfer Reactions. *Chem. Rev.* **2010**, *110*, 6939–6960.
- (199) (a) Soudackov, A. V.; Hammes-Schiffer, S. Probing Nonadiabaticity in the Proton-Coupled Electron Transfer Reaction Catalyzed by Soybean Lipoxygenase. *J. Phys. Chem. Lett.* **2014**, *5*, 3274–3278. (b) Sirjoosingh, A.; Hammes-Schiffer, S. Proton-Coupled Electron Transfer versus Hydrogen Atom Transfer: Generation of Charge-Localized Diabatic States. *J. Phys. Chem. A* **2011**, *115*, 2367–2377. (c) Muñoz-Rugeles, L.; Alvarez-Idaboy, J. R. A Proton–Electron Sequential Transfer Mechanism: Theoretical Evidence about Its Biological Relevance. *Phys. Chem. Chem. Phys.* **2015**, *17*, 28525–28528.
- (200) Yang, L.; Powell, D. R.; Houser, R. P. Structural Variation in Copper(I) Complexes with Pyridylmethylamide Ligands: Structural Analysis with a New Four-Coordinate Geometry Index, τ_4 *Dalton Trans.*, **2007**, No. 9, 955–964.
- (201) Connelly, N. G.; Geiger, W. E. Chemical Redox Agents for Organometallic Chemistry. *Chem. Rev.* **1996**, *96*, 877–910.
- (202) Complex **403** reacts with TEMPOH with a second-order rate constant of $5.8(2) \times 10^3 \text{ M}^{-1} \text{ s}^{-1}$ at -80°C in THF (KIE = 2.6) (measured using stopped-flow kinetics), which is two orders of magnitude faster than the same reaction of **402** ($2.4 \text{ M}^{-1} \text{ s}^{-1}$, ref. *J. Am. Chem. Soc.* **2017**, *139*, 10220) but is slower than the reaction of **401**, which is too fast to be measured accurately. Because of this latter problem, we focus here instead on slower reactions with TTBP and DHA.
- (203) Brigati, G.; Lucarini, M.; Mugnaini, V.; Pedulli, G. F. Determination of the Substituent Effect on the O–H Bond Dissociation Enthalpies of Phenolic Antioxidants by the EPR Radical Equilibration Technique. *J. Org. Chem.* **2002**, *67*, 4828–4832.
- (204) Maeder, M.; King, P. *Reactlab*, Jplus Consulting Pty Ltd: East Freemantle, WA. Australia, 2009.

-
- (205) Ferguson, J.; Reeves, L. W.; Schneider, W. G. Vapor Absorption Spectra and Oscillator Strengths of Naphthalene, Anthracene and Pyrene. *Can. J. Chem.* **1957**, *35*, 1117–1123.
- (206) Comparison of the rate of decay of **403** upon treatment with DHA and DHA-d₄ (–25 °C, 500 equiv, 1,2-DFB) revealed a k_H/k_D of ~62.
- (207) Stowasser, R.; Hoffmann, R. What Do the Kohn-Sham Orbitals and Eigenvalues Mean? *J. Am. Chem. Soc.* **1999**, *121*, 3414.
- (208) Bím, D.; Maldonado-Domínguez, M.; Rulišek, L.; Srnc, M. Beyond the Classical Thermodynamic Contributions to Hydrogen Atom Abstraction Reactivity. *Proc. Natl. Acad. Sci.* **2018**, *115*, E10287–E10294.
- (209) Knizia, G. Intrinsic Atomic Orbitals: An Unbiased Bridge between Quantum Theory and Chemical Concepts. *J. Chem. Theory Comput.* **2013**, *9*, 4834–4843.
- (210) (a) Knizia, G.; Klein, J. E. M. N. Electron Flow in Reaction Mechanisms-Revealed from First Principles. *Angew. Chemie Int. Ed.* **2015**, *54*, 5518–5522. (b) Ching, W.-M.; Zhou, A.; Klein, J. E. M. N.; Fan, R.; Knizia, G.; Cramer, C. J.; Guo, Y.; Que, L. Characterization of the Fleeting Hydroxoiron(III) Complex of the Pentadentate TMC-Py Ligand. *Inorg. Chem.* **2017**, *56*, 11129–11140.
- (211) Mandal, M.; Elwell, C. E.; Bouchey, C. J.; Zerk, T. J.; Tolman, W. B.; Cramer, C. J. Mechanisms for hydrogen-atom abstraction by mononuclear copper(III) cores: Hydrogen-atom transfer or concerted proton-coupled electron transfer? *J. Am. Chem. Soc.* **2019**, *141*, 17236–17244.
- (212) Weigend, F.; Ahlrichs, R. Balanced Basis Sets of Split Valence, Triple Zeta Valence and Quadruple Zeta Valence Quality for H to Rn: Design and Assessment of Accuracy. *Phys. Chem. Chem. Phys.* **2005**, *7*, 3297–3305.
- (213) Dereli, B.; Momeni, M. R.; Cramer, C. J. Density Functional Modeling of Ligand Effects on Electronic Structure and C–H Bond Activation Activity of Copper(III) Hydroxide Compounds. *Inorg. Chem.* **2018**, *57*, 9807–9813.
- (214) Kitagawa, Y.; Saito, T.; Ito, M.; Nakanishi, Y.; Shoji, M.; Koizumi, K.; Yamanaka, S.; Kawakami, T.; Okumura, M.; Yamaguchi, K. Geometry Optimization Method Based on Approximate Spin Projection and Its Application to F₂, CH₂, CH₂OO, and Active Site of Urease. *Int. J. Quantum Chem.* **2007**, *107*, 3094–3102.
- (215) Szabo, A.; Ostlund, N. S. *Modern Quantum Chemistry*; Dover Publications: New York, 1996; Chapter 3, p 205.
- (216) Yamaguchi, K.; Takahara, Y.; Fueno, T.; Houk, K. N. Extended Hartree-Fock (EHF) Theory of Chemical Reactions. *Theor. Chim. Acta* **1988**, *73*, 337–364.
- (217) (a) Hratchian, H. P.; Schlegel, H. B. Accurate Reaction Paths Using a Hessian Based Predictor–Corrector Integrator. *J. Chem. Phys.* **2004**, *120*, 9918–9924. (b) Hratchian, H. P.; Schlegel, H. B. Using Hessian Updating To Increase the Efficiency of a Hessian Based Predictor-Corrector Reaction Path Following Method. *J. Chem. Theory Comput.* **2005**, *1*, 61–69.
- (218) Hirshfeld, F. L. Bonded-Atom Fragments for Describing Molecular Charge Densities. *Theor. Chim. Acta* **1977**, *44*, 129–138.
- (219) (a) Neese, F. The ORCA Program System. *Wiley Interdiscip. Rev. Comput. Mol. Sci.* **2012**, *2*, 73–78. (b) Neese, F. Software Update: The ORCA Program System, Version 4.0. *Wiley Interdiscip. Rev. Comput. Mol. Sci.* **2018**, *8*, e1327.
- (220) Weigend, F.; Ahlrichs, R. Balanced Basis Sets of Split Valence, Triple Zeta Valence and Quadruple Zeta Valence Quality for H to Rn: Design and Assessment of Accuracy. *Phys. Chem. Chem. Phys.* **2005**, *7*, 3297–3305.
- (221) Weigend, F. Accurate Coulomb-Fitting Basis Sets for H to Rn. *Phys. Chem. Chem. Phys.* **2006**, *8*, 1057.
- (222) (a) Knizia, G.; Klein, J. E. M. N. Electron Flow in Reaction Mechanisms-Revealed from First Principles. *Angew. Chemie Int. Ed.* **2015**, *54*, 5518–5522. (b) G. Knizia, <http://www.iboview.org/>

-
- (223) (a) Mirica, L. M.; Ottenwaelder, X.; Stack, T. D. P. Structure and Spectroscopy of Copper-Dioxygen Complexes. *Chem. Rev.* **2004**, *104*, 1013-1045. (b) Lewis, E. A.; Tolman, W. B. Reactivity of Copper-Dioxygen Systems. *Chem. Rev.* **2004**, *104*, 1047-1076.
- (224) (a) Trammell, R.; See, Y. Y.; Herrmann, A. T.; Xie, N.; Diaz, D. E.; Siegler, M. A.; Baran, P. S.; Garcia-Bosch, I. Decoding the Mechanism of Intramolecular Cu-Directed Hydroxylation of sp^3 C–H Bonds. *J. Org. Chem.* **2017**, *82*, 7887–7904. (b) Ryland, B. L.; Stahl, S. S. Practical Aerobic Oxidations of Alcohols and Amines with Homogeneous Copper/TEMPO and Related Catalyst Systems. *Angew. Chem. Int. Ed.* **2014**, *53*, 8824–8838.
- (225) (a) Ciano, L.; Davies, G. J.; Tolman, W. B.; Walton, P. H. Bracing copper for the catalytic oxidation of C–H bonds. *Nature Catal.* **2018**, *1*, 571–577. (b) Quist, D. A.; Diaz, D. E.; Liu, J. J.; Karlin, K. D. Activation of dioxygen by copper metalloproteins and insights from model complexes. *J. Biol. Inorg. Chem.* **2017**, *22*, 253–288.
- (226) (a) Gagnon, N.; Tolman, W. B. $[CuO]^+$ and $[CuOH]^{2+}$ complexes: intermediates in oxidation catalysis? *Acc. Chem. Res.* **2015**, *48*, 2126–2131. (b) Spaeth, A. D.; Gagnon, N. L.; Dhar, D.; Yee, G. M.; Tolman, W. B. Determination of the Cu(III)–OH Bond Distance by Resonance Raman Spectroscopy Using a Normalized Version of Badger's Rule. *J. Am. Chem. Soc.* **2017**, *139*, 4477–4485.
- (227) Mayer, J. M. Proton-coupled electron transfer: a reaction chemist's view. *Annu. Rev. Phys. Chem.* **2004**, *55*, 363–390.
- (228) Elwell, C. E.; Mandal, M.; Bouchev, C. J.; Que, L., Jr.; Cramer, C. J.; Tolman, W. B. Carboxylate Structural Effects on the Properties and Proton-Coupled Electron Transfer Reactivity of $[CuO_2CR]^{2+}$ Cores. *Inorg. Chem.* **2019**, *58*, 15872–15879.
- (229) Tumanov, V. E.; Denisov, E. T. Estimation of the Dissociation Energies of O–O, C–O, and O–H Bonds in Acyl Peroxides, Acids, and Esters from Kinetic Data on the Degradation of Diacyl Peroxides. *Pet. Chem.* **2004**, *45*, 237–248.
- (230) Zhao, W.; Li, G.; Tang, Z. Metal–Organic Frameworks as Emerging Platform for Supporting Isolated Single-Site Catalysts. *Nano Today* **2019**, *27*, 178–197.
- (231) (a) Wasson, M. C.; Buru, C. T.; Chen, Z.; Islamoglu, T.; Farha, O. K. Metal–Organic Frameworks: A Tunable Platform to Access Single-Site Heterogeneous Catalysts. *Appl. Catal. A Gen.* **2019**, *586*, 117214. (b) Wei, Y.-S.; Zhang, M.; Zou, R.; Xu, Q. Metal–Organic Framework-Based Catalysts with Single Metal Sites. *Chem. Rev.* **2020** (<https://dx.doi.org/10.1021/acs.chemrev.9b00757>).
- (232) Thomas, J. M.; Raja, R.; Lewis, D. W. Single-Site Heterogeneous Catalysts. *Angew. Chem. Int. Ed.* **2005**, *44*, 6456–6482.
- (233) V. Dal Santo, M. Guidotti, R. Psaro, L. Marchese, F. Carniato, C. Bisio, Rational design of single-site heterogeneous catalysts: towards high chemo-, regio- and stereoselectivity. *Proc. Roy. Soc. A* **2012**, *468*, 1904–1926.
- (234) (a) Muylaert, I.; Van Der Voort, P. Supported Vanadium Oxide in Heterogeneous Catalysis: Elucidating the Structure–Activity Relationship with Spectroscopy. *Phys. Chem. Chem. Phys.* **2009**, *11*, 2826-2832. (b) Langeslay, R. R.; Kaphan, D. M.; Marshall, C. L.; Stair, P. C.; Sattelberger, A. P.; Delferro, M. Catalytic Applications of Vanadium: A Mechanistic Perspective. *Chem. Rev.* **2019**, *119*, 2128–2191.
- (235) (a) Magg, N.; Immaraporn, B.; Giorgi, J. B.; Schroeder, T.; Bäumer, M.; Döbler, J.; Wu, Z.; Kondratenko, E.; Cherian, M.; Baerns, M.; Stair, P. C.; Sauer, J.; Freund, H.-J. Vibrational Spectra of Alumina- and Silica-Supported Vanadia Revisited: An Experimental and Theoretical Model Catalyst Study. *J. Catal.* **2004**, *226*, 88–100. (b) Beck, B.; Harth, M.; Hamilton, N. G.; Carrero, C.; Uhlrich, J. J.; Trunschke, A.; Shaikhutdinov, S.; Schubert, H.; Freund, H.-J.; Schlögl, R.; Sauer, J.; Schomäcker, R. Partial Oxidation of Ethanol on Vanadia Catalysts on Supporting Oxides with Different Redox Properties Compared to Propane. *J. Catal.* **2012**, 120–131.

- (236) Rogge, S. M. J.; Bavykina, A.; Hajek, J.; Garcia, H.; Olivos-Suarez, A. I.; Sepúlveda-Escribano, A.; Vimont, A.; Clet, G.; Bazin, P.; Kapteijn, F.; Daturi, M.; Ramos-Fernandez, E. V.; Llabre 's i Xamena, F. X.; Van Speybroeck, V.; Gascon J. Metal-Organic and Covalent Organic Frameworks as Single-Site Catalysts. *Chem. Soc. Rev.* **2017**, *46*, 3134–3184.
- (237) Cui, Y.; Rimoldi, M.; Platero-Prats, A. E.; Chapman, K. W.; Hupp, J. T.; Farha, O. K. Stabilizing a Vanadium Oxide Catalyst by Supporting on a Metal–Organic Framework. *ChemCatChem* **2018**, *10*, 1772–1777.
- (238) Thomas, J. M. The Concept, Reality and Utility of Single-Site Heterogeneous Catalysts (SSHCs). *Phys. Chem. Chem. Phys.* **2014**, *16*, 7647–7661.
- (239) Bernales, V.; Ortuño, M. A.; Truhlar, D. G.; Cramer, C. J.; Gagliardi, L. Computational Design of Functionalized Metal–Organic Frameworks Nodes for Catalysis. *ACS Cent. Sci.* **2018**, *4*, 5-19
- (240) Nguyen, H. G. T.; Schweitzer, N. M.; Chang, C. Y.; Drake, T. L.; So, M. C.; Stair, P. C.; Farha, O. K.; Hupp, J. T.; Nguyen, S. T. Vanadium-Node-Functionalized UiO-66: A Thermally Stable MOF-Supported Catalyst for the Gas-Phase Oxidative Dehydrogenation of Cyclohexene. *ACS Catal.* **2014**, *4*, 2496–2500.
- (241) Bulánek, R.; Čičmanec, P.; Kotera, J.; Boldog, I. Efficient Oxidative Dehydrogenation of Ethanol by VO_x@MIL-101: On Par with VO_x/ZrO₂ and Much Better than MIL-47(V). *Catal. Today* **2019**, *324*, 106–114.
- (242) Otake, K. I.; Cui, Y.; Buru, C. T.; Li, Z.; Hupp, J. T.; Farha, O. K. Single-Atom-Based Vanadium Oxide Catalysts Supported on Metal-Organic Frameworks: Selective Alcohol Oxidation and Structure-Activity Relationship. *J. Am. Chem. Soc.* **2018**, *140*, 8652–8656.
- (243) Planas, N.; Mondloch, J. E.; Tussupbayev, S.; Borycz, J.; Gagliardi, L.; Hupp, J. T.; Farha, O. K.; Cramer, C. J. Defining the Proton Topology of the Zr₆-Based Metal–Organic Framework NU-1000. *J. Phys. Chem. Lett.* **2014**, *5*, 3716–3723.
- (244) Otake, K.; Ye, J.; Mandal, M.; Islamoglu, T.; Buru, C. T.; Hupp, J. T.; Delferro, M.; Truhlar, D. G.; Cramer, C. J.; Farha, O. K. Enhanced Activity of Heterogeneous Pd(II) Catalysts on Acid-Functionalized Metal–Organic Frameworks. *ACS Catal.* **2019**, *9*, 5383–5390.
- (245) Andrae, D.; Häußermann, U.; Dolg, M.; Stoll, H.; Preuß, H. Energy-Adjusted *ab initio* Pseudopotentials for the Second and Third Row Transition Elements. *Theor. Chim. Acta* **1990**, *77*, 123–141.
- (246) (a) Alecu, I. M.; Zheng, J.; Zhao, Y.; Truhlar, D. G. Computational Thermochemistry: Scale Factor Databases and Scale Factors for Vibrational Frequencies Obtained from Electronic Model Chemistries. *J. Chem. Theory Comput.* **2010**, *6*, 2872–2887. (b) Kesharwani, M. K.; Brauer, B.; Martin, J. M. L. Frequency and Zero-Point Vibrational Energy Scale Factors for Double-Hybrid Density Functionals (and Other Selected Methods): Can Anharmonic Force Fields Be Avoided? *J. Phys. Chem. A* **2015**, *119*, 1701–1714.
- (247) (a) Döbler, J.; Pritzsche, M.; Sauer, J. Oxidation of Methanol to Formaldehyde on Supported Vanadium Oxide Catalysts Compared to Gas Phase Molecules. *J. Am. Chem. Soc.* **2005**, *127*, 10861–10868. (b) Kropp, T.; Paier, J.; Sauer, J. Support Effect in Oxide Catalysis: Methanol Oxidation on Vanadia/Ceria. *J. Am. Chem. Soc.* **2014**, *136*, 14616–14625.
- (248) (a) Yamaguchi, K.; Takahara, Y.; Fueno, T.; Houk, K. N. Extended Hartree-Fock (EHF) Theory of Chemical Reactions. *Theor. Chim. Acta* **1988**, *73*, 337–364. (b) Kitagawa, Y.; Saito, K.; Yamaguchi, K. Approximate Spin Projection for Broken-Symmetry Method and Its Application in *Symmetry (Group Theory) and Mathematical Treatment in Chemistry*; IntechOpen: Rijeka, 2018; Chapter 7, pp. 121-139.
- (249) Dhar, D.; Yee, G. M.; Spaeth, A. D.; Boyce, D. W.; Zhang, H.; Dereli, B.; Cramer, C. J.; Tolman, W. B. Perturbing the Copper(III)-Hydroxide Unit through Ligand Structural Variation. *J. Am. Chem. Soc.* **2016**, *138*, 356–368.
- (250) Keller, D. E.; Visser, T.; Soulimani, F.; Koningsberger, D. C.; Weckhuysen, B. M. Hydration Effects on the Molecular Structure of Silica-Supported Vanadium Oxide Catalysts: A Combined IR, Raman, UV-Vis and EXAFS Study. *Vib. Spectrosc.* **2007**, *43*, 140–151.

- (251) (a) Hofmann, A.; Ganduglia-Pirovano, M. V.; Sauer, J. Vanadia and Water Coadsorption on Tetragonal Zirconia Surfaces. *J. Phys. Chem. C* **2009**, *113*, 18191–18203. (b) Sauer, J.; Pritzsche, M.; Döbler, J. Catalytically Active Vanadia Species on Silica: Effect of Oxygen and Water. *J. Phys. Chem. C* **2014**, *118*, 29159–29163.
- (252) (a) Ruitenbeek, M.; van Dillen, A. J.; de Groot, F. M. F.; Wachs, I. E.; Geus, J. W.; Koningsberger, D. C. The Structure of Vanadium Oxide Species on γ -Alumina; an in Situ X-Ray Absorption Study during Catalytic Oxidation. *Top. Catal.* **2000**, *10*, 241–254. (b) Weckhuysen, B. M.; Jehng, J.-M.; Wachs, I. E. In Situ Raman Spectroscopy of Supported Transition Metal Oxide Catalysts: $^{18}\text{O}_2$ – $^{16}\text{O}_2$ Isotopic Labeling Studies. *J. Phys. Chem. B* **2000**, *104*, 7382–7387. (c) Busca, G. Differentiation of Mono-Oxo and Polyoxo and of Monomeric and Polymeric Vanadate, Molybdate and Tungstate Species in Metal Oxide Catalysts by IR and Raman Spectroscopy. *J. Raman Spectrosc.* **2002**, *33*, 348–358.
- (253) (a) Gijzeman, O. L. J.; van Lingen, J. N. J.; van Lenthe, J. H.; Tinnemans, S. J.; Keller, D. E.; Weckhuysen, B. M. A New Model for the Molecular Structure of Supported Vanadium Oxide Catalysts. *Chem. Phys. Lett.* **2004**, *397*, 277–281. (b) Ding, X.-L.; Xue, W.; Ma, Y.-P.; Zhao, Y.-X.; Wu, X.-N.; He, S.-G. Theoretical Investigation of the Selective Oxidation of Methanol to Formaldehyde on Vanadium Oxide Species Supported on Silica: Umbrella Model. *J. Phys. Chem. C* **2010**, *114*, 3161–3169.
- (254) Butler, A.; Walker, J. V. Marine Haloperoxidases. *Chem. Rev.* **1993**, *93*, 1937–1944.
- (255) (a) Waidmann, C. R.; DiPasquale, A. G.; Mayer, J. M. Synthesis and Reactivity of Oxo-Peroxy-Vanadium(V) Bipyridine Compounds. *Inorg. Chem.* **2010**, *49*, 2383–2391. (b) Palmajumder, E.; Patra, S.; Drew, M. G. B.; Mukherjee, K. K. Vanadium Bromoperoxidase (VBrPO) Mimics: Synthesis, Structure and a Comparative Account of the Catalytic Activity of Newly Synthesized Oxidovanadium and Oxido-Peroxidovanadium Complexes. *New J. Chem.* **2016**, *40*, 8696–8703.
- (256) Molinari, J. E.; Wachs, I. E. Presence of Surface Vanadium Peroxo-Oxo Umbrella Structures in Supported Vanadium Oxide Catalysts: Fact or Fiction? *J. Am. Chem. Soc.* **2010**, *132*, 12559–12561.
- (257) Yang, D.; Bernales, V.; Islamoglu, T.; Farha, O. K.; Hupp, J. T.; Cramer, C. J.; Gagliardi, L.; Gates, B. C. Tuning the Surface Chemistry of Metal Organic Framework Nodes: Proton Topology of the Metal-Oxide-Like Zr_6 Nodes of UiO-66 and NU-1000. *J. Am. Chem. Soc.* **2016**, *138*, 15189–15196.
- (258) Goodrow, A.; Bell, A. T. A Theoretical Investigation of the Selective Oxidation of Methanol to Formaldehyde on Isolated Vanadate Species Supported on Silica. *J. Phys. Chem. C* **2007**, *111*, 14753–14761.
- (259) Knizia, G. Intrinsic Atomic Orbitals: An Unbiased Bridge between Quantum Theory and Chemical Concepts. *J. Chem. Theory Comput.* **2013**, *9*, 4834–4843.
- (260) Klein, J. E. M. N.; Knizia, G. cPCET versus HAT: A Direct Theoretical Method for Distinguishing X–H Bond-Activation Mechanisms. *Angew. Chem. Int. Ed.* **2018**, *57*, 11913–11917.
- (261) Mandal, M.; Cramer, C. J.; Truhlar, D. G.; Sauer, J.; Gagliardi, L. Structure and reactivity of metal–organic framework supported single-site heterogeneous vanadium catalyst. *Submitted*
- (262) (a) Pelletier, J. D. A.; Basset, J. M. Catalysis by Design: Well-Defined Single-Site Heterogeneous Catalysts. *Acc. Chem. Res.* **2016**, *49*, 664–677. (b) Dal Santo, V.; Guidotti, M.; Psaro, R.; Marchese, L.; Carniato, F.; Bisio, C. Rational Design of Single-site Heterogeneous Catalysts: Towards High Chemo-, Regio- and Stereoselectivity. *Proc. R. Soc. A Math. Phys. Eng. Sci.* **2012**, *468*, 1904–1926.
- (263) (a) Thomas, J. M. The Societal Significance of Catalysis and the Growing Practical Importance of Single-site Heterogeneous Catalysts. *Proc. R. Soc. A Math. Phys. Eng. Sci.* **2012**, *468*, 1884–1903. (b) Groppo, E.; Lamberti, C.; Bordiga, S.; Spoto, G.; Zecchina, A. The Structure of Active Centers and the Ethylene Polymerization Mechanism on the Cr/SiO₂ Catalyst: A Frontier for the Characterization Methods. *Chem. Rev.* **2005**, *105*, 115–183. (c) Hlatky, G. G. Heterogeneous Single-Site Catalysts for Olefin Polymerization. *Chem. Rev.* **2000**, *100*, 1347–1376.

- (264) (a) Gu, W.; Stalzer, M. M.; Nicholas, C. P.; Bhattacharyya, A.; Motta, A.; Gallagher, J. R.; Zhang, G.; Miller, J. T.; Kobayashi, T.; Pruski, M.; Delferro, M.; Marks, T. J. Benzene Selectivity in Competitive Arene Hydrogenation: Effects of Single-Site Catalyst...Acidic Oxide Surface Binding Geometry. *J. Am. Chem. Soc.* **2015**, *137*, 6770–6780. (b) Klet, R. C.; Kaphan, D. M.; Liu, C.; Yang, C.; Kropf, A. J.; Perras, F. A.; Pruski, M.; Hock, A. S.; Delferro, M., Evidence for Redox Mechanisms in Organometallic Chemisorption and Reactivity on Sulfated Metal Oxides. *J. Am. Chem. Soc.* **2018**, *140*, 6308–6316. (c) Kaphan, D. M.; Klet, R. C.; Perras, F. A.; Pruski, M.; Yang, C.; Kropf, A. J.; Delferro, M., Surface Organometallic Chemistry of Supported Iridium(III) as a Probe for Organotransition Metal–Support Interactions in C–H Activation. *ACS Catal.* **2018**, *8*, 5363–5373.
- (265) (a) Kaur, K.; Wanchoo, R. K.; Toor, A. P. Sulfated Iron Oxide: A Proficient Catalyst for Esterification of Butanoic Acid with Glycerol. *Ind. Eng. Chem. Res.* **2015**, *54*, 3285–3292. (b) Il Kim, S.; Ihl Woo, S. The Effect of Modifying Alumina with Sulfate and Phosphate on the Catalytic Properties of Mo/Al₂O₃ in HDS Reaction. *J. Catal.* **1992**, *133*, 124–135. (c) Arata, K.; Matsushashi, H.; Hino, M.; Nakamura, H. Synthesis of Solid Superacids and Their Activities for Reactions of Alkanes. *Catal. Today* **2003**, *81*, 17–30.
- (266) (a) Corma, A. Inorganic Solid Acids and Their Use in Acid-Catalyzed Hydrocarbon Reactions. *Chem. Rev.* **1995**, *95*, 559–614. (b) Ma, Y.; Tong, H.; Zou, H.; Suib, S. L. A review of zeolite-like porous materials. *Micro. Mes. Mater.* **2000**, *37*, 243–252. (c) Zhang, H.; Hardy, G. C.; Khimiyak, Y. Z.; Rosseinsky, M. J.; Cooper, A. I. Synthesis of Hierarchically Porous Silica and Metal Oxide Beads Using Emulsion-Templated Polymer Scaffolds. *Chem. Mater.* **2004**, *16*, 4245–4256. (d) Småtå, J. H.; Weidenthaler, C.; Rosenholm, J. B.; Lindén, M. Hierarchically Porous Metal Oxide Monoliths Prepared by the Nanocasting Route. *Chem. Mater.* **2006**, *18*, 1443–1450.
- (267) (a) Eddaoudi, M.; Sava, D. F.; Eubank, J. F.; Adil, K.; Guillerme, V. Zeolite-like Metal–Organic Frameworks (ZMOFs): Design, Synthesis, and Properties. *Chem. Soc. Rev.* **2015**, *44*, 228–249. (b) Furukawa, H.; Cordova, K. E.; O’Keeffe, M.; Yaghi, O. M., The Chemistry and Applications of Metal–Organic Frameworks. *Science* **2013**, *341*, 6149. (c) O’Keeffe, M.; Yaghi, O. M. Deconstructing the Crystal Structures of Metal–Organic Frameworks and Related Materials into Their Underlying Nets. *Chem. Rev.* **2012**, *112*, 675–702. (d) Li, J.-R.; Kuppler, R. J.; Zhou, H.-C. Selective Gas Adsorption and Separation in Metal–Organic Frameworks. *Chem. Soc. Rev.* **2009**, *38*, 1477–1504. (e) Lee, J.; Farha, O. K.; Roberts, J.; Scheidt, K. A.; Nguyen, S. T.; Hupp, J. T. Metal–Organic Framework Materials as Catalysts. *Chem. Soc. Rev.* **2009**, *38*, 1450–1459. (23) Ferey, G.; Serre, C. Large Breathing Effects in Three-dimensional Porous Hybrid Matter: Facts, Analyses, Rules and Consequences. *Chem. Soc. Rev.* **2009**, *38*, 1380–1399.
- (268) (a) Mondloch, J. E.; Bury, W.; Fairen-Jimenez, D.; Kwon, S.; DeMarco, E. J.; Weston, M. H.; Sarjeant, A. A.; Nguyen, S. T.; Stair, P. C.; Snurr, R. Q.; Farha, O. K.; Hupp, J. T., Vapor-Phase Metalation by Atomic Layer Deposition in a Metal–Organic Framework. *J. Am. Chem. Soc.* **2013**, *135*, 10294–10297. (b) Li, Z.; Peters, A. W.; Platero-Prats, A. E.; Liu, J.; Kung, C.-W.; Noh, H.; DeStefano, M. R.; Schweitzer, N. M.; Chapman, K. W.; Hupp, J. T.; Farha, O. K., Fine-Tuning the Activity of Metal–Organic Framework-Supported Cobalt Catalysts for the Oxidative Dehydrogenation of Propane. *J. Am. Chem. Soc.* **2017**, *139*, 15251–15258. (c) Islamoglu, T.; Goswami, S.; Li, Z.; Howarth, A. J.; Farha, O. K.; Hupp, J. T. Postsynthetic Tuning of Metal–Organic Frameworks for Targeted Applications. *Acc. Chem. Res.* **2017**, *50*, 805–813.
- (269) (a) Peng, Y.; Huang, H.; Zhang, Y.; Kang, C.; Chen, S.; Song, L.; Liu, D.; Zhong, C. A versatile MOF-based trap for heavy metal ion capture and dispersion. *Nat. Commun.* **2018**, *9*, 187. (b) Elumalai, P.; Mamlouk, H.; Yiming, W.; Feng, L.; Yuan, S.; Zhou, H.-C., Recyclable and Reusable Heteroleptic Nickel Catalyst Immobilized on Metal–Organic Framework for Suzuki–Miyaura Coupling. *ACS Appl. Mater. Interfaces* **2018**, *10*, 41431–41438. (c) Ji, P.; Manna, K.; Lin, Z.; Feng, X.; Urban, A.; Song, Y.; Lin, W., Single-Site Cobalt Catalysts at New Zr₁₂(μ₃-O)₈(μ₃-OH)₈(μ₂-OH)₆ Metal–Organic Framework Nodes for Highly Active Hydrogenation of Nitroarenes, Nitriles, and Isocyanides. *J. Am. Chem. Soc.* **2017**, *139*, 7004–7011. (d) Noh, H.; Cui, Y.; Peters, A. W.; Pahls, D. R.; Ortuño, M. A.; Vermeulen, N. A.; Cramer, C. J.; Gagliardi, L.; Hupp, J. T.; Farha, O. K., An Exceptionally Stable Metal–Organic Framework Supported Molybdenum(VI) Oxide Catalyst for Cyclohexene Epoxidation. *J. Am. Chem. Soc.* **2016**, *138*, 14720–14726. (e) Kim, I. S.; Li, Z.; Zheng, J.; Platero-Prats, A. E.; Mavrandonakis, A.; Pellizzeri, S.; Ferrandon, M.; Vjunov, A.; Gallington, A.; Webber, T.; Vermeulen, N. A.; Lee Penn, R.; Getman, R. B.; Cramer, C. J.; Chapman, K. W.; Camaioni, D. M.; Fulton, J.L.; Lercher, J.A.; Farha, O. K.; Hupp,

-
- J. T.; Martinson, A. B. F., Sinter-Resistant Platinum Catalyst Supported by Metal–Organic Framework. *Angew. Chem. Int. Ed.* **2018**, *57*, 909–913. (f) Yang, D.; Odoh, S. O.; Wang, T. C.; Farha, O. K.; Hupp, J. T.; Cramer, C. J.; Gagliardi, L.; Gates, B. C., Metal–Organic Framework Nodes as Nearly Ideal Supports for Molecular Catalysts: NU-1000- and UiO-66-Supported Iridium Complexes. *J. Am. Chem. Soc.* **2015**, *137*, 7391–7396.
- (270) (a) Jiang, J.; Yaghi, O. M. Brønsted Acidity in Metal–Organic Frameworks. *Chem. Rev.* **2015**, *115*, 6966–6997. (b) Howarth, A. J.; Wang, T. C.; Al-Juaid, S. S.; Aziz, S. G.; Hupp, J. T.; Farha, O. K. Efficient Extraction of Sulfate from Water using a Zr-Metal–Organic Framework. *Dalt. Trans.* **2016**, *45*, 93–97. (c) Furukawa, H.; Gándara, F.; Zhang, Y.-B.; Jiang, J.; Queen, W. L.; Hudson, M. R.; Yaghi, O. M. Water Adsorption in Porous Metal–Organic Frameworks and Related Materials. *J. Am. Chem. Soc.* **2014**, *136*, 4369–4381. (d) Jiang, J.; Gándara, F.; Zhang, Y. B.; Na, K.; Yaghi, O. M.; Klemperer, W. G. Superacidity in Sulfated Metal–Organic Framework-808. *J. Am. Chem. Soc.* **2014**, *136*, 12844–12847.
- (271) Trickett, C. A.; Osborn Popp, T. M.; Su, J.; Yan, C.; Weisberg, J.; Huq, A.; Urban, P.; Jiang, J.; Kalmutzki, M. J.; Liu, Q.; Baek, J.; Head-Gordon, M. P.; Somorjai, G. A.; Reimer, J. A.; Yaghi, O. M. Identification of the Strong Brønsted Acid Site in a Metal–Organic Framework Solid Acid Catalyst. *Nature Chem.*, **2018**, *11*, 170–176.
- (272) (a) Larsen, G.; Lotero, E.; Parra, R. D.; Petkovic, L. M.; Silva, H. S.; Raghavan, S. Characterization of Palladium Supported on Sulfated Zirconia Catalysts by DRIFTS, XAS and n-butane Isomerization Reaction in the Presence of Hydrogen. *Appl. Catal. A, Gen.* **1995**, *130*, 213–226. (b) Dong, J.; Wang, J.; Wang, J.; Yang, M.; Li, W.; Shen, M. Enhanced Thermal Stability of Palladium Oxidation Catalysts using Phosphate-modified Alumina Supports. *Catal. Sci. Technol.* **2017**, *7*, 5038–5048.
- (273) (a) Echavarren, A. M. Nobel Prize Awarded for Catalysis. *ChemCatChem.* **2010**, *2*, 1331–1332. (b) Johansson Seechurn, C. C. C.; Kitching, M. O.; Colacot, T. J.; Snieckus, V. Palladium-catalyzed cross-coupling: a historical contextual perspective to the 2010 Nobel Prize. *Angew. Chem. Int. Ed.* **2012**, *51*, 5062–5085. (c) Pagliaro, M.; Pandarus, V.; Ciriminna, R.; Béland, F.; DemmaCarà, P. Heterogeneous versus Homogeneous Palladium Catalysts for Cross-Coupling Reactions. *ChemCatChem* **2012**, *4*, 432–445. (d) Molnár, Á. Efficient, Selective, and Recyclable Palladium Catalysts in Carbon–Carbon Coupling Reactions. *Chem. Rev.* **2011**, *111*, 2251–2320.
- (274) (a) Engle, K. M.; Wang, D. H.; Yu, J. Q. Ligand-Accelerated C–H Activation Reactions: Evidence for a Switch of Mechanism. *J. Am. Chem. Soc.* **2010**, *132*, 14137–14151. (b) Liu, Z.; Derosa, J.; Engle, K. M. Palladium(II)-Catalyzed Regioselective syn-Hydroarylation of Disubstituted Alkynes Using a Removable Directing Group. *J. Am. Chem. Soc.* **2016**, *138*, 13076–13081. (c) Ruan, J.; Li, X.; Saidi, O.; Xiao, J. Oxygen and Base-Free Oxidative Heck Reactions of Arylboronic Acids with Olefins. *J. Am. Chem. Soc.* **2008**, *130*, 2424–2425. (d) Zhou, Y. B.; Wang, Y. Q.; Ning, L. C.; Ding, Z. C.; Wang, W. L.; Ding, C. K.; Li, R. H.; Chen, J. J.; Lu, X.; Ding, Y. J.; Zhan, Z. P. Conjugated Microporous Polymer as Heterogeneous Ligand for Highly Selective Oxidative Heck Reaction. *J. Am. Chem. Soc.* **2017**, *139*, 3966–3969. (e) Velthoven, N. V.; Waitschat, S.; Chavan, S. M.; Liu, P.; Smolders, S.; Vercammen, J.; Bueken, B.; Bals, S.; Lillerud, K. P.; Stock, N.; De Vos, D. E. Single-site metal–organic framework catalysts for the oxidative coupling of arenes via C–H/C–H activation. *Chem. Sci.* **2019**, *10*, 3616–3622.
- (275) (a) Duan, H.; Li, M.; Zhang, G.; Gallagher, J. R.; Huang, Z.; Sun, Y.; Luo, Z.; Chen, H.; Miller, J. T.; Zou, R.; Lei, A.; Zhao, Y. Single-Site Palladium(II) Catalyst for Oxidative Heck Reaction: Catalytic Performance and Kinetic Investigations. *ACS Catal.* **2015**, *5*, 3752–3759. (b) Zhang, C.; Ji, J.; Sun, P. Palladium-Catalyzed Alkenylation via sp² C–H Bond Activation Using Phenolic Hydroxyl as the Directing Group. *J. Org. Chem.* **2014**, *79*, 3200–3205.